



Schriftenreihe Lehrstuhl Hybride Konstruktionen - Massivbau
Brandenburgische Technische Universität Cottbus-Senftenberg

Yangwen Zhang

**Self-sufficient semi-active vibration control
of high-rise buildings under wind excitation
by moveable double-skin facades**

Herausgeber

Univ.-Prof. Dr.-Ing. Achim Bleicher

Lehrstuhl Hybride Konstruktionen - Massivbau

Impressum

Brandenburgische Technische Universität Cottbus-Senftenberg

Univ.-Prof. Dr.-Ing. Achim Bleicher

Lehrstuhl Hybride Konstruktionen - Massivbau

Konrad-Wachsmann-Allee 2

03046 Cottbus

T +49 (0)355 69 – 2471

F +49 (0)355 69 – 2478

E fg-hybride-konstruktionen-massivbau@b-tu.de

www.b-tu.de/fg-hybride-konstruktionen-massivbau

Veröffentlicht unter einer „CC BY 4.0“-Lizenz unter der Autorenschaft von Yangwen Zhang

Titelbild: Demonstrator einer adaptiven Doppelfassade, © Multimediazentrum/BTU-CS

Schriftenreihe Hybride Konstruktionen - Massivbau

2023 - Heft 15

ISSN 2569-2798

DOI: <https://doi.org/10.26127/BTUOpen-6381>

Self-sufficient semi-active vibration control of high-rise buildings under wind excitation by moveable double-skin facades

Von der Fakultät für Architektur, Bauingenieurwesen und Stadtplanung
der Brandenburgischen Technischen Universität Cottbus-Senftenberg
zur Erlangung des akademischen Grades eines

Doktor der Ingenieurwissenschaften
- Dr.-Ing. -

genehmigte Dissertation

vorgelegt von

Master of Science

Yangwen Zhang

aus Zhejiang, China

Gutachter: Prof. Dr.-Ing. Achim Bleicher, BTU Cottbus-Senftenberg

Gutachter: Prof. Dr. Di Su, University of Tokyo

Gutachter: Dr. Thomas Schauer, TU Berlin

Tag der Disputation: 06. Januar 2023

Abstract

Self-sufficient semi-active vibration control of high-rise buildings under wind excitation by moveable double-skin facades

The accelerated urbanization has led to increasing tension on urban land use. In this context, more and more slender high-rise buildings are being built worldwide in pursuit of better economic benefits. However, these structures are susceptible to wind excitation due to their lower first natural frequency. Different passive, semi-active, and active damping systems have been developed to reduce wind-induced structural vibration. Among them, the tuned mass dampers are widely used and proved as a very effective method in practice. However, this system requires a large additional damping mass. This also causes additional reinforcement, which increases the cost and carbon footprint. A huge space near the top story of the building is needed for the installation. In this research, a novel system named distributed-Multiple Tuned Facade Damping (d-MTFD) system is proposed by using specially designed parallel moveable Double-Skin Facade (DSF) outer skin as damping mass. These moveable facade elements can be installed on the upper stories of the high-rise building. Smooth-running guide rail systems are used to achieve the parallel moveability. Multi-objective optimization based on the Genetic Algorithm (GA) is applied to reduce the maximum top floor acceleration (Objective I) and to reduce the maximum facade relative displacement (Objective II) simultaneously. The optimization results for the passive and semi-active systems are presented in the form of the Pareto front. The trade-off between these selected two competing optimization objectives is observed. This approach was first validated in a simulation using a 306 m tall reference building for a wind speed of 13.5 m/s at 10 m above ground level with a return period of 10 years. Acceptable peak accelerations at the top story for hotel use and a maximum facade relative displacement of less than ± 0.5 m could be achieved for the benchmark building with the d-MTFD system. For semi-active control, the variable damping coefficient can be achieved by using stepper motors in generator mode. The electrical damping coefficient can be continuously adjusted by the developed power electronics. In addition, electrical energy can be generated and stored in a battery. A full-scale prototype with one parallel moveable facade element was built. Based on the prototype, the functionality of the semi-active control using a stepper motor and its energy harvesting performance was tested by applying Hardware-in-the-Loop (HiL) simulations. Grey-box system identification was used to estimate some parameters (spring stiffness, friction, etc.) in the connection. The accurate system identification results ensure further validation using HiL simulations. The HiL simulations successfully demonstrated the feasibility of a self-powered semi-active d-MTFD system.

Keyword: moveable facade, kinetic facade, Double-Skin Facade (DSF), distributed-Multiple Tuned Facade Damping (d-MTFD) system, energy harvesting, wind-induced vibration, semi-active vibration control, super-slender tall building, power electronics, multi-objective optimization, Genetic Algorithm (GA), ground-hook control, system identification, Hardware-in-the-Loop (HiL) simulation, prototype, electric damper, resource efficiency.

Zusammenfassung

Autarke semi-aktive Schwingungskontrolle von Hochhäusern unter Windanregung durch bewegliche Doppelfassaden

Die beschleunigte Urbanisierung hat zu zunehmenden Spannungen über der Flächen-nutzung in den Städten geführt. In diesem Zusammenhang werden weltweit immer mehr schlanke Hochhäuser gebaut, um einen besseren wirtschaftlichen Nutzen zu erzielen. Diese Strukturen sind jedoch aufgrund ihrer niedrigeren ersten Eigenfrequenz anfällig für dynamische Windlasten. Es wurden verschiedene passive, semi-aktive und aktive Dämpfungssysteme entwickelt, um windinduzierte Strukturschwingungen zu reduzieren. Unter ihnen sind die abgestimmten Massendämpfer weit verbreitet und haben sich in der Praxis als sehr wirksame Methode erwiesen. Dieses System erfordert jedoch eine große zusätzliche Dämpfungsmasse. Dies führt auch zu einer zusätzlichen Verstärkung des Tragwerks, was die Kosten und den CO₂-Fußabdruck erhöht. Für die Installation wird ein großer Raum in den obersten Stockwerken des Gebäudes benötigt. In dieser Arbeit wird ein innovatives System mit der Bezeichnung "distributed-Multiple Tuned Facade Damping (d-MTFD) System" vorgestellt, bei dem eine speziell entwickelte, parallel bewegliche Außenhaut der Doppelfassade (DSF) als Dämpfungsmasse verwendet wird. Diese beweglichen Fassadenelemente können in den oberen Stockwerken des Hochhauses installiert werden. Um die parallele Verschiebbarkeit zu erreichen, werden leichtgängige Führungsschienensysteme eingesetzt. Eine multikriterielle Optimierung mittels des genetischen Algorithmus (GA) wird angewandt, um gleichzeitig die maximale Beschleunigung im obersten Stockwerk (Ziel I) und die maximale Verschiebung zwischen der Primärstruktur und der beweglichen Außenhaut (Ziel II) zu reduzieren. Die Optimierungsergebnisse für die passiven und semiaktiven Systeme werden in Form der Pareto-Front dargestellt. Der Kompromiss zwischen diesen beiden ausgewählten konkurrierenden Optimierungszielen wird beobachtet. Dieser Ansatz wurde zunächst in einer Simulation mit einem 306 m hohen Referenzgebäude für eine Windgeschwindigkeit von 13,5 m/s in 10 m Höhe über Grund mit einer Wiederkehrperiode von 10 Jahren validiert. Mit dem d-MTFD System konnten für das Referenzgebäude akzeptable Spitzenbeschleunigungen im obersten Stockwerk für die Hotelnutzung und eine maximale Fassaden-Relativverschiebung von weniger als $\pm 0,5$ m erreicht werden. Bei der semiaktiven Regelung kann der variable Dämpfungskoeffizient durch den Einsatz von Schrittmotoren im Generatorbetrieb erreicht werden. Der elektrische Dämpfungskoeffizient kann durch die entwickelte Leistungselektronik stufenlos eingestellt werden. Darüber hinaus kann elektrische Energie erzeugt und in einer Batterie gespeichert werden. Ein maßstäblicher Prototyp mit einem parallel beweglichen Fassadenelement wurde gebaut. Anhand des Prototyps wurden die Funktionalität der semiaktiven Regelung unter Verwendung eines Schrittmotors und die Leistung der Energiegewinnung mittels Hardware-in-the-Loop (HiL)-Simulationen getestet. Die Grey-Box-Systemidentifikation wird zur Schätzung der Parameter (Federsteifigkeit, Reibung, usw.) in der Verbindung verwendet. Die genauen Ergebnisse der Systemidentifikation gewährleisten eine weitere Validierung durch HiL-Simulationen. Die HiL-Simulationen haben erfolgreich die Machbarkeit eines autarken semiaktiven d-MTFD Systems demonstriert.

Keyword: bewegliche Fassade, kinetische Fassade, Doppelfassade, Energiegewinnung, Distributed-Multiple Tuned Facade Damping (d-MTFD) System, windinduzierte Schwingungen, semi-aktive Schwingungskontrolle, superschlankes Hochhaus, Leistungselektronik, multi-kriterielle Optimierung, Genetischer Algorithmus (GA), Ground-Hook-Regelung, Systemidentifikation, Hardware-in-the-Loop (HiL)-Simulation, Prototyp, elektrischer Dämpfer, Ressourceneffizienz

Acknowledgments

I would like to express my utmost appreciation to my professor, Achim Bleicher. He consistently reminded me that research serves to solve engineering problems and guided me to approach my research with this mindset. His expertise and insights have been instrumental in the successful completion of my research.

I would also like to express my gratitude to Dr. Thomas Schauer for his invaluable guidance and support throughout my research program. He introduced me to the world of control engineering and made me passionate about this field. His extensive knowledge and expertise have been critical in shaping my research, and I am deeply grateful for his valuable suggestions, and constant encouragement.

I appreciate the opportunity to participate in the BBSR Zukunft Bau project. The support and resources provided by the project were essential in enabling me to conduct my research successfully. I am grateful for the collaboration with my colleagues Laurenz Wernicke and Wulf Wulff, as well as our industrial partner Gartner GmbH, who helped us build the prototype. Special thanks to Dr. Michael Engelmann, who provided guidance and expertise in the development of the prototype.

Additionally, I would like to express my gratitude to Associate Professor Di Su and Professor Tomonori Nagayama from the University of Tokyo for inviting me for academic exchange. Their mentorship and support allowed me to expand my research in the field of structural health monitoring, and I gained valuable knowledge from working with colleagues in their department.

Furthermore, I also want to thank all my friends and colleagues, Dr. Yue Liu, Dr. Qianwen He, Dr. Zheng Li, Jian Wang, Robert Jirasek, Paul Marker, Tim Höltnke, etc., who have supported me through thick and thin during my PhD journey. Their emotional support, encouragement, and advice have been a constant source of motivation.

I would like to acknowledge the financial support provided by the Graduate Research School (GRS) in the form of the Graduiertenförderungsverordnung (GradV) scholarship. The scholarship allowed me to focus on my research program without worrying about financial constraints, and I am grateful for their support.

Lastly, I would like to express my thanks and apologies to my family. The loss of my father and my grandmother during my PhD was a profound sadness for me. I regret that I could not be around them as much as I would have liked. I will carry their memories and values with me

in all that I do. I would like to express my deepest gratitude and appreciation to my mother. She is a strong woman who has been a constant source of encouragement and inspiration to me. Thanks to my family for being my pillars of strength and believing in me. I would also like to express gratitude to myself for remaining optimistic despite all that I've been through during my PhD. I have experienced difficult times personally and academically, but I am grateful for the strength and resilience that have helped me overcome these obstacles. I firmly believe that everything that doesn't kill me only makes me stronger, and I am thankful for the lessons learned and personal growth achieved.

Contents

Abstract	i
Zusammenfassung	iii
Acknowledgements	v
List of Tables	xi
List of Figures	xiii
List of Abbreviations and Symbols	xvii
1 Introduction	1
1.1 Research background	3
1.1.1 Emergence of super-slender high-rise buildings	3
1.1.2 Vibration problem of high-rise buildings and solutions	4
1.1.3 Double-Skin Facade (DSF) and its potential use for vibration suppression	5
1.2 Research objective and structure of dissertation	7
1.3 Main contributions	10
1.4 Publications	11
2 Literature review	13
2.1 Energy dissipating damping systems	15
2.2 Auxiliary mass damping systems	17
2.2.1 Tuned Mass Dampers (TMDs)	17
2.2.2 Multiple Tuned Mass Dampers (MTMDs)	19
2.2.3 Distributed-Multiple Tuned Mass Dampers (d-MTMDs)	21
2.3 Vibration control using moveable facade	23
2.3.1 Double-Skin Facade (DSF)	23
2.3.2 Facade isolation	25
2.3.3 Facade as damping mass	27
2.4 Dual-functional dampers with energy harvesting	29

2.5	Active control systems	30
2.6	Conclusions	32
3	Conceptual analysis using a 2DoF model	35
3.1	Facade isolation using perpendicular connection	37
3.1.1	System modeling	37
3.1.2	Parametric studies of the vibration behavior	38
3.1.3	Parametric studies of energy harvesting	40
3.2	Facade damping using parallel connection	42
3.2.1	System modeling	42
3.2.2	Parametric studies of the vibration behavior	43
3.2.3	Parametric studies of energy harvesting	44
3.3	Conclusion	44
4	System modeling	47
4.1	Structural modeling	49
4.2	Benchmark building with d-MTFD system	52
4.3	Wind modeling	54
4.4	Conclusion and remark	55
5	Passive/semi-active system optimization	57
5.1	Methods	59
5.1.1	Multi-objective GA optimization	59
5.1.2	Semi-active control algorithms	60
5.1.3	Multi-objective GA optimized semi-active d-MTFD system	61
5.2	Numerical simulation and results analysis	62
5.2.1	Optimized passive d-MTFD system	62
5.2.2	Optimized semi-active d-MTFD system	65
5.3	Discussion	70
5.4	Conclusions	71
6	Electric machine modeling and circuit design	73
6.1	linear to rotational motion conversion	77
6.2	Electric machine modeling	77
6.2.1	Modeling of DC motor/generator	77
6.2.2	Modeling of hybrid stepper motor/generator	80
6.3	Power electronics for resistance emulation and energy harvesting	84
6.3.1	Design of Energy Harvesting Circuit (EHC)	84
6.3.2	EHC for hybrid stepper motor	86
6.4	Generator selection and design of power electronics and battery	87
6.5	Electronics of the damper	92
6.6	Summary and conclusions	96

7	Prototype	97
7.1	Introduction of the prototype	99
7.2	Components of the prototype	101
7.2.1	Spring system	101
7.2.2	Guide rail system	103
7.2.3	Electronically controlled damper	106
7.3	Components of the test rig	108
7.3.1	Spring system	108
7.3.2	Guide rail system	110
7.3.3	Actuator system	110
7.3.4	Electrical enclosure with electrical supply and safety sensor system . . .	110
7.3.5	Desktop PC with GUI for configuration, monitoring and HiL simulations . .	111
7.4	Summary	113
8	Experimental verification using Hardware-in-the-Loop simulations	115
8.1	System identification	117
8.1.1	Stage 1	117
8.1.2	Stage 2	118
8.2	Semi-active d-MTFD system optimization based on identified prototype	119
8.3	Hardware-in-the-Loop (HiL) simulation	122
8.4	Experimental results analysis	124
8.4.1	Comparison of simulated and measured facade relative displacement . .	125
8.4.2	Realization of the desired damping coefficients with the stepper motor . .	126
8.4.3	Energy generation and self-sufficient operation	128
8.4.4	Total energy assessment for the benchmark building	129
8.5	Discussion	130
8.6	Summary and conclusions	131
9	Conclusions and future work	133
9.1	Conclusions	133
9.2	Future work	135
A	Appendix	137
A.1	Explicit matrices in the governing equation	137
	Bibliography	139

List of Tables

4.1	Natural frequency of benchmark building with/without conventional DSF	53
5.1	Limit range of the perceptible acceleration in the design of high-rise buildings [1]	60
5.2	Average optimized n_f upper floors with parallel moveable DSF (j : Number of interpolation points for linear interpolation)	65
5.3	Optimized parameters, i.e., facade connection damping ratios, for Case 3 (cf. Figure 5.6 and 5.7b)	69
5.4	Comparison of uncontrolled system, optimized passive d-MTFD system (Case 1, Case 2) and optimized semi-active d-MTFD system using DBB control (Case 3) .	69
6.1	Governing equations for DC motor in motor and generator mode	79
6.2	Governing equations for two-phase stepper motor in motor and generator mode	82
6.3	Governing equations for two-phase stepper motor in motor and generator mode in rotating (d,q) coordinate system	82
6.4	Induced voltage at 100 rpm for different motor type (DC motor from maxon group, stepper motor from Moons' Electric Co., Ltd.)	88
7.1	Parameters of stepper motor and EHC	109
8.1	Estimated parameters of stage 1.	118
8.2	Estimated parameters of stage 2.	119
8.3	HiL simulation setup for five different selected stories according to the optimized Case 2	125
8.4	NRMSE/NMSE fitness value of the facade relative displacement based on the identified model	126
8.5	NRMSE/NMSE fitness value of the electrical damping force based on the identified model	127
8.6	Average dissipated mechanical power $P_{sm,e}$, average power loss due to parasitic damping P_p , and average harvested power P_h as well as the average energy harvesting efficiency at different story	129
8.7	Mass calculation of moveable facade elements for the benchmark building. . . .	130

List of Figures

1.1	Same scale slenderness comparison between former WTC and 432 Park Avenue	3
1.2	Steinway Tower with a slenderness ratio of 1:24	4
1.3	PTMD in Taipei 101	5
1.4	GSW headquarters with DSF	6
1.5	Concept of the moveable DSF using perpendicular and parallel moveable connection	7
1.6	Structure of dissertation	9
2.1	Energy dissipating damping system [2]	15
2.2	Summary of construction, hysteretic behavior, physical models, advantages, and disadvantages of passive energy dissipation devices for seismic protection applications [3]	16
2.3	TMD in Citicorp Center [4]	17
2.4	TMD in Steinway Tower	18
2.5	TMD in Rottweil Test Tower (Left: Pendulum rope supported TMD mass, Right: Linear Motor as actuator)	18
2.6	Different types of tuned mass damper (m : primary structure mass; m_1, m_2 : damping mass)	20
2.7	Vertically distributed-MTMDs based on mode shapes [5]	22
2.8	Steiff factory hall	24
2.9	Different types of DSF according to three classification methods [6]	24
2.10	Concept diagram of facade isolation and its simplified 2DoF system [7]	26
2.11	Concept diagram of distributed MTMDs within the DSF cavities [7]	27
2.12	Suggested perpendicular connection [8]	28
2.13	Schematic diagram of active control	30
2.14	Completed adaptive high-rise building D1244 [9]	31
2.15	Stress ribbon bridge with sensors, actuators and a controller [10]	32
3.1	2DoF facade isolation model	37

3.2	Dynamic magnification factor for structure motion β_{DX} and relative facade motion β_{DXf}	39
3.3	Dimensionless power flow to electrical circuit P_{ave}	41
3.4	2DoF facade damping system (TMD)	42
3.5	Dynamic magnification factor of structure motion (a) / TMD stroke (b)	44
3.6	Dimensionless Power Flow to Electrical Circuit P_{ave}	45
4.1	Analytical model of d-MTFD system	50
4.2	Equivalent friction coefficient $\mu_{r,i}$ of the upper 30 stories	54
4.3	Time histories of wind forces at different floors of the benchmark building	55
5.1	Flowchart of multi-objective Genetic Algorithm	59
5.2	Schematic of the multi-objective GA optimized semi-active control	62
5.3	Optimization parameters of passive d-MTFD system	63
5.4	Pareto front of passive d-MTFD system	64
5.5	Optimized numbers n_f of upper floors with parallel moveable DSF	65
5.6	Optimization parameters of semi-active d-MTFD system	66
5.7	Pareto front of semi-active d-MTFD system	67
5.8	Peak facade relative displacement at different stories (cf. Figure 5.7)	68
5.9	Top floor facade relative displacement x_{fr,n_f}	68
5.10	Top floor semi-active control force u_{n_f} (Case 3)	68
6.1	Power flow and signal flow of the electric machine as adjustable electrical damper/generator	73
6.2	Components of the electric machine as adjustable electrical damper/generator	74
6.3	The equivalent dynamic model of the DC motor in motor and generator mode	78
6.4	DC motor in generator mode connected to an external load resistance	80
6.5	The equivalent dynamic model of the two-phase stepper motor in motor mode and generator mode	81
6.6	Each phase of the two-phase stepper motor in generator mode connected to a same external load resistance R_l	83
6.7	Block diagram of power converter for energy harvesting application	84
6.8	The schematic of a two-stage EHC	85
6.9	The schematic of dual two-stage EHC for two-phase hybrid stepper motor ($C_1 = C_3, C_2 = C_4$)	86
6.10	Simulink model of hybrid stepper motor with dual two-stage EHC	87
6.11	The schematic of the test bench for the stepper motor	89
6.12	Fixed coupling between the asynchronous motor and the tested stepper motor	90
6.13	Measured and estimated electrical counter torque M_e of the stepper motor in generator mode for different duty cycles and corresponding emulated resistances ($R = R_l(d) + R_a$)	91

6.14 Measured and estimated electrical damping coefficient \bar{c}_e of the stepper motor in generator mode for different duty cycles and corresponding emulated resistances ($R = R_l(d) + R_a$). Measurements for very low speeds are slightly subject to errors due to the measurement setup in use	91
6.15 The front and rear view of the IVE-box	92
6.16 Side view of the opened IVE-box (left is the rear view, right is the front view) . . .	93
6.17 Top view of the power electronics board (real and 3D rendered)	94
6.18 Isolation concept for the power electronics board	95
7.1 Proposed constructional design of the parallel moveable Double-Skin Facade (DSF)	99
7.2 Rendering overview of prototype and test rig (Rendering by Therese Schmidt, Chair of Hybrid Structures - Structural Concrete, BTU Cottbus-Senftenberg). . .	100
7.3 Overview of the completed prototype and test rig	101
7.4 Prototype on the actuated test rig during an experimental investigation	102
7.5 Top view of the prototype	102
7.6 Front view of the prototype	103
7.7 Side view of the prototype on the test rig with details (the moveable part of the prototype is marked in green).	104
7.8 Spring system of the moveable DSF	105
7.9 Upper/lower guide rail system	105
7.10 Rolling bearings used in the prototype	106
7.11 Friction model	106
7.12 Electronically controlled damper consisting of the selected two-phase stepper motor and the IVE-box mounted on the building frame	107
7.13 The schematic of EHC	108
7.14 Spring system and guide rail system of the test rig	109
7.15 Installed NiLAB controlled electric drive of type LM075P	110
7.16 Electrical enclosure for the prototype test rig	111
7.17 Desktop PC and Simulink GUI for configuration of the electronically controlled damper and testing of the prototype	112
8.1 Stages for system identification	117
8.2 Measured/estimated relative displacement of facade outer skin	119
8.3 Measured/estimated stepper motor interaction force	120
8.4 Pareto front for the optimized passive and semi-active system	121
8.5 Hardware-in-the-Loop (HiL) simulation	123
8.6 Comparison of simulated and measured facade relative displacement	125
8.7 Comparison of the desired and recorded actual damping force	126
8.8 Comparison of the minimum and maximum desired and actual damping force . .	127
8.9 Measured power flow for the 57th and 76th stories	128

9.1 Power flow of a high-rise building installed with d-MTFD system 135

List of Abbreviations and Symbols

Abbreviations

2DoF	two Degree-of-Freedom
AC	Alternating Current
ADMF	Acceleration Dynamic Magnification Factor
AI	Artificial Intelligence
ASM	Asynchronous Machine
BBSR	Bundesinstitut für Bau-, Stadt-, und Raumforschung
BRBs	Buckling Restrained Braces
CCM	Continuous Current Mode
CTBUH	Council on Tall Buildings and Urban Habitat
d-MTFD	distributed-Multiple Tuned Facade Damper
d-MTMD	distributed-Multiple Tuned Mass Damper
DBB	Displacement-reducing Bang-Bang
DBG	Displacement Based Groundhook
DCM	Discontinuous Current Mode
DC	Direct Current
DDMF	Displacement Dynamic Magnification Factor
DoF	Degree-of-Freedom
DSF	Double-Skin Facade
EHC	Energy Harvesting Circuit
GA	Genetic Algorithm
GUI	Graphical User Interface
HiL	Hardware-in-the-Loop
HV	High Voltage
IVE	Intelligent Vibration control and Energy harvesting unit
LQR	Linear Quadratic Regulator
LV	Low Voltage
mDoF	multiple Degree-of-Freedom

MOSFE	Metaloxide-Semiconductor Field-Effect Transistor
MTMD	Multiple Tuned Mass Damper
NMSE	Normalized Mean Squared Error
NRMSE	Normalized Root Mean Squared Error
NSGA	Non-dominated Sorting Genetic Algorithm
OCF	Open Cavity Facade
PMSM	Permanent-Magnet Synchronous Motor
PSO	Particle Swarm Optimization
PTMD	Pendulum Tuned Mass Damper
PWM	Pulse-Width Modulation
RMS	Root Mean Square
sDoF	single Degree-of-Freedom
SSF	Single-Skin Facade
TMD	Tuned Mass Damper
VBG	Velocity Based Groundhook
VFD	Variable-Frequency Drive

Symbols

α	Lead of conversion (radius of the pinion)
α_s	Step angle
β_{DXf}	Dynamic magnification factors for stroke of the moveable facade mass
β_{DX}	Dynamic magnification factors for primary structure
η	Excitation influence matrix
\mathbf{B}_f	Friction influence matrix
\mathbf{C}_M	Reduced modal damping matrix
\mathbf{C}_s	Damping matrix
\mathbf{f}_{fi}	Vector of friction
\mathbf{f}_w	Vector of across-wind excitation
\mathbf{K}_M	Reduced modal stiffness matrix
\mathbf{K}_s	Stiffness matrix
\mathbf{M}_M	Reduced modal mass matrix
\mathbf{M}_s	Mass matrix
η	Total efficiency of energy harvesting
η_{le}	Energy harvesting efficiency of the circuit
St	Strouhal number
μ_r	Equivalent friction coefficient
μ_{r_1}	Friction coefficient of the rolling bearings used to carry the self-weight of the parallel moveable facade
μ_{r_2}	friction coefficient of the rolling bearings used to withstand along-wind forces
Ω	Angular frequency of the excitation

ω	Angular velocity
ω_1	Structural first natural angular frequency
ω_f	TMD natural angular frequency
$\bar{c}_{m,fs}$	Guide rail system viscous friction coefficient
$\bar{c}_{m,fs}$	Viscous friction coefficient of the whole guide rail system (upper and lower)
$\bar{c}_{m,sm}$	Stepper motor viscous friction coefficient
$\bar{c}_{m,sm}$	Viscous friction coefficient of the stepper motor
\bar{c}_m	Total viscous friction (prototype)
\bar{f}_C	Total Coulomb friction magnitude (prototype)
$\bar{f}_{brk,fs}$	Guide rail system breakaway friction
$\bar{f}_{brk,sm}$	Stepper motor breakaway friction
\bar{f}_{brk}	Total breakaway friction
$\bar{f}_{C,fs}$	Guide rail system Coulomb friction
$\bar{f}_{C,sm}$	Stepper motor Coulomb friction
$\bar{f}_{fs,Col}$	Coulomb friction
$\bar{f}_{fs,r}$	Friction force of the guide rail system
$\bar{f}_{fs,Str}$	Stribeck friction
$\bar{f}_{fs,Vis}$	Viscous friction
\bar{f}_{int}	Interaction force
$\bar{f}_{sm,ace}$	Reaction force due to acceleration of stepper motor
$\bar{f}_{sm,Col}$	Coulomb friction in stepper motor
$\bar{f}_{sm,det}$	Reaction force due to detent torque of stepper motor
$\bar{f}_{sm,Str}$	Stribeck friction in stepper motor
$\bar{f}_{sm,Vis}$	Viscous friction in stepper motor
\bar{f}_{sm}	Stepper motor reaction force
\bar{k}_f	Stiffness of the spring system (prototype)
\bar{m}	Mass ratio
\bar{m}_f	Facade outer skin mass (prototype)
ρ	Excitation ratio
ρ_a	Air density
ρ_f	Overall surface density
ξ	Structural damping ratio
ξ_{ref}	Reference damping ratio
$\xi_{d.opt}$	Optimum damping ratio
ξ_e	Electrical damping ratio
ξ_m	Mechanical damping ratio
A_f	Along-wind force acting area
B_f	Mechanical/frictional viscous damping factor
C_1, C_2, C_3, C_4	Buck-boost converter capacitance
C_d	Drag coefficient
c_e	Electrical damping coefficient

C_f	Total connection damping coefficient
C_m	Mechanical damping coefficient
$C_{e,r}$	Rotational electrical damping coefficient
$C_{m,r}$	Rotational mechanical/parasitic damping coefficient
d	Duty cycle
e	Euler's number
f	Tuning ratio
F_w	Wind force amplitude
f_w	Sinusoidal force
f_{opt}	Optimum tuning ratio
f_{sw}	MOSFET switching frequency
f_{vs}	Frequency of vortex shedding
$f_{w,al}$	Mean along-wind force
J	Stepper motor rotor inertia
k_e	Electrical constant
k_n	Speed constant
k_t	Torque constant
L_a	Stepper motor winding inductance
L_c	Buck-boost converter inductance
M_{eff}	First effective modal mass
N	Rotor teeth number
P_g	Constant basic power consumption
P_h	Average harvested power
P_{AVE}	Average power flow
P_{ave}	Dimensionless average power flow
P_p	Average power loss due to parasitic damping
$P_{sm,e}$	Average dissipated energy due to the stepper motor
$P_{T,e}$	Total dissipated power due to electrical damping for the upper 20 stories
R	Total resistance
R_a	Stepper motor winding resistance
R_l	External load resistance
T_d	Detent torque amplitude
T_f	Friction torque
T_L	External torque
v_o	Output voltage
v_R	Rectified DC voltage
v_s	Source voltage
v_{10m}	Reference mean wind velocity at 10m above ground (return period of 10 years)
v_{top}	Top story mean wind velocity
v_{back}	Back Electromotive Force (EMF) induced voltage

V_{bat}	Rechargeable batteries nominal voltage
V_{brk}	Breakaway friction velocity
V_{Coul}	Coulomb velocity threshold
V_{fr}	Relative facade velocity
V_{st}	Stribeck velocity threshold
X	Amplitude of structural vibration
X_f	Amplitude of facade relative displacement
X_{st}	Structure static deformation

1 Introduction

Due to the increasing global urbanization, the urban land resources for construction are becoming increasingly tight. Under this background, slender high-rise buildings are being built worldwide in pursuit of better economic benefits. Different technologies have been developed to reduce wind-induced vibrations of these wind-sensitive slender structures. In my research, an innovative distributed-Multiple Tuned Facade Damping (d-MTFD) system is proposed and fully investigated. In this chapter, the research background and motivation are introduced in detail in Section 1.1. The objectives as well as the structure of this dissertation are outlined in Section 1.2. The main contribution of this dissertation is summarized in Section 1.3, and publications related to this dissertation are listed at the end of this chapter.

1.1. RESEARCH BACKGROUND

1.1 RESEARCH BACKGROUND

1.1.1 Emergence of super-slender high-rise buildings

A report from the Council on Tall Buildings and Urban Habitat (CTBUH) shows that, in 2020, the number of high-rise buildings (above 200 m) has almost tripled since the year 2010 [11]. In 2050, around 70% of the global population is estimated to live in cities [12]. With our limited ground space and always increasing population in big cities, high-rise buildings give us a solution, which can provide more living space on a limited amount of land.

Nowadays, the new generation of skyscrapers is always getting taller and more slender. The former World Trade Center (WTC) north tower, as shown in Figure 1.1a, used to be the tallest building in 1971 with a height of 417 m, and the ratio of its base to height was a little less than 1:7. The recently built residential tower 432 Park Avenue in Manhattan, New York City, as shown in Figure 1.1b, reaches a height of 426 m, which is taller than the former WTC north tower, and its slenderness ratio is only 1:15. In Figure 1.1c, the same scale comparison is made between these two super tall buildings. New York has the largest number of super-slender skyscrapers [13].

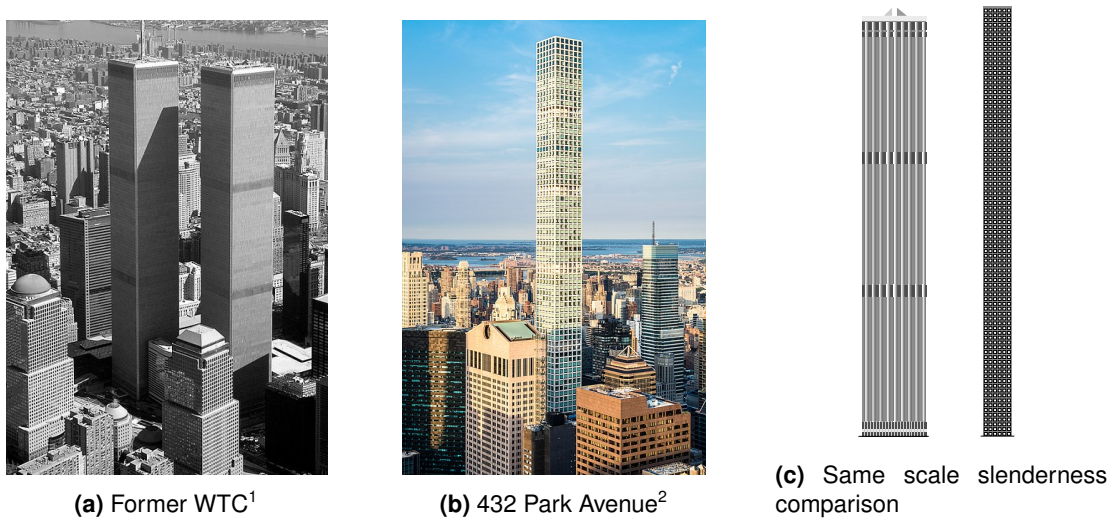


Figure 1.1: Same scale slenderness comparison between former WTC and 432 Park Avenue.

Among these slender skyscrapers, the Steinway Tower, with a slenderness ratio of 1:24, is currently the slenderest skyscraper in the world, which is located in Manhattan near central park, as shown in Figure 1.2. Getting slender is the result of inner-city concentration, which is now a new trend, especially in a metropolis like New York City. However, such slender buildings bring challenges to structural engineers.

¹"World Trade Center, New York City - aerial view (March 2001)" by Jeffmock, used under Creative Commons CC BY-SA 3.0 (<https://creativecommons.org/licenses/by-sa/3.0/deed.en>) / adapted from original

²"432 Park Avenue from Rockefeller Center" by dconvertini, used under Creative Commons CC BY-SA 2.0 (<https://creativecommons.org/licenses/by-sa/2.0/deed.en>)



Figure 1.2: Steinway Tower with a slenderness ratio of 1:24³.

1.1.2 Vibration problem of high-rise buildings and solutions

Across-wind excitation due to vortex shedding and seismic excitation are two of the most important dynamic excitations that cause vibration problems of high-rise buildings. The induced vibrations can damage the primary structure or the secondary components of the buildings and can cause discomfort to the residents. The relative importance of these two dynamic loads depends on the site location, building height, building shape, and structural system of the designed high-rise buildings. For steel structures in seismically active regions, the transition from earthquake dominant to across-wind dominant occurs when the building height reaches approximately 100 m. Concrete buildings, due to their larger mass, are controlled by seismic excitation up to at least a height of 250 m, since the additional gravity load increases the effect of the seismic excitation [14]. For super-slender high-rise buildings, the design is primarily governed by across-wind excitation.

Recent developments in materials science and engineering have resulted in significant increases in the strength of traditional civil engineering materials such as steel, concrete, and composite materials. Although the strength of these materials has essentially increased, the modulus of elasticity changes very little or remains constant compared to the increase in strength. The lag in material stiffness versus material strength also leads to problems in satisfying serviceability requirements for various motion parameters, such as acceleration [14]. In consideration of human comfort, acceleration needs to be restricted. Humans begin to feel uncomfortable when the acceleration reaches about 0.02 g. Bachmann and Ammann have comprehensively discussed the human comfort criteria [15].

One of the widely used methods to mitigate wind-induced vibrations is to install auxiliary damping devices. An example of this is the Tuned Mass Damping (TMD) system, which has

³"111, West 57th Street" by Gabriel Beland, used under Creative Commons CC BY 2.0 (<https://creativecommons.org/licenses/by/2.0/>)

1.1. RESEARCH BACKGROUND

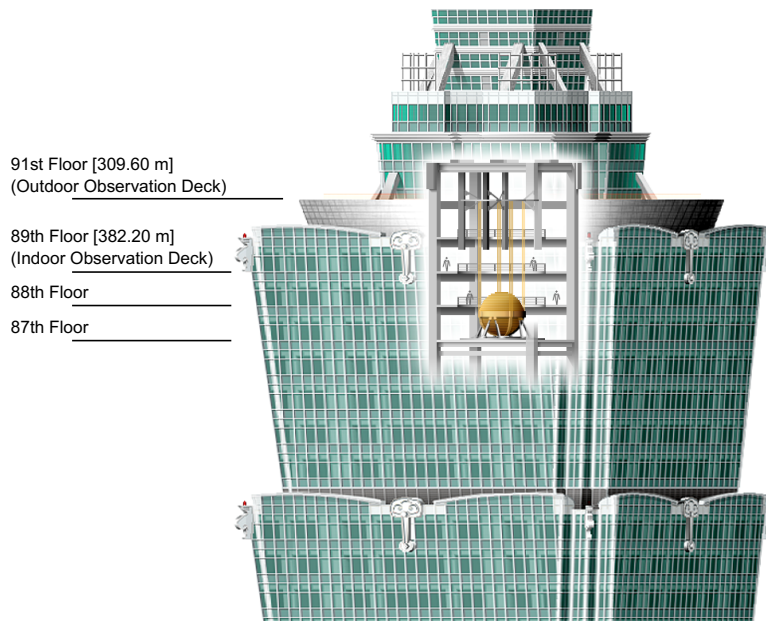


Figure 1.3: PTMD in Taipei 101⁴.

been proven to be a very reliable solution and has been applied in many completed high-rise buildings, such as the Taipei 101 (see Figure 1.3). The Pendulum Tuned Mass Damper (PTMD) system installed on top of the Taipei 101 can generate a horizontal force through its relative motion that is opposite to the motion of the floor. Traditional TMD systems can reduce the vibration response of high-rise buildings by 40% to 60% via energy dissipation. Due to their simple implementation and effectiveness, TMD systems are widely used. However, the conventional single TMD system has several main drawbacks: first, a large additional damping mass weighing hundreds of tons is required; second, a huge space crossing several floors near the top of the building is required for its installation; third, a more material-intensive support structure is needed to carry this additional mass; fourth, the mistuning or off-optimum damping ratio of the TMD significantly decreases its effectiveness; and fifth, there is no redundancy for conventional single TMD systems. Due to these drawbacks, the TMD system may not be the best choice for emerging super-slender high-rise buildings.

More damping systems have been proposed to mitigate wind-induced structural vibrations. A comprehensive literature review has been conducted in Chapter 2.

1.1.3 Double-Skin Facade (DSF) and its potential use for vibration suppression

The Conventional Double-Skin Facade (DSF) is an efficient solution for high-rise buildings that allows for natural ventilation and lighting. The GSW headquarters in Berlin utilizes a west-facing DSF that acts as a thermal flue, as shown in Figure 1.4. This strategy allows the building to be naturally ventilated for around 70% of the year, significantly reducing air-conditioning energy

⁴"Taipei 101 Tuned Mass Damper" by Someformofhuman, used under Creative Commons CC BY-SA 4.0 (<https://creativecommons.org/licenses/by-sa/4.0/>) / adapted from original

usage [16]. By replacing the stationary connection of the outer skin to the primary structure with actuators, various cavity depths can be adjusted to achieve an optimal airflow rate. Cooling and heating seasons demand different cavity depths to reduce energy consumption [17, 18]. The energy used for space heating, cooling, lighting, and ventilation accounts for more than 50% of the energy consumption in buildings [19]. Recently, user comfort and interaction with the facade have also become a design aspect. Artificial Intelligence (AI) trained with user behavior data has been applied in the adaptive control system of innovative facades to achieve more user convenience [20].



Figure 1.4: GSW headquarters with DSF⁵.

In recent decades, moveable double-skin facades are proposed to reduce wind-induced structural vibrations. Kareem first proposed the concept of using moveable building cladding to isolate the dynamic wind loads from the structural system [21]. Moon further developed this approach by using the double-skin facade [22]. As shown in Concept 1 in Figure 1.5, the DSF's outer skin is designed to move back and forth perpendicular to the primary structure to isolate the primary structure from the dominant across-wind excitation due to vortex shedding. By using perpendicular connections with low-axial stiffness, the movement of the primary structure can be significantly mitigated. However, the reduction of structural vibration is accompanied by severe movement of the DSF's outer skin. For practical application, excessive outer skin movement is a critical design limitation. To reduce the facade vibration, Moon proposed the TMD/DSF damping interaction system [23]. The TMD with a relatively small mass ratio in this system can mitigate the facade outer skin vibration significantly, but extra damping mass is

⁵"GSW Building in Berlin" by Emanuele, used under Creative Commons CC BY-SA 2.0 (<https://creativecommons.org/licenses/by-sa/2.0/deed.en>)

1.2. RESEARCH OBJECTIVE AND STRUCTURE OF DISSERTATION

required again. There is other research using moveable facades to reduce structural vibrations under seismic excitation. Detailed reviews are described in Chapter 2.

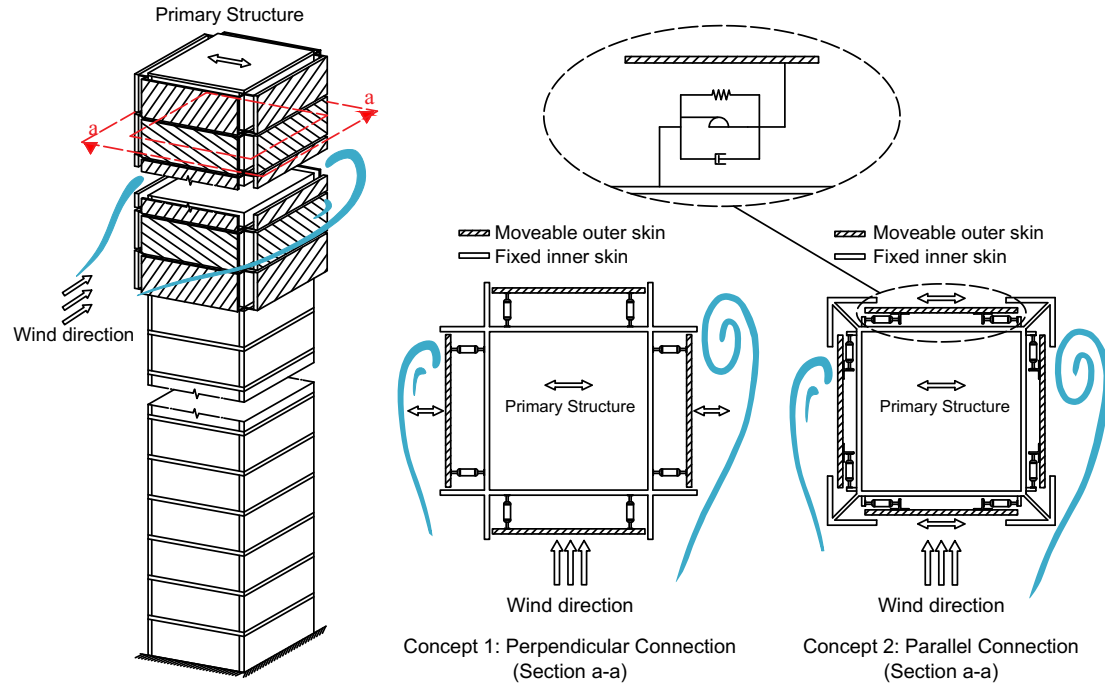


Figure 1.5: Concept of the moveable DSF using perpendicular and parallel moveable connection.

1.2 RESEARCH OBJECTIVE AND STRUCTURE OF DISSERTATION

As described in the research background, the traditional TMD system becomes not that optimal for the emerging slender high-rise buildings to reduce wind-induced structural vibrations. The early proposed concept using perpendicular moveable double-skin facade is practically difficult to be realized due to its severe outer skin motion. Therefore, the concept of parallel moveable double-skin facade is proposed [24], as shown in Concept 2 in Figure 1.5. Compared with the perpendicular connection, the relative displacement of parallel moveable DSF's outer skins can be significantly reduced to achieve the same damping performance.

For skyscrapers under wind excitation, the most governing design criterion is to reduce the wind-induced oscillation in the across-wind direction (orthogonal to the wind direction) due to vortex shedding. By using perpendicular connections, the moveable DSF's outer skin begins to oscillate under wind excitation, and this oscillation is then transmitted to the primary structure. Consequently, the design goal is to make the transmission as small as possible without exceeding the allowable movement of the DSF's outer skin. With parallel connections, the moveable DSF's outer skin is fixed in the direction perpendicular to the primary structure, but moveable in the direction parallel to the primary structure. The parallel movement of the outer skin is independent on each floor. The wind-induced structural lateral vibration causes the front and rear parallel moveable facades on different floors to vibrate, which in turn damps the primary struc-

1.2. RESEARCH OBJECTIVE AND STRUCTURE OF DISSERTATION

ture's motion. The moveable DSF's outer skin is coupled on each side of each story and can slide into the fixed corner of the facade. The design of the fixed corners ensures that flow separation always occurs at these corners [25], thereby reducing the impact of the parallel moveable facades on the vortex shedding phenomenon. These parallel moveable facades distributed over the upper stories of the high-rise building create a damping system. Physically, this system is similar to the distributed-Multiple Tuned Mass Damping (d-MTMD) system. However, existing non-structure facade mass is used as damping mass, so no external mass is needed and its installation does not occupy valuable inner space of the building. This system was named the distributed-Multiple Tuned Facade Damping (d-MTFD) system [24].

Based on this proposed damping system, several considerations are raised:

- Smaller relative displacement of DSF's outer skin is always desired in practice. How to optimally design the d-MTFD system to achieve the best damping performance with possibly small facade relative displacement?
- Whether electrical machines can be applied as adjustable damping devices for semi-active control and simultaneously as energy harvesters to partially harvest the vibration energy?
- How to integrate all the required components in traditional DSF to achieve parallel moveability of the outer skin and semi-active control of the system? A constructional design needs to be proposed, and a prototype has been built based on the design.
- How much power can be harvested and whether it is enough for a self-sustainable operation of the semi-active control? Experimental investigations need to be conducted based on the built prototype.

Therefore, the overall objective of this dissertation is to establish a semi-active distributed-Multiple Tuned Facade Damper (d-MTFD) system to effectively mitigate wind-induced vibrations of slender high-rise buildings and at the same time harvest the vibration energy efficiently. The harvested energy is used as the energy supply for the semi-active control. It is desired to achieve energy self-sufficient semi-active control. The whole structure of this dissertation is illustrated in the flowchart in Figure 1.6.

The detailed research accomplished in each chapter of this dissertation can be summarized as follows:

- Chapter 2 offers a literature survey on different vibration mitigation methods and technologies for civil structures, as well as some relevant work on vibration energy harvesting and dual-functional dampers.
- Chapter 3 investigates and discusses the differences in the vibration control performances and energy harvesting performances between the facade isolation concept using perpendicular connections and the proposed d-MTFD system using parallel connections. Simplified two Degree-of-Freedom (2DoF) systems under harmonic excitation are used for the analysis.

1.2. RESEARCH OBJECTIVE AND STRUCTURE OF DISSERTATION

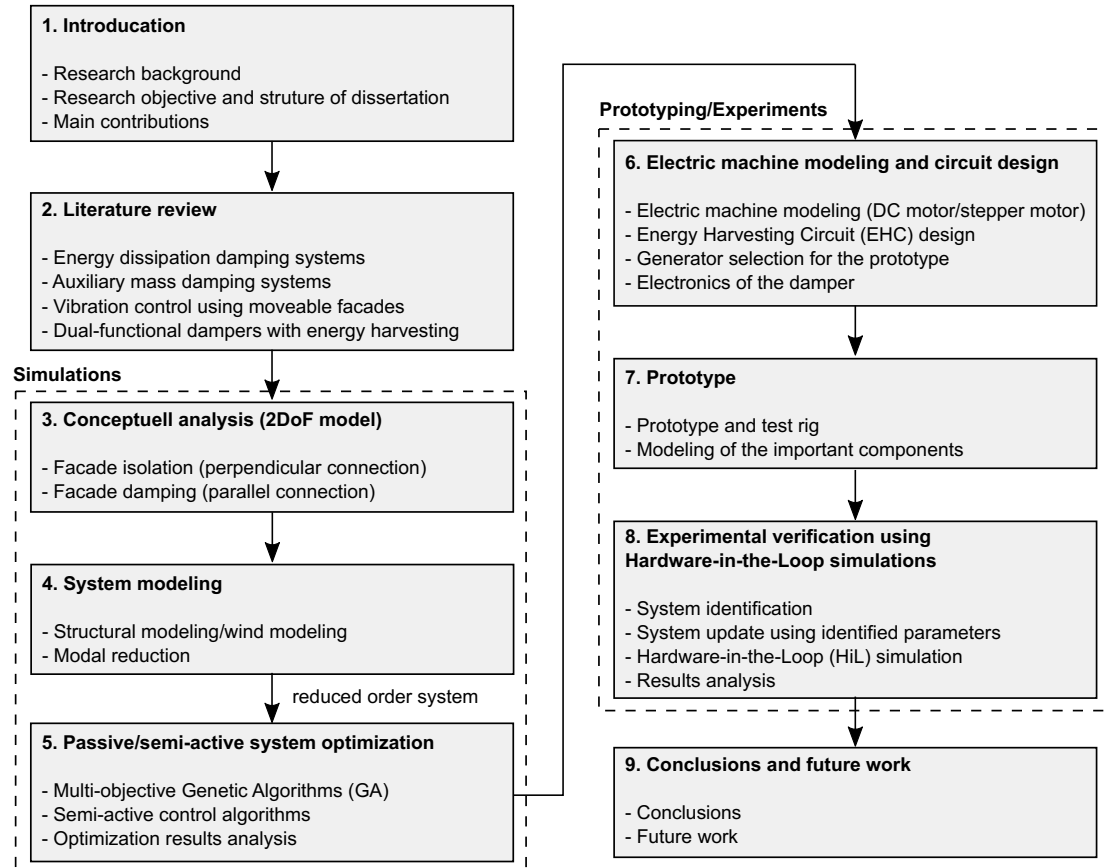


Figure 1.6: Structure of dissertation.

- Chapter 4 describes the modeling of the d-MTFD system installed on a 76-story high benchmark building, and modal reduction is introduced to derive a reduced-order system without much loss of accuracy. The use of a reduced-order system saves much simulation time for further system optimization.
- Chapter 5 introduces the multi-objective Genetic Algorithm (GA) that has been used to optimize the passive and semi-active d-MTFD system based on two objectives: first, to reduce the top floor acceleration; second, to reduce the facade's outer skin relative displacement. Different semi-active control policies are investigated, and the influence of the inevitable rolling friction is also considered. It is concluded that smaller rolling friction is beneficial to the optimization results.
- Chapter 6 introduces using an electric machine together with an energy harvesting circuit (EHC) to achieve adjustable electrical damping coefficient and simultaneous energy harvesting. The modeling of two different electric machines, i.e., DC motor and stepper motor, is described in motor mode and generator mode. The differences are addressed. A two-phase hybrid stepper motor with dual two-stage EHC is selected for the application and the parameters of the motor are identified.

- Chapter 7 presents the prototype with one full-scale moveable facade element. The components of the prototype and test rig are introduced. The modeling of some important components is described.
- Chapter 8 describes the steps to estimate the model parameters of the entire prototype using grey-box system identification. High fitness values are obtained by comparing the measured and estimated data. Hardware-in-the-Loop (HiL) simulations are performed to validate the prototype and demonstrate the feasibility of an adjustable electrical damper using a stepper motor. The energy harvesting performance was analyzed and it is shown that a self-sufficient semi-active d-MTFD system can be realized.
- Chapter 9 presents the conclusion and points out the future research direction.

1.3 MAIN CONTRIBUTIONS

The contributions of this dissertation⁶ can be summarized as follows:

- This research is interdisciplinary as it combines structural engineering, control engineering, and electrical engineering. It connects several different fields and creates new knowledge in an interdisciplinary area.
- The distributed-Multiple Tuned Facade Damping (d-MTFD) system has been proposed by using the existing DSF's outer skin mass as the damping mass. Compared with the traditional solutions, the d-MTFD system requires no additional damping mass, which minimizes the amount of building material and reduces the carbon footprint for society.
- The developed adjustable electrical damper, using a stepper motor, enables the damping device to evolve from the traditional energy dissipation strategy to the novel energy harvesting strategy. The energy dissipation strategy has been the dominant method to mitigate structural vibration in the past half-century. The energy harvesting strategy paves a new way for semi-active control without an external power supply, which increases the reliability and self-sustainability of semi-active control systems.
- Structural vibration control using moveable double-skin facades has received a lot of attention from researchers in the last decade. However, all these studies are based on theoretical analyses and numerical simulations. In this research, a prototype with a full-scale parallel moveable facade has been developed with all the integrated components under the support of the industry partner Josef Gartner GmbH.
- By using Hardware-in-the-Loop (HiL) simulations, the motion of the DSF's outer skin can be reproduced as closely as possible under across-wind excitation. Therefore, the functionality of semi-active control and simultaneous energy harvesting can be validated

⁶This dissertation is in the frame of the Bundesinstitut für Bau-, Stadt-, und Raumforschung (BBSR) project (Projekt-nummer: 10.08.18.7-18.22). The teamwork in Chapter 6 and Chapter 7 has been specified in the Author's Contribution at the beginning of the chapters.

1.4. PUBLICATIONS

based on the prototype. The experimental validation makes the application of the system in practice more possible.

1.4 PUBLICATIONS

Parts of this research were (or will be) published in the following articles:

- [P1] **Yangwen Zhang**, Thomas Schauer, and Achim Bleicher. Assessment of wind-induced vibration suppression and energy harvesting using facades. In *20th CONGRESS OF IABSE New York City*, pages 352–356, 2019
- [P2] **Yangwen Zhang**, Thomas Schauer, Laurenz Wernicke, Wulf Wulff, and Achim Bleicher. Facade-Integrated Semi-Active Vibration Control for Wind-Excited Super-Slender Tall Buildings. *IFAC-PapersOnLine*, 53(2):8395–8400, 2020. doi: <https://doi.org/10.1016/j.ifacol.2020.12.1585>
- [P3] **Yangwen Zhang**, Thomas Schauer, Laurenz Wernicke, Apostolos Vrontos, Michael Engelmann, Wulf Wulff, and Achim Bleicher. Design of moveable facade elements for energy harvesting and vibration control of super slender tall buildings under wind excitation. In *POWERSKIN CONFERENCE*, pages 327–338. TU Delft Open Munich, Germany, 2021
- [P4] Achim Bleicher, Thomas Schauer, Robert Jirasek, Tim Höltke, **Yangwen Zhang**, Paul Marker, Wulf Wulff, Johannes Manfrecola, and Therese Schmidt. Hybride Konstruktionen an der BTU Cottbus-Senftenberg. *Bautechnik*, 98(12):907–920, 2021. doi: <https://doi.org/10.1002/bate.202100056>
- [P5] Thomas Schauer, Achim Bleicher, **Yangwen Zhang**, Wulf Wulff, and Laurenz Wernicke. *Schwingungsdämpfung und Energiegewinnung mit beweglichen Doppelfassaden: Entwurf, Optimierung und Validierung eines autarken verteilten semiaktiven Systems zur Reduktion Wind-induzierter Schwingungen bei schlanken Hochhäusern*. BBSR-Online-Publikation 08/2022, Bonn, April 2022
- [P6] **Yangwen Zhang**, Thomas Schauer, and Achim Bleicher. Optimized passive/semi-active vibration control using distributed-multiple tuned facade damping system in tall buildings. *Journal of Building Engineering*, 52:104416, 2022. doi: <https://doi.org/10.1016/j.job.2022.104416>
- [P7] Michael Engelmann, Wulf Wulff, Thomas Lorenz, Simon Frey, Laurenz Wernicke, **Yangwen Zhang**, Thomas Schauer, and Achim Bleicher. How to Exploit the Glass Mass for Damping a Building? In *Challenging Glass Conference Proceedings*, volume 8, 2022. doi: <https://doi.org/10.47982/cgc.8.425>
- [P8] **Yangwen Zhang**, Wulf Wulff, Laurenz Wernicke, Michael Engelmann, Thomas Schauer, and Achim Bleicher. Moveable facade elements for sustainable high-rise buildings. In *IABSE Congress Nanjing 2022 - Bridges and Structures: Connection, Integration and Harmonisation*, Nanjing, China, September 21–23, 2022. IABSE

1.4. PUBLICATIONS

- [P9] **Yangwen Zhang**, Wulf Wulff, Laurenz Wernicke, Michael Engelmann, Thomas Schauer, and Achim Bleicher. Experimental identification and verification of a moveable facade element for energy harvesting and vibration control. *Journal of Building Engineering*, 65:105712, 2023. doi: <https://doi.org/10.1016/j.jobbe.2022.105712>
- [P10] **Yangwen Zhang**, Laurenz Wernicke, Wulf Wulff, Achim Bleicher, and Thomas Schauer. Design and validation of a dual-functional damper based on a stepper motor for energy harvesting and vibration control. Manuscript submitted for publication

2 Literature review

High-rise buildings constructed with traditional materials such as steel and concrete have low inherent damping. Therefore, the energy dissipated per cycle is small. When the structures are under dynamic wind/seismic excitation, the input energy cannot be dissipated instantly, which results in large structural vibrations. The vibrations at the resonant frequency can be 50 to 100 times larger than the static deformation, i.e., the dynamic amplification factor can reach 50 to 100. In this chapter, a literature survey of different types of structural vibration control methods and applications is given. Auxiliary mass dampers are the main focus of the review. In addition, a detailed review of vibration control using moveable facades is also presented. Moreover, this review covers active control systems and dual-functional dampers that function as both dampers and energy harvesters simultaneously.

2.1. ENERGY DISSIPATING DAMPING SYSTEMS

2.1 ENERGY DISSIPATING DAMPING SYSTEMS

The energy dissipating damping systems are installed by highly integrating dampers within the primary structure of the buildings to optimally control and mitigate seismic and wind-induced vibration, as shown in Figure 2.1. The damping force is dependent upon the relative velocity. Different types of dampers are used to dissipate vibration energy. By installing dampers at vantage positions (such as on the bracings, walls, joints, etc.) of the building, the overall damping coefficient of the building can be increased, thereby reducing structural vibrations.

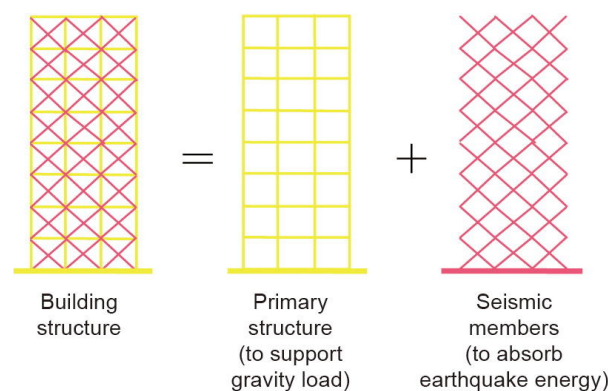


Figure 2.1: Energy dissipating damping system [2]⁷.

Energy dissipating damping systems have been widely used in many high-rise buildings around the world. A wide variety of energy dissipating dampers, which have been developed and installed in buildings, can be categorized into four major categories: viscous fluid damper, viscoelastic solid damper, friction damper, and metallic damper. These four major energy dissipation devices have been intensively studied and their characteristics are summarized in Figure 2.2 [3, 26].

In each tower of the former World Trade Center in New York City, more than 10000 viscoelastic dampers were installed in the lower chord of trusses that support the floors to reduce wind-induced vibrations [27]. For seismic excitation, Buckling Restrained Braces (BRBs), which belongs to metallic dampers, can be used as the seismic members, which yield first during the earthquake to dissipate the seismic energy [28]. For the energy dissipating damping system, the vibration energy is directly dissipated, which is different from the auxiliary mass damping system, where a secondary mass is needed. In the auxiliary mass damping system, the vibration energy is dissipated indirectly, which is through the relative vibration of the secondary mass. Different kinds of auxiliary mass damping systems are reviewed in the following section.

⁷Copyright ©2019, Takagi and Wada. Under Creative Commons CC BY-NC-ND 4.0 license (<https://creativecommons.org/licenses/by-nc-nd/4.0/>).

2.1. ENERGY DISSIPATING DAMPING SYSTEMS

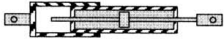

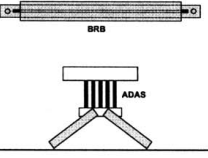
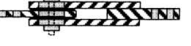
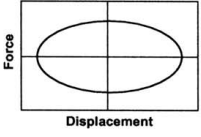
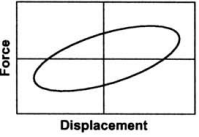
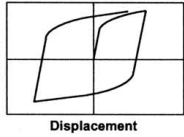
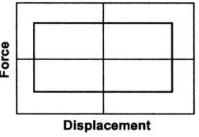
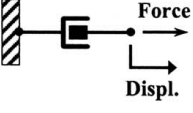
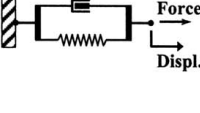
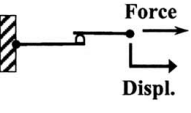
	Viscous Fluid Damper	Viscoelastic Solid Damper	Metallic Damper	Friction Damper
Basic Construction				
Idealized Hysteretic Behavior				
Idealized Physical Model			Idealized Model Not Available	
Advantages	<ul style="list-style-type: none"> - Activated at low displacements - Minimal restoring force - For linear damper, modeling of damper is simplified. - Properties largely frequency and temperature-independent - Proven record of performance in military applications 	<ul style="list-style-type: none"> - Activated at low displacements - Provides restoring force - Linear behavior, therefore simplified modeling of damper 	<ul style="list-style-type: none"> - Stable hysteretic behavior - Long-term reliability - Insensitivity to ambient temperature - Materials and behavior familiar to practicing engineers 	<ul style="list-style-type: none"> - Large energy dissipation per cycle - Insensitivity to ambient temperature
Disadvantages	<ul style="list-style-type: none"> - Possible fluid seal leakage (reliability concern) 	<ul style="list-style-type: none"> - Limited deformation capacity - Properties are frequency and temperature-dependent - Possible debonding and tearing of VE material (reliability concern) 	<ul style="list-style-type: none"> - Device damaged after earthquake; may require replacement - Nonlinear behavior; may require nonlinear analysis 	<ul style="list-style-type: none"> - Sliding interface conditions may change with time (reliability concern) - Strongly nonlinear behavior; may excite higher modes and require nonlinear analysis - Permanent displacements if no restoring force mechanism provided

Figure 2.2: Summary of construction, hysteretic behavior, physical models, advantages, and disadvantages of passive energy dissipation devices for seismic protection applications [3]⁸.

⁸Copyright ©2008, ASCE. Reprinted by permission from ASCE and Copyright Clearance Center (license ID 1257870-1).

2.2. AUXILIARY MASS DAMPING SYSTEMS

2.2 AUXILIARY MASS DAMPING SYSTEMS

For auxiliary mass damping systems, additional mass is installed in the primary structure and tuned near the natural frequency of the primary structure. The dynamic interaction between the primary structure and the damping mass is tailored to be out of phase to manifest structural vibration suppression [29]. Different types of auxiliary mass damping systems are described as follows.

2.2.1 Tuned Mass Dampers (TMDs)

Tuned Mass Damper (TMD) is the most widely used mass damper system. For TMDs, a huge mass is attached to the building through springs and dampers near the top, whose inertia force transmits to the building frame to reduce the motion. The frequency of the damper needs to be tuned close to the natural frequency of the building mode of concern so that when that frequency is excited, the damper will also resonate out of phase with the structural motion. The effectiveness of TMD depends on the accuracy of its tuning and the frequency range of its excitation [30]. The optimum tuning and optimum damping ratio are first derived in detail using the fixed point method by Den Hartog [31]. For structures subjected to long-duration, narrow-band excitation, TMD is a very efficient solution for vibration suppression.

For real applications, different kinds of TMDs have been designed. Generally, they can be grouped into two categories: (1) translational TMDs, whose damping mass rests on bearings that allow it to translate laterally; (2) pendulum TMDs, whose mass is hung by cables. The damping mass usually weights around 0.25% - 0.75% of the total building mass, which is corresponding approximately to 1% - 2% of its first effective modal mass [32].

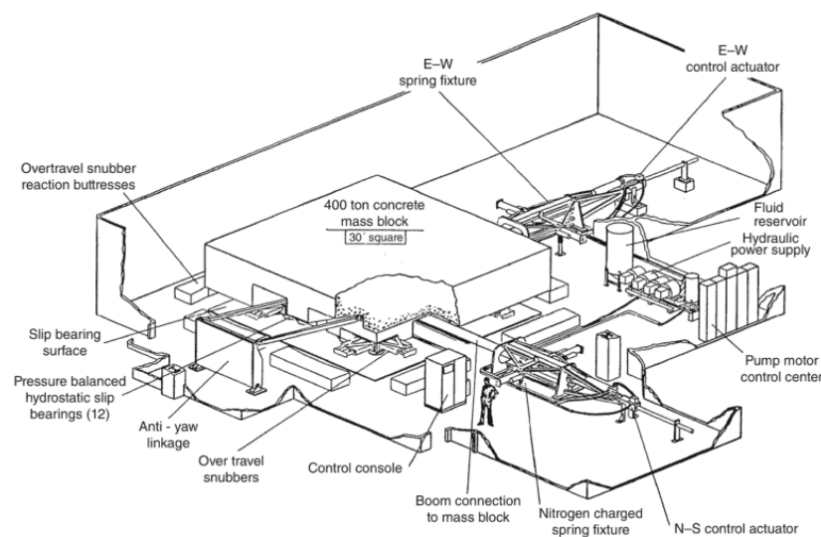


Figure 2.3: TMD in Citicorp Center [4]⁹.

⁹Copyright ©2019, John Wiley and Sons. Reprinted by permission from John Wiley and Sons and Copyright Clearance Center (license Number 5367890092364).

2.2. AUXILIARY MASS DAMPING SYSTEMS

One famous application of translational TMDs is the Citicorp Center in New York. The Citicorp TMD, as shown in Figure 2.3, installed on the 63rd floor of the building, has a huge concrete mass of around 360 t, which is about 2% of the effective modal mass of the first mode. This system is designed to reduce the structure vibration amplitude by about 50% with a peak relative displacement of ± 1.4 m [14]. The translational TMDs installed in John Hancock Tower in Chicago followed the same design principle. However, in the case of John Hancock Tower, a dual TMD system consisting of two 300 t mass blocks is used not only for lateral response control but also for torsional control if these two mass block moves out of phase [33].

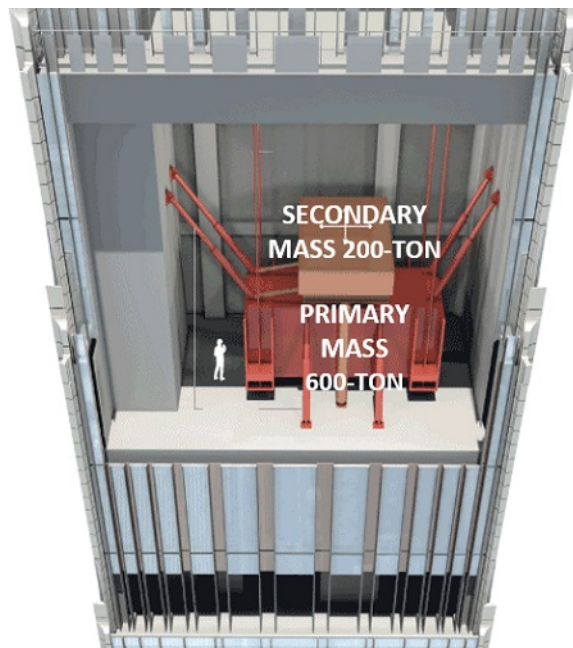


Figure 2.4: TMD in Steinway Tower¹⁰.



Figure 2.5: TMD in Rottweil Test Tower (Left: Pendulum rope supported TMD mass, Right: Linear Motor as actuator)¹¹.

Among the pendulum TMDs, the 37-story office building Crystal Tower in Osaka, which is the

¹⁰Reprinted by permission from SHoP Architects, WSP (Copyright ©SHoP Architects, WSP) .

¹¹Copyright ©2017 Meinhardt, Nikitas and Demetriou. under Creative Commons CC BY-NC-ND 4.0 (<https://creativecommons.org/licenses/by-nc-nd/4.0/>) .

2.2. AUXILIARY MASS DAMPING SYSTEMS

first high-rise building installed with pendulum TMD, is worth to be mentioned. Six ice thermal storage tanks for air conditioning, each weighting 90 t, are used as the damping mass, therefore, no additional mass is needed, which significantly reduces the cost. 50% of the wind-induced vibration is reduced by this system [29]. Another recent famous example of pendulum TMD is the case of the 438 m high super-slender Steinway Tower in New York. The slenderness of this new iconic building reaches 1:24, which means it is very susceptible to dynamic wind excitation. To mitigate the wind-induced motion, an 800 t mass damper is installed at the top. Due to the narrow width of the building, the space allowed for the relative displacement of damping mass is quite limited. Therefore, the mass damper with two masses consisting of steel plates is proposed [34], as shown in Figure 2.4. The larger one (600 t) is suspended from the ceiling using a series of cables. The smaller one (200 t) is supported from the floor below. These two masses move in tandem to compensate for the tower motion. Another very unique example of the pendulum TMD system is the case of the Rottweil Test Tower in Germany [35]. This TMD system is a so-called Dual Use TMD, as shown in Figure 2.5. It functions as a normal passive TMD system to reduce wind-induced structural vibrations. An active control system with a linear motor as the actuator was applied to excite the tower artificially to test building sway-sensitive equipment in the tower.

The classic TMD has been proven effective and has the advantages of simplicity and reliability. However, the advantage is that its effectiveness is very sensitive to the tuning ratio. The mistuning or the off-optimum damping ratio of TMD will significantly reduce its effectiveness [36].

2.2.2 Multiple Tuned Mass Dampers (MTMDs)

Due to the above-mentioned shortcomings of classic single TMD, Multiple Tuned Mass Dampers (MTMDs) were proposed. As its name described, MTMDs consists of a number of TMDs which are connected to the primary structure in series or parallel [37], as illustrated in Figure 2.6. Most of the research is about MTMDs in parallel. Therefore, parallel MTMDs will be first introduced.

The idea of MTMDs was developed from the initial investigation of the dual tuned mass damper. Iwanami and Seto investigated the optimal design of a dual tuned mass damper for the structure under harmonically forced oscillation, which shows better robustness than single TMD [38]. However, the improvement is not that significant. The MTMDs were then first proposed by Igusa and Xu [39, 40]. The performance of MTMDs with closely spaced natural frequencies for a structure subjected to a wide-band random base excitation was investigated by Igusa and Xu using the asymptotic analysis technique [41, 42]. Yamaguchi and Harnpornchai have done a comprehensive parametric study of MTMDs for the structure under harmonically forced excitation, which confirmed its efficiency and insensitivity to the offset in the frequency tuning [43]. Their research was based on numerical simulation, and analytical results were not obtained. In the study of Fujino [44], explicit closed-form formulas to estimate the effectiveness of the MTMD subjected to harmonic forces were derived. Based on these formulas, a design procedure for designing MTMDs was proposed. Kareem and Kline investigated the characteris-

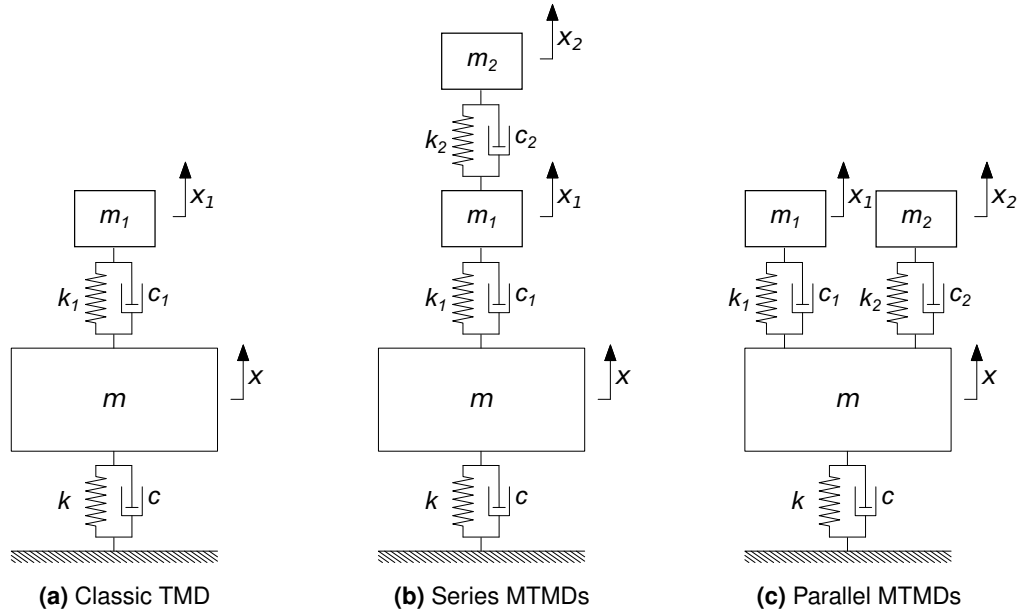


Figure 2.6: Different types of tuned mass damper (m : primary structure mass; m_1, m_2 : damping mass).

tics of MTMDs with distributed natural frequencies under narrow- and wide-banded excitations represented by wind and seismic loads [45]. The findings of this study were generally in agreement with the study by Yamaguchi and Harnpornchai [43].

Although the effectiveness and robustness of MTMDs have been investigated intensively, the optimization of MTMDs has not been studied. In 1997, Joshi and Jangid first published a paper about the optimization of MTMDs under white noise random base excitation [46]. Minimization of the Root Mean Square (RMS) displacement of the primary structure is selected as the criterion in their work. Jangid has further optimized the MTMDs under harmonic base excitation using a numerical searching technique [47]. In the research by Li, minimization of the maximum Displacement Dynamic Magnification Factor (DDMF) and maximum Acceleration Dynamic Magnification Factor (ADMF) is used as optimization criteria [48, 49]. Li and his group have also done a lot of research about active MTMDs in the following years [50, 51, 52, 53]. By using a simple numerical searching technique, constraints need to be given for the parameters. In 2005, Hoang and Warnitichai proposed a new method of designing MTMDs, which uses a numerical optimizer that follows the Davidon-Fletcher-Powell algorithm [54]. In this method, parameters are treated as unconstrained variables. Zuo and Nayfeh proposed a very innovative method [55]. They considered parameter optimization as a decentralized optimal control problem, in which the control gain is composed of the spring stiffnesses and damping coefficients. Then the gradient-based H_2 optimization is applied to minimize the RMS response of the primary structure. Li and Ni also optimized the MTMDs using a gradient-based method, but their optimization criterion is to minimize the maximum DDMF [56]. To optimize a large number of parameters, traditional optimization methods such as numerical searching techniques or

2.2. AUXILIARY MASS DAMPING SYSTEMS

gradient based methods are very cumbersome and need extensive computational resources. Therefore, Genetic Algorithms (GA) have been used to optimize parameters of MTMDs [57]. By using genetic algorithms, all the optimization process is automatic. There is no need to design MTMDs based on tuning to the nearby frequency of a concerned mode. In their study, the primary structure is modeled as a multiple Degree-of-Freedom (mDoF) system, which means different modes are contained in this system. Therefore, the optimization has also considered the influence of higher modes. For early studies [41, 42, 45, 48, 55], only the first mode is considered, so the primary structure is always simplified as a single Degree-of-Freedom (sDoF) system. All these studies focused on single-mode vibration control. Under certain conditions, these MTMDs are equivalent to a TMD [58].

By modeling the primary structure as a mDoF system, the MTMDs can be tuned to several modes of structure vibration to realize multiple mode vibration control. The damping masses can be placed at different floors, which is called distributed-Multiple Tuned Mass Dampers (d-MTMDs). The d-MTMDs is comprehensively reviewed in Section 2.2.3.

Parallel MTMDs have been widely investigated and the parameters have been optimized with different methods. However, there are not many studies about series MTMDs compared with parallel MTMDs. Carneiro, et al. first proposed the so-called interconnected multiple tuned mass dampers, which is the original name of series MTMDs. They compared the dynamic suppression performance of parallel MTMDs with series MTMDs and close results are obtained [59]. Zuo named this type of system as series MTMDs, or series TMDs [37]. In his paper, decentralized H_2 and H_∞ control methods are adopted to optimize the parameters of series MTMDs under random and harmonic excitation. It is found that the series MTMDs are more effective and robust than parallel MTMDs of the same mass ratio. Tang and Zuo have also extended their study of series MTMDs to active and semi-active approaches, and the Taipei 101 tower is simplified to a sDoF system for all the numerical simulations [60]. Ni and Zuo et al. combined energy harvesting in a double mass series TMDs to test its vibration suppression and energy harvesting performance. Although both have good performance, the motion stroke is six times larger than the double mass parallel TMDs [61]. Later on, Zuo and Cui proposed a novel retrofittable approach for dual-functional energy-harvesting and robust vibration control by integrating the TMD and electromagnetic shunted resonant damping [62]. He further tested the double mass series TMDs implemented with an electromagnetic shunted resonant damper, which shows good vibration control and energy harvesting performance. Furthermore, the motion stroke only increases by 19% instead of more than six times.

2.2.3 Distributed-Multiple Tuned Mass Dampers (d-MTMDs)

In the 1980s, the large-scale tuned mass damper has been widely investigated and has already installed in high-rise buildings like the Citicorp Center Building in New York to reduce first mode motion [63]. Traditional TMD was proved to be effective for reducing wind-induced vibrations but was not recommended for reducing the seismic response of buildings [64].

In this background, the original idea of tuning d-MTMDs to different natural frequencies of the structure was proposed by Clark to against seismic excitation. Bergmann et al. investigated

the effectiveness of d-MTMDs under wind excitation [65]. The studies by Chen and Wu were focused on the multistage, multimode tuned mass dampers strategy for structures under seismic excitation [58, 66, 67]. A practical and accurate procedure has been developed to optimize the placement of mass dampers at different floors, which can reduce floor accelerations effectively [67]. Compared with the research of MTMDs on the same floor, d-MTMDs have been less investigated in the 1990s and 2000s. It was not until the last decade that more and more papers about d-MTMDs were published.

Moon designed vertically d-MTMDs for a 60-story tall building subjected to representative dynamic wind loads [5]. These mass dampers are tuned to the first or second natural frequency of the primary structure to reduce the first and second mode vibration passively. The installation floors of mass dampers for each mode are determined based on the primary structure's mode shape, as shown in Figure 2.7.

Modal energy was also studied to find out the energy absorption of the structural system under seismic excitation by Rahman et al. to evaluate the efficiency of d-MTMDs [68]. It is observed that single TMD and MTMDs installed on the top floor have better performance during the free vibration which is controlled only by the first mode after the earthquake. However, during earthquakes, when the response is governed by a broad range of excitation frequencies, d-MTMDs is more effective.

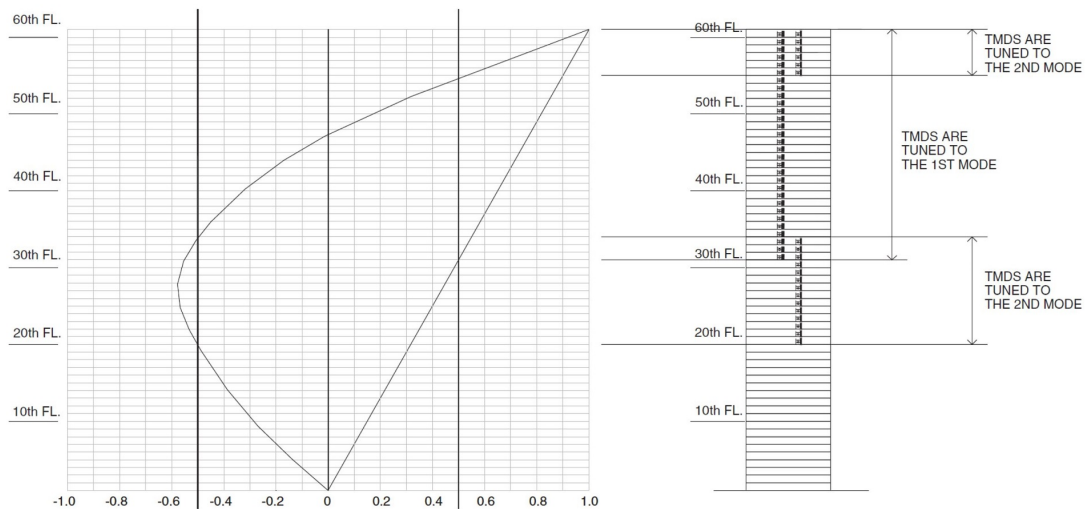


Figure 2.7: Vertically distributed-MTMDs based on mode shapes [5]¹².

Elias et al. investigated the across wind response control of a 76-story benchmark building with d-MTMDs [69, 70]. They controlled the first five modes in the d-MTMDs. The number of modes is decided according to the desired total modal mass participation. The TMDs are placed where the mode shape amplitude of the building is the largest/large in the first five modes and each is tuned with the corresponding modal frequency. The dynamic performance using d-MTMDs is compared with the performance of MTMDs placed on the same floor and

¹²Copyright ©2019, John Wiley & Sons, Ltd.. Reprinted by permission from John Wiley and Sons and Copyright Clearance Center (license Number 5367921154086).

2.3. VIBRATION CONTROL USING MOVEABLE FACADE

the performance of a single TMD with the same mass ratio. It is concluded in their study that the d-MTMDs is the most efficient approach to control the wind-induced vibration of a high-rise building. Based on this 76-story benchmark model, the performance of d-MTMDs under seismic excitation has also been studied [71]. Except for this benchmark model, a mDoF chimney model with d-MTMDs is also adopted to test the performance under seismic excitation [72], and under along wind excitation [73]. As listed above, Elias et al. have published a lot of papers about d-MTMDs in recent years. They have tested the d-MTMDs under different excitation and used different models to prove their effectiveness. However, they focused primarily on the multi-mode control strategy and place the TMDs where the mode shape amplitude of the structure is the largest or larger in the concerned mode. Rahmani and Könke developed an algorithm based on the Non-dominated Sorting Genetic Algorithm (NSGA-II) method to optimize the placement and parameters of d-MTMDs under earthquake excitation [74]. The results show that the optimum locations are related to the stories of the maximum modal displacement of the lower modes, which is highly activated by the earthquake excitation. With the development of artificial intelligence, many intelligent algorithms have been used to solve optimization problems automatically. The optimum results can be easily obtained, but what's important is whether the results can be theoretically perfect interpreted or whether a new theory can be developed from the results.

The idea of d-MTMDs was already proposed in the late 1980s, but as reviewed above, it was only intensively studied in the last ten years. The d-MTMDs also need additional mass as damping mass but the additional damping masses are distributed at different stories. Some researchers further proposed using the mass of facade or shading fins as the damping mass, which is reviewed in Section 2.3.3.

2.3 VIBRATION CONTROL USING MOVEABLE FACADE

2.3.1 Double-Skin Facade (DSF)

Before introducing the use of moveable facades for vibration control, a brief review of the conventional Double-Skin Facade (DSF) is conducted. The original concept of DSF traces back to the time when many houses in Europe used box windows to improve thermal insulation. The Steiff factory hall in Giengen, Germany, which is designed by Richard Steiff in 1903, is considered the first building installed with DSF [75], as shown in Figure 2.8. DSF originated in Europe but has gained more attention in North America and other Australasia countries in recent years [76].

There are many types of DSF according to different ways of classifications. The cavity ventilation mode, cavity ventilation type, and cavity partitioning are commonly used in the classification, as shown in Figure 2.9. The ventilation mode refers to the way air flows in the cavity between the outer and inner skins. The air-tightened DSF can provide better thermal insulation for the building to reduce heat loss in winter, while ventilated DSF can decrease heat gain in summer [77]. Cavity ventilation types can be categorized into natural ventilation, mechanical ventilation, and hybrid ventilation. According to the geometric structures of hot aisles in the

2.3. VIBRATION CONTROL USING MOVEABLE FACADE

double skin facades, DSFs can also be classified into box-window facade, shaft-box facade, corridor facade, and multi-story facade [78].



Figure 2.8: Steiff factory hall¹³.

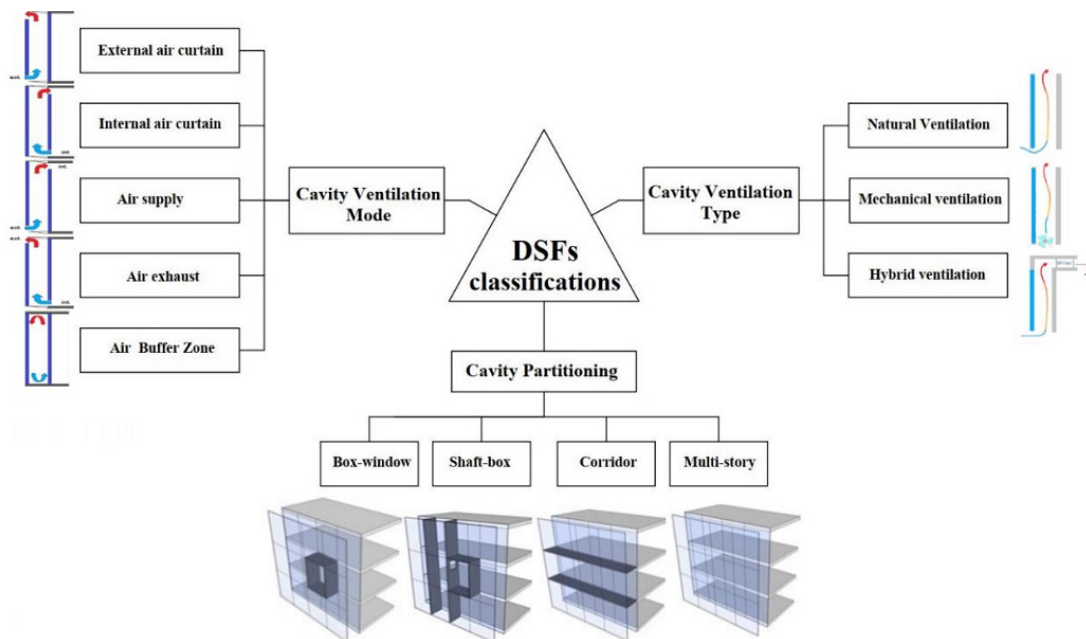


Figure 2.9: Different types of DSF according to three classification methods [6]¹⁴.

¹³"Denkmalgeschützte Fabrikhalle der Firma Steiff" by Zacharias L., used under Creative Commons CC BY-SA 3.0 (<https://creativecommons.org/licenses/by-sa/3.0>)

¹⁴Copyright ©2022, Al-awag and Wahab. Under Creative Commons CC BY 3.0 license (<https://creativecommons.org/licenses/by/3.0/>).

2.3. VIBRATION CONTROL USING MOVEABLE FACADE

Energy consumption can be significantly reduced by using DSF. The use of DSF leads to about 10-15% energy saving for cooling in the peak of summer due to heat exhausted by natural ventilation, and about 20-30% energy saving for heating in winter due to the greenhouse effect [79]. The research by Chan et al. indicates that DSF with single clear glazing as the inner skin and double reflective glazing as the outer skin can provide an annual energy saving of approximately 26% for building cooling, as compared to a conventional Single-Skin Facade (SSF) with single absorptive glazing [80]. Air-tightened DSFs have good performance in reducing heat loss during cold seasons. However, for hot and even subtropical climates, ventilated DSFs are more appropriate to improve human thermal comfort [80, 81]. Adjustable shading devices can be integrated as part of the DSF system to improve human thermal comfort further in hot seasons [82]. The transparency of DSFs ensures the advantages of using DSF have been investigated from the environmental, aesthetic, and economical aspects. From the environmental point of view, energy consumption can be significantly reduced by using DSF. The use of DSF leads to about 10-15% energy saving for cooling in the peak of summer due to heat exhausted by natural ventilation, and about 20-30% energy saving for heating in winter due to the greenhouse effect [79]. The research by Chan et al. indicates that DSF with single clear glazing as the inner skin and double reflective glazing as the outer skin can provide an annual energy saving of approximately 26% for building cooling, as compared to a conventional Single-Skin Facade (SSF) with single absorptive glazing [80]. Air-tightened DSFs have good performance in reducing heat loss during cold seasons, but they may have the risk of overheating in summer [83]. For hot and even subtropical climates, ventilated DSFs are more appropriate to improve human thermal comfort [80, 81]. Adjustable shading devices can be integrated as part of the DSF system to improve human thermal comfort further in hot seasons [82]. The transparency of DSF ensures sufficient daylight for the interior spaces without glare, which is an important factor of energy saving [84]. DSFs also have good performance of acoustic insulation, which can reduce noise levels at loud locations, such as highways or airports [85]. Additionally, the aesthetic value of DSF has attracted a lot of attention from architects, developers, and owners [81]. Economically, DSFs have a higher initial investment cost, but this can be balanced by the relatively lower running costs. However, DSFs have higher maintenance costs than traditional SSFs [18].

The types and advantages of the conventional double-skin facade have been briefly introduced, and the research on the use of moveable facades to reduce structural vibrations is reviewed as follows.

2.3.2 Facade isolation

Kareem proposed the concept of using moveable building cladding to isolate the dynamic wind loads from the structural system [21]. Using this new approach, the building facade is isolated from the primary structure, therefore, the dynamic wind loads can be avoided to act directly on the structure. By further spatially dividing the cladding (facade) into regular and isolated panels over the height of the buildings, the wind load correlation can be broken up, hence the overall load will be reduced [86].

2.3. VIBRATION CONTROL USING MOVEABLE FACADE

Although this concept has been proposed for more than 20 years, it wasn't until 2009 that Moon investigated it theoretically for the first time [22]. Double-skin facade, which has obtained a lot of attention in Europe due to its contribution to energy saving, is firstly investigated for its vibration suppression potential. In his study, the moveable DSF outer skin is perpendicularly connected with the building's primary structure using low-axial-stiffness spring and damper components so that the transmissibility of the dynamic wind loads can be reduced, as shown in Figure 2.10. The whole system is simplified as a two Degree-of-Freedom (2DoF) system and the dynamic wind loads are simplified as sinusoidal loads to represent the wind loads under the vortex-shedding condition. The parametric study of this system shows that the primary structure vibration is largely reduced using low-axial-stiffness connections but with the sacrifice of excessive outer skin facade vibration, which is a serious design limitation. Azad et al. have done a similar analysis, which came to the same conclusion as Moon [87].

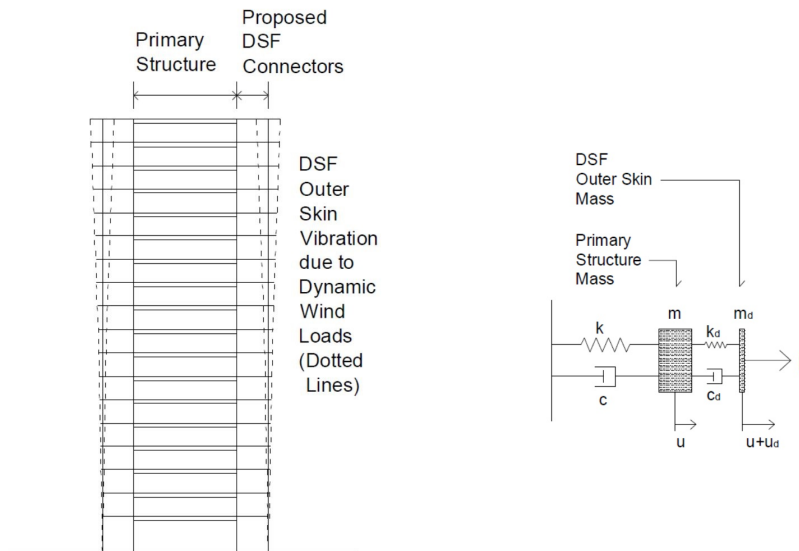


Figure 2.10: Concept diagram of facade isolation and its simplified 2DoF system [7]¹⁵.

Because of this limitation, Moon also proposed adding vertically distributed small tuned mass dampers within the DSF cavities [7], as shown in Figure 2.11. The DSF outer skins are fixed to the primary structure and the small additional masses vibrate within the cavities to dampen out the structure vibration, which functions as d-MTMDs. A big difference between facade isolation using the perpendicular moveable connection and d-MTMDs is that by facade isolation the wind loads first act on the moveable facade and then transmit to the primary structure, and by d-MTMDs the wind loads act directly on the primary structure as the facade is fixed to the primary structure.

¹⁵Copyright ©2011 Published by Elsevier Ltd.. Reprinted by permission from Elsevier and Copyright Clearance Center (license number 5367930404543).

2.3. VIBRATION CONTROL USING MOVEABLE FACADE

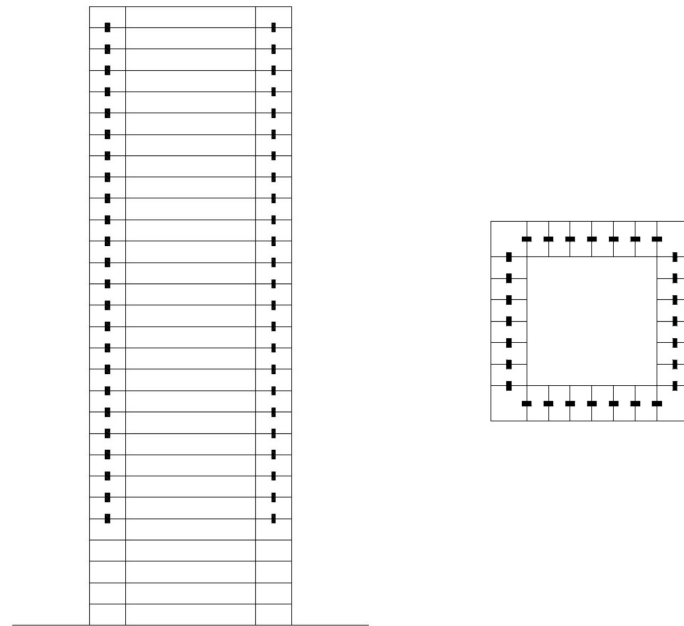


Figure 2.11: Concept diagram of distributed TMDs within the DSF cavities [7]¹⁶.

To mitigate the excessive vibration of the DSF outer skins under wind excitation, the tuned mass damper (TMD) and DSF damping (DSFD) interaction system was further proposed [23]. Compared with the traditional TMD system, the TMD/DSFD interaction system requires small additional damping mass and small installation space to achieve the same vibration control performance. Compared with the facade isolation system or DSF damping system, the TMD/DSFD interaction system has much smaller vibrations of the DSF outer skins. Therefore, this innovative system combines the advantages of these two systems, which makes it more possible to be realized.

2.3.3 Facade as damping mass

Facade isolation is proposed to reduce the wind-induced vibration of tall buildings. The dynamic wind loads act on the moveable facade element, then transmit to the primary structure. However, under seismic excitation, the seismic loads act on the primary structure first and then transmit to the moveable facade. Therefore, under seismic excitation, the facade isolation system using the perpendicular moveable connection is equivalent to d-MTMDs with facade mass as damping mass. The difference is that the optimum tuning of the system is different.

The moveable DSF is not the first non-structural member of the building used as damping mass to reduce primary structure vibration. Fu and Johnson first proposed using external shading fins as damping mass [88]. A pattern search optimization method was adopted to optimize the system that can significantly mitigate the structure vibration. However, pattern search is

¹⁶Copyright ©2011 Published by Elsevier Ltd.. Reprinted by permission from Elsevier and Copyright Clearance Center (license number 5367930404543).

2.3. VIBRATION CONTROL USING MOVEABLE FACADE

subjected to convergence to local optimums and produces different optimum results with different initial values. Therefore, with this method, only near-optimal results can be found. It is also observed that the increased performance of the primary structure comes at the expense of large movements of the damping mass. There is a trade-off between the structure vibration and damping mass stroke. Fu and Johnson further expanded their research of this system using active control [89]. LQR methodology is applied to further mitigate the structure vibration. In the same year, Fu formulated the facade damper system with different configurations and optimized the damper parameters using the same pattern search algorithm to minimize the structural responses to stochastic and historical earthquake excitations [90]. Same active control using LQR methodology has also been implemented in the facade damper system [8]. The suggested perpendicular connection by Fu and Zhang is shown in Figure 2.12. Barone et al. have also considered the flexural stiffness of the outer skin in their modeling [91]. Two global optimization methods, i.e., Genetic Algorithm (GA) and Particle Swarm Optimization (PSO) have been adopted to optimize the system. The PSO optimized results show in general better performance. Therefore, based on PSO, different objective functions are further investigated under different seismic events by this research group [92]. An average objective function that simultaneously takes into account multiple earthquake records is adopted to increase the robustness of the system.

Another similar damping system is the Hula Mass-damper System (HMS) [93], which is developed by the Obayashi Corporation. The entire outer skins of the DSF are considered rigid and connected to the primary structure using many compact high-damping rubbers. It has been experimentally confirmed by the Obayashi Technical Research Institute that the system can reduce about 20% to 30% of the seismically excited structural motion. The system has been used in the Hanae Mori Building in Tokyo to effectively protect the structure during earthquakes with a seismic intensity of magnitude 6 or higher [94].

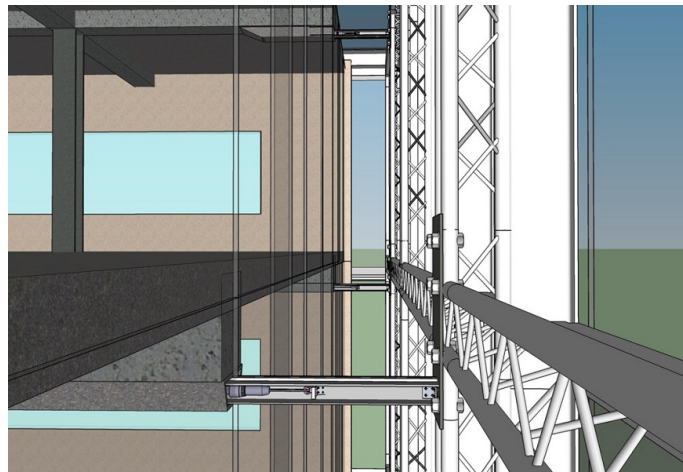


Figure 2.12: Suggested perpendicular connection [8]¹⁷.

¹⁷Copyright ©2016, American Society of Civil Engineers. Reprinted by permission from ASCE and Copyright Clearance Center (license ID 1257882-1).

2.4. DUAL-FUNCTIONAL DAMPERS WITH ENERGY HARVESTING

In all these studies, the flexibly connected facade can move back and forth perpendicular to the primary structure. For wind excitation, it can be designed as a facade isolation system, and for seismic excitation, it can be designed as d-MTMDs using moveable facade mass as damping mass. The difference is the tuning of the perpendicular moveable connection. In this dissertation, the innovative d-MTFD system using parallel moveable connections is proposed. Physically, the d-MTFD system has no difference from d-MTMDs. However, with a specially designed parallel connection, the system can be also used to mitigate wind-induced structural vibration and is more practical to be realized compared with the facade isolation system using the perpendicular connection. The difference between the perpendicular connection and parallel connection is illustrated in Figure 1.5.

2.4 DUAL-FUNCTIONAL DAMPERS WITH ENERGY HARVESTING

In the last decades, most of the research was focused on the application of harvesting energy from high-frequency vibrations with frequencies above 10 Hz. The oscillation is on the order of millimeters. The piezoelectric transducer is the dominant technology in these applications. The harvested power is from the scale of microwatts to milliwatts [95], which can be used in self-powered wireless sensors and other low-power electronics for structural health monitoring [96, 97]. Even though only quite limited energy is harvested but it is very meaningful, which brings breakthroughs in its applications. For the traditional portable electronics and wireless sensors, whose power supply in most cases are conventional batteries, problems occur because of the finite lifespan of their battery. Battery replacement is often not practical out of the consideration of high cost and sometimes inaccessible locations and so on. By harvesting waste mechanical energy, the life of the power supply can be prolonged, and the captured energy is ideally enough for the whole lifespan of the devices [97].

The vibrations of tall buildings, towers, and long-span bridges are usually with low frequency and large amplitude. These structures are very sensitive to dynamic loads, such as wind, earthquake, and traffic loads. Typically, the frequency of these large-scale structure vibrations is below 1 Hz and the potential power can reach the order of kilowatts. Thus, energy harvesting from large-scale vibrations has attracted more attention. The electromagnetic transducer is preferred for energy harvesting from large-scale vibration. The electromagnetic transducer also generates electrical damping force to reduce the vibration. As a result, energy dissipation strategies have evolved into energy harvesting strategies in structural vibration control by using dual-functional dampers that can not only reduce structural vibration but also generate energy [98, 99].

Electromagnetic motors have been widely used in vehicle suspensions. Because of the road roughness, accelerations, decelerations, and unevenness of the road, the undesired vibration will be excited. Using high-speed linear electromagnetic motors, the active-controlled vehicle suspension system is developed by Bose Corporation, which significantly improves the comfort of the passengers. With regenerative switching power amplifiers, the power consumption in the active control can be reduced by 1/3 [100]. For the rotational electromagnetic motor, the linear motion from the vibration needs to be transferred to rotational motion. The ball screw

mechanism is traditionally used to transform rotational motion into linear motion in the linear actuator, which can also inversely drive the rotational electromagnetic motor used as an energy harvester. Kawamoto et al. proposed a regenerative shock absorber using a ball screw mechanism [101]. Rack-and-pinion mechanism is also used to realize linear and rotational motion transform [102].

Palomera-Arias et al. studied the feasibility of passive electromagnetic dampers and pointed out their possible semi-active operation by modifying the circuit impedance [103]. Cassidy et al. developed an electromagnetic transducer by coupling a permanent-magnet synchronous with a back-driven ball screw [104]. This transducer was attached to a tuned mass damper to demonstrate its energy harvesting capacity. Different energy harvesting circuits (EHC) were also investigated in the TMD system by many researchers to achieve better vibration mitigation and energy harvesting performance [62, 105, 106]. Shen et al. investigated the pendulum-type energy regenerative TMD applied to a 76-story wind-excited benchmark building with fully considering the nonlinearities of the EM damper and EHC [107].

2.5 ACTIVE CONTROL SYSTEMS

Active control systems have been created to further enhance the structural vibration control ability compared to passive and semi-active systems [108]. These systems are designed to reduce the vibrations caused by different excitations, such as strong wind or seismic excitation. Active control can be effective in suppressing vibrations through the use of actuators, sensors, and feedback control algorithms. However, the setup and components of these systems are complex, and they require a considerable amount of external energy to operate during natural hazards [109]. The schematic diagram of active control is shown in Figure 2.13.

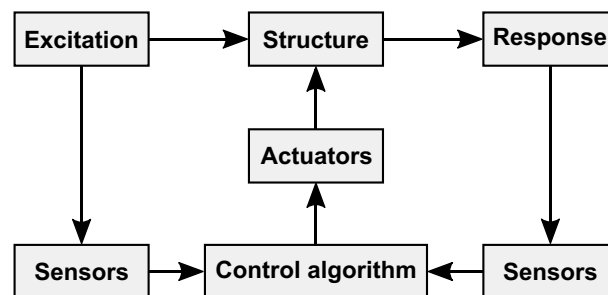


Figure 2.13: Schematic diagram of active control.

Active control for civil structures can be classified into two groups: active control of static characteristics, and active control of dynamic characteristics. The control of static characteristics involves monitoring the structure and taking corrective measures to restore it to a safe and functional state whenever safety or functionality criteria are breached. Conversely, the control of dynamic characteristics aims to ensure safety and functionality even under conditions of excessive dynamic excitations, such as earthquakes, wind, and environmental vibrations.

Worldwide, researchers have extensively studied numerous methods and techniques of active control for civil structures. Several review papers have provided a comprehensive overview

2.5. ACTIVE CONTROL SYSTEMS

of state of the art in the development of active control methods [108, 109, 110, 111, 112]. Some promising research, particularly conducted in Germany, is described below:

Sobek et al. conducted a study on the use of active elements with variable length and stiffness in static indeterminate structures to control deflections and redistribute forces [113]. They presented a bridge with actively controlled elements that can reduce stress peaks and homogenize force distribution. In another study, an actuation system was integrated into a 6-meter-long adaptive truss at the Structures Laboratory of University College London [114]. The aim of the system was to redirect the load path and maintain deflection limits without the need for additional material to withstand rare but strong loading events. These adaptive systems, which use active control, promote resource efficiency in the built environment.

The University of Stuttgart has been researching these systems for many years, culminating in the construction of the world's first adaptive high-rise building, the D1244 demonstrator (as shown in Figure 2.14), for experimental testing [9]. The tower is 36.5 meters tall and has 24 hydraulic actuators integrated into its steel structure, enabling flexible testing and validation of various technologies and materials. The ultimate goal of this research is to minimize energy and material usage, as well as greenhouse gas emissions.

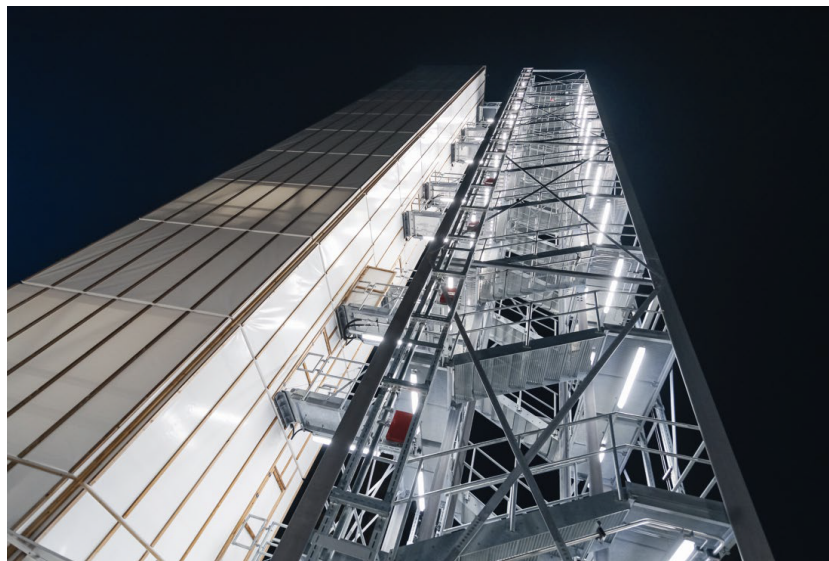


Figure 2.14: Completed adaptive high-rise building D1244 [9]¹⁸.

Bleicher constructed a stress ribbon footbridge with a span of 13 meters and a structural height of only 1 millimeter using high-strength carbon fiber reinforced plastic in the lab of the Chair of Conceptual and Structural Design at TU Berlin [115] (see Figure 2.15). To counteract pedestrian-induced vibrations, an active vibration control concept was developed and implemented in the footbridge. The concept incorporates sensors, closed-loop controls, and pneumatic muscle actuators embedded in the handrail to control the first three vertical modes of the bridge. A model-based controller was designed and implemented, demonstrating the effective-

¹⁸Copyright ©2022, John Wiley and Sons. Reprinted by permission from John Wiley and Sons and Copyright Clearance Center (license ID 5515410661993).

ness of the multimodal active vibration control by reducing pedestrian-induced accelerations by up to 90% [10]. Additional control for the first torsional mode was subsequently implemented using the root locus method on a reduced-order finite element model [116].



Figure 2.15: Stress ribbon bridge with sensors, actuators and a controller [10]¹⁹.

The reliability of active control systems over the long term has been a subject of dispute, especially for civil structures with lifetimes of a century or more and exposure to infrequent loads. While active control systems have been successfully implemented in several structures, particularly in Japan [117], their widespread acceptance has been restricted due to concerns over cost-effectiveness and reliability [111].

2.6 CONCLUSIONS

In this chapter, the review starts with the general damping methods such as using integrated energy dissipating dampers. The big category of mass dampers is then reviewed in depth. Especially, a detailed description of various Multiple Tuned Mass Dampers (MTMDs) is given from the time they were proposed to the present research process. For all these mass dampers, additional damping masses are needed. The research history of using moveable double-skin facade to reduce structural vibration is also fully described, from the early facade isolation concept using perpendicular moveable low-axial stiffness connections to use perpendicular moveable facade outer skin mass as damping mass to reduce seismic excited structural motion. As reviewed above, all the studies are based on the perpendicular moveable DSF. In this dissertation, the innovative parallel moveable DSF is proposed to reduce wind-induced structural vibration. Dual-functional damper combined with energy harvesting is reviewed, which is also implemented in my research. But with one step further, the harvested energy is used in this

¹⁹Copyright ©2012, John Wiley and Sons. Reprinted by permission from John Wiley and Sons and Copyright Clearance Center (license ID 5515421487364).

2.6. CONCLUSIONS

research as the energy source for the sensors and microcontroller to achieve the self-sufficient operation of semi-active control. At the end of this chapter, active control systems are also briefly introduced.

2.6. CONCLUSIONS

3 Conceptual analysis using a 2DoF model

In this chapter, the vibration reduction performance and energy harvesting potential of the facade isolation concept using perpendicular connection and our proposed d-MTFD system using parallel connection are investigated respectively under harmonic excitation based on a simplified two Degree-of-Freedom (2DoF) system. The harmonic excitation represents the dynamic wind excitation due to vortex shedding. Dynamic amplification factors are used to investigate the vibration reduction performance. The dimensionless power flow is used to investigate the energy harvesting potential. For the proposed d-MTFD system, the simplified 2DoF system is identical to the single TMD system. The different characteristics of these two approaches can be analyzed and discussed based on the simplified 2DoF system.

Copyright Statement

Parts of the research, text, and figures of this chapter are based on or have been published in the following article:

- [118] Yangwen Zhang, Thomas Schauer, and Achim Bleicher. Assessment of wind-induced vibration suppression and energy harvesting using facades. In *20th CONGRESS OF IABSE New York City*, pages 352–356, 2019²⁰

Figure 3.2 and Figure 3.3 have been published in [118].

²⁰Author's contribution: The author's contribution to [118] includes Conceptualization, Methodology, Software, Formal analysis, Investigation, Writing - Original Draft, Writing - Review & Editing, Visualization. No formal reuse license required for a thesis.

3.1. FACADE ISOLATION USING PERPENDICULAR CONNECTION

3.1 FACADE ISOLATION USING PERPENDICULAR CONNECTION

3.1.1 System modeling

Harmonic excitation, representing dynamic wind excitation, creates a condition very close to across-wind excitation due to vortex shedding. The vortex shedding induced lock-in phenomenon occurs when the vortex shedding frequency is very close to the first natural frequency of the high-rise building, which produces the most severe vibration problems. As the first mode of high-rise buildings is most easy to be excited, to simplify the analysis, the structure can be reduced to only maintain its first mode. The higher mode can be reduced. Hence, the first effective modal mass m and the corresponding stiffness k and damping coefficient c are used to build a single Degree-of-Freedom (sDoF) system to represent the primary structure of the high-rise building. With the attached facade m_f , which represents the whole perpendicular moveable facade mass, the facade isolation system can be simplified as a 2DoF system, as shown in Figure 3.1.

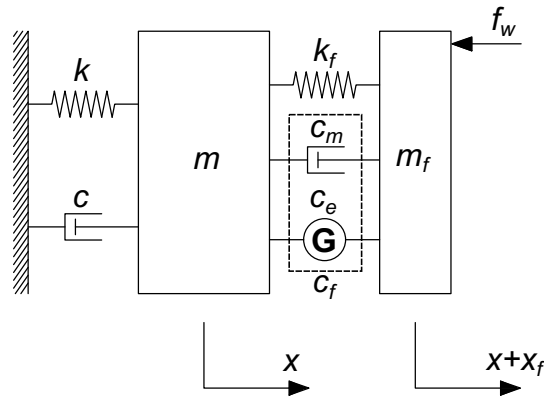


Figure 3.1: 2DoF facade isolation model.

The governing equations can be written as:

$$\begin{cases} m_f(\ddot{x} + \ddot{x}_f) + c_f\dot{x}_f + k_f x_f = f_w \\ m\ddot{x} + c\dot{x} + kx = c_f\dot{x}_f + k_f x_f \\ f_w = F_w \sin \Omega t \end{cases}, \quad (3.1)$$

where f_w is the sinusoidal force, which represents the simplified dynamic wind excitation, F_w is the wind force amplitude, and Ω is the angular frequency of the excitation. Electric machines are installed in the connection between the main structure and the moveable facade, which provide the electrical damping force with the electrical damping coefficient c_e . The mechanical damping due to viscous friction is modeled as mechanical damping coefficient c_m . The total connection damping coefficient c_f is the sum of the electrical damping and the mechanical damping coefficient, i.e., $c_f = c_e + c_m$.

The mechanical power part $c_m\dot{x}_f^2$ is dissipated as heat. The power part $c_e\dot{x}_f^2$ flows to the electrical circuit. In the circuit, part of the power is still dissipated because of the resistance.

This part of power loss is not discussed in the analysis.

3.1.2 Parametric studies of the vibration behavior

To analyze the steady-state response of this system, the Equations (3.1) can be transformed to the frequency domain using Laplace transform under the assumption that all initial conditions are zero.

In the frequency domain, the dynamic magnification factors for the primary structure and the stroke of the moveable facade mass can be derived as:

$$\beta_{DX} = \frac{X}{X_{st}} = \frac{\sqrt{f^4 + 4\xi_f^2 f^2 \rho^2}}{\sqrt{(f^2 - \rho^2 - (\bar{m}+1)f^2 \rho^2 + \rho^4 - 4\xi_f \xi_f f \rho^2)^2 + (2\xi_f f \rho + 2\xi_f \rho f^2 - 2\xi_f \rho^3 - 2\xi_f (\bar{m}+1)\rho^3 f)^2}} \quad (3.2)$$

$$\beta_{DXf} = \frac{X_f}{X_{st}} = \frac{1}{\bar{m}} \cdot \frac{\sqrt{(\rho^2 - 1)^2 + 4\xi_f^2 \rho^2}}{\sqrt{(f^2 - \rho^2 - (\bar{m}+1)f^2 \rho^2 + \rho^4 - 4\xi_f \xi_f f \rho^2)^2 + (2\xi_f f \rho + 2\xi_f \rho f^2 - 2\xi_f \rho^3 - 2\xi_f (\bar{m}+1)\rho^3 f)^2}} \quad (3.3)$$

some newly appearing notations are defined below:

$$\text{Amplitude of structural vibration:} \quad X \quad (3.4a)$$

$$\text{Amplitude of facade relative displacement:} \quad X_f \quad (3.4b)$$

$$\text{Structure static deformation:} \quad X_{st} = \frac{F_w}{k} \quad (3.4c)$$

$$\text{Mass ratio:} \quad \bar{m} = \frac{m_f}{m} \quad (3.4d)$$

$$\text{Tuning ratio:} \quad f = \frac{\omega_f}{\omega} \quad (3.4e)$$

$$\text{TMD natural angular frequency:} \quad \omega_f = \sqrt{k_f/m_f} \quad (3.4f)$$

$$\text{Structure natural angular frequency:} \quad \omega = \sqrt{k/m} \quad (3.4g)$$

$$\text{Excitation ratio:} \quad \rho = \frac{\Omega}{\omega} \quad (3.4h)$$

$$\text{Angular frequency of } f_w: \quad \Omega \quad (3.4i)$$

$$\text{TMD damping ratio:} \quad \xi_f = \frac{C_f}{2m_f\omega_f} = \xi_e \left(\frac{C_e}{2m_f\omega_f} \right) + \xi_m \left(\frac{C_m}{2m_f\omega_f} \right) \quad (3.4j)$$

$$\text{Structure damping ratio:} \quad \xi = \frac{C}{2m\omega} \quad (3.4k)$$

The facade mass ratio \bar{m} is realistically chosen as 1%, which represents the mass of the whole facade system around the building. The structural damping ratio ξ taken from the benchmark model is 1% [119]. The dynamic magnification factor for structure motion β_{DX} is plotted in Figure 3.2 with $\xi_f = 0.3$, $f = [0, 8]$ and $\rho = [0, 2]$. Near $f = 1$, the amplitude of the main structure is amplified because of resonance. As \bar{m} is given, f can be determined by the stiffness of the facade connection k_f . With large k_f , the facade can be viewed as fixed facade. Using connection with small k_f (i.e., small f), the vibration of the main structure can be efficiently reduced (see Figure 3.2a). However, the small stiffness connection brings simultaneously excessive motion of the facade, as shown in Figure 3.2b. To better observe the variation of β_{DXf} with the excitation ratio ρ , Figure 3.2b is plotted using dB (decibel). The maximum β_{DXf} (highlighted

3.1. FACADE ISOLATION USING PERPENDICULAR CONNECTION

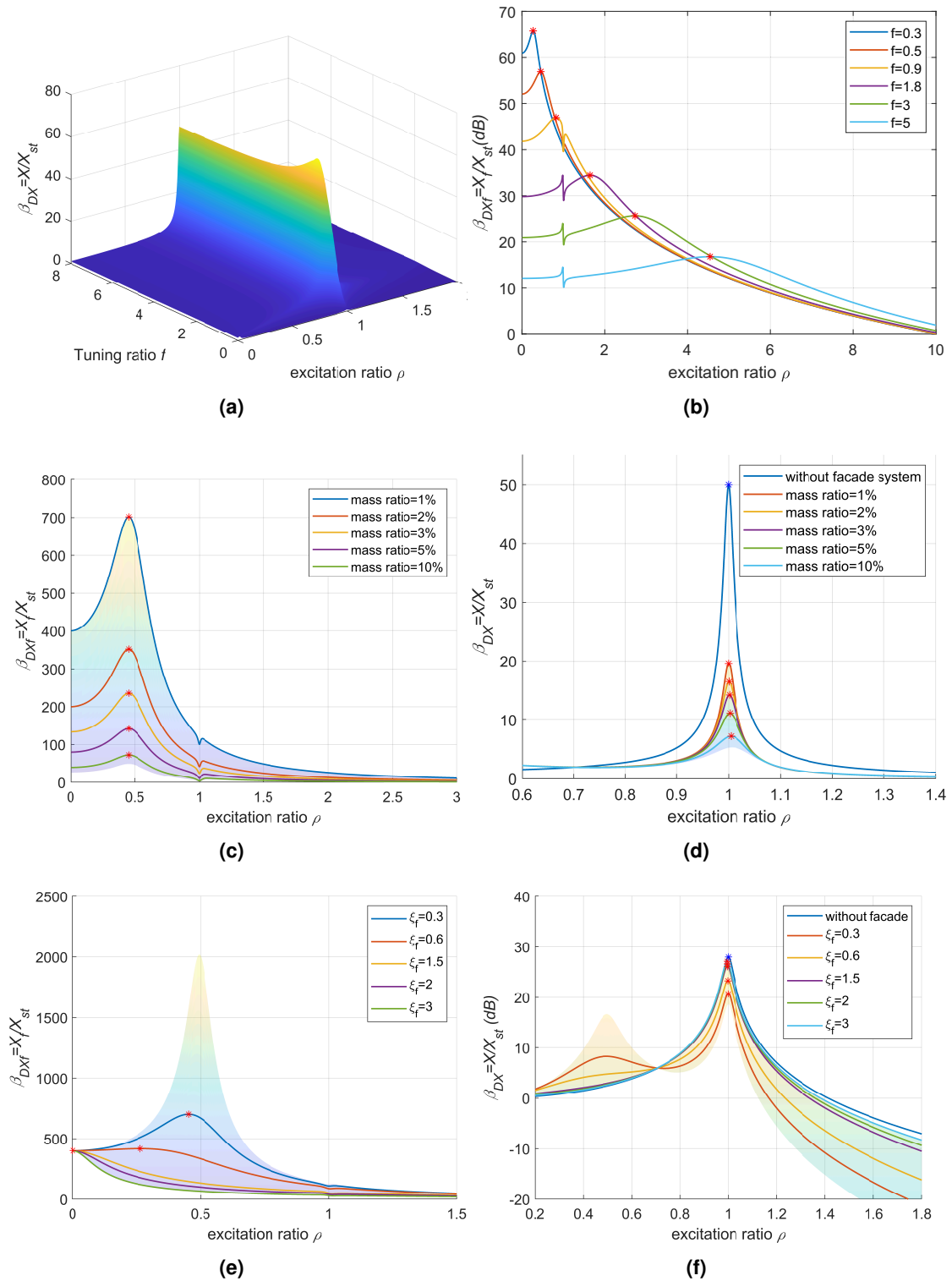


Figure 3.2: Dynamic magnification factor for structure motion β_{DX} and relative facade motion β_{DXf} .

3.1. FACADE ISOLATION USING PERPENDICULAR CONNECTION

with *) happens when ρ is a little smaller than f , which is because the defined tuning ratio f is based on undamped natural angular frequency of sDoF system. With low f , β_{DXf} is extremely high. As shown in Figure 3.2b, when $f = 0.3$, β_{DXf} reaches 1943 (65.77 dB). However, for the main structure, the maximum amplitude is greatly reduced. When $f = 5$, β_{DXf} goes down to 6.88 (16.75 dB), but the vibration of main structure cannot be reduced. In other words, when $f = 5$, the facade system doesn't have too much dynamic influence on the main structure, but the facade still vibrates, which is possible for the use of energy harvesting.

Increasing the mass ratio \bar{m} can effectively reduce the vibration of the facade, as shown in Figure 3.2c ($f = 0.5$, $\xi_f = 0.3$, $\rho = [0, 3]$). When ρ is near zero, then the excitation is viewed as static. β_{DXf} shows then the ratio of the static relative displacement of the facade to X_{st} . The static relative displacement of facade decreases greatly with the increasing \bar{m} . Increasing \bar{m} not only reduces the facade vibration, but also mitigates the main structure vibration, as shown in Figure 3.2d ($f = 0.5$, $\xi_f = 0.3$). Increasing facade mass m_f seems to be an effective method, but practically m_f only accounts for 1% of the main structure mass. Increasing the facade damping ratio also reduces excessive facade motion, as shown in Figure 3.2e ($f = 0.5$, $\bar{m} = 1\%$). As ξ_f increases, the relative facade motion slowly transitions from underdamped phase to overdamped phase, i.e., the damped natural frequency decreases from near its tuning ratio $f = 0.5$ until it becomes 0. Hence, for a large ξ_f , the peak of β_{DXf} caused by resonance gradually disappears, the maximum β_{DXf} happens when the excitation ratio is 0. However, for the main structure, when tuning ratio $f = 0.5$, large facade damping ratio makes the structure motion severe, as shown in Figure 3.2f ($f = 0.5$, $\bar{m} = 1\%$).

3.1.3 Parametric studies of energy harvesting

With electric machine, part of the power flow to the electrical circuit can be harvested. The average power flow to the electrical circuit in the frequency domain is investigated. For a system under harmonic excitation, the average power flow to the electrical circuit can be calculated as:

$$P_{AVE} = (c_e \Omega^2 X_f^2) / 2 = \xi_e f \bar{m} (\rho \beta_{DXf})^2 \cdot \frac{F_w^2}{m\omega}, \quad (3.5)$$

where ξ_e is the electrical damping ratio, which is defined in the Equation (3.4j). The excitation amplitude F_w , main structure mass m and structure natural angular frequency ω are system parameters that cannot be changed. Therefore, the dimensionless power flow P_{ave} is used for further investigation.

$$\begin{aligned} P_{ave} &= \frac{P_{AVE}}{(F_w^2/m\omega)} = \xi_e f \bar{m} (\rho \cdot \beta_{DXf})^2 \\ &= \frac{1}{\bar{m}} \cdot \frac{\xi_e f \rho^2 ((1 - \rho^2)^2 + 4\rho^2 \xi_f^2)}{(f^2 - \rho^2 - (\bar{m} + 1)f^2 \rho^2 + \rho^4 - 4\xi_f \xi_f f \rho^2)^2 + (2\xi_f f \rho + 2\xi_f \rho f^2 - 2\xi_f \rho^3 - 2\xi_f (\bar{m} + 1)\rho^3 f)^2} \end{aligned} \quad (3.6)$$

Figure 3.3a plots P_{ave} with $\bar{m} = 1\%$, $f = 0.5$, and mechanical damping ratio ξ_m (see Equation (3.4j)) due to friction is 0.1. It is observed that the maximum P_{ave} appears at $\xi_e = \xi_m = 0.1$, and the excitation ratio $\rho \cong f = 0.5$. It is well understood that the maximum

3.1. FACADE ISOLATION USING PERPENDICULAR CONNECTION

P_{ave} occurs when $\rho \cong f$. Regarding $\xi_e \cong \xi_m$, if $\xi = 0$, it can be strictly proved that:

$$\frac{dP_{ave}}{d\xi_e} = 0 \rightarrow \xi_e = \xi_m \quad (3.7)$$

When $\xi = 1\%$, the influence on the results can be neglected. As shown in Figure 3.3b ($\rho = f = 0.5, \bar{m} = 1\%$), the maximum P_{ave} always occurs when $\xi_e \cong \xi_m$. It should be noted that this is based on that the mechanical damping coefficient is given unchanged. By changing ξ_e , the facade damping coefficient ξ_f also changes. If ξ_f is unchanged, P_{ave} and ξ_e exhibit a linear incremental relationship. This relationship can also be observed in Equation (3.6), because β_{DXf} is only related to ξ_f .

Figure 3.3c shows that P_{ave} decreases with the growth of \bar{m} . The previous study shows that the larger the mass ratio \bar{m} , the better the vibration reduction performance of the main structure and facade. Hence, there is a trade-off between the energy harvesting and vibration suppression.

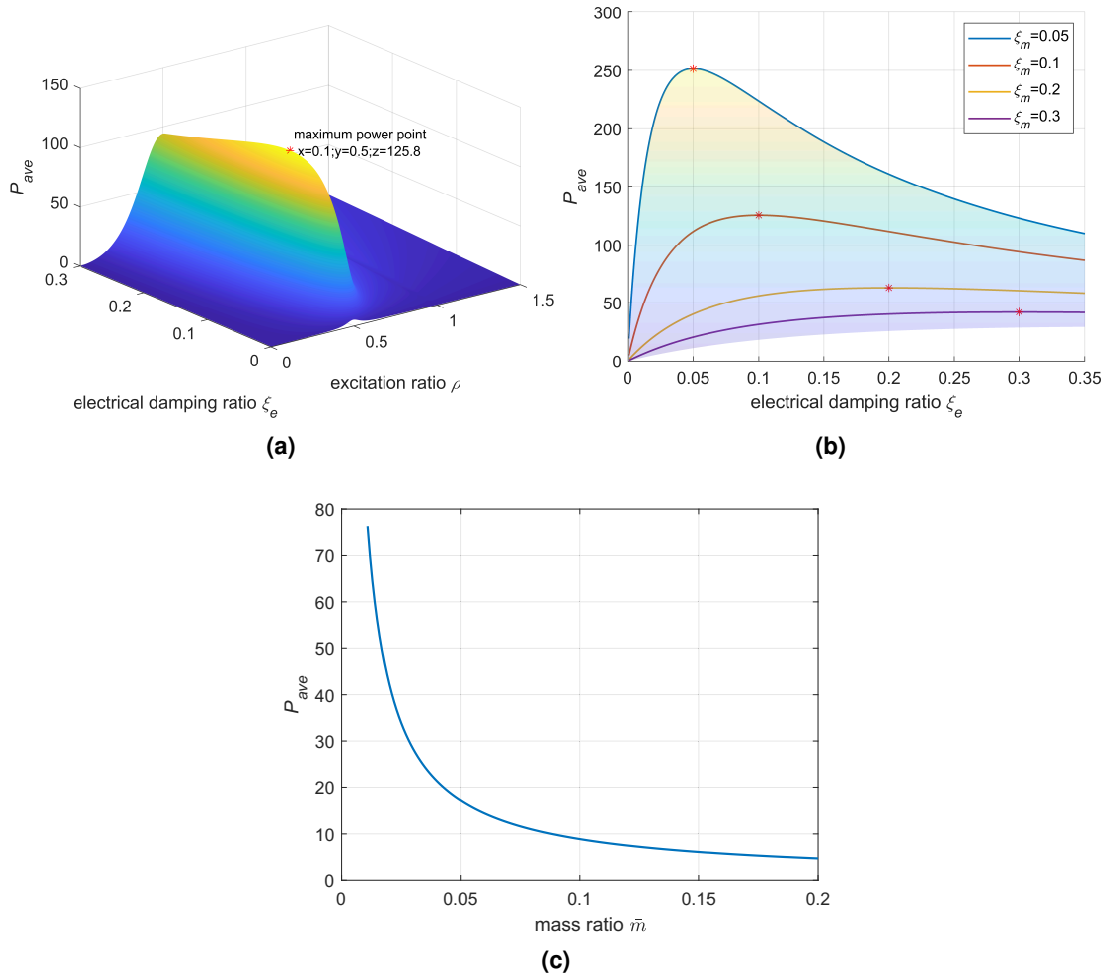


Figure 3.3: Dimensionless power flow to electrical circuit P_{ave} .

3.2 FACADE DAMPING USING PARALLEL CONNECTION

For our proposed d-MTFD system using parallel connection, the moveable facade mass functions as damping mass. Although the d-MTFD system is a multiple degree of freedom system, a simplified 2DoF system is still used to analyze the system conceptually. When the system is simplified as a 2DoF system, it is identical to a single TMD system. The damper need to be tuned near the predominant frequency (the first natural frequency) of the high-rise building to mitigate the structure dynamic response effectively.

The original concept of TMD system was first proposed by Frahm in 1909 [120], to reduce the undesirable rolling vibrations in ships. However, the Frahm’s dynamic absorber is only composed of a mass and a spring, without damping devices. Ormondroyd and Den Hartog introduced some damping in the TMD system in 1928 [121], which significantly enhanced its vibration control performance. The importance of their work is not only about the refinement of the system, but also the development of a general optimization method in the frequency domain, which is comprehensively described in Hartog’s famous book *Mechanical Vibration* [31]. The proposed optimization method is still widely used by engineers to determine the optimum parameters for the passive TMD system.

3.2.1 System modeling

The difference between the facade isolation concept and facade damping concept lies in the location of the across wind excitation caused by vortex shedding. For d-MTFD system, the parallel moveable facade is fixed in perpendicular direction. Therefore, the wind excitation acts directly on the primary structure. The 2DoF system is shown in Figure 3.4.

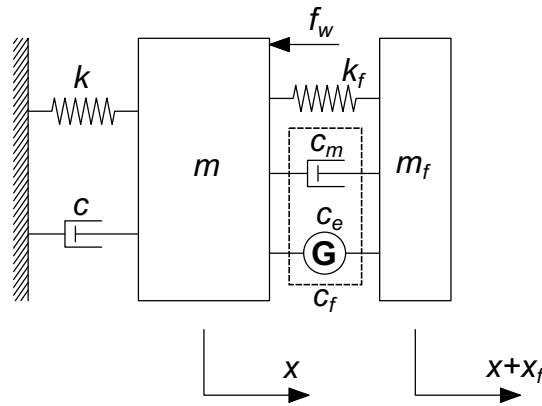


Figure 3.4: 2DoF facade damping system (TMD).

The governing equations can be written as:

$$\begin{cases} m_f(\ddot{x} + \ddot{x}_f) + c_f\dot{x}_f + k_f x_f = 0 \\ m\ddot{x} + c\dot{x} + kx - c_f\dot{x}_f - k_f x_f = f_w \\ f_w = F_w \sin \Omega t \end{cases} \quad (3.8)$$

3.2. FACADE DAMPING USING PARALLEL CONNECTION

To further study its energy harvesting potential, electric machines are used. The total damping coefficient c_f of the connection consists of electrical damping coefficient c_e in the electric machine and mechanical damping coefficient c_m due to all the viscous friction in the connection, i.e., $c_f = c_e + c_m$. The mechanical power part $c_m \dot{x}_f^2$ is dissipated as heat. The power part $c_e \dot{x}_f^2$ flows to the electrical circuit, which can be potentially harvested.

3.2.2 Parametric studies of the vibration behavior

To analyze the steady-state response of this system, the Equations (3.8) can be transformed to the frequency domain using Laplace transform under the assumption that all initial conditions are zero.

In frequency domain, the dynamic magnification factors for primary structure and the relative displacement of the facade damping mass can be derived as:

$$\beta_{DX} = \frac{X}{X_{st}} = \frac{\sqrt{(f^2 - \rho^2)^2 + 4\xi_f^2 f^2 \rho^2}}{\sqrt{(f^2 - \rho^2 - (\bar{m}+1)f^2 \rho^2 + \rho^4 - 4\xi_f \xi_f f \rho^2)^2 + (2\xi_f f \rho + 2\xi_f \rho f^2 - 2\xi_f \rho^3 - 2\xi_f (\bar{m}+1)\rho^3 f)^2}} \quad (3.9)$$

$$\beta_{DXf} = \frac{X_f}{X_{st}} = \frac{\rho^2}{\sqrt{(f^2 - \rho^2 - (\bar{m}+1)f^2 \rho^2 + \rho^4 - 4\xi_f \xi_f f \rho^2)^2 + (2\xi_f f \rho + 2\xi_f \rho f^2 - 2\xi_f \rho^3 - 2\xi_f (\bar{m}+1)\rho^3 f)^2}} \quad (3.10)$$

The simplified 2DoF facade damping system is physically identical to the single TMD system. Unlike the facade isolation system, the optimum tuning and damping ratio have been mathematically rigorously derived for the single TMD system. Den Hartog has derived the optimum tuning ratio and damping ratio using fixed point method [31], as listed below:

$$\begin{cases} f_{opt} = \frac{1}{1 + \bar{m}} \\ \xi_{d.opt} = \sqrt{\frac{3\bar{m}}{8(1 + \bar{m})}} \end{cases} \quad (3.11)$$

To better compare with facade isolation system, the moveable facade mass ratio is practically taken as 1%. Hence, the optimum tuning ratio and TMD damping ratio can be both calculated: $f_{opt} = 0.990$ and $\xi_{d.opt} = 0.061$. The optimum damping ratio $\xi_{d.opt}$ from Hartog is derived to achieve smallest primary structure response, but not the smallest TMD stroke response (relative displacement of moveable facade). The TMD stroke (facade relative displacement) is also an important design criterion. Isao Nishimura proposed the optimum TMD damping ratio to achieve the minimum TMD stroke response [122]. The equation is listed as:

$$\xi_{d.opt} = \sqrt{\frac{\bar{m}}{2(1 + \bar{m})}} \quad (3.12)$$

Therefore, with $\bar{m} = 1\%$, the optimum TMD damping ratio proposed by Isao Nishimura can be calculated as 0.07. For reinforced concrete structure, the structure damping ratio ξ is usually between 1% to 2%. In both mathematical derivation of Den Hartog and Isao Nishimura, ξ is assumed as 0. The dynamic amplification factors for the structure motion and TMD stroke with different TMD damping ratio are plotted in Figure 3.5a and Figure 3.5b.

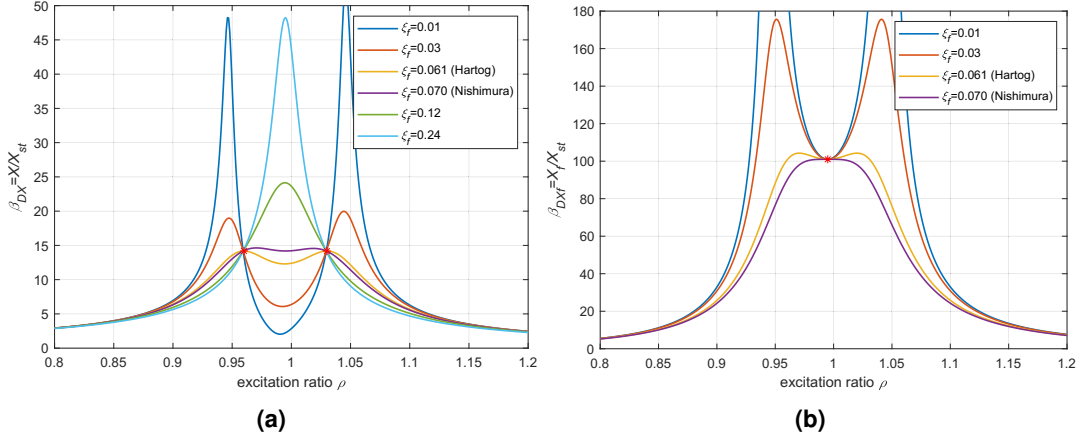


Figure 3.5: Dynamic magnification factor of structure motion (a) / TMD stroke (b).

As observed above, the small discrepancy between ξ_f (Hartog) and ξ_f (Nishimura) does not significantly influence the primary structure response. The peak of the primary structure is just a little more reduced using ξ_f (Hartog) rather than ξ_f (Nishimura), but the damping augmentation makes the peak of TMD stroke smaller, which makes Nishimura's optimization more favorable from an engineering point of view.

3.2.3 Parametric studies of energy harvesting

For facade damping system, the derived equation of average power flow to the electrical circuit in frequency domain is the same as the equation for facade isolation, as listed in Equation (3.6). The dimensionless power flow P_{ave} for facade damping system is further derived as below by substituting the dynamic magnification factor:

$$\begin{aligned}
 P_{ave} &= \frac{P_{AVE}}{(F^2/m\omega)} = \xi_e f \bar{m} (\rho \cdot \beta_{DXf})^2 \\
 &= \frac{\xi_e f \bar{m} \rho^6}{(f^2 - \rho^2 - (\bar{m} + 1)f^2 \rho^2 + \rho^4 - 4\xi_f \xi_e f \rho^2)^2 + (2\xi_f f \rho + 2\xi_e \rho f^2 - 2\xi_e \rho^3 - 2\xi_f (\bar{m} + 1)\rho^3 f)^2}
 \end{aligned} \tag{3.13}$$

The dimensionless power flows are plotted in Figure 3.6. $\bar{m} = 1\%$ is used for the Figure 3.6a and Figure 3.6b. The optimum tuning damping ratio ξ_f is calculated as 0.07 by the Equation (3.12) proposed by Nishimura. As the total ξ_f is already fixed, it can be observed that with the increasing electrical damping ratio ξ_e , more power flows into the electrical circuit. In Figure 3.6c ($\xi_e = \xi_m$), the dimensionless power flow P_{ave} decreases with the growth of \bar{m} .

3.3 CONCLUSION

In this chapter, based on simplified 2DoF systems, the vibration reduction performance of the facade isolation concept using perpendicular connections and the proposed d-MTFD system using parallel connections are investigated under harmonic excitation, respectively. By replac-

3.3. CONCLUSION

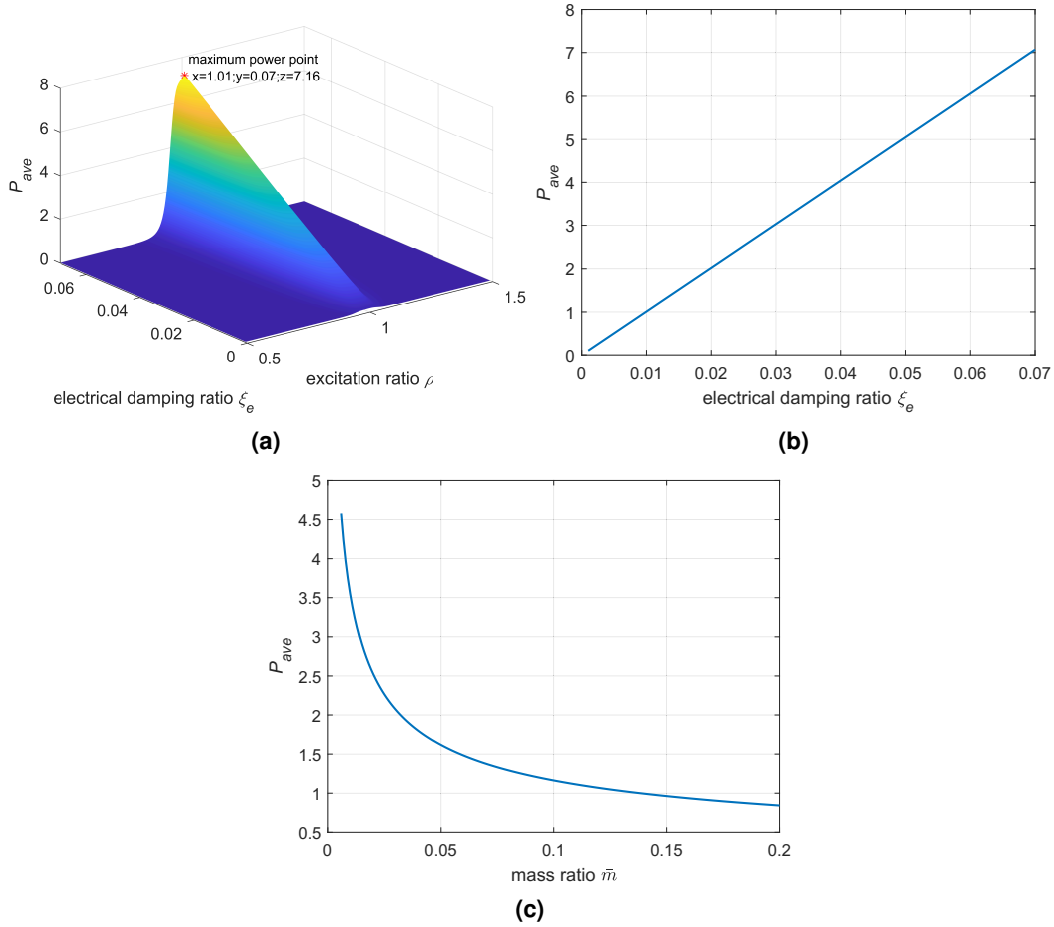


Figure 3.6: Dimensionless Power Flow to Electrical Circuit P_{ave} .

ing the conventional energy dissipating damping devices with electric machines, the energy harvesting potential of both systems has also been investigated. By assuming the facade mass ratio as 1%, the dynamic amplification factor of the structural motion can be reduced from 50 (conventional DSF) to 20. However, the dynamic amplification factor of the perpendicular facade motion reaches 700 (see Figure 3.2), which is unacceptable in practice. As a comparison, with the same mass ratio 1%, for the simplified 2DoF system using parallel connection that follows Den Hartog's optimum tuning, the dynamic amplification factor of the structural motion can be reduced to 15, and the dynamic amplification factor of the parallel facade motion is around 100 (see Figure 3.5). This result was also confirmed by Di Giovanni and Bernardini [123]. Therefore, our subsequent research is focused on parallel moveable facades that are more likely to be realized in real projects. From the aspect of energy harvesting, as the optimum total facade damping ratio for a simplified 2DoF facade damping system is also given by Den Hartog, increasing the electrical damping ratio can increase the dissipated energy in the electrical domain, which increases the potential of energy harvesting. The analysis in this chapter gives us a general theoretical understanding of these two systems and provides a direction for further investigation.

3.3. CONCLUSION

4 System modeling

In this chapter, to better introduce the integration of the proposed d-MTFD system in the building, the high-rise building is modeled as a multiple Degree-of-Freedom (mDoF) lumped mass system under the assumption of a shear building model. The modeling of the system is described in detail in Section 4.1. The governing equations of the system in the physical and modal coordinates are expressed respectively. Modal reduction is used to reduce the order of the system to accelerate the simulation speed without much loss of accuracy in the results. The reduced-order state-space model is derived for optimization in Chapter 5. A 76-story high benchmark building used for further simulation is introduced in Section 4.2. The proposed d-MTFD system is assumed to be installed on the upper stories of this benchmark building. Three different equivalent rolling friction coefficient is assumed in the model for further analysis. The corresponding across-wind excitation for this benchmark building is introduced in Section 4.3.

Copyright Statement

Parts of the research, text, and figures of this chapter are based on or have been published in the following article:

- [124] Yangwen Zhang, Thomas Schauer, and Achim Bleicher. Optimized passive/semi-active vibration control using distributed-multiple tuned facade damping system in tall buildings. *Journal of Building Engineering*, 52:104416, 2022²¹

Figure 4.1 and Figure 4.2 have been published in [124].

²¹ Author's contribution: The author's contribution to [124] includes Conceptualization, Methodology, Software, Formal analysis, Investigation, Writing - Original Draft, Writing - Review & Editing, Visualization. Copyright ©2020 Zhang, Schauer and Bleicher. Under Creative Commons CC BY 4.0 license (<https://creativecommons.org/licenses/by/4.0/>).

4.1. STRUCTURAL MODELING

4.1 STRUCTURAL MODELING

The proposed d-MTFD system is assumed to be installed on the upper n_f stories of a high-rise building. Under across-wind excitation, the front and rear parallel moveable DSF's outer skin at the upper stories are activated and function as damping mass. The mass of the moveable facade outer skin on each side of the building is coupled per story. The summarized moveable facade mass (sum of front and rear moveable facade outer skin mass) at each upper story is indicated as $m_{f,i}$, where $i = 1, 2, \dots, n_f$. The parallel moveability is achieved by the specially designed connections, which consist of the spring system, the guide rail system (with rolling bearings, which brings inevitable rolling friction to the system), and the electrical damping unit. A constructional design has been proposed together with Josef Gartner GmbH, which is described in detail in Chapter 7. The connection can be modeled by introducing the facade connection stiffness, facade connection damping coefficient, and rolling friction. Therefore, the corresponding summarized connection stiffness, damping coefficient and rolling friction are indicated as $k_{f,i}$, $c_{f,i}$ and $f_{fri,i}$, respectively. The facade connection damping coefficient $c_{f,i}$ consists of two parts: the inherent mechanical damping part $c_{m,i}$ due to viscous friction and the adjustable electrical damping part $c_{e,i}$ realized by the electric machines.

The deformation of high-rise buildings under horizontal loads consists of shear deformation and bending deformation. With the increasing slenderness ratio, the bending deformation increases significantly, which cannot be ignored in the modeling [1, 125]. For super-slender high-rise buildings, the shear bending model including the rotational Degree-of-Freedoms (DoFs) can be more accurate for describing the dynamic structural behavior. However, in this section, to better introduce the integration of the proposed system in the building, the tall building is simply modeled as a multiple Degree-of-Freedom (mDoF) lumped mass system under the assumption of a shear building model. Each story is modeled as a lumped mass following the procedure in [119]. As shown in Figure 4.1, the analytical model of a n -story high building is illustrated, whose upper n_f stories are installed with parallel moveable DSF. m_1, m_2, \dots, m_n are the lumped story masses of the building and $f_{w,1}, f_{w,2}, \dots, f_{w,n}$ are the across-wind loads acting on different stories.

The governing equation of a high-rise building installed with the d-MTFD system can be expressed as:

$$\mathbf{M}_s \ddot{\mathbf{x}} + \mathbf{C}_s \dot{\mathbf{x}} + \mathbf{K}_s \mathbf{x} = \boldsymbol{\eta} \mathbf{f}_w + \mathbf{B}_f \mathbf{f}_{fri}, \quad (4.1)$$

in which $\mathbf{M}_s \in \mathbb{R}^{n_s \times n_s}$, $\mathbf{C}_s \in \mathbb{R}^{n_s \times n_s}$, $\mathbf{K}_s \in \mathbb{R}^{n_s \times n_s}$ are mass, damping, and stiffness matrices of the whole system, where $n_s = n + n_f$. $\mathbf{x} = [x_1, x_2, \dots, x_n, x_{f,1}, x_{f,2}, \dots, x_{f,n_f}]^T \in \mathbb{R}^{n_s}$ is the vector of absolute structural displacements and absolute facade displacements. $\mathbf{f}_w = [f_{w,1}, f_{w,2}, \dots, f_{w,n}]^T \in \mathbb{R}^n$ is the across-wind excitation vector and $\boldsymbol{\eta} \in \mathbb{R}^{n_s \times n}$ is the excitation influence matrix. $\mathbf{f}_{fri} = [f_{fri,1}, f_{fri,2}, \dots, f_{fri,n_f}]^T \in \mathbb{R}^{n_f}$ is the rolling friction of each story between the moveable DSF's outer skin and the fixed inner skin due to the guide rail system. $\mathbf{B}_f \in \mathbb{R}^{n_s \times n_f}$ is the friction influence matrix. Explicit expressions for the matrices of \mathbf{M}_s , \mathbf{C}_s , \mathbf{K}_s , $\boldsymbol{\eta}$ and \mathbf{B}_f are given in the Appendix A.1. The Coulomb friction model is assumed for the rolling friction, which

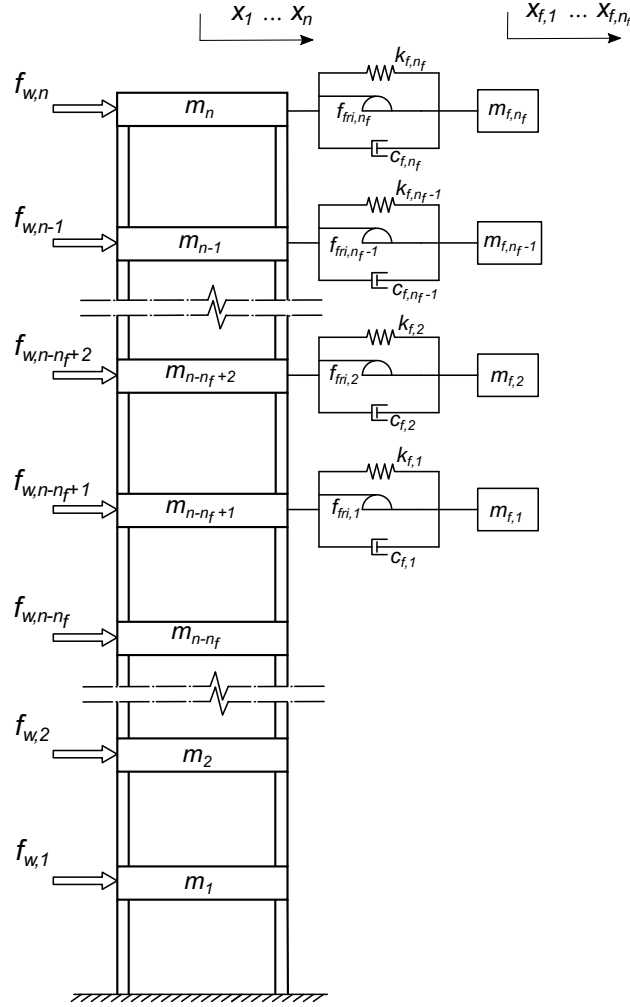


Figure 4.1: Analytical model of d-MTFD system.

can be written in the following equations [126]:

$$\begin{cases} f_{fr,i} = -\text{sgn}(\dot{x}_{fr,i})\bar{f}_{fr,i} \\ \dot{x}_{fr,i} = \dot{x}_{f,i} - \dot{x}_{n-n_f+i} \end{cases} \quad i = (1, 2, \dots, n_f) \quad (4.2)$$

Coulomb's law takes into account only the direction of the relative velocity of the facade at each story $\dot{x}_{fr,i}$, not the magnitude. The direction of rolling friction is opposite to the direction of the relative velocity $\dot{x}_{fr,i}$. $\bar{f}_{fr,i}$ is the magnitude of the rolling friction. It includes the friction caused by the self-weight of the parallel moveable facade and the friction caused by the along-wind force perpendicularly acting on the parallel moveable facade. The equation can be written as:

$$\bar{f}_{fr,i} = \mu_{r_1} \cdot m_{f,i}g + \mu_{r_2} \cdot f_{w,al,i} \quad i = (1, 2, \dots, n_f), \quad (4.3)$$

in which μ_{r_1} is the friction coefficient of the rolling bearings used to carry the self-weight of the

4.1. STRUCTURAL MODELING

parallel moveable facade, μ_{r_2} is the friction coefficient of the rolling bearings used to withstand along-wind forces, and g is the gravitational acceleration. The friction coefficient of the rolling bearings depends significantly on the used rolling elements, such as balls or different kinds of rollers. The mean along-wind force $f_{w,al,i}$ can be calculated as:

$$\begin{cases} f_{w,al,i} = \frac{1}{2} \rho_a C_d A_{f,i} U_i^2 \\ m_{f,i} = A_{f,i} \cdot \rho_f \end{cases} \quad i = (1, 2, \dots, n_f), \quad (4.4)$$

where ρ_a is the air density, ρ_f is the overall surface density, C_d is the drag coefficient, $A_{f,i}$ is the area where the along-wind force acts, U_i is mean along-wind speed [127]. By rearranging the Equations (4.3) and (4.4), $\bar{f}_{fri,i}$ can be calculated by introducing the equivalent rolling friction coefficient $\mu_{r,i}$, as written below:

$$\begin{cases} \bar{f}_{fri,i} = \mu_{r,i} \cdot m_{f,i} g \\ \mu_{r,i} = \mu_{r_1} + \frac{\rho_a C_d U_i^2}{2 \rho_f g} \cdot \mu_{r_2} \end{cases} \quad i = (1, 2, \dots, n_f), \quad (4.5)$$

To make the implementation of multi-objective optimization (see Section 5.1.1) efficient, increasing the simulation speed is necessary. Across-wind loads primarily excite the lower modes of the structure, hence, higher modes can be reduced to accelerate the simulation speed without much loss of the accuracy of results. Modal reduction is adopted to derive a reduced order system [128]. By introducing $\mathbf{x} = \Phi \mathbf{z}$, the governing Equation (4.1) in the physical coordinates \mathbf{x} can be transformed to the modal coordinates \mathbf{z} as follows:

$$\underbrace{\Phi^T \mathbf{M}_s \Phi}_{\mathbf{M}_M} \ddot{\mathbf{z}} + \underbrace{\Phi^T \mathbf{C}_s \Phi}_{\mathbf{C}_M} \dot{\mathbf{z}} + \underbrace{\Phi^T \mathbf{K}_s \Phi}_{\mathbf{K}_M} \mathbf{z} = \Phi^T \boldsymbol{\eta} \mathbf{f}_w + \Phi^T \mathbf{B}_f \mathbf{f}_{fri}, \quad (4.6)$$

where $\mathbf{M}_M \in \mathbb{R}^{n_{red} \times n_{red}}$, $\mathbf{C}_M \in \mathbb{R}^{n_{red} \times n_{red}}$, $\mathbf{K}_M \in \mathbb{R}^{n_{red} \times n_{red}}$ are the reduced modal mass, damping, and stiffness matrices. $\Phi \in \mathbb{R}^{n_s \times n_{red}}$ is the matrix of the reduced n_{red} mode shapes. $\mathbf{z} = [z_1, z_2, \dots, z_{n_{red}}]^T \in \mathbb{R}^{n_{red}}$, $\dot{\mathbf{z}} \in \mathbb{R}^{n_{red}}$, and $\ddot{\mathbf{z}} \in \mathbb{R}^{n_{red}}$ represents the system modal displacement, velocity and acceleration vector, respectively. The governing equation (4.6) can be rewritten in state-space form:

$$\begin{aligned} \dot{\mathbf{z}} &= \mathbf{A} \mathbf{z} + \mathbf{B} \mathbf{f}_w + \mathbf{E} \mathbf{f}_{fri} \\ \mathbf{y}_1 &= \mathbf{C}_1 \mathbf{z} + \mathbf{D} \mathbf{f}_w + \mathbf{F} \mathbf{f}_{fri} \\ \mathbf{y}_2 &= \mathbf{C}_2 \mathbf{z}, \end{aligned} \quad (4.7)$$

where the state variables $\mathbf{Z} = [\mathbf{z}^T, \dot{\mathbf{z}}^T]^T \in \mathbb{R}^{2 \cdot n_{red}}$ are the modal displacement and velocity of the whole system. The $\mathbf{A} \in \mathbb{R}^{2 \cdot n_{red} \times 2 \cdot n_{red}}$, $\mathbf{B} \in \mathbb{R}^{2 \cdot n_{red} \times n}$, $\mathbf{E} \in \mathbb{R}^{2 \cdot n_{red} \times n_f}$ matrices are:

$$\mathbf{A} = \begin{bmatrix} 0 & \mathbf{I} \\ -\mathbf{M}_M^{-1} \mathbf{K}_M & -\mathbf{M}_M^{-1} \mathbf{C}_M \end{bmatrix}, \quad \mathbf{B} = \begin{bmatrix} 0 \\ \mathbf{M}_M^{-1} \Phi^T \boldsymbol{\eta} \end{bmatrix}, \quad \mathbf{E} = \begin{bmatrix} 0 \\ \mathbf{M}_M^{-1} \Phi^T \mathbf{B}_f \end{bmatrix} \quad (4.8)$$

The performance output $\mathbf{y}_1 \in \mathbb{R}^{n_f+1}$ contains relative displacement of facade mass at the n_f top stories and the top floor structural acceleration. The defined objective functions can be

4.2. BENCHMARK BUILDING WITH D-MTFD SYSTEM

calculated based on the performance output and evaluated during the optimization. \mathbf{y}_1 can be obtained by matrices $\mathbf{C}_1 \in \mathbb{R}^{(n_f+1) \times 2 \cdot n_{red}}$, $\mathbf{D} \in \mathbb{R}^{(n_f+1) \times n}$, $\mathbf{F} \in \mathbb{R}^{(n_f+1) \times n_f}$, as listed below:

$$\mathbf{C}_1 = \mathbf{S}_1 \cdot \begin{bmatrix} 0 & \mathbf{T}\Phi\mathbf{I} \\ -\Phi\mathbf{M}_M^{-1}\mathbf{K}_M & -\Phi\mathbf{M}_M^{-1}\mathbf{C}_M \end{bmatrix}, \quad \mathbf{D} = \mathbf{S}_1 \cdot \begin{bmatrix} 0 \\ \Phi\mathbf{M}_M^{-1}\Phi^T\boldsymbol{\eta} \end{bmatrix}, \quad \mathbf{F} = \mathbf{S}_1 \cdot \begin{bmatrix} 0 \\ \Phi\mathbf{M}_M^{-1}\Phi^T\mathbf{B}_f \end{bmatrix}, \quad (4.9)$$

where $\mathbf{T} \in \mathbb{R}^{n_s \times n_s}$ is the transfer matrix to obtain the relative displacement, and $\mathbf{S}_1 \in \mathbb{R}^{n_f+1 \times 2 \cdot n_s}$ is the selecting matrix to output the values of chosen floors.

The measurement output $\mathbf{y}_2 \in \mathbb{R}^{n_{sel}}$ includes the selected structural displacement and velocity, facade relative displacement and facade relative velocity, which are used in the implemented semi-active control logic. \mathbf{y}_2 is obtained by matrix $\mathbf{C}_2 \in \mathbb{R}^{n_{sel} \times 2 \cdot n_{red}}$, as presented below:

$$\mathbf{C}_2 = \mathbf{S}_2 \cdot \begin{bmatrix} \mathbf{T}\Phi\mathbf{I} & 0 \\ 0 & \mathbf{T}\Phi\mathbf{I} \end{bmatrix}, \quad (4.10)$$

where $\mathbf{S}_2 \in \mathbb{R}^{n_{sel} \times 2 \cdot n_s}$ is the selecting matrix to output the values of chosen floors.

4.2 BENCHMARK BUILDING WITH D-MTFD SYSTEM

To illustrate the effectiveness of the d-MTFD system in mitigating structural responses, the widely used 76-story 306 m high benchmark building, proposed by Yang et al. [119], is assumed to be equipped with the proposed d-MTFD system. This building has a square 42 m \times 42 m cross-section, hence it is slender with a slenderness ratio of 7.3, making it dynamically sensitive to wind excitation. This 76-story benchmark building is modeled as a vertical cantilever beam (Bernoulli-Euler beam). A finite element model was built by regarding the portion of the building between two adjacent floors as a uniform thickness beam element, which leads to 76 translational and 76 rotational DOFs. The rotational DoFs are then removed using static condensation. The remaining 76 translational DOFs represent the displacement of each floor in the lateral direction and form the lumped mass model, as shown in Figure 4.1. The first five natural frequencies of this building are 0.160, 0.765, 1.992, 3.790 and 6.395 Hz. The damping matrix of the benchmark building is calculated using Rayleigh's approach by assuming 1% damping ratio for the first five modes. More details about this benchmark building are described by Yang et al. [119].

The upper n_f stories of the benchmark model are assumed to be installed with the parallel moveable DSF. The overall damping mass, which includes the mass of the moveable outer skin on the windward and leeward sides and the mass of the guide rail system, can be approximately estimated as 30 tons per story, i.e. $m_{f,i} = 30$ t, which corresponds to an average area density of about 90 kg/m². Under across-wind excitation, the high-rise building oscillates near its first natural frequency due to vortex shedding. According to the modal analysis of this benchmark building conducted by Ni et al. [61], the first mode contributes to 93.67% of the total structure acceleration. Hence, it is deemed appropriate to tune all the parallel moveable facades to the fundamental frequency of the benchmark building. The connection stiffness coefficients at all

4.2. BENCHMARK BUILDING WITH D-MTFD SYSTEM

the upper n_f stories then can be calculated as:

$$k_{f,i} = m_{f,i} \cdot \omega_1^2 \quad i = (1, 2, \dots, n_f), \quad (4.11)$$

in which ω_1 is the first natural angular frequency of the primary structure. The whole system can be reduced to a $n_{red} = n_f + 5$ DoF system using modal reduction, which includes all the facade modes and the first five modes of the benchmark building. The reduced model has been proven to be accurate enough.

The first five natural frequencies of the benchmark building without DSF and with conventional DSF (fixed connected, $n_f = 30$) are given in the Table 4.1.

Table 4.1: Natural frequency of benchmark building with/without conventional DSF.

Mode	without DSF	with conventional DSF
1	0.160 Hz	0.159 Hz
2	0.765 Hz	0.763 Hz
3	1.992 Hz	1.988 Hz
4	3.790 Hz	3.780 Hz
5	6.395 Hz	6.380 Hz

The rolling friction $f_{fri,i}$ can be calculated based on the Equations (4.2) to (4.5). The equivalent rolling friction coefficient $\mu_{r,i}$ is dependent on the along-wind forces and the type of rolling bearing used in the guide rail system. The mean along-wind velocity U_i can be determined using the widely used power-law profile with the profile exponent selected as 0.3 for terrain category IV (urban area) [127]. The reference mean wind velocity at 10 m height is set as 13.5 m/s, to keep it consistent with the wind tunnel tests for which across-wind data were obtained, as described in Section 4.3. Sealed deep groove ball bearings (Type 2RS) are assumed to be used to carry the self-weight of the parallel moveable facade. The friction coefficient for deep groove ball bearings is given approximately as 0.0015 [129]. The sealing type 2RS with a moulded rubber seal on both sides gives optimum protection in contaminated environments, but causes increased friction. The seal friction normally exceeds the sum of all other sources of friction in the bearing unit [130]. Therefore, the friction coefficient μ_{r_1} for the sealed deep groove ball bearings can be estimated as 0.0035. For carrying the along-wind forces, sealed cylindrical roller bearings (Type ZZ) are assumed to be used. The friction coefficient for cylindrical roller bearings is approximately given as 0.0013 [129]. The sealing Type ZZ is a non-removable, non-contact bearing closure with a metal seal on both sides. This type of seal has no contact with the inner ring. Therefore, there is no major influence on rolling friction. Therefore, the friction coefficient μ_{r_2} for the sealed cylindrical roller bearings is estimated as 0.0015. Based on this assumption, when the upper 30 stories are assumed to be installed with the moveable facade, the obtained $\mu_{r,i}$ of the upper 30 stories is plotted in Figure 4.2. The difference between $\mu_{r,1}$ and $\mu_{r,30}$ is only 7.53%, which will be neglected in the following analysis. The along the height consistent equivalent rolling friction coefficient, denoted as μ_r , will be used for the simulation.

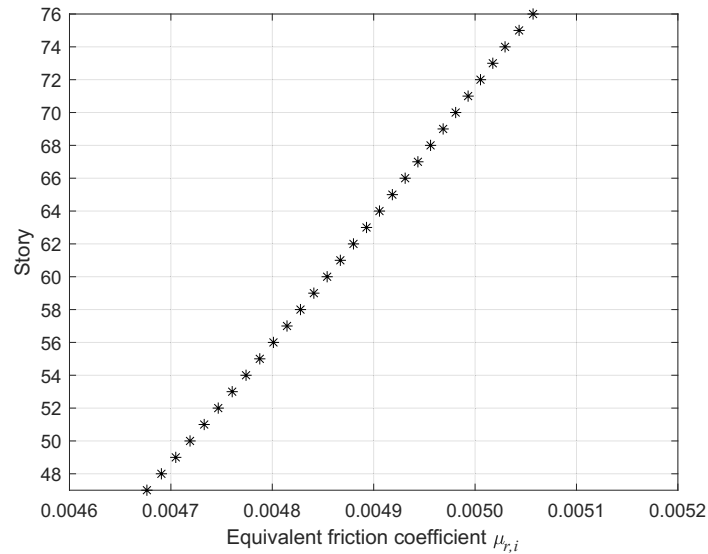


Figure 4.2: Equivalent friction coefficient $\mu_{r,i}$ of the upper 30 stories.

The friction coefficients μ_{r1} and μ_{r2} based on the assumed rolling bearings can also be varied. For example, the parallel moveability of the DSF's outer skin can also be achieved by using sliding bearings [131]. Sliding bearings have much higher friction in comparison to rolling bearings. The friction coefficient can also be influenced by using different lubricants. In the case of sealed rolling bearings (Type 2RS), the seals can also be removed to achieve lower friction. The friction can be varied within a certain range. To determine the influence of the friction on the damping performance, different amounts of rolling friction need to be considered in the system modeling as well as controller design (see Chapter 5). In this research, the system is investigated by assuming three different along the height consistent equivalent rolling friction coefficient $\mu_r = 0$, $\mu_r = 0.005$, and $\mu_r = 0.01$.

4.3 WIND MODELING

Due to vortex shedding, the across-wind structural response is more dominant for the serviceability of the high-rise building than the along-wind structural response. Therefore, in the design of the serviceability limit state, the across-wind excitation is critical for slender high-rise buildings.

The across-wind loads acting on this benchmark building were determined from the wind tunnel test based on a scaled model. The details of the wind tunnel tests are described by Samali et al. [132]. The model to prototype scale for the building is 1:400 and the velocity scale is 1:3, thus the time scale is about 1:133. 27 seconds of wind data were recorded in the wind tunnel test, which corresponds to approximately 1 hour of prototype data. The reference mean wind velocity of $v_{10m} = 13.5$ m/s at 10m above ground level with a return period of 10 years (according to AS1170.2-1989 [133], in the suburban area) represents the serviceability level wind velocity, at which the occupants' comfort is an important design criterion. Based on the

4.4. CONCLUSION AND REMARK

power law according to Hellmann with an exponent of 0.365 [134], as shown in the equation below, the top story wind velocity of the benchmark building can be calculated as 47.25 m/s.

$$v_{\text{top}} = \left(\frac{306 \text{ m}}{10 \text{ m}} \right)^{0.365} \cdot v_{10\text{m}} \quad (4.12)$$

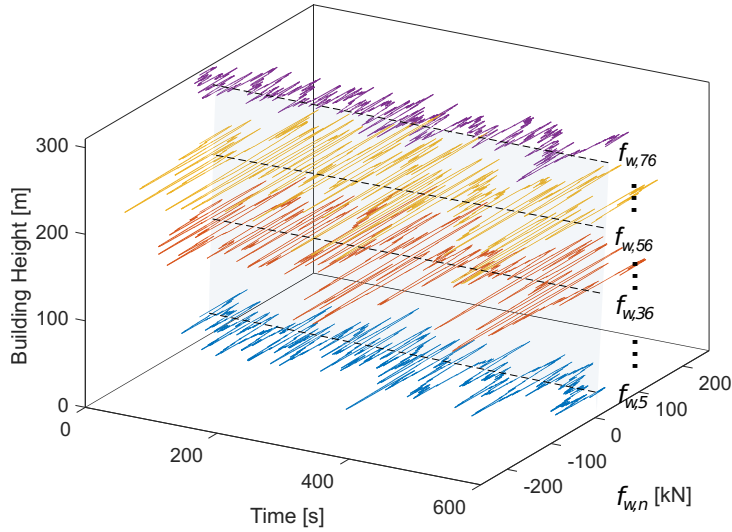


Figure 4.3: Time histories of wind forces at different floors of the benchmark building.

To determine the across-wind force for other wind conditions, the top wind velocity v_{top} can be calculated based on the current wind velocity $v_{10\text{m}}$, and then the across-wind excitation ($v_{10\text{m}} = 13.5 \text{ m/s}$) are scaled by the factor $(v_{\text{top}}/47.25)^2$. Thus, different across-wind excitation can be obtained for different wind velocity. The time histories of the dynamic component of the crosswind force at different floors of the benchmark building for $v_{10\text{m}} = 13.5 \text{ m/s}$ are shown in Figure 4.3. The average pressure coefficient is approximately zero. It should be noted that the scaled across-wind force data is always site-dependent, which means it only corresponds to the environment that same as the wind tunnel test. Therefore, the subsequent optimization of the d-MTFD system is always under the assumed environment of the benchmark building. Ten minutes of the across-wind excitation data is used in the further multi-objective optimization in Chapter 5 to reduce the computational burden and improve the optimization efficiency.

4.4 CONCLUSION AND REMARK

In this chapter, the integration of the proposed d-MTFD system in the high-rise building model is described in the structural modeling. The 76-story high benchmark building is introduced. The d-MTFD system is assumed to be installed on the upper n_f stories of the benchmark building. By assuming that different rolling bearings are used in the guide rail system, different equivalent rolling friction coefficients $\mu_{r,i}$ can be possibly achieved. To further analyze the influence of

4.4. CONCLUSION AND REMARK

the rolling friction on the optimized passive/semi-active system in Chapter 5, three different equivalent rolling coefficients ($\mu_r = 0$, $\mu_r = 0.005$, and $\mu_r = 0.01$) are assumed in the model. As a remark, the influence of the along-wind force on the friction is also considered in the simulation in Chapter 5. However, the along-wind forces cannot be reproduced during experimental tests. Therefore, the part of friction caused by along-wind force is not considered in the experimental validation using Hardware-in-the-Loop (HiL) simulation in Chapter 8.

5 Passive/semi-active system optimization

In this chapter, the passive/semi-active d-MTFD system, which is assumed to be installed on a 76-story benchmark building under across-wind excitation, is optimized using multi-objective Genetic Algorithms (GA) for two defined objectives: minimizing the peak top floor acceleration and controlling the maximum peak relative displacement of all the moveable DSF's outer skins. On-off groundhook control and displacement-reducing bang-bang control are used as semi-active control strategies. The three different assumed equivalent rolling friction coefficients in Chapter 4 are considered in the passive/semi-active system optimization, respectively. The optimization results are presented in the form of Pareto fronts. The rolling friction caused by the guide rail system has a considerable impact on the optimization results. Optimized parameters can be selected to yield a good trade-off between both objectives. The passive/semi-active d-MTFD systems can significantly improve the structural response after optimization using multi-objective GA. The Root Mean Square (RMS) value of the top floor acceleration in the selected passive/semi-active optimization cases can be reduced by approximately 40% compared with the uncontrolled system. Different from the optimized passive d-MTFD system, the use of semi-active control can also reduce the displacement of the DSF's outer skin significantly. Comparing the selected optimized cases with similar peak top floor acceleration, the peak top floor facade relative displacement using displacement-reducing bang-bang control decreases 58.3%, and the RMS value decreases 61.4%.

Copyright Statement

Parts of the research, text, and figures of this chapter are based on or have been published in the following articles:

- [124] Yangwen Zhang, Thomas Schauer, and Achim Bleicher. Optimized passive/semi-active vibration control using distributed-multiple tuned facade damping system in tall buildings. *Journal of Building Engineering*, 52:104416, 2022²²

All figures in this chapter have been published in [124].

²²Author's contribution: The author's contribution to [124] includes Conceptualization, Methodology, Software, Formal analysis, Investigation, Writing - Original Draft, Writing - Review & Editing, Visualization. Copyright ©2020 Zhang, Schauer and Bleicher. Under Creative Commons CC BY 4.0 license (<https://creativecommons.org/licenses/by/4.0/>).

5.1 METHODS

5.1.1 Multi-objective GA optimization

Evolutionary algorithms represent an important category of machine learning techniques that perform adaptation and optimization by mimicking the process of natural selection. Genetic Algorithms (GA) are one of the most widely used evolutionary algorithms.

A population of individuals is called a generation. Each individual corresponds to a set of parameters to be optimized. The initial generation is randomly populated and the performance of each individual is evaluated according to the defined objective functions. Individuals with lower objective values have a higher probability of advancing to the next generation. There is a set of genetic operations that determine how individuals successfully progress to the next generation. The genetic operations consist of elitism, replication, crossover, and mutation. More details can be found in the reference [135]. In this research, the multi-objective GA is implemented to optimize the d-MTFD system. The goal of the multi-objective GA is to seek a set of optimized solutions that exhibit the best possible trade-off performance for the chosen objectives. Non-dominated sorting is used to assign the solutions to different fronts based on their dominance relationships. The Pareto front that plots all non-inferior results is generated. According to the Pareto front, the designer can choose from the optimization results a possible solution that better meets the actual requirements of the design.

The flow chart of multi-objective GA is depicted schematically in Figure 5.1. The passive or semi-active d-MTFD system is modelled in reduced order state-space form in Simulink. The optimization was run using MATLAB's function `gamultiobj` from its powerful Optimization Toolbox (The Mathworks, Inc., USA).

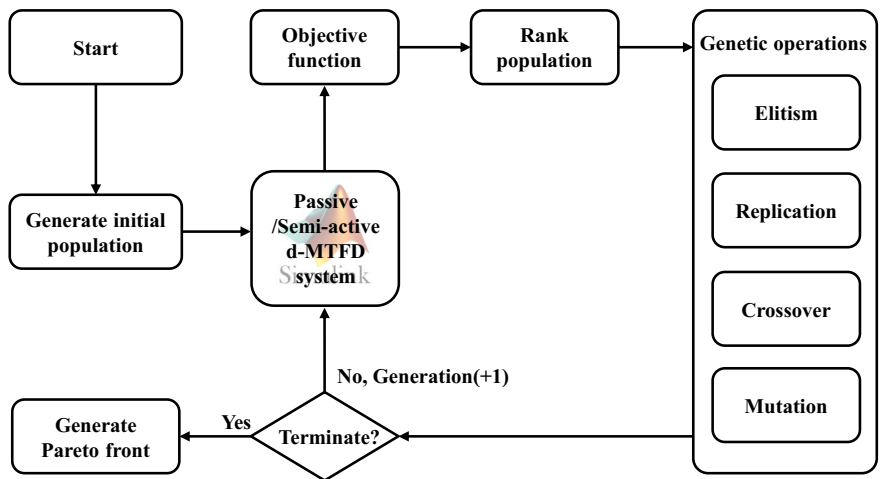


Figure 5.1: Flowchart of multi-objective Genetic Algorithm.

To optimize the d-MTFD system, two objective functions are presented to evaluate the system performance:

$$\begin{cases} J_1(\mathbf{y}_1) = \max(|\ddot{x}_n(t)|) \\ J_2(\mathbf{y}_1) = \max(\| [x_{fr,1}(t), x_{fr,2}(t), \dots, x_{fr,n_f}(t)]^T \|_\infty) \end{cases}, \quad t \in [0, T] \quad (5.1)$$

The first objective function J_1 is the peak acceleration at the top occupied floor, which is an important design criterion for high-rise buildings to ensure their serviceability under strong wind excitation. The human inner ear is very sensitive to acceleration, thus the frequent occurrence of high sway acceleration can cause discomfort to occupants. Table 5.1 gives the limit range of the perceptible acceleration.

Table 5.1: Limit range of the perceptible acceleration in the design of high-rise buildings [1].

Occupancy type	Horizontal acceleration (m/s ²)	
	return wind period 1 year	return wind period 10 year
Office	0.098 - 0.128	0.196 - 0.245
Hotel	0.069 - 0.098	0.147 - 0.196
Apartment	0.049 - 0.069	0.118 - 0.147

The second objective function J_2 is the peak relative displacement of moveable facades at the upper n_f stories. There are currently no guidelines to define the maximum allowable movement of the facade that is psychologically acceptable to occupants, as this is a new characteristic caused by this new system. However, for constructional reasons and occupant comfort, the maximum facade motion is desired to be as small as possible while fulfilling the damping requirements of the building.

For the determination of these two objective functions, the high-rise building with the corresponding passive or semi-active d-MTFD system is simulated for a period $T = 600$ s under the across-wind excitation with a return period of 10 years. The applied across-wind excitation is introduced in Section 4.3.

5.1.2 Semi-active control algorithms

Groundhook control

The groundhook control policy is a variation of the well-known skyhook control [136]. The original skyhook control was developed to reduce the response of vehicles in the early 1970s [137]. Skyhook control is designed to reduce the vibration of the sprung mass, i.e. the damping mass. Therefore, it is not suitable for vibration control in tall buildings. The groundhook control is altered to reduce the vibration of the unsprung mass, i.e. the building structure. Groundhook control has been applied to the semi-active TMD system to increase the effectiveness of reducing structural response [138, 139]. On-off Velocity Based Groundhook (VBG) control and on-off Displacement Based Groundhook (DBG) control are applied in the semi-active d-TMFD system. The control logic can be mathematically summarized in the following equations:

5.1. METHODS

on-off VBG control

$$\begin{aligned} \text{if } \dot{x}_{n-n_f+i} \cdot \dot{x}_{fr,i} \geq 0, \text{ then } c_{f,i} &= c_{\min,i} \\ \text{if } \dot{x}_{n-n_f+i} \cdot \dot{x}_{fr,i} < 0, \text{ then } c_{f,i} &= c_{\max,i} \end{aligned} \quad (5.2)$$

on-off DBG control

$$\begin{aligned} \text{if } x_{n-n_f+i} \cdot \dot{x}_{fr,i} \geq 0, \text{ then } c_{f,i} &= c_{\min,i} \\ \text{if } x_{n-n_f+i} \cdot \dot{x}_{fr,i} < 0, \text{ then } c_{f,i} &= c_{\max,i} \end{aligned} \quad (5.3)$$

Displacement-reducing Bang-Bang Control

Displacement-reducing bang-bang (DDB) control can be applied to energy dissipation devices, i.e. electric machines in our application, to improve the ability of dissipating energy compared with conventional passive devices. The working principle of DDB control is that when the relative displacement $x_{fr,i}$ and relative velocity $\dot{x}_{fr,i}$ of the parallel moveable facade outer skin are in the same direction, the adjustable damping coefficient of the electric machine will be set higher to resist further increasing relative displacement. The electric machine functions like a brake. More energy can be dissipated. And when the relative displacement $x_{fr,i}$ and relative velocity $\dot{x}_{fr,i}$ are in opposite directions, the damping coefficient decreases, so that the restriction on relative displacement can reduce. The control logic can be captured as:

$$\begin{aligned} \text{if } x_{fr,i} \cdot \dot{x}_{fr,i} \geq 0, \text{ then } c_{f,i} &= c_{\max,i} \\ \text{if } x_{fr,i} \cdot \dot{x}_{fr,i} < 0, \text{ then } c_{f,i} &= c_{\min,i} \end{aligned} \quad (5.4)$$

The encoder can be mounted on the electric machine to measure the relative displacement $x_{fr,i}$ and relative velocity $\dot{x}_{fr,i}$ of the parallel moveable facade outer skin (see Figure 7.12a), DDB control does not need any other sensors. For on-off VBG (cf. Equation (5.2)), inertial sensors are required to measure the story accelerations. Based on that, the story velocity \dot{x}_{n-n_f+i} can be derived by numerical integration and high-pass filtering. For on-off DBG control (cf. Equation (5.3)), the story displacement is needed inside the control policy. It is practically more difficult to measure the story displacement. Laser-based sensors might be used to measure the building story displacement. Therefore, in practical applications, DDB control requires fewer sensors than groundhook control.

5.1.3 Multi-objective GA optimized semi-active d-MTFD system

The architecture of multi-objective GA optimized semi-active control is shown schematically in Figure 5.2.

This procedure has a well-defined control task, which is formulated in terms of minimizing the two objective functions J_1 and J_2 . The objective functions can be evaluated based on the performance output y_1 . The measurement output y_2 is used in the implemented control logic.

5.2. NUMERICAL SIMULATION AND RESULTS ANALYSIS

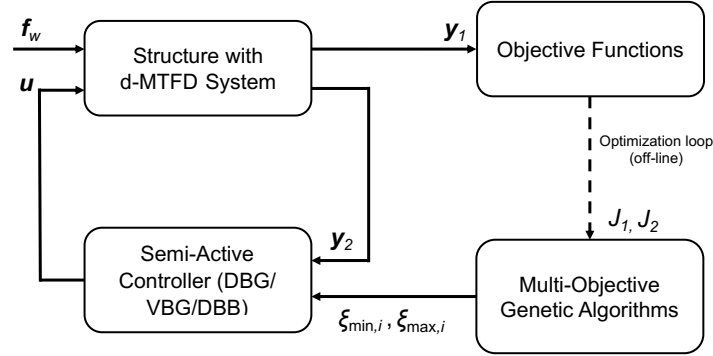


Figure 5.2: Schematic of the multi-objective GA optimized semi-active control.

The damping ratios $\xi_{min,i}$, $\xi_{max,i}$, optimized by the multi-objective GA, determine the damping coefficient $c_{f,i}$. Their relation can be calculated as:

$$c_{f,i} = \begin{cases} c_{min,i} = 2\xi_{min,i}\sqrt{m_{f,i}k_{f,i}} \\ c_{max,i} = 2\xi_{max,i}\sqrt{m_{f,i}k_{f,i}} \end{cases} \quad i = (1, 2, \dots, n_f) \quad (5.5)$$

The time-varying $c_{f,i}$ is integrated in the system damping matrix \mathbf{C}_s . Alternatively, the varying damping coefficients can be taken out of the system damping matrix and calculated as the time-varying semi-active control force $\mathbf{u} = [u_1, u_2, \dots, u_{n_f}]^T \in \mathbb{R}^{n_f}$, which can be presented as:

$$u_i = c_{f,i} \cdot \dot{x}_{fr,i} \quad i = (1, 2, \dots, n_f). \quad (5.6)$$

5.2 NUMERICAL SIMULATION AND RESULTS ANALYSIS

5.2.1 Optimized passive d-MTFD system

As the stiffness coefficient has been determined based on Equation (4.11), the parameters, which can be optimized in the passive d-MTFD system, are the number of n_f upper stories installed with the parallel moveable DSF and the damping coefficient $c_{f,i}$ of the corresponding connections. The damping coefficient can be determined by the damping ratio $\xi_{f,i}$.

For a single TMD system under harmonic excitation, the optimum damping ratio has been given by Den Hartog [31], as expressed in Equation (5.7). It can be used as a reference value to determine the searching domain of the damping ratios in the d-MTFD system.

$$\begin{cases} \xi_{ref} = \sqrt{\frac{3\tilde{m}}{8(1+\tilde{m})^3}} \\ \tilde{m} = \frac{\sum_{i=1}^{n_f} m_{f,i}}{M_{eff}} \end{cases} \quad (5.7)$$

where M_{eff} is the first effective modal mass of the primary structure [140].

As the vibration of the primary structure is primarily dominated by its first mode under across-wind excitation, the maximum relative displacement of the facade increases along the story, i.e. $\|x_{fr,1}\|_\infty < \|x_{fr,2}\|_\infty < \dots < \|x_{fr,n_f}\|_\infty$, when the same damping ratio ξ_{ref} is set for all the moveable facades. To decrease the peak relative displacement of moveable facades at

5.2. NUMERICAL SIMULATION AND RESULTS ANALYSIS

these n_f stories, the damping ratios of the upper stories can be set higher than the damping ratios of the lower stories, i.e. $\xi_{f,1} < \xi_{f,2} < \dots < \xi_{f,n_f}$. To reduce optimization parameters, only the lowest floor damping ratio ξ_{f,s_1} (ξ_{f,s_1}), the highest floor damping ratio ξ_{f,n_f} (ξ_{f,s_j}) and the damping ratios of some uniformly distributed floors in between ($\xi_{f,s_2}, \dots, \xi_{f,s_{j-1}}$) are selected as the optimization parameters of multi-objective GA. Linear interpolation ($j = 2$) or piece-wise linear interpolation ($j > 2$) is used to determine the damping ratios of the stories between the optimized damping ratios of the selected stories. All the optimization parameters required for the passive d-MTFD system are shown in Figure 5.3.

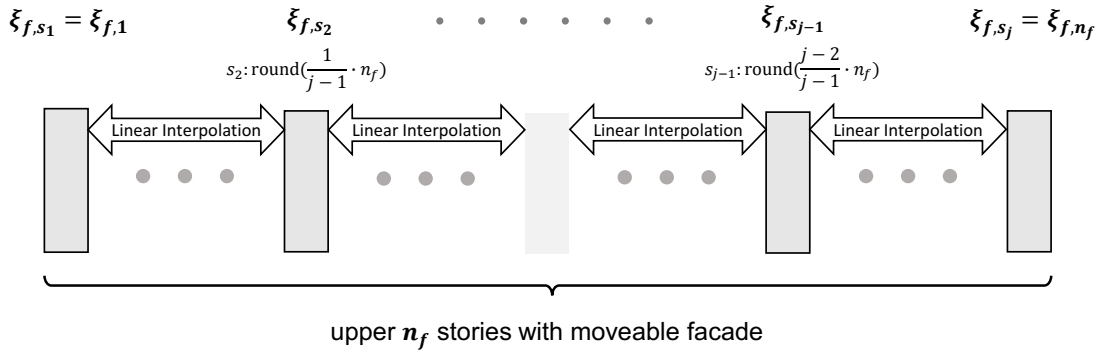


Figure 5.3: Optimization parameters of passive d-MTFD system.

Before implementing the multi-objective GA, the constraints for the optimization parameters need to be set up. The range of n_f is set between 5 and 30. The corresponding reference facade connection damping ratio ξ_{ref} can be calculated as 0.022 - 0.055 (first effective modal mass $M_{\text{eff}} = 111715$ t). The searching domain of all the selected facade connection damping ratios to be optimized is then set between 0.004 and 0.15. The facade connection damping ratios ($\xi_{f,s_1}, \xi_{f,s_2}, \dots, \xi_{f,s_j}$) of two, three and five uniformly distributed stories ($j = 2, j = 3$ and $j = 5$) among the upper n_f stories are selected to be optimized under three different rolling friction conditions ($\mu_r = 0, \mu_r = 0.005$ and $\mu_r = 0.01$ respectively). The population size of the multi-objective GA is set as 150 and then evolved for 50 generations.

The optimization results are presented in the form of Pareto fronts, as shown in Figure 5.4. A competitive relationship between the two selected objectives can be observed from all the plotted Pareto fronts. Although the inevitable rolling friction also provides partial damping, it has a negative impact on the optimization results. Figure 5.4d shows that, with the same maximum peak facade relative displacement, higher rolling friction can result in a weakened ability to mitigate peak floor acceleration. Under the same rolling friction condition, similar optimization results are obtained by using different selected stories, as shown in Figure 5.4a, Figure 5.4b and Figure 5.4c. With the same population size and evolving generations setting in the optimization algorithm, selecting more uniformly distributed stories among the above n_f stories to optimize their facade connection damping ratios does not lead to better optimization results. When the rolling friction coefficient is 0.005, the optimization results of choosing three stories ($j = 3$) to optimize their facade connection damping ratios are slightly better than the other two in a certain region. When $j = 3$, the n_f values of all the optimized cases (cases in

5.2. NUMERICAL SIMULATION AND RESULTS ANALYSIS

the Pareto front) are plotted in Figure 5.5 under three different rolling friction conditions. The algorithm can freely search for the optimum number n_f of upper stories to install the parallel moveable DSF's outer skin within the searching domain [5, 30]. As the friction coefficient μ_r increases, the damping effect of parallel moveable DSF at lower stories decreases, so it is removed by the algorithm. At lower stories, the building acceleration caused by across-wind excitation is small, and if the friction is high, it is difficult for the parallel moveable DSF's outer skin to overcome the friction and consume more energy to damp the building vibrations. It is economically also a good strategy to deactivate the moveable facade with decreased damping effect at lower stories. Table 5.2 lists the average optimized n_f . The average optimized n_f for all three selecting options ($j = 2$, $j = 3$ and $j = 5$) under the same rolling friction conditions are basically the same.

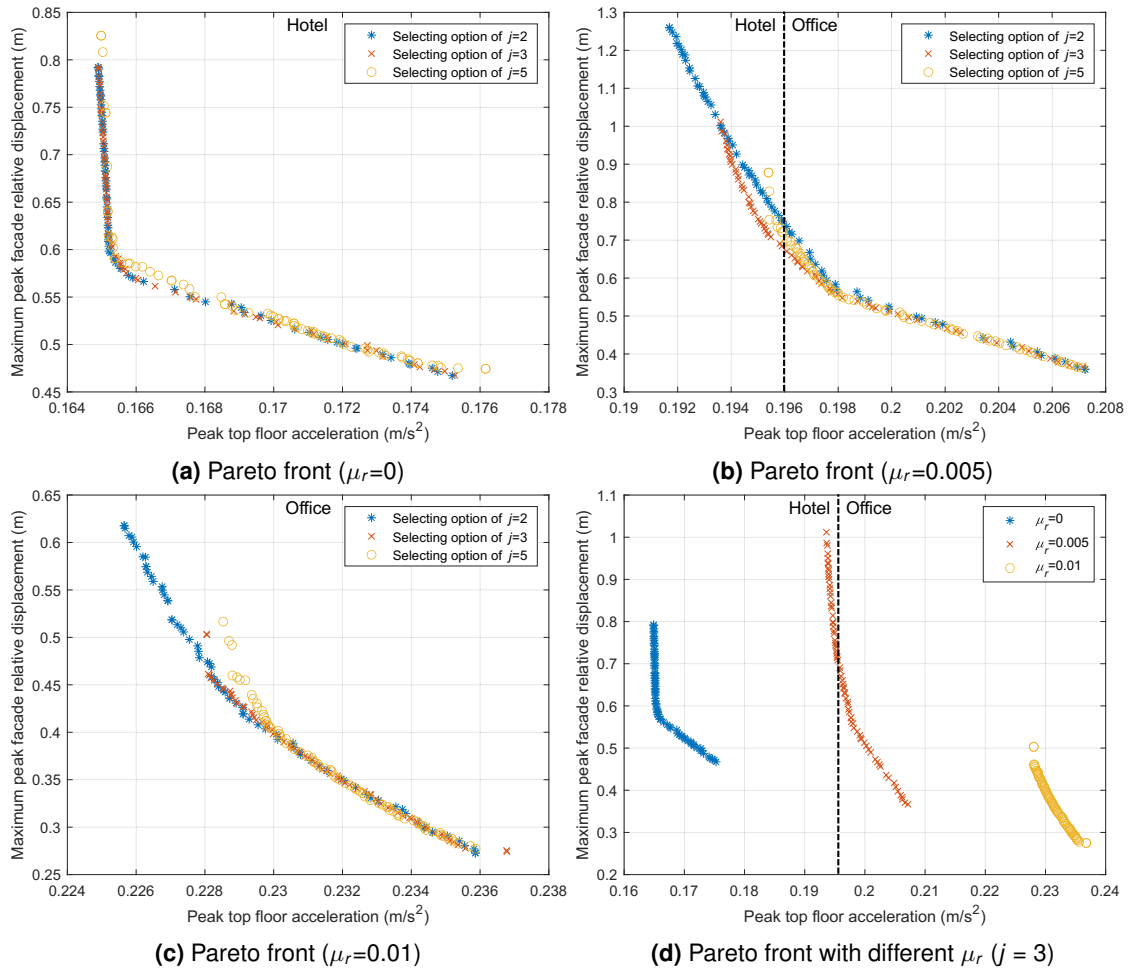


Figure 5.4: Pareto front of passive d-MTFD system.

5.2. NUMERICAL SIMULATION AND RESULTS ANALYSIS

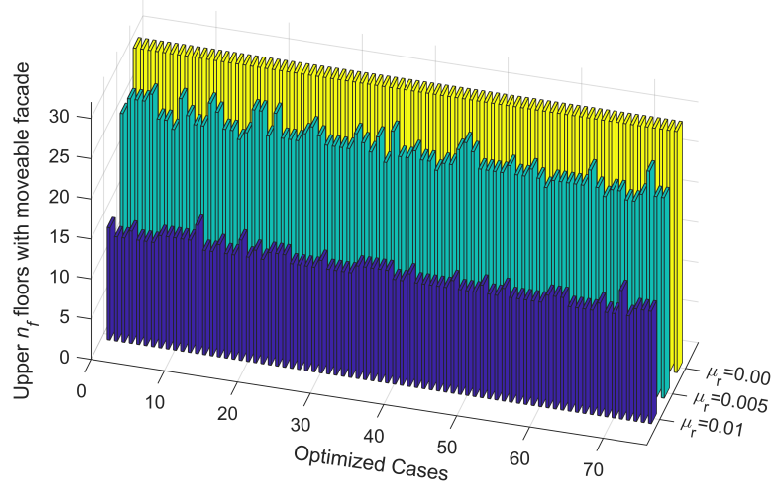


Figure 5.5: Optimized numbers n_f of upper floors with parallel moveable DSF.

Table 5.2: Average optimized n_f upper floors with parallel moveable DSF (j : Number of interpolation points for linear interpolation).

rolling friction coefficient	selected stories $n_f \in \{1, 2, \dots, 30\}$		
	($j = 2$)	($j = 3$)	($j = 5$)
$\mu_r = 0$	30	30	30
$\mu_r = 0,005$	25	26	24
$\mu_r = 0,01$	14	13	13

5.2.2 Optimized semi-active d-MTFD system

For the on-off semi-active d-MTFD system, the stiffness coefficients can also be calculated based on Equation (4.11). The facade connection damping coefficients $c_{f,i}$ includes $c_{\max,i}$ and $c_{\min,i}$ for all the parallel moveable DSF at each story using groundhook control or DBB control. Therefore, $\xi_{\max,i}$ and $\xi_{\min,i}$ at chosen stories are optimized and stories in between are linear interpolated. Based on the optimization results of the passive d-MTFD system, when the setups of population size and evolving generations are the same in the algorithm, selecting more uniformly distributed stories, i.e., larger j , among the above n_f stories does not lead to better optimization results. Therefore, for the semi-active system, only three stories of the upper n_f stories ($j = 3$) are selected to optimize their connection damping ratios and the rest in between are linear interpolated, as shown in Figure 5.6. The searching domain of all the selected facade connection damping ratios is also set between 0.004 and 0.15. The relation between the damping states ($\xi_{\max,s_j} > \xi_{\min,s_j}$) is defined in the optimization setup. To increase the efficiency of the optimization, the number of upper stories n_f that are installed with parallel moveable facades will also no longer be used as an optimization parameter, because the average optimized n_f corresponding to different rolling friction conditions has been determined from the passive d-MTFD system optimization results, as shown in Table 5.2. Therefore, for the rolling friction coefficient $\mu_r = 0$, $\mu_r = 0.005$ and $\mu_r = 0.01$, n_f is chosen as 30, 25 and 14,

respectively. For a better comparison with the optimization results of the semi-active system, the passive d-MTFD system is also optimized again using a fixed n_f under three different rolling friction conditions. The population size of the multi-objective GA is again set as 150 and then evolved for 50 generations.

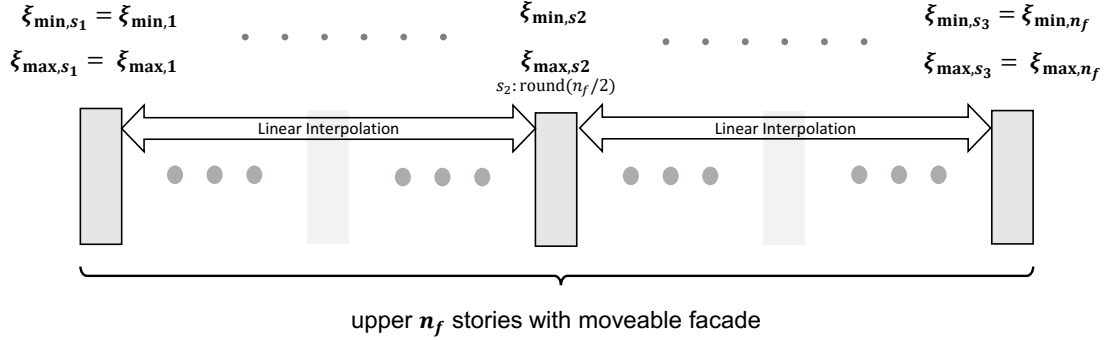


Figure 5.6: Optimization parameters of semi-active d-MTFD system.

The optimization results for the semi-active d-MTFD system are presented in the form of Pareto fronts, as shown in Figure 5.7. With the same optimization settings, the optimization results of the semi-active d-MTFD system with on-off DBG/VBG control and DBB control are plotted with the optimized passive d-MTFD system together. As observed in Figure 5.7a, Figure 5.7b and Figure 5.7c, under the same rolling friction condition, by using semi-active control, both defined objectives are better optimized compared with the passive d-MTFD system. Semi-active control using DBB control has better performance in most of the optimized cases than using on-off DBG/VBG control. For the optimized semi-active d-MTFD system with DBB control, the optimal results are plotted together in Figure 5.7d under three different rolling friction conditions. For the optimized semi-active d-MTFD system, a larger rolling friction coefficient also leads to unfavourable optimization results, which is the same as the results for the optimized passive d-MTFD system under different rolling friction conditions.

Five cases are chosen from the optimization results for further comparison, as marked in Figure 5.7. Case 3, 4 and 5 are the optimized d-MTFD system using DBB control under different rolling friction conditions. The maximum peak facade relative displacements for Case 3 and 4 are both near 0.5 m. The peak facade relative displacements at different stories of these three cases are plotted together in Figure 5.8a for comparison. As observed, in Case 4, when the rolling friction coefficient μ_r is assumed to be 0, the peak relative displacement of all the moveable DSF's outer skin at the upper 30 stories of the 76-story benchmark building is around 0.5 m. For case 3 with the rolling friction of 0.005, even if only the upper 25 stories of the benchmark building are installed with the moveable DSF's outer skin, just half of them can reach near the maximum peak facade relative displacement of 0.5 m. When the rolling friction coefficient μ_r increases, moveable facades at lower stories have more difficulty overcoming the friction and then damping the structural motion. Figure 5.8b shows the peak facade relative displacement of three cases (optimized passive and optimized semi-active) under the same rolling friction coefficient condition ($\mu_r = 0.005$). The optimized passive d-MTFD systems Case

5.2. NUMERICAL SIMULATION AND RESULTS ANALYSIS

1 and Case 2 are selected to be compared with the optimized semi-active d-MTFD system Case 3. Case 1 has similar peak top floor accelerations to Case 3, and Case 2 has similar maximum peak facade relative displacement to Case 3. The time course of the top floor facade relative displacement for Case 1, Case 2 and Case 3 is plotted in Figure 5.9. It is observed that the top floor facade relative displacement of Case 3 using DBB control is largely reduced compared with that of Case 1, although they both achieve similar peak top floor acceleration. The time course of the top floor semi-active control force u_{n_f} for Case 3 is plotted in Figure 5.10. The optimized parameters for Case 3 are listed in Table 5.3. Since the upper 25 stories of the benchmark building are assumed to be installed with the parallel moveable facade, the facade connection damping ratios of three selected stories are optimized by the algorithm, i.e., the lowest 52nd story, the highest 76th story, and the 64th story in the middle. The damping ratios of the other stories in between are obtained by linear interpolation.

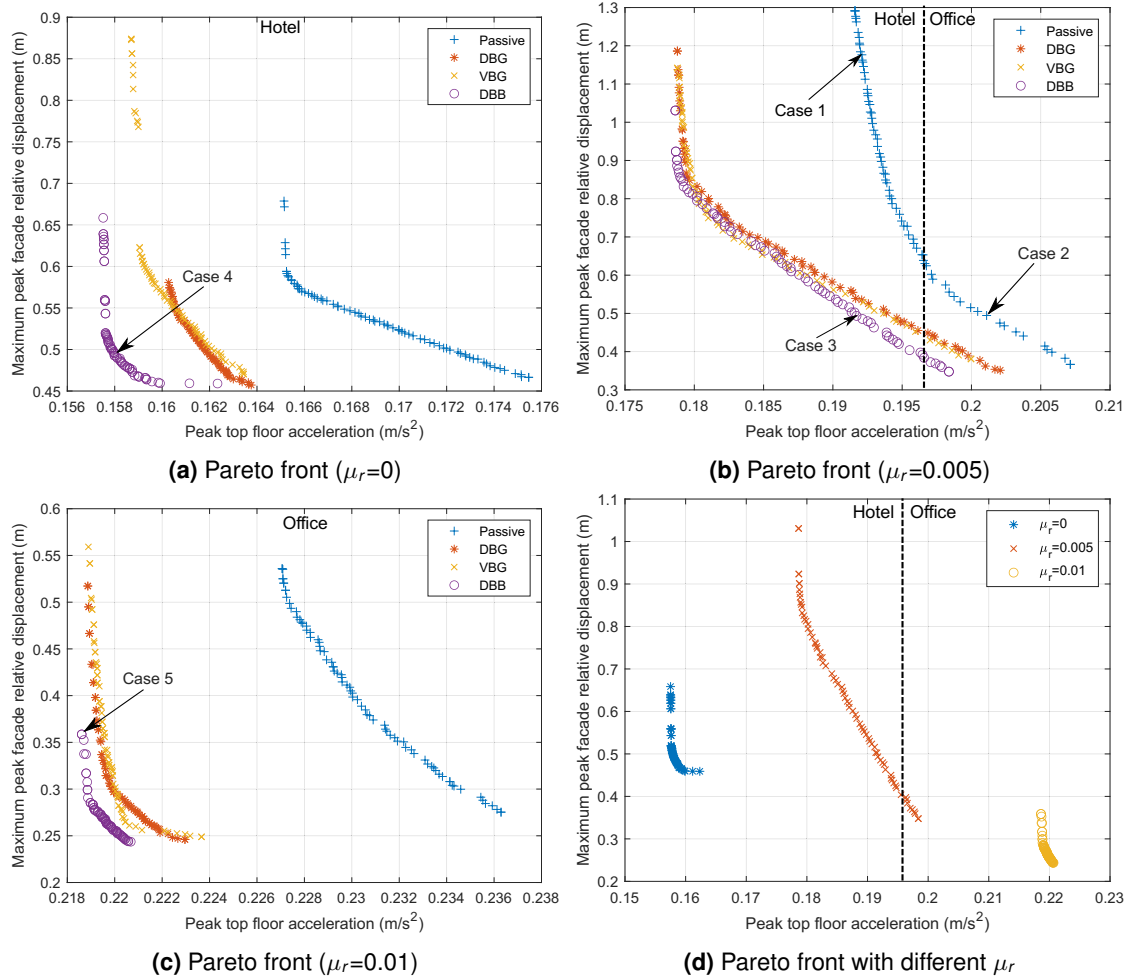
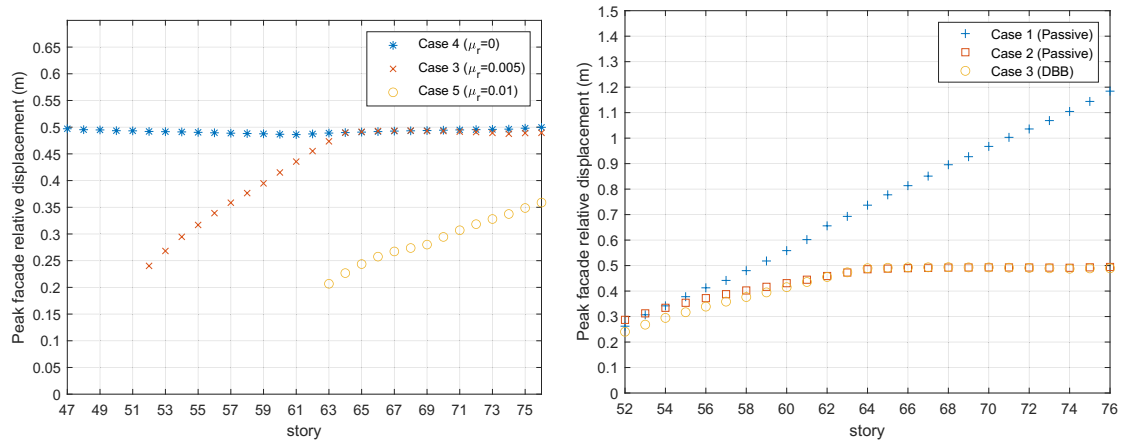


Figure 5.7: Pareto front of semi-active d-MTFD system.

5.2. NUMERICAL SIMULATION AND RESULTS ANALYSIS



(a) Three chosen cases using DBB control under different μ_r (b) Three chosen cases under same $\mu_r=0.005$ (cf. Figure 5.7b)

Figure 5.8: Peak facade relative displacement at different stories (cf. Figure 5.7).

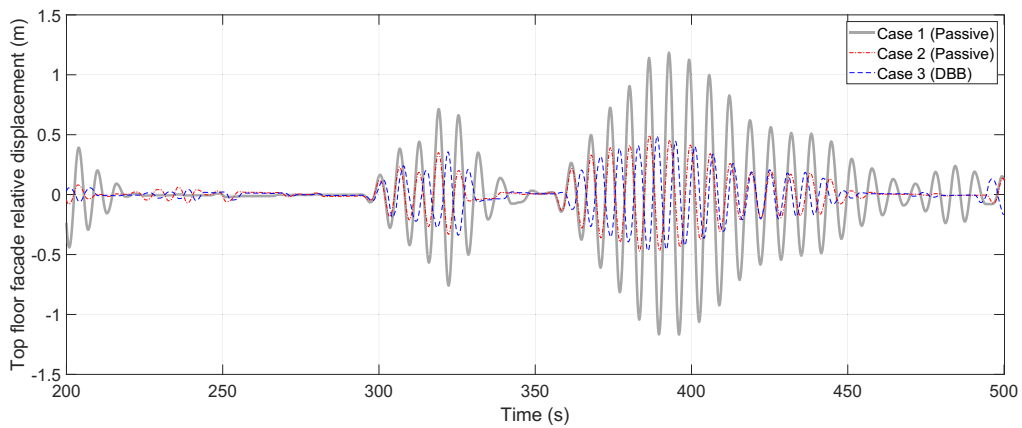


Figure 5.9: Top floor facade relative displacement x_{fr,n_f} .

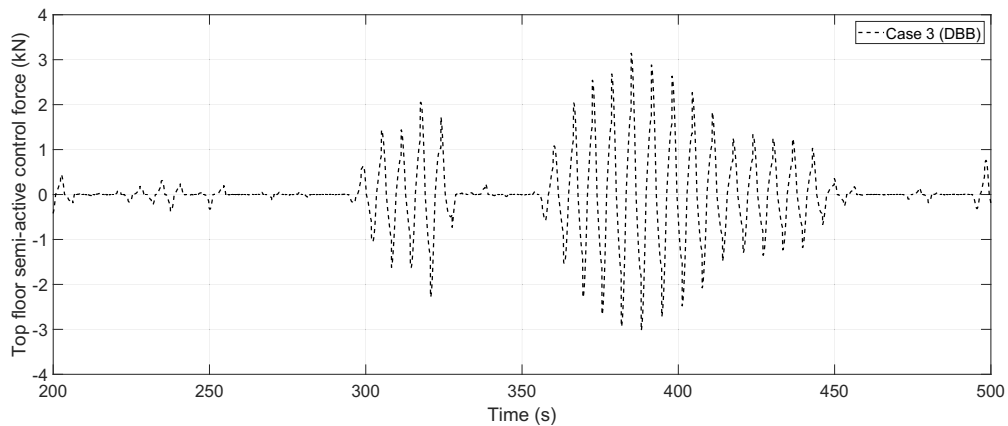


Figure 5.10: Top floor semi-active control force u_{n_f} (Case 3).

5.2. NUMERICAL SIMULATION AND RESULTS ANALYSIS

Table 5.3: Optimized parameters, i.e., facade connection damping ratios, for Case 3 (cf. Figure 5.6 and 5.7b).

Optimized low/high damping ratio	52nd story ($j = 1$)	64th story ($j = 2$)	76th story ($j = 3$)
low damping ratio ξ_{\min, s_j}	0.0046	0.0064	0.0637
high damping ratio ξ_{\max, s_j}	0.0322	0.0631	0.1071

Under the same wind excitation, the uncontrolled benchmark building with conventional DSF is also simulated and added to the comparison with the optimized passive d-MTFD system (Case 1, Case 2) and the optimized semi-active d-MTFD system using DBB control (Case 3). The peak top floor displacement $\|x_{76}\|_{\infty}$, Root Mean Square (RMS) value of top floor displacement x_{76}^{rms} , the peak top floor acceleration $\|\ddot{x}_{76}\|_{\infty}$, RMS value of top floor acceleration \ddot{x}_{76}^{rms} , the peak top floor facade relative displacement $\|x_{fr, n_f}\|_{\infty}$, and RMS value of top floor facade relative displacement x_{fr, n_f}^{rms} are compared and listed in Table 5.4.

Table 5.4: Comparison of uncontrolled system, optimized passive d-MTFD system (Case 1, Case 2) and optimized semi-active d-MTFD system using DBB control (Case 3).

System	Uncontrolled	Passive (Case 1)	Passive (Case 2)	Semi-active (Case 3)
$\ x_{76}\ _{\infty}$ (m)	0.349	0.298 (-14.6%)	0.325 (-6.9%)	0.321 (-8.0%)
x_{76}^{rms} (m)	0.116	0.081 (-30.2%)	0.088 (-24.1%)	0.087 (-25.0%)
$\ \ddot{x}_{76}\ _{\infty}$ (m/s ²)	0.270	0.192 (-28.9%)	0.201 (-25.6%)	0.192 (-4.5% [†])
\ddot{x}_{76}^{rms} (m/s ²)	0.104	0.061 (-41.3%)	0.070 (-32.7%)	0.066 (-5.7% [†])
$\ x_{fr, n_f}\ _{\infty}$ (m)	/	1.184	0.495	0.494 (-58.3% [‡])
x_{fr, n_f}^{rms} (m)	/	0.355	0.144	0.137 (-61.4% [‡])

[†] reduction percentage compared with Case 2.

[‡] reduction percentage compared with Case 1, other reduction percentages without footnotes are compared with the uncontrolled system.

Compared with the uncontrolled benchmark building with conventional DSF (fixed outer skin), the optimized passive and semi-active d-MTFD systems both perform much better in reducing the wind-induced vibrations. As for top floor displacement, they all conform to the design criteria $h/500$ ($h = 306$ m is the building height) [1], which is relatively easy to satisfy. Therefore, compared with the top floor acceleration, the top floor displacement is not a high priority as an optimization objective. Case 1 was specifically chosen, as it has a similar optimized peak top floor acceleration to Case 3. Therefore, the focus of the comparison is on the facade relative displacement. As calculated, compared with Case 1, the peak top floor facade relative displacement using DBB control by Case 3 decreases 58.3%, and its RMS value decreases 61.4%. Case 2 is specifically chosen to have a similar maximum peak facade relative displacement to Case 3. Hence, the focus of the comparison is on the top floor acceleration. The peak top floor acceleration by Case 3 decreases 4.5% and its RMS value decreases 5.7% compared with Case 2. All the reduction percentages are listed in Table 5.4. As observed, by using semi-active control, the further reduction of building acceleration is not significant.

However, the motion of the DSF's outer skin can be largely mitigated, which is meaningful for serviceability.

5.3 DISCUSSION

The benchmark building with a slenderness ratio of 7.3 is assumed to be installed with the d-MTFD system and investigated as a case study. Newly built tall buildings have become much taller and more slender up to a slenderness ratio of 24.3, such as the Steinway tower in Manhattan [141]. The slenderness has an influence on the natural frequency of the structure. With the same material, the natural frequency of a more slender structure tends to be lower.

The Strouhal number St , as expressed in Equation (5.8), gives the frequency f_{vs} at which vortices are shed from the side of the building, causing the periodic across-wind excitation at this frequency.

$$St = \frac{f_{vs}L}{U} \quad (5.8)$$

Here f_{vs} is the frequency of vortex shedding, L is the building width, and U is the wind speed. For the wind flow around buildings, the Strouhal number is a constant and varies only with the building cross-section. For buildings with a square cross-section, the Strouhal number is around 0.13 [142]. When the natural frequency of the structure matches the vortex shedding frequency, the across-wind structural response can be amplified due to resonance. Assuming the building width L is a constant, if the building is taller (more slender), which brings a lower natural frequency, resonance will occur at relatively lower wind speed. For the benchmark building, the first and second natural frequencies are 0.160 Hz and 0.765 Hz, respectively. The second mode of the benchmark building can hardly be excited even during strong wind events. Therefore, the moveable facade elements installed on the benchmark building are all tuned to the first natural frequency. However, for taller (more slender) high-rise buildings, the wind speed increases with the height, and the second natural frequency also tends to become smaller. Consequently, the second mode is also more likely to be excited. Multi-mode control can be implemented in d-MTFD to reduce not only the first mode structural motion but also the second mode. By adjusting the stiffness of the springs, the moveable facade elements at some stories can be tuned to the second natural frequency of the building.

Semi-active control with different control strategies has been investigated. Semi-active control is a special form of passive control. In our application, the electrical damping coefficients are adjustable, which means the energy dissipating rates are adjustable. The semi-active forces are not active forces, but passive forces, which are always opposite to the direction of the facade motion. Therefore, different from active control, semi-active control only dissipates energy. It does not inject energy to shift the natural frequency of the structure to achieve vibration control like using active control. Therefore, the spillover effect by using active control will not occur.

Different types of MTMD systems have been intensively studied and proven to have better robustness than traditional single TMD systems [43, 44, 143]. Single TMD has only one single mass, which can be only tuned to one frequency, which means the first natural frequency

5.4. CONCLUSIONS

of the structure. Once the structural parameter changes or detuning happens, the damping performance of a single TMD system decreases significantly. For a single TMD system, it is narrow-band vibration control. However, for multiple masses, they can be tuned within a range, for example, near the 5% range of the first natural frequency of the structure. Of course, it can also be tuned to the second or third modes of the structure to realize multi-mode control. A relative broadband vibration can be mitigated. Therefore, even if the structural parameter changes a little bit, it is still in that range. And for the problem of detuning, if the problem of detuning happens at one story, the other stories may still work. Of course, regular maintenance is required to avoid detuning problems.

For the proposed system, we modified the existing conventional DSF system to be parallel moveable. Therefore, from an economic point of view, extra initial costs arise only due to the added components (the guide rail system, the spring system, the electrical damper, etc.). In addition, the installation and maintenance effort might be slightly higher compared with traditional DSF. The facade mass belongs to the mass of the building. No extra material for the load-bearing structure is necessary. As no internal installation space is required for the proposed system, the saved space can also be used for economic purposes. For passive and semi-active systems, there is not much difference in cost between these two solutions. Semi-active system requires sensors and microcontrollers, but these components are inexpensive compared with other components such as the guide rail system. For detailed investigations, a life-cycle cost analysis is necessary.

The design limitation of this system is the maximum relative displacement of the moveable facade outer skin. Using semi-active control, the movement of the DSF outer skin can be reduced to a relatively small value. But whether residents can psychologically accept this level of movement needs to be investigated.

Piece-wise linear interpolation has been applied to increase the efficiency of system optimization. The higher the number of interpolation points used, the higher the order of nonlinearity that can be considered. However, selecting all upper stories as optimization parameters would be time-consuming. Therefore, it is necessary to provide some guidance to the algorithm. The fundamental idea is that since the first mode is dominant under across-wind excitation, we can manually set it so that the damping ratio at higher floors is higher than that at lower floors. This reduces the problem to how the damping ratio increases linearly or nonlinearly from the lower to the higher floors. Nonlinear distribution can be described using a nonlinear function or simplified piece-wise linear interpolation. These methods can significantly increase optimization efficiency. From the results, we can observe that piece-wise linear interpolation using three interpolation points has achieved very satisfactory results.

5.4 CONCLUSIONS

Based on the obtained simulation results and discussion in the previous sections, some conclusions can be summarized as follows:

(1) The optimized passive and semi-active d-MTFD systems have both significantly improved the structural responses under across-wind excitation compared with the uncontrolled

structure. The use of semi-active control can only slightly reduce structural vibrations compared with the optimized passive d-MTFD system. With similar maximum peak facade relative displacement of Case 2 (passive) and Case 3 (DBB control), the peak top floor acceleration of Case 3 only decreases by a further 4.5% compared with Case 2, and the RMS value of Case 3 decreases by 5.7%. However, the movement of the DSF's outer skin can be significantly mitigated using semi-active control. Comparing the selected optimized cases (Case 1 with passive control and Case 3 with DBB control) with similar peak top floor acceleration, the peak top floor facade relative displacement of Case 3 decreases 58.3%, and the RMS value decreases 61.4%.

(2) The inevitable rolling friction caused by the guide rail system has a considerable impact on the optimization results. For both, the passive and semi-active d-MTFD system, a larger rolling friction coefficient leads to unfavourable optimization results. When the rolling friction coefficient μ_r increases, it is more difficult for the moveable facades at lower stories to overcome the friction to damp the structural vibration. Hence, achieving a smaller rolling friction coefficient is meaningful for the optimal design of the system. This conclusion provides a theoretical basis for the selection and implementation of the guide rail system for the prototype (see Chapter 7).

(3) The optimization results using different semi-active control strategies show that most of the optimized cases using DBB control have better performance than using on-off DBG/VBG control. Simulation-based performance studies of different semi-active control strategies are important for our final decision on which control strategy to use in the prototype. Different control strategies have different requirements for the sensors. The control logic of the DBB control only needs the movement information of the facade outer skin. Therefore, fewer sensors are required for DBB control compared with groundhook control.

6 Electric machine modeling and circuit design

In this chapter, an adjustable damping coefficient is realized by using an electric machine. The parallel facade relative displacement is transformed to the rotation of the electric machine through rack-and-pinion. The kinetic energy of the facade's outer skin motion can be harvested and stored in the battery. The electric machine functions not only as a viscous damper but also as a generator. By controlling the duty cycle of the Pulse-Width Modulation (PWM) signal in the specially designed power electronics, the equivalent resistance connected to the electric machine is adjusted, which in turn generates an adjustable damping force that damps the wind-excited structural vibration. The PWM signal is generated by a microcontroller running the semi-active algorithm discussed in Chapter 5. The power flow and signal flow are summarized in Figure 6.2 below:

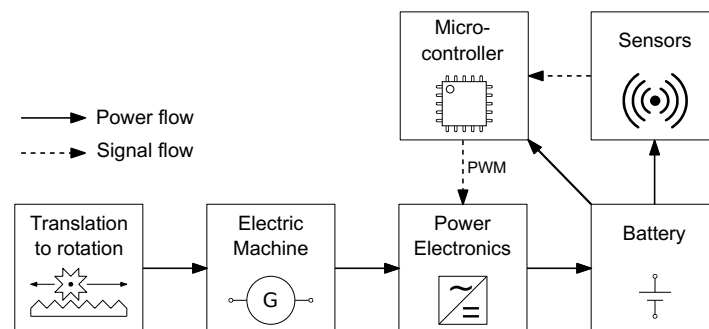


Figure 6.1: Power flow and signal flow of the electric machine as adjustable electrical damper/-generator.

The electric machine and other components are integrated in the cavity of one double-skin facade element, as illustrated in Figure 6.2. The initial sensor measures the floor acceleration, the floor velocity is then obtained by numerical integration and high-pass filtering. The encoder measures the facade relative displacement and the facade relative velocity. The initial sensor and encoder are required for the VBG semi-active control algorithm running in the microcontroller. There is also a force sensor to measure the interaction force of the electric machine. The measured interaction force is only used for the system identification to validate the semi-active control (see Section 8.1).

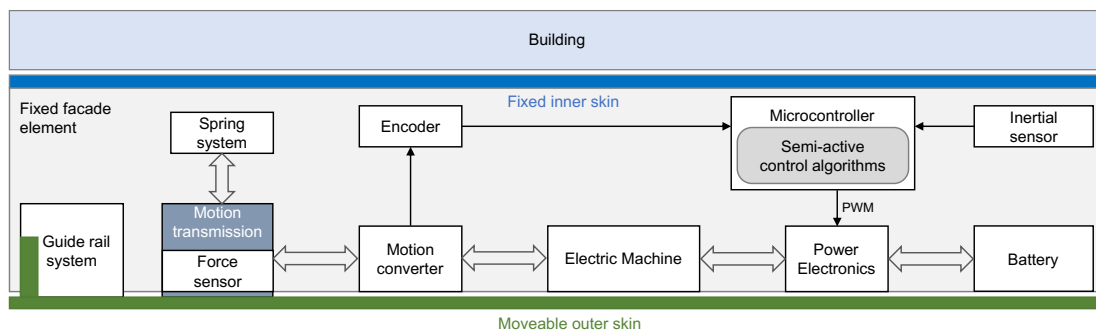


Figure 6.2: Components of the electric machine as adjustable electrical damper/generator.

The principle of realizing this system is described in detail in this chapter. Two types of electric machines, i.e, DC motor and stepper motor, are analyzed respectively in motor mode and generator mode. A two-phase hybrid stepper motor is selected for this application. The specially designed dual two-stage power converter is applied as the Energy Harvesting Circuit (EHC). The whole system is theoretically derived and a simulation model is also built in Simulink. Based on the experimentally measured data, the model parameters are estimated using the Optimization Toolbox in MATLAB. The experimental results and estimated simulation results fit very well. The investigation in this chapter provides the prerequisites for the success of the following experiment using Hardware-in-the-Loop (HiL) simulation in Chapter 8.

Copyright Statement

Parts of the research, text, and figures of this chapter are based on and have been/will be published in the following articles:

- [144] Thomas Schauer, Achim Bleicher, Yangwen Zhang, Wulf Wulff, and Laurenz Wernicke. *Schwingungsdämpfung und Energiegewinnung mit beweglichen Doppelfassaden: Entwurf, Optimierung und Validierung eines autarken verteilten semiaktiven Systems zur Reduktion Wind-induzierter Schwingungen bei schlanken Hochhäusern*. BBSR-Online-Publikation 08/2022, Bonn, April 2022
- [145] Yangwen Zhang, Laurenz Wernicke, Wulf Wulff, Achim Bleicher, and Thomas Schauer. Design and validation of a dual-functional damper based on a stepper motor for energy harvesting and vibration control. Manuscript submitted for publication²³

Figures 6.15 to 6.18 have been published in [144], and Figures 6.3 to 6.14 will be published in [145].

²³The author's contribution to [145] includes Conceptualization, Data curation, Methodology, Software, Formal analysis, Investigation, Writing - Original Draft, Writing - Review & Editing, Validation, Visualization. Copyright ©2020 Zhang, Wernicke, Wulff, Bleicher and Schauer. Under Creative Commons CC BY 4.0 license (<https://creativecommons.org/licenses/by/4.0/>).

Author's Contribution

In this chapter, the selection of the stepper motor and build-up of the IVE-box were done by team member Laurenz Wernicke of the BBSR project [144]. The test bench was built by team member Wulf Wulff of the BBSR project [144]. The author conducted the literature review of different kinds of energy harvesting circuits and did the modeling and simulation part of the electric machine with the connected energy harvesting circuit. The author also did the experiment using the test bench together with Dr. Thomas Schauer and did the identification based on the measured data.

6.1. LINEAR TO ROTATIONAL MOTION CONVERSION

6.1 LINEAR TO ROTATIONAL MOTION CONVERSION

The linear facade outer skin motion needs to be transmitted to the rotation of the motor. There are some mechanism to realize the conversion from linear to rotational motion, such as ball screw or rack-and-pinion [146]. Both mechanisms can be expressed as the equation below by introducing the lead of the conversion α :

$$v = \alpha \cdot \omega, \quad (6.1)$$

where v is the facade outer skin linear relative velocity and ω is the rotational velocity. For rack-and-pinion, the lead of conversion α is equal to the radius of the pinion. The mechanism of rack-and-pinion is more suitable for our application. The radius of the pinion is 5 cm for our selected rack-and-pinion, i.e., $\alpha = 0.05$ m.

6.2 ELECTRIC MACHINE MODELING

Electric machines are the connection between the mechanical and the electrical domain. Therefore, the dynamics of any electric machine consist of two parts: the mechanical part and the electrical part. We focus on rotating electrical machines. For rotating electrical machines, the mechanical part is governed by Newton's laws relating the torque to the angular acceleration. The electrical part is governed by Kirchhoff's laws and can be derived by the equivalent circuit model. Modeling of two types of rotating electric machines, i.e., DC motor/generator and stepper motor/generator, is introduced in the following subsections.

6.2.1 Modeling of DC motor/generator

DC motors or Permanent-Magnet Synchronous Motors (PMSM) are quite similar, and both are often used as generators. When used as generators, Alternating Current (AC) can be induced in armature conductors. Built-in commutators are applied in the DC generators to convert the induced AC to Direct Current (DC). DC motors are mainly divided into brushed DC motors and brushless DC motors. The difference between a brushed DC motor and a brushless DC motor is the kind of commutator that is used. The mechanical commutator is used in brushed DC motors, where the electrical brushes made of carbon or graphite need to be reversed through a mechanical approach. It can cause issues such as noise, sparks, and overheating. The mechanical commutators are consumable parts that require periodic maintenance, such as brush replacement. Due to these disadvantages, the use of brushed DC motors is in decline [147]. The electrical commutator is used in the brushless DC motor. Less maintenance is required for the electrical commutator. For power conversion, due to the absence of brushes, brushless DC motors are more efficient than brushed DC motors [148]. The use of brushes increases the mechanical energy loss due to friction. For efficient energy harvesting, the built-in commutator in the DC motor should be removed and replaced by a rectifier to realize AC to DC conversion, which is introduced in Section 6.3.

Most brushed DC motors are single-phase. Brushless DC motors can be constructed with

different numbers of phases, but three-phase brushless DC motors are the most common. The modeling of a single-phase DC motor/generator is introduced. The equivalent dynamic model of the DC motor in motor and generator mode can be depicted in the following Figure 6.3. The armature coils of the DC motor can be modeled as a resistance R_a and a flux leakage inductance L_a .

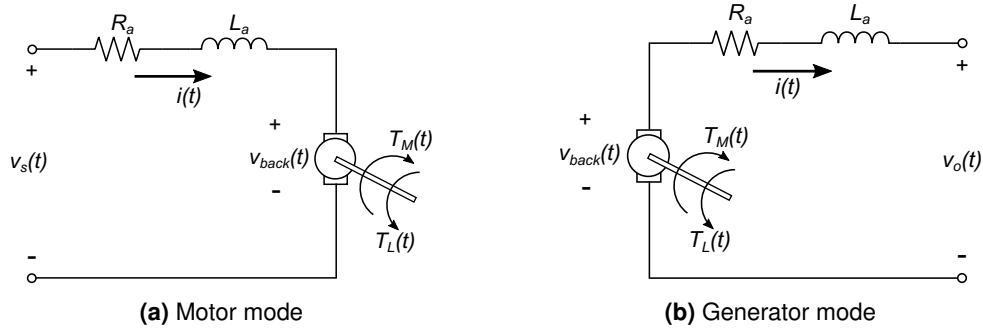


Figure 6.3: The equivalent dynamic model of the DC motor in motor and generator mode.

The dynamic model of the motor mode can be explained in the electrical domain and mechanical domain as follows:

Electrical Domain

According to Kirchhoff's voltage law, the governing equation of the electrical part can be written as:

$$R_a \cdot i(t) + L_a \cdot \frac{di(t)}{dt} + v_{back}(t) = v_s(t), \quad (6.2)$$

where $i(t)$ is the armature current, $v_{back}(t)$ is the back Electromotive Force (EMF) induced voltage and $v_s(t)$ is the voltage source. The back EMF induced voltage $v_{back}(t)$ is proportional to the angular velocity $\omega(t)$ of the rotor in the motor, which can be expressed as:

$$v_{back}(t) = k_e \cdot \omega(t), \quad (6.3)$$

where k_e is the electrical constant. The torque constant k_t ($\text{N} \cdot \text{m}/\text{A}$) is theoretically equal to k_e ($\text{V} \cdot \text{s}/\text{rad}$), which can be proved under conservation of power. The developed electromechanical torque can be calculated as:

$$T_M(t) = k_t \cdot i(t) \quad (6.4)$$

Mechanical Domain

Under the external torque T_L , the mechanical part of the DC motor is written as:

$$J \cdot \dot{\omega}(t) = T_M(t) - T_L(t) - T_f(t), \quad (6.5)$$

where $\dot{\omega}(t)$ is the angular acceleration, J is the moment of inertia of the rotor, T_f is the friction torque, which is usually modeled as $T_f(t) = B_f \cdot \omega(t)$ with B_f being the mechanical or frictional

6.2. ELECTRIC MACHINE MODELING

viscous damping factor.

Based on the governing equations, the state space form can be derived as below:

$$\begin{bmatrix} \dot{i}(t) \\ \dot{\omega}(t) \end{bmatrix} = \begin{bmatrix} -\frac{R_a}{L_a} & -\frac{k_e}{L_a} \\ -\frac{k_t}{J} & -\frac{B_f}{J} \end{bmatrix} \begin{bmatrix} i(t) \\ \omega(t) \end{bmatrix} + \begin{bmatrix} \frac{1}{L_a} \\ 0 \end{bmatrix} v_s(t) + \begin{bmatrix} 0 \\ -\frac{1}{J} \end{bmatrix} T_L(t), \quad (6.6)$$

where the armature current $i(t)$ and the rotational speed $\omega(t)$ are the two states. The input voltage v_s and the external torque T_L are two external inputs.

When in generator mode, the external torque becomes the energy source, and the source voltage v_s does not exist. The back EMF induced voltage $k_e \cdot \omega(t)$ is the input voltage in the electrical part. $v_o(t)$ is the output voltage. The governing equations for DC motor in motor and generator mode are summarized in Table 6.1 for comparison.

Table 6.1: Governing equations for DC motor in motor and generator mode.

	Motor Mode	Generator Mode
Electrical Domain	$R_a \cdot i(t) + L_a \cdot \frac{di(t)}{dt} + k_e \cdot \omega(t) = v_s(t)$	$R_a \cdot i(t) + L_a \cdot \frac{di(t)}{dt} + v_o(t) = k_e \cdot \omega(t)$
Mechanical Domain	$J \cdot \dot{\omega}(t) = k_t \cdot i(t) - T_L(t) - T_f(t)$	$T_L(t) = k_t \cdot i(t) + T_f(t) + J \cdot \dot{\omega}(t)$

Derivation of Electrical Damping Coefficient

The power flow is analyzed in generator mode. The equation of the power flow can be expressed as below:

$$T_L(t) \cdot \omega(t) = k_t \cdot i(t) \cdot \omega(t) + B_f \cdot \omega(t)^2 + J \cdot \dot{\omega}(t) \cdot \omega(t) \quad (6.7)$$

In steady state, the last term $J \cdot \dot{\omega}(t) \cdot \omega(t)$ does not exist. As $v_{back}(t) = k_e \cdot \omega(t)$, the equation above can be rewritten as:

$$T_L(t) = \underbrace{\frac{k_t k_e i(t)}{v_{back}(t)}}_{c_{e,r}} \cdot \omega(t) + \underbrace{B_f}_{c_{m,r}} \cdot \omega(t), \quad (6.8)$$

in which, $c_{e,r}$ ($N \cdot m \cdot s/rad$) is the rotational electrical damping coefficient, $c_{m,r}$ ($N \cdot m \cdot s/rad$) is the rotational mechanical/parasitic damping coefficient.

In steady state, when an external load resistance R_l is connected to the terminals (see Figure 6.4), the equation of the rotational electrical damping coefficient can be written as:

$$c_{e,r} = \frac{k_t k_e i(t)}{v_{back}(t)} \approx \frac{k_t^2}{(R_a + R_l)} = \frac{k_t^2}{R}, \quad (6.9)$$

where $k_t = k_e$, as k_t and k_e are theoretically the same, $R = R_a + R_l$ is the total resistance which consists of the internal resistance of the motor R_a and the connected external load resistance R_l . By varying the external load resistance, adjustable rotational electrical damping coefficient $c_{e,r}$ can be realized.

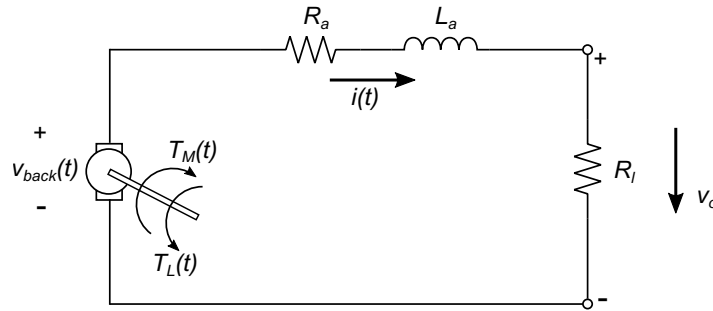


Figure 6.4: DC motor in generator mode connected to an external load resistance.

By connecting motion conversion mechanisms, the linear electrical damping coefficient c_e (N · s/m) can be derived as follows:

$$c_e \approx \frac{k_t^2}{\alpha^2(R_a + R_l)} = \frac{k_t^2}{\alpha^2 R}, \quad (6.10)$$

where α is the lead of conversion, which is equal to the radius of the pinion for rack-and-pinion.

6.2.2 Modeling of hybrid stepper motor/generator

Stepper motors, whose rotation is divided into several equal steps, can convert electrical energy into mechanical shaft rotation by using digital pulses. The advantages of stepper motors are their low cost, high reliability, high torque at low speeds, and simple, robust construction that allows them to operate in almost any environment [149]. As a generator, it can produce large induced voltages even at low speed compared with other types of generators.

Since the most commonly used stepper motors are of the two-phase type, a two-phase hybrid stepper motor is used as an example for the modeling. The equivalent dynamic model of the two-phase stepper motor in motor and generator mode can be depicted in the following Figure 6.5. Each phase of the motor has dependent coils. The coils of each phase can be modeled as the resistance R_a and the flux leakage inductance L_a .

The mathematical equations for a two-phase stepper motor in motor mode are also given in the electrical domain and the mechanical domain.

Electrical Domain

The electrical equations can be described as [150]:

$$\begin{cases} v_a(t) = R_a \cdot i_a(t) + L_a \cdot \frac{di_a(t)}{dt} + k_e \cdot \omega(t) \cdot \sin(N \cdot \theta(t)) \\ v_b(t) = R_a \cdot i_b(t) + L_a \cdot \frac{di_b(t)}{dt} - k_e \cdot \omega(t) \cdot \cos(N \cdot \theta(t)), \end{cases} \quad (6.11)$$

where $v_a(t)$ and $v_b(t)$ are the source phase voltages (V), $i_a(t)$ and $i_b(t)$ are the currents of phases A and B (A), R_a is the internal resistance of each phase (Ω), L_a is the inductance of each phase (H), k_e is the electrical constant (V · s/rad), $\omega(t)$ is the angular velocity of the rotor (rad/s),

6.2. ELECTRIC MACHINE MODELING

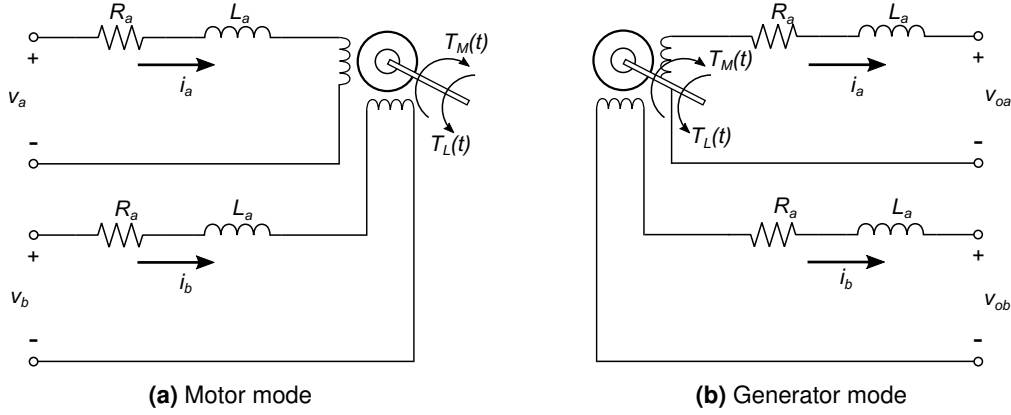


Figure 6.5: The equivalent dynamic model of the two-phase stepper motor in motor mode and generator mode.

$\theta(t) = \int_0^t \omega(t) \cdot dt$ is the mechanical rotor position (rad), and N is the rotor teeth number of the stepper motor. The terms $k_e \cdot \omega(t) \cdot \sin(N \cdot \theta(t))$ and $-k_e \cdot \omega(t) \cdot \cos(N \cdot \theta(t))$ are the back EMF voltages in phase A and B, which are proportional to the angular velocity $\omega(t)$.

The torque constant k_t ($N \cdot m/A$) is theoretically equal to the electrical constant k_e ($V \cdot s/rad$). The developed electromechanical torque can be expressed as:

$$T_M(t) = k_t \cdot (-i_a(t) \cdot \sin(N \cdot \theta(t)) + i_b(t) \cdot \cos(N \cdot \theta(t))) \quad (6.12)$$

Mechanical Domain

The mechanical equations can be written as:

$$\begin{aligned} J \cdot \dot{\omega}(t) &= T_M(t) - T_L(t) - T_{det}(t) - T_f(t) \\ &= T_M(t) - T_L(t) - T_d \cdot \sin(4N \cdot \theta(t)) - T_f(t) \end{aligned} \quad (6.13)$$

where J is the moment of inertia of the rotor ($kg \cdot m^2$), $T_f(t)$ is the friction torque ($N \cdot m$), which is usually modeled as $T_f(t) = B_f \cdot \omega(t)$ with B_f ($N \cdot m \cdot s/rad$) being the frictional viscous damping factor, and $T_L(t)$ is the load torque ($N \cdot m$). A big difference between DC and stepper motors is that there is a certain level of torque called detent torque $T_{det}(t)$ due to the attraction force of the rotor magnet. T_d is the detent torque amplitude.

When in generator mode, the external torque $T_L(t)$ becomes the energy source, and the source voltages $v_a(t)$ and $v_b(t)$ do not exist. The back EMF induced voltages $-k_e \cdot \omega(t) \cdot \sin(N \cdot \theta(t))$ and $k_e \cdot \omega(t) \cdot \cos(N \cdot \theta(t))$ are the input voltages of the phase A and B in the electrical domain, respectively. $v_{oa}(t)$ and $v_{ob}(t)$ are the output voltages of phase A and B, respectively. The detent torque also exists even when the windings are not energized. The governing equations for the two-phase stepper motor in motor and generator mode are summarized in Table 6.2 below.

Park transformation/direct-quadrature (DQ) transformation can be applied to transfer the

Table 6.2: Governing equations for two-phase stepper motor in motor and generator mode.

	Motor Mode	Generator Mode
Electrical	$v_a(t) = R_a i_a(t) + L_a \frac{di_a(t)}{dt} + k_e \omega(t) \sin(N\theta(t))$	$R_a i_a(t) + L_a \frac{di_a(t)}{dt} + v_{oa} = -k_e \omega(t) \sin(N\theta(t))$
Domain	$v_b(t) = R_a i_b(t) + L_a \frac{di_b(t)}{dt} - k_e \omega(t) \cos(N\theta(t))$	$R_a i_b(t) + L_a \frac{di_b(t)}{dt} + v_{ob} = k_e \omega(t) \cos(N\theta(t))$
Mechanical	$J\dot{\omega}(t) = -T_L(t) - T_d \sin(4N\theta(t)) - T_f(t)$	$T_L(t) = T_d \sin(4N\theta(t)) + T_f(t) + J\dot{\omega}(t)$
Domain	$+k_t(-i_a(t) \sin(N\theta(t)) + i_b(t) \cos(N\theta(t)))$	$+k_t(-i_a(t) \sin(N\theta(t)) + i_b(t) \cos(N\theta(t)))$

mathematical model to a rotating coordinate system (d, q). The equations are shown as below:

$$\begin{bmatrix} i_d \\ i_q \end{bmatrix} = \begin{bmatrix} \cos(N\theta) & \sin(N\theta) \\ -\sin(N\theta) & \cos(N\theta) \end{bmatrix} \begin{bmatrix} i_a \\ i_b \end{bmatrix}, \quad (6.14)$$

where i_d is the direct current, which corresponds to the component of the stator magnetic field along the axis of the motor magnetic field; i_q is the quadrature current, which corresponds to the orthogonal component. By applying DQ transformation, the governing equation can be transformed as listed in Table 6.3.

Table 6.3: Governing equations for two-phase stepper motor in motor and generator mode in rotating (d,q) coordinate system.

	Motor Mode	Generator Mode
Electrical	$v_d(t) = R_a i_d(t) + L_a \frac{di_d(t)}{dt} - NL_a \omega(t) i_q(t)$	$R_a i_d(t) + L_a \frac{di_d(t)}{dt} + v_{od}(t) - NL_a \omega(t) i_q(t) = 0$
Domain	$v_q(t) = R_a i_q(t) + L_a \frac{di_q(t)}{dt} + NL_a \omega(t) i_d(t) + k_e \omega(t)$	$R_a i_q(t) + L_a \frac{di_q(t)}{dt} + v_{oq}(t) + NL_a \omega(t) i_d(t) = k_e \omega(t)$
Mechanical	$J\dot{\omega}(t) = k_t i_q(t) - T_L(t) - T_d \sin(4N\theta(t)) - T_f(t)$	$T_L(t) = k_t i_q(t) + T_d \sin(4N\theta(t)) + T_f(t) + J\dot{\omega}(t)$
Domain		

Derivation of Electrical Damping Coefficient

Similar to the DC motor, the power flow is analyzed for the hybrid stepper motor in generator mode. The equation is listed as below:

$$T_L(t) \cdot \omega(t) = k_t \cdot i_q(t) \cdot \omega(t) + T_d \cdot \sin(4N \cdot \theta(t)) \cdot \omega(t) + B_f \cdot \omega(t)^2 + J \cdot \dot{\omega}(t) \cdot \omega(t) \quad (6.15)$$

In steady state, if both phases of the stepper motor are short circuited ($v_{od} = v_{oq} = 0$), the quadrature current i_q can be derived as:

$$i_q \approx \frac{k_e \omega R_a}{L_a^2 N^2 \omega^2 + R_a^2} \quad (6.16)$$

In steady state, the last term $J \cdot \dot{\omega}(t) \cdot \omega(t)$ does not exist. Therefore, the rotational motor

6.2. ELECTRIC MACHINE MODELING

reaction torque can be rewritten as:

$$T_L \approx \underbrace{\frac{k_t k_e R_a}{(L_a^2 N^2 \omega^2 + R_a^2)}}_{c_{e,r}} \cdot \dot{\omega}(t) + \underbrace{B_f}_{c_{m,r}} \cdot \dot{\omega}(t) + T_d \sin(4N\theta(t)), \quad (6.17)$$

in which, $c_{e,r}$ is the rotational electrical damping coefficient, $c_{m,r}$ is the rotational mechanical/parasitic damping coefficient.

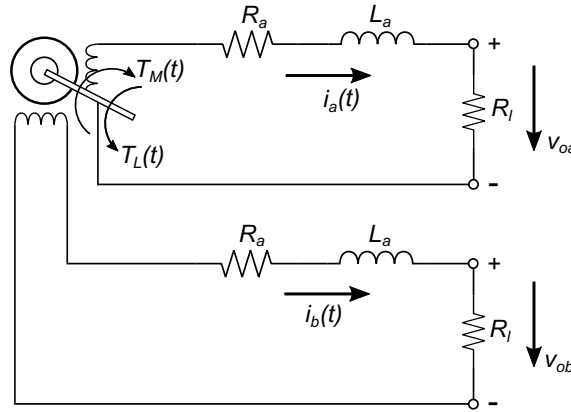


Figure 6.6: Each phase of the two-phase stepper motor in generator mode connected to a same external load resistance R_l .

When each phase is connected to a same external load resistance R_l , as illustrated in Figure 6.6, the equation of the rotational and linear electrical damping coefficient can be written as:

$$c_{e,r} \approx \frac{k_t^2 R}{(L_a^2 N^2 \omega^2 + R^2)} = \frac{k_t^2 (R_a + R_l)}{(L_a^2 N^2 \omega^2 + (R_a + R_l)^2)} \quad (6.18)$$

$$c_e \approx \frac{k_t^2 R}{\alpha^2 (L_a^2 N^2 \omega^2 + R^2)} = \frac{k_t^2 (R_a + R_l)}{\alpha^2 (L_a^2 N^2 \omega^2 + (R_a + R_l)^2)}, \quad (6.19)$$

where $k_t = k_e$, as k_t and k_e are theoretically the same, and $R = R_a + R_l$. The lead of conversion α is defined in Equation (6.1).

As observed, the electrical damping coefficient for the DC motor (see Equation (6.10)) and the two-phase hybrid stepper motor (see Equation (6.19)) is slightly different. There is a non-linear relationship between the rotational speed ω and the electrical damping coefficient c_e of the stepper motor. However, for small ω and small phase inductance L_a , the non-linear influence can be neglected, the electrical damping coefficients for DC motor and stepper motor are approximately the same. Both c_e can be adjusted by varying the connecting external load resistance R_l .

Specially designed power electronics can be implemented to achieve the resistance emulation of the variable R_l and simultaneously harvest energy, which is introduced in detail in the following Section 6.3

6.3 POWER ELECTRONICS FOR RESISTANCE EMULATION AND ENERGY HARVESTING

The electrical damping coefficient c_e for both introduced electric machines can be adjusted by varying the total resistance R . The total resistance R consists of the fixed resistance of the motor coil R_a and the external load resistance R_l which is possibly variable. Therefore, the design of a connecting circuit that can emulate an adjustable equivalent resistance R_l in a certain range is important for achieving the adjustable c_e . The Energy Harvesting Circuit (EHC) can harvest energy and store it in a battery while achieving the function of resistance emulation.

6.3.1 Design of Energy Harvesting Circuit (EHC)

Numerous studies have been conducted to harvest kinetic energy using different energy conversion mechanisms and their associated electronics [151]. According to the different energy conversion mechanisms, there are three major categories: electromagnetic generators, piezoelectric generators, and electrostatic generators [152, 153, 154]. All the electric machines belong to the category of electromagnetic generators. The output of this category, regardless of its type, is an AC quantity [155]. The DC generator can generate DC due to its built-in commutator. Without the commutator, it still generates AC. Because of the low efficiency of the commutator, it is replaced by economical rectifiers. Therefore, to generate the required DC output voltage, AC-to-DC power conversion is required for the electromagnetic generators.

The AC-to-DC power conversion can be categorized into two types: the conventional two-stage power conversion and the single-stage power conversion, as shown in Figure 6.7.

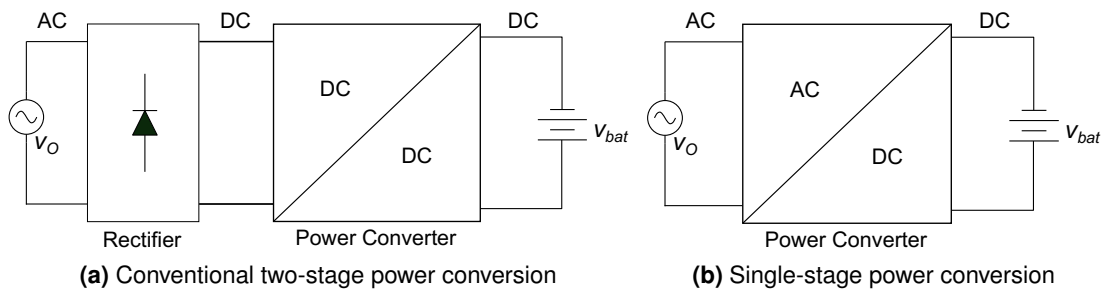


Figure 6.7: Block diagram of power converter for energy harvesting application.

Conventional two-stage power converters mostly consist of a rectifier followed by a buck-boost converter. Rectifiers such as widely used bridge rectifiers are used for the conversion of an AC input to DC output, and then the followed buck-boost converter is to convert the DC voltage to the required DC output voltage. For low-voltage energy harvesting, the major disadvantage in using two-stage power converters is that the diode forward voltage drop causes a large amount of power loss, which makes the power conversion inefficient [156]. Therefore, the direct AC-to-DC single-stage power converters that are more efficient for low-voltage energy harvesting are proposed to address the problem [155, 156, 157, 158]. For high-voltage energy harvesting, the influence of diode voltage drop is relatively small, so the conventional two-stage

6.3. POWER ELECTRONICS FOR RESISTANCE EMULATION AND ENERGY HARVESTING

power conversion is widely used topology for EHC [62, 106, 107, 159].

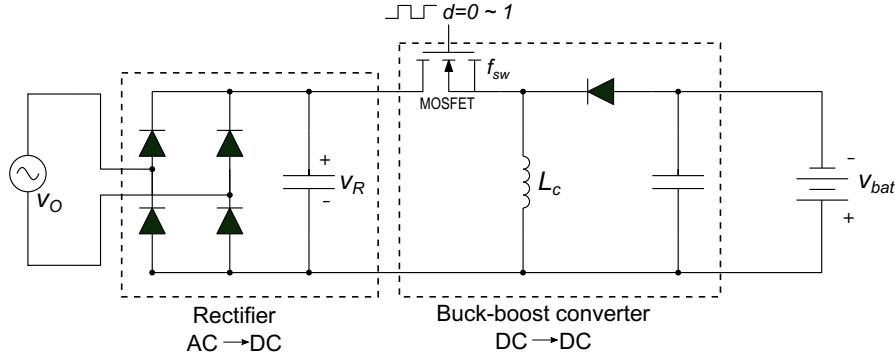


Figure 6.8: The schematic of a two-stage EHC.

Shen et al. investigated the dual function (i.e., vibration control and energy harvesting) of an energy regenerative TMD system in a high-rise building [107]. This system consists of a pendulum-type TMD, an electromagnetic damper, and an EHC. The employed EHC has a two-stage power conversion topology, as shown in Figure 6.8. It consists of a bridge rectifier, a fixed duty-cycle buck-boost converter, and a rechargeable battery. The AC voltage generated by the electric machine is converted to DC voltage through the bridge rectifier. Schottky diodes are used in the rectifier due to their low forward voltage drop. The following connected capacitor can smooth the DC voltage waveform before entering to the buck-boost converter. When operating in Discontinuous Current Mode (DCM), the buck-boost converter with a fixed duty cycle d acts similar to a constant resistor. To maintain DCM, the following equation needs to be satisfied [160]:

$$v_R \leq \frac{1-d}{d} \cdot v_{bat}, \quad (6.20)$$

where v_R is the rectified DC voltage and v_{bat} is the battery voltage. Under this condition, the equivalent load resistance of the circuit R_l can be calculated as [154]:

$$R_l = \frac{2 \cdot f_{sw} \cdot L_C}{d^2}, \quad (6.21)$$

where L_C is the inductance of the buck-boost converter, and f_{sw} is the switching frequency of the Metal-Oxide-Semiconductor Field-Effect Transistor (MOSFET). When the duty cycle d is fixed and satisfies the condition of Equation (6.20), the equivalent resistance R_l can be maintained nearly constant. If the circuit works in Continuous Current Mode (CCM), the constant R_l can not be maintained. Therefore, the function of the electric machine as a damper would be negatively influenced. In the study by Shen et al., a passive system with a constant damping coefficient was investigated, so a low-power clock oscillator IC was used to generate the Pulse-Width Modulation (PWM) signal with a switching frequency of 32.768 Hz and a fixed duty cycle of 0.5 [107].

Therefore, the power electronic converter plays two important roles: first, to regulate the AC input of the electronic machine to the required DC level to ensure energy harvesting; and

second, to achieve the desired electrical damping coefficient for the vibration control purpose. The electrical damping coefficient can be varied by changing the equivalent resistance of the EHC through the duty cycle of the input PWM signal. Semi-active control can be achieved by generating an input PWM signal with varying duty cycles from the microcontroller. The time-varying duty cycle is determined by the semi-active control logic running on the microcontroller.

6.3.2 EHC for hybrid stepper motor

The most widely used hybrid stepper motor is the two-phase type. When in generator mode, sinusoidal voltages shifted by 90° are induced at the windings of these two phases. A dual two-stage EHC is proposed for the two-phase hybrid stepper motor, as shown in Figure 6.9. The induced AC voltage of each phase is first connected to a bridge rectifier and a capacitor to obtain a smoothed DC voltage and then connected to a buck-boost converter to obtain the required voltage for energy harvesting. The two-stage EHC of each phase is connected in parallel to a single rechargeable battery. To ensure the same operation behaviour as the single-phase electric machine, the components of the power converter are the same for each phase, and the MOSFETs of the parallel power converters are driven by the same PWM signal with the same switching frequency f_{sw} and same duty cycle d .

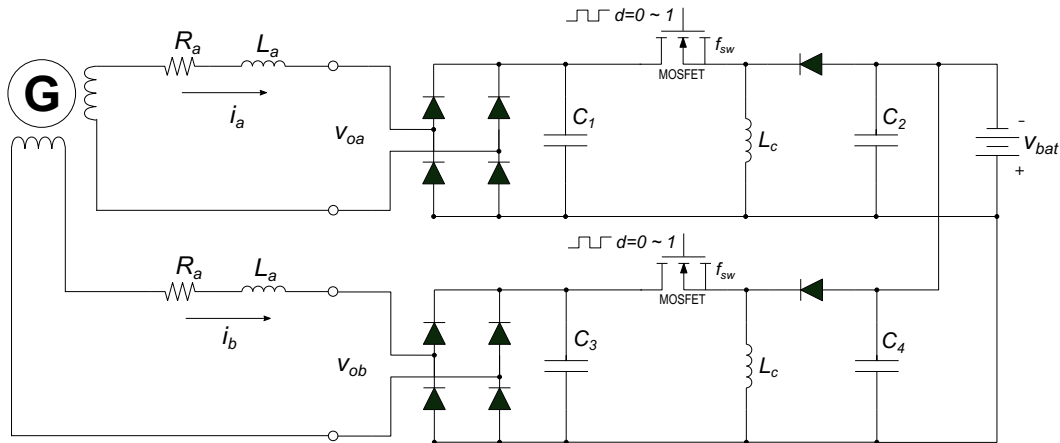


Figure 6.9: The schematic of dual two-stage EHC for two-phase hybrid stepper motor ($C_1 = C_3, C_2 = C_4$).

The model of the two-phase hybrid stepper motor with dual two-stage EHC is fully built in Simulink (The Mathworks, Inc., USA) using Simscape, as shown in Figure 6.10. Simscape enables the rapid creation of models for physical systems within the Simulink environment. Different types of motors and batteries are directly available as standard blocks and can be assembled into schematics with other basic components such as diodes and inductors. Therefore, different motors and power electronics can be tested based on the simulation.

The final Simulink model will be built and identified for the selected motor with the corresponding EHC, and further integrated into the whole comprehensive simulation model of the prototype with moveable facade element for the identification of other parameters (see Chapter 8).

6.4. GENERATOR SELECTION AND DESIGN OF POWER ELECTRONICS AND BATTERY

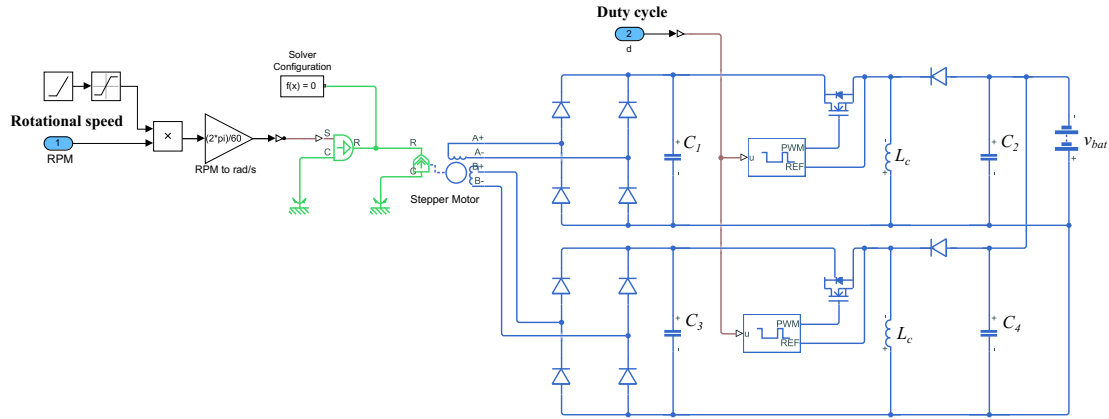


Figure 6.10: Simulink model of hybrid stepper motor with dual two-stage EHC.

6.4 GENERATOR SELECTION AND DESIGN OF POWER ELECTRONICS AND BATTERY

To select the appropriate electrical damper/generator for the moveable facade elements in our proposed system, the expected range of rotational speed and the minimum and maximum damping coefficient required for the optimized semi-active control provide good guidance for the selection. Based on the simulation results in Chapter 5, the maximum speed of the generator is about 100 rpm using a pinion with a radius of 5 cm.

In the motor structure, stepper motors have more pole pairs than DC motors. Therefore, a stepper motor can produce much higher voltage than a DC motor at the same rotational speed, which means the torque constant k_t of a stepper motor is much higher. The speed constant k_n is also a parameter that shows their difference more directly. The relationship between the speed constant k_n and the torque constant k_t can be described as:

$$k_n = \frac{30}{\pi} \cdot \frac{1}{k_t} \text{ (rpm/V)} \quad (6.22)$$

In Table 6.4, the speed constant, torque constant, and the induced voltages at 100 rpm are listed for different types of motors without gearbox. For the listed DC motors, the speed constants and torque constants are given by the manufacturer. For the stepper motors, these constants are usually not specified but can be approximately calculated according to the holding torque and rated current given in the information of data sheet. By dividing the holding torque to the rated current of the stepper motor, the approximate torque constant can be calculated. Then the speed constant can be further calculated based on the Equation (6.22).

DC motors can also generate higher voltages by connecting a gearbox to increase the input rotational speed. However, the attached gearbox increases additional energy loss due to friction, which is undesirable from the energy harvesting point of view. Therefore, it is finally decided to use a stepper motor in our application.

The required minimum and maximum damping coefficients ($c_{n-j+n_f}^{\min}$ and $c_{n-j+n_f}^{\max}$) for the floor j are obtained from the optimization results from Chapter 5. Since the optimized damping coefficient consists of the electrical damping from the generator and the mechanical damping

6.4. GENERATOR SELECTION AND DESIGN OF POWER ELECTRONICS AND BATTERY

Table 6.4: Induced voltage at 100 rpm for different motor type (DC motor from maxon group, stepper motor from Moons' Electric Co., Ltd.).

Motor type	Model Number	Speed constant	Torque constant	Voltage per 100 rpm
Brushed DC	DCX 22 L	109 rpm/V	0.0876 N · m/A	0.917 V
Brushed DC	DCX 35 L	129 rpm/V	0.0741 N · m/A	0.775 V
Brushless DC	EC 60	65 rpm/V	0.147 N · m/A	1.538 V
Brushless DC	EC frameless 90 flat	33.4 rpm/V	0.286 N · m/A	2.994 V
Stepper motor	ML42HS0L4600	4.66 rpm/V	2.050 N · m/A	21.468 V
Stepper motor	ML42HS0L4210	1.66 rpm/V	5.762 N · m/A	60.350 V
Stepper motor	ML42HS3L4270	0.83 rpm/V	11.481 N · m/A	120.292 V

due to viscous friction, only part of the damping is electrical damping. Furthermore, each moveable facade element is equipped with one generator. Thus, when N_d moveable facade elements are divided for each story, N_d generators work together to achieve the optimized damping coefficient for floor j . When the mechanical damping coefficient is known (identified) as \bar{c}_m for one moveable facade element, the nominal electrical damping coefficients can be calculated as follows:

$$\bar{c}_{e,n-j+n_f}^{\min} \equiv c_{n-j+n_f}^{\min}/N_d - \bar{c}_m = 2 \cdot \xi_{n-j+n_f}^{\min} \sqrt{\bar{m}_f \bar{k}_f} - \bar{c}_m, \quad (6.23)$$

$$\bar{c}_{e,n-j+n_f}^{\max} \equiv c_{n-j+n_f}^{\max}/N_d - \bar{c}_m = 2 \cdot \xi_{n-j+n_f}^{\max} \sqrt{\bar{m}_f \bar{k}_f} - \bar{c}_m. \quad (6.24)$$

As shown in the above equations, the optimized damping ratios $\xi_{n-j+n_f}^{\min}$ and $\xi_{n-j+n_f}^{\max}$ together with the mass \bar{m}_f and the spring stiffness $\bar{k}_f = k_f/N_d$ of a single moveable facade element can also be used to determine the nominal electrical damping coefficients. The determined coefficients can then be implemented in the derived Equation (6.19) for two-phase stepper motor as follows:

$$\bar{c}_{e,n-j+n_f}^{\min} = \frac{k_t^2 (R_a + R_{l,n-j+n_f}^{\max})}{\alpha^2 [L_a^2 N^2 \omega^2 + (R_a + R_{l,n-j+n_f}^{\max})^2]} \quad (6.25)$$

$$\bar{c}_{e,n-j+n_f}^{\max} = \frac{k_t^2 (R_a + R_{l,n-j+n_f}^{\min})}{\alpha^2 [L_a^2 N^2 \omega^2 + (R_a + R_{l,n-j+n_f}^{\min})^2]} \quad (6.26)$$

With low rotational speed, the velocity dependent term can be neglected. Therefore, the required equivalent resistance can be easily determined. For minimum electrical damping, the maximum equivalent resistance $R_{l,n-j+n_f}^{\max}$ is required, and for the maximum electrical damping, the minimum equivalent resistance $R_{l,n-j+n_f}^{\min}$ is required. A fundamental principle in the selection of stepper motor is that it should be selected so that, in the case of a short circuit ($R_{l,n-j+n_f}^{\min} = 0$),

6.4. GENERATOR SELECTION AND DESIGN OF POWER ELECTRONICS AND BATTERY

the electrical damping coefficient must exceed $C_{e,n-j+n_t}^{\max}$.

The final selected electrical machine for each moveable facade element is a two-phase hybrid stepper motor (Type ML42HS3L4270, Moons' Electric Co., Ltd., China). The approximate torque constant k_t of this selected stepper motor can be calculated as 11.48 Nm/A, and the speed constant as 0.83 rpm/V. Therefore, when the stepper motor is idling with an input rotational speed of 100 rpm, a peak voltage of 120.3 V can be theoretically induced. The torque constant has also been experimentally determined by a test bench, as shown in Figure 6.11.

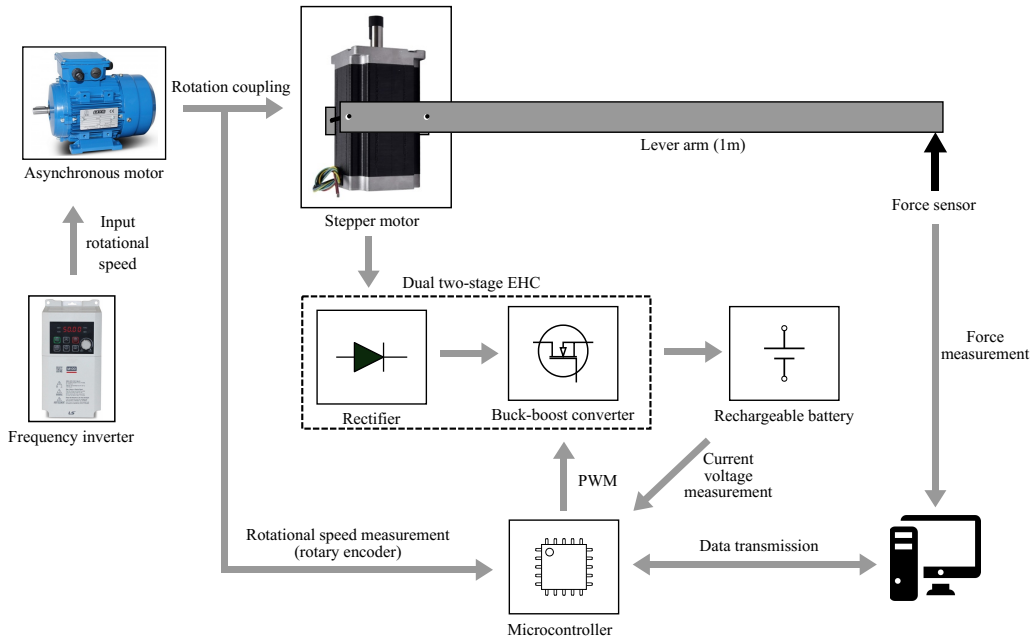


Figure 6.11: The schematic of the test bench for the stepper motor.

The rotation of the stepper motor is driven by an asynchronous motor with a constant input rotational speed. The rotational coupling is as shown in Figure 6.12. The shaft of the generator is rotated with a constant input rotational speed, and the amplitude of the induced sinusoidal voltage at the terminals is measured with an oscilloscope. Four different input rotational speeds of 25 rpm, 50 rpm, 75 rpm, and 100 rpm are tested. Based on the experiment, the average torque constant can be determined as 7.61 Nm/A, which is about 30% smaller than the theoretical value, but still large enough for our application. The speed constant can be calculated as 1.255 rpm/V. With the expected maximum input rotational speed of 100 rpm, a peak voltage of 80 V can be induced. Using an LCR meter, the internal resistance R_a and inductance L_a for each phase of this stepper motor are measured as 4.2 Ω and 80 mH respectively.

According to Equations (6.25) and (6.26), the equivalent resistance of the EHC can be first designed to vary approximately in the range of 100 to 2000 Ω to meet the desired electrical damping coefficient c_e . The equivalent resistance is determined by the switching frequency f_{sw} and the inductance of the buck-boost converter L_c , and the duty cycle d (see Equation (6.21)). The switching frequency f_{sw} , the inductance L_c are selected as fixed values, while the duty cycle d is a variable input from the microcontroller. The switching frequency needs to be above 20

6.4. GENERATOR SELECTION AND DESIGN OF POWER ELECTRONICS AND BATTERY

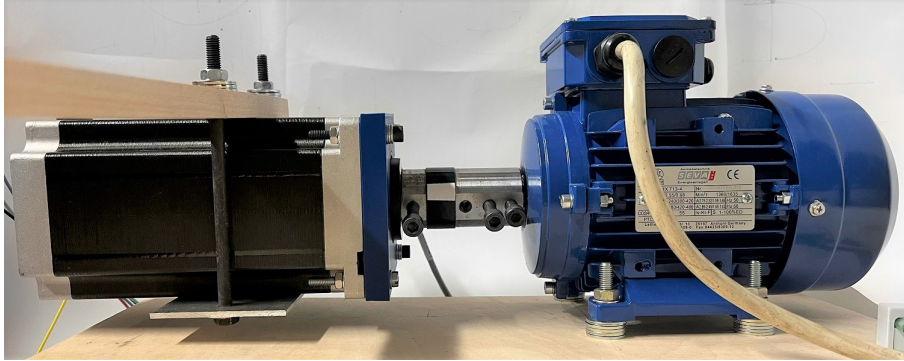


Figure 6.12: Fixed coupling between the asynchronous motor and the tested stepper motor (Source: Thomas Schauer, Technische Universität Berlin).

kHz so that it is not audible and below 100 kHz due to the technical limitation of the microcontroller. Due to the limited size of the circuit board, the choice of inductance is also restricted. Furthermore, the allowed range of the duty cycle should be as large as possible to have little quantization in the realization of the resistors (the duty cycle can be adjusted with an accuracy of 1% in the later realized system). The range of the duty cycle is restricted by the maximum duty cycle due to the required condition of Discontinuous Current Mode (DCM). A higher battery voltage can increase the allowed maximum duty cycle (see Equation (6.20)). Simulations based on the developed Simulink model (see Figure 6.10) provided important instructions for the final decision of all the components that are applied in the dual two-stage EHC. The final used switching frequency f_{sw} is 100 kHz, the inductance L_c in the buck-boost converter is 22 mH, and a rechargeable 24 V lead-acid battery is applied.

The duty cycles $d_{n-j+n_f}^{\min}$ and $d_{n-j+n_f}^{\max}$ to obtain the corresponding equivalent resistance $R_{l,n-j+n_f}^{\max}$ and $R_{l,n-j+n_f}^{\min}$ can be calculated by the following equations:

$$R_{l,n-j+n_f}^{\max} = \frac{2 \cdot f_{sw} \cdot L_c}{(d_{n-j+n_f}^{\min})^2} \quad (6.27)$$

$$R_{l,n-j+n_f}^{\min} = \frac{2 \cdot f_{sw} \cdot L_c}{(d_{n-j+n_f}^{\max})^2} \quad (6.28)$$

Under different duty cycles and different input rotational speeds, the experimentally obtained and estimated electrical counter torques M_e and the resulting electrical damping coefficient c_e generated by the stepper motor are plotted in Figure 6.13 and Figure 6.14 respectively. The estimated plot is obtained by fitting the measured values using the Optimization Toolbox in MATLAB (The MathWorks, Inc., USA). The identified parameters are $k_t = 8.38$ Nm/A and $L_a = 155$ mH.

As shown in Fig. 6.14, the experimentally determined electrical damping coefficient shows deviations when the rotational speed is below 20 rpm. The reason is due to the detent torque T_{det} in the stepper motor. The detent torque during the rotation is a sinusoidal torque, whose frequency is proportional to the rotational speed ω . At low speeds, the expected average of

6.4. GENERATOR SELECTION AND DESIGN OF POWER ELECTRONICS AND BATTERY

zero for the detent torque cannot be accurately determined, and affects the measured average counter torque negatively.

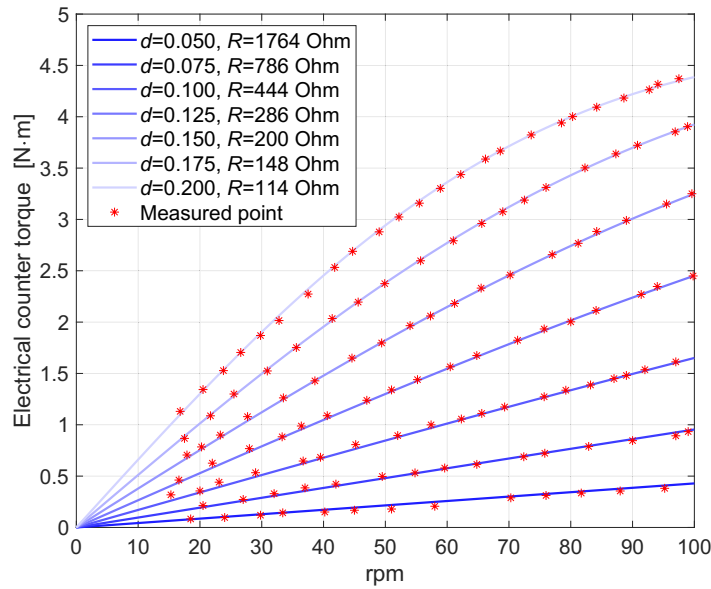


Figure 6.13: Measured and estimated electrical counter torque M_e of the stepper motor in generator mode for different duty cycles and corresponding emulated resistances ($R = R_a + R_l(d)$).

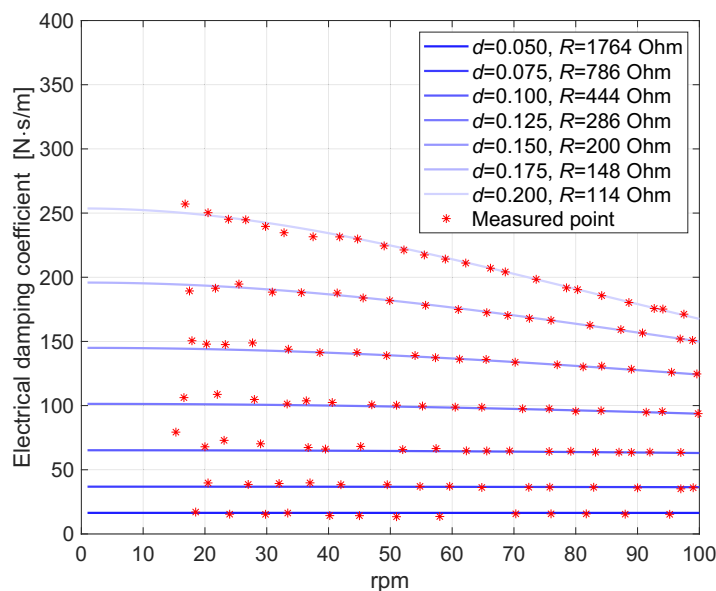


Figure 6.14: Measured and estimated electrical damping coefficient \bar{c}_e of the stepper motor in generator mode for different duty cycles and corresponding emulated resistances ($R = R_a + R_l(d)$).

6.5 ELECTRONICS OF THE DAMPER

The entire electronics for achieving the adjustable electrical damping and energy harvesting works as a unit named as *IVE - Intelligent Vibration control and Energy harvesting unit*. All the electronic components are housed in the IVE-box. The key components are the developed dual two-stage power converter, a microcontroller board, two sensor shields, and two series-connected 12 V rechargeable batteries. In addition, a galvanically isolated USB to RS232/RS485/TTL converter is also located in the IVE-box, enabling the bidirectional serial communication via USB with the Simulink interface on the computer. The front and rear views of the IVE-box are as shown in Figure 6.15.



(a) Front view of the IVE-box



(b) Rear view of the IVE-box

Figure 6.15: The front and rear view of the IVE-box (Source: Laurenz Wernicke, Technische Universität Berlin).

There are four LEDs on the front of the IVE-box (see Figure 6.15a). The function of each LED is explained below:

- Yellow (SYS. STATUS) → Flashes with a frequency of 0.5 Hz when electrical damping is activated
- Green (HARVESTING) → On when a positive current is flowing into the battery
- Red (BAT. LOW) → On when the battery voltage is low

6.5. ELECTRONICS OF THE DAMPER

- Blue (BAT. FULL) → On when the battery is fully charged

There is a switch with three positions on the top right of the front IVE-box. In position 0 (OFF), the battery is disconnected and the device is turned off. Position II (DAMPING ACTIVE) is when the system is in operation, i.e., the power electronics and all sensors are activated. Position I (EXT. BAT. CHARGING) is when the battery is externally charged by connecting the charging socket on the rear side of the IVE-box (see Figure 6.15b). Below this switch is two sockets. On the left is a 5-pin socket (ENCODER) for the rotary encoder to measure the relative motion of moveable facade outer skin, and on the right is a 4-pin socket (GENERATOR) to connect the generator (two-phase hybrid stepper motor). There is also a USB-A socket (EXT. PC INTERFACE) on the lower left side of the front IVE-box, which enables serial communication with the Simulink interface on the computer through USB. On the left side of the mentioned charging socket on the rear IVE-box (see Figure 6.15b), there are two 4 mm lab jacks that can be connected with an external 25 Ω load resistor to discharge the battery if necessary (the battery is full). A USB-B socket is also on the rear of the IVE-box, which can be connected to the PC to update the firmware of the microcontroller. During the firmware update, the slide switch above the USB-B socket needs to be set to the ON position. When the update is complete, it needs to be switched back to the OFF position.



Figure 6.16: Side view of the opened IVE-box (left is the rear view, right is the front view) (Source: Laurenz Wernicke, Technische Universität Berlin).

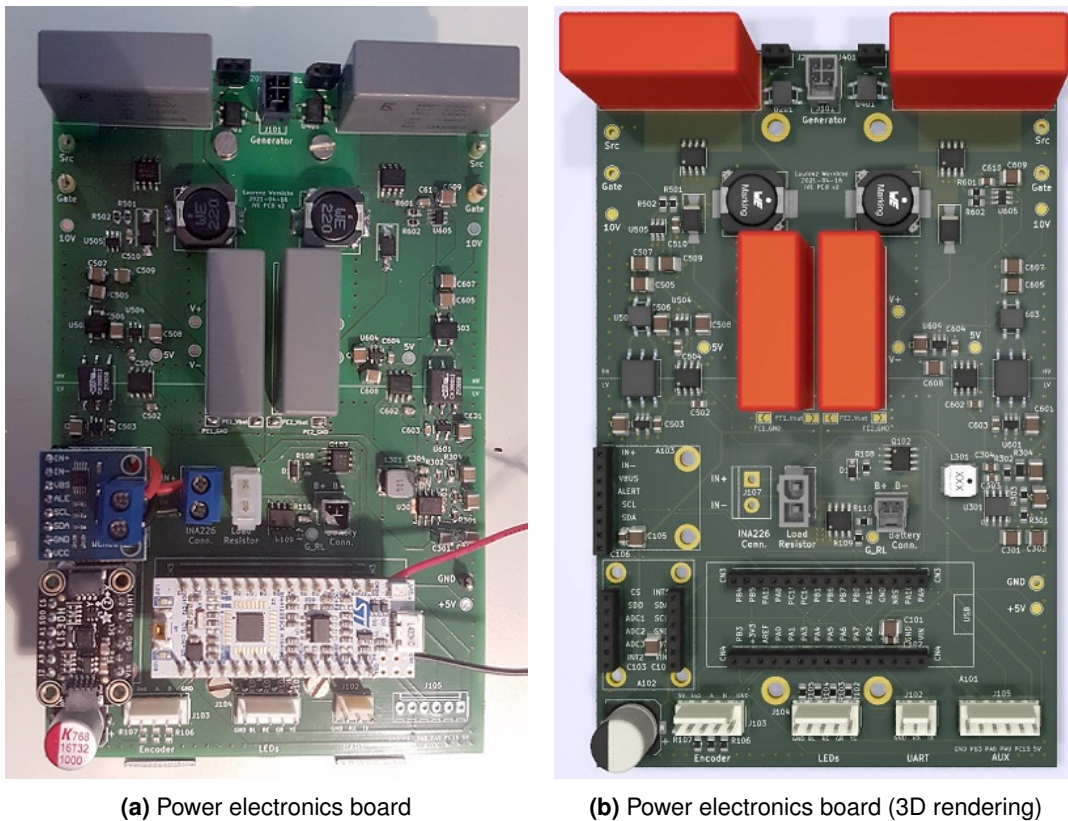


Figure 6.17: Top view of the power electronics board (real and 3D rendering) (Source: Laurenz Wernicke, Technische Universität Berlin).

Figure 6.16 shows the side view of the opened IVE-box. Two 12 V batteries with a capacity of 2.9 Ah (Type 12LS-2.9, AKKU SYS Akkumulator und Batterietechnik Nord GmbH, Germany) are placed at the upper part of the box. They are connected in series to achieve a 24 V nominal voltage. The batteries are protected by a Medium Acting 250 V/3.15 A fuse. The black box on the lower right side is the TTL/USB converter from the company Waveshare. As shown in Figure 6.16, the power electronics board is disassembled from the housing, and it can be screwed to the IVE-box.

Figure 6.17 shows the top view of the power electronics board (real and 3D rendering). In addition to a microcontroller board, the power electronics board also contains a three-axis acceleration sensor (LIS3DH, STMicroelectronics, Switzerland) and a sensor for measuring the current and voltage of the battery (INA226, Texas Instruments, USA). They are all designed as shields (plug-on components) so that they can be easily replaced in case of failure. On the real power electronics board, they are shown in the lower left area of the board (see Figure 6.17a).

An isolation concept is implemented on the power electronics board to protect the application. The board is spatially separated into two areas, i.e., high voltage (HV) area, and low voltage (LV) area. On the HV area, voltages up to 100 V induced by the generator can be applied. The LV area contains the microcontroller, sensors, and all low-power connectors such as

6.5. ELECTRONICS OF THE DAMPER

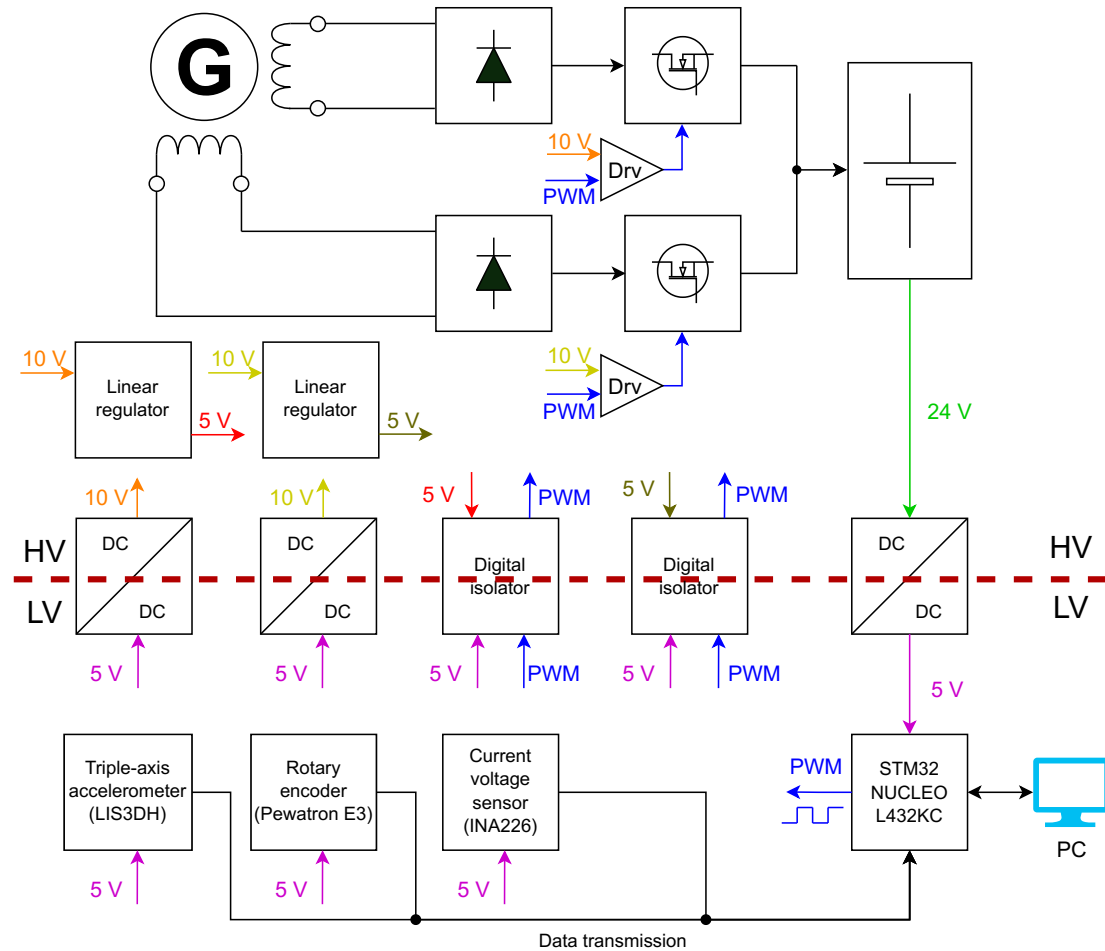


Figure 6.18: Isolation concept for the power electronics board.

the encoder and UART communication via TTL/USB interface. The overview of all the electric components marked with their voltage level is shown in the isolation concept in Figure 6.18.

To ensure a self-sufficient operation of the system, the microcontroller (STM32 NUCLEO L432KC, STMicroelectronics, Switzerland) is selected due to its low power consumption. The sensors are read with a frequency of 100 Hz. The duty cycle of the PWM signal that determines the electrical damping coefficient is adjusted by the microcontroller based on the movement of the building and facade element. FreeRTOS is used as the operating system of the microcontroller to meet the real-time requirements of our application. The relative displacement of the moveable facade outer skin is measured by the encoder on the stepper motor (E3 Optical Kit encoder, US Digital, USA), and its relative velocity is numerically derived. The acceleration sensor measures the story acceleration of the building, so the IVE-box should be attached to the fixed inner skin or the building structure. The acceleration sensor is quite sensitive, so the measured data is processed with a high-pass filter before it is used as an input signal to the microcontroller. Through the bidirectional serial communication, the measured data of sensors can be transmitted to the computer with a frequency of 100 Hz. Meanwhile, the operation mode

of the IVE-box (e.g. passive or semi-active damping, encoder reset, activation of battery discharge, etc.) or the system parameters can be changed in the developed Simulink interface in the computer.

6.6 SUMMARY AND CONCLUSIONS

In this chapter, the theoretical electrical damping coefficient of a two-phase hybrid stepper motor is derived and compared with that of an ordinary DC motor. A dual two-stage EHC is proposed to realize adjustable electrical damping through resistance emulation, and to simultaneously harvest energy. A test bench has been built to test the adjustable electrical damping of a selected two-phase hybrid stepper motor with the dual two-stage EHC. The whole dual-functional damper was modeled in Simulink. Based on the experimentally measured data, the parameters in the model have been estimated using the Optimization Toolbox in MATLAB. The experimental results and estimated simulation results fit very well. The electronics to realize this system has also been introduced. Two conclusions can be summarized as follows:

(1) Since stepper motors have more pole pairs than DC motors, dual-functional dampers using stepper motors inherently have higher damping density than those using DC motors, i.e., higher torque constant, higher induced voltage, and higher electrical damping coefficient. Also, due to the construction of stepper motors, the sinusoidal detent torque is a unique feature of stepper motors. However, in many applications, its influence can be neglected, or avoided during the design stage.

(2) The theoretical equation for the electrical damping coefficient of two-phase stepper motors has been derived and experimentally validated. The nonlinear relationship between the rotational speed and the electrical damping coefficient can be well revealed in the derived equation. The electrical damping coefficient of stepper motors is approximately linear at relatively low duty cycles (corresponding to high emulated resistances), or at low rotation speeds.

The tested two-phase hybrid stepper motor in this chapter has been integrated in the cavity of the moveable DSF. The feasibility of adjustable electrical damping and energy harvesting has been tested using Hardware-in-the-Loop simulations in Chapter 8.

7 Prototype

This chapter presents the constructional design of a parallel moveable Double-Skin Facade (DSF) system and the construction of a prototype with one full-scale moveable facade element. A general description of the parallel moveable facade damping system is given in Section 7.1. The constructional design of this system is developed together with Josef Gartner GmbH. The important components of the prototype are then described specifically in two parts. The first part (Section 7.2) introduces all the main components of the moveable facade element in detail, such as the spring system, the guide rail system, and the electronically controlled damper using a stepper motor. The modeling of these components is also introduced, which is the basis for the grey-box system identification in Chapter 8. The second part (Section 7.3) describes the components of the prototype test rig, such as the test rig actuator, test rig spring system, etc. These components are not part of the moveable facade system itself, but are essential for the implementation of the Hardware-in-the-Loop simulations in Chapter 8.

Copyright Statement

Parts of the research, text, and figures of this chapter are based on and have been published in the following articles:

- [161] Achim Bleicher, Thomas Schauer, Robert Jirasek, Tim Höltnke, Yangwen Zhang, Paul Marker, Wulf Wulff, Johannes Manfrecola, and Therese Schmidt. Hybride Konstruktionen an der BTU Cottbus-Senftenberg. *Bautechnik*, 98(12):907–920, 2021²⁴
- [124] Yangwen Zhang, Thomas Schauer, and Achim Bleicher. Optimized passive/semi-active vibration control using distributed-multiple tuned facade damping system in tall buildings. *Journal of Building Engineering*, 52:104416, 2022²⁵

²⁴Author's contribution: The author's contribution to [161] includes Conceptualization, Methodology, Software, Formal analysis, Investigation, Visualization. Copyright ©2021 Ernst & Sohn Verlag für Architektur und technische Wissenschaften GmbH & Co. KG, Berlin. Reprinted by permission from John Wiley and Sons and Copyright Clearance Center (license ID 5511571215355).

²⁵Author's contribution: The author's contribution to [124] includes Conceptualization, Methodology, Software, Formal analysis, Investigation, Writing - Original Draft, Writing - Review & Editing, Visualization. Copyright ©2020 Zhang, Schauer and Bleicher. Under Creative Commons CC BY 4.0 license (<https://creativecommons.org/licenses/by/4.0/>).

- [144] Thomas Schauer, Achim Bleicher, Yangwen Zhang, Wulf Wulff, and Laurenz Wernicke. *Schwingungsdämpfung und Energiegewinnung mit beweglichen Doppelfassaden: Entwurf, Optimierung und Validierung eines autarken verteilten semiaktiven Systems zur Reduktion Wind-induzierter Schwingungen bei schlanken Hochhäusern*. BBSR-Online-Publikation 08/2022, Bonn, April 2022
- [162] Yangwen Zhang, Wulf Wulff, Laurenz Wernicke, Michael Engelmann, Thomas Schauer, and Achim Bleicher. Experimental identification and verification of a moveable facade element for energy harvesting and vibration control. *Journal of Building Engineering*, 65:105712, 2023²⁶

Figure 7.1 is adapted from the figure published in [161].

Figure 7.5, Figure 7.6, Figure 7.8, and Figure 7.16 have been published in [144].

Figure 7.2, Figure 7.4, Figure 7.7, Figure 7.9, Figure 7.10, Figure 7.11, Figure 7.12, Figure 7.13, Figure 7.14, Figure 7.15, and Figure 7.17 have been published in [162].

Author's Contribution

In this chapter, the design and build-up of the prototype and test rig were done by team member Wulf Wulff of the BBSR project with the support of the industrial partner Josef Gartner GmbH [144]. Wulf Wulff developed a 3D model of the prototype and test rig using SolidWorks (Dassault Systèmes SOLIDWORKS Corp., USA). The author did the global and local static analysis for the built prototype and test rig. The load-bearing capacity and serviceability of the test rig have been verified. The fatigue analysis has also been done by the author to ensure its safety during the tests. The author has modeled the various components of the prototype. The Graphical User Interface (GUI) was developed by the author in Simulink. The position control of the test rig actuator was done by a master student supervised by the author and Dr. Thomas Schauer [163].

²⁶Author's contribution: The author's contribution to [162] includes Conceptualization, Data curation, Methodology, Software, Formal analysis, Investigation, Writing - Original Draft, Writing - Review & Editing, Validation, Visualization. Copyright ©2020 Zhang, Wulff, Wernicke, Engelmann, Schauer and Bleicher. Under Creative Commons CC BY 4.0 license (<https://creativecommons.org/licenses/by/4.0/>).

7.1. INTRODUCTION OF THE PROTOTYPE

7.1 INTRODUCTION OF THE PROTOTYPE

Together with Josef Gartner GmbH, the constructional design of a parallel moveable Double-Skin Facade (DSF) is proposed for the d-MTFD system based on the concept of the Open Cavity Facade (OCF), as shown in Figure 7.1 Section B-B.

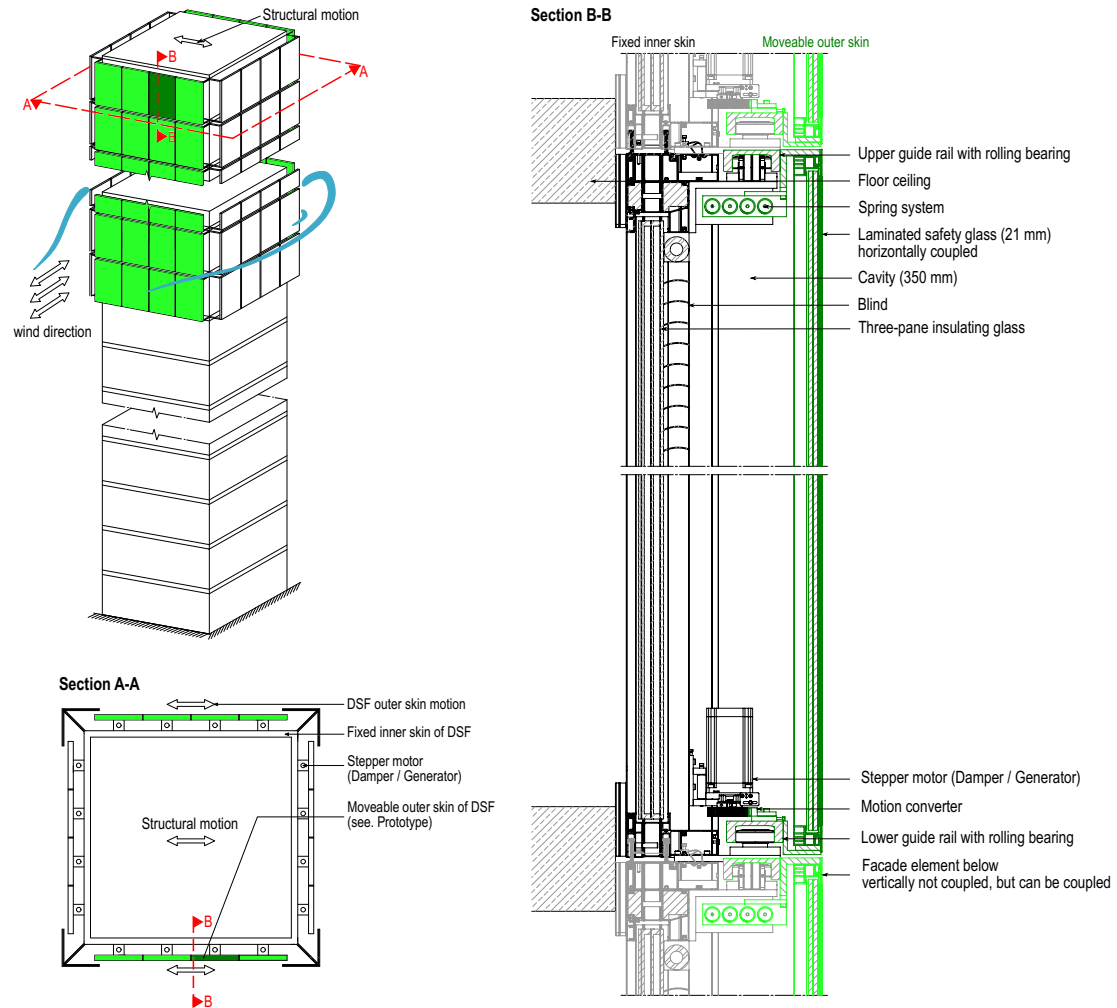


Figure 7.1: Proposed constructional design of the parallel moveable Double-Skin Facade (DSF).

The inner skin facade elements made of three-pane insulating glass are fixed to the building structure. The parallel moveable outer skin facade elements are made of 21 mm thick laminated safety glass (VSG 1010.4 – 10 mm glass + 10 mm glass + 4×0.38 mm folio) and are marked in green in Figure 7.1. The moveability is achieved by mounting the facade outer skin on the guide rail system consisting of upper/lower guide rails. The spring system connecting the facade outer skin and inner skin is tuned to the first natural frequency of the building structure. The stepper motor installed in the cavity functions as an adjustable damper and also as a

7.1. INTRODUCTION OF THE PROTOTYPE

generator. The blind is installed in the cavity by connecting it to the fixed inner skin to cover the relative movement of the outer skin during strong winds. This design reduces the disturbance of the moveable outer skin to the residents. The facade outer skin also provides protection to all the components located within the cavity. To ensure the high precision of the electrical dampers/generators, the future moveable DSF elements will be completely prefabricated in the factory and assembled on-site as a unit.

These moveable facade outer skins are installed at the upper stories of the buildings. All moveable facade elements are horizontally coupled to each other at each story. The wind-induced structural lateral vibration causes the front and rear parallel moveable facades on different floors to move synchronously, which in turn damps the primary structural motion (see Figure 7.1 Section A-A). The moveable facade elements can also be vertically coupled to reduce the number of the components, such as damper/generator units, motion converters, etc. The reverse motion of the moveable facade can also counteract the torsional vibrations of the structure. The vertically coupled system and torsional vibration control is not studied in this research.

Based on this design, a full-scale parallel moveable facade element ($2.8 \text{ m} \times 2.6 \text{ m}$) has been constructed for further experimental validation using Hardware-in-the-Loop (HiL) simulations [162, 164]. Figure 7.2 shows the rendering of the developed DSF prototype and test rig. Figure 7.3 shows the overview of the completed DSF prototype and test rig. Figure 7.4 shows the prototype on the actuated test rig during the HiL simulations. The Details and dimensions are illustrated in the technical drawings in Figure 7.5 to Figure 7.7.

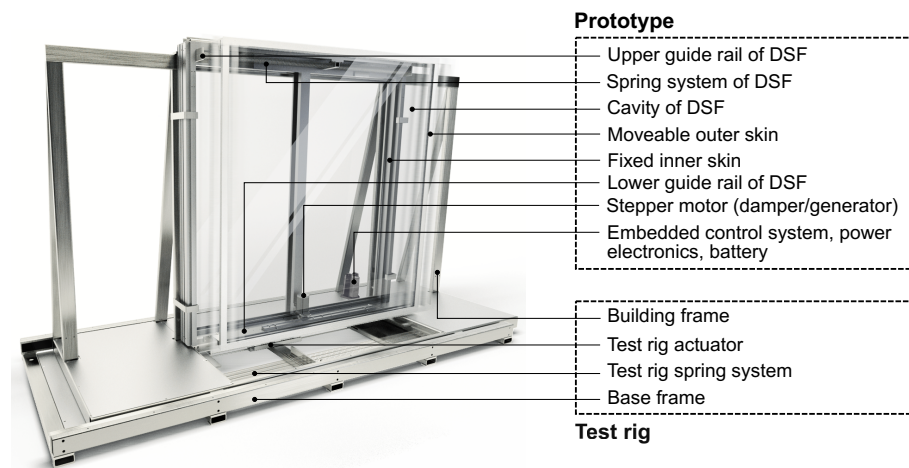


Figure 7.2: Rendering overview of prototype and test rig (Rendering by Therese Schmidt, Chair of Hybrid Structures - Structural Concrete, BTU Cottbus-Senftenberg).

This test rig consists of two main parts: the base frame, and the building frame, as illustrated in Figure 7.7. The building frame, representing the building structure, can slide on the base frame through the test rig guide rail system. The test rig actuator and the test rig spring system work together to drive the movement of the building frame, accurately reproducing the selected story motion of the benchmark high-rise building under wind excitation. The DSF prototype is

7.2. COMPONENTS OF THE PROTOTYPE



Figure 7.3: Overview of the completed prototype and test rig (Source: Ralf Schuster, BTU Cottbus-Senftenberg).

rigidly attached with the facade's inner skin to the building frame. The moveable outer skin is connected to the inner skin by using upper and lower guide rails and the DSF spring system. Based on this detailed design, the mass of the moveable facade outer skin with a guide rail system is expected to be around 640 kg. The maximum allowed parallel movement of the outer skin that can be achieved on the prototype is ± 500 mm. The hybrid stepper motor, together with the corresponding microcontroller, power electronics and the battery, functions as an adjustable electrical damper and energy harvester simultaneously.

The major components of the prototype and test rig are introduced in the following sections. The components that connect the moveable outer skin and fixed inner skin, i.e., the spring system, the guide rail system, and the electronically controlled damper, are highlighted, and their accurate modeling is essential for the following grey-box system identification in Chapter 8. Components of the test rig, such as the test rig actuator, the test rig spring system, etc., are also briefly introduced. They are also essential for the implementation of the HiL simulations.

7.2 COMPONENTS OF THE PROTOTYPE

7.2.1 Spring system

The spring system of the moveable DSF is as shown in Figure 7.8. The applied springs are specially manufactured by the company Gutekunst Formfedern GmbH, Germany. The stiffness

7.2. COMPONENTS OF THE PROTOTYPE

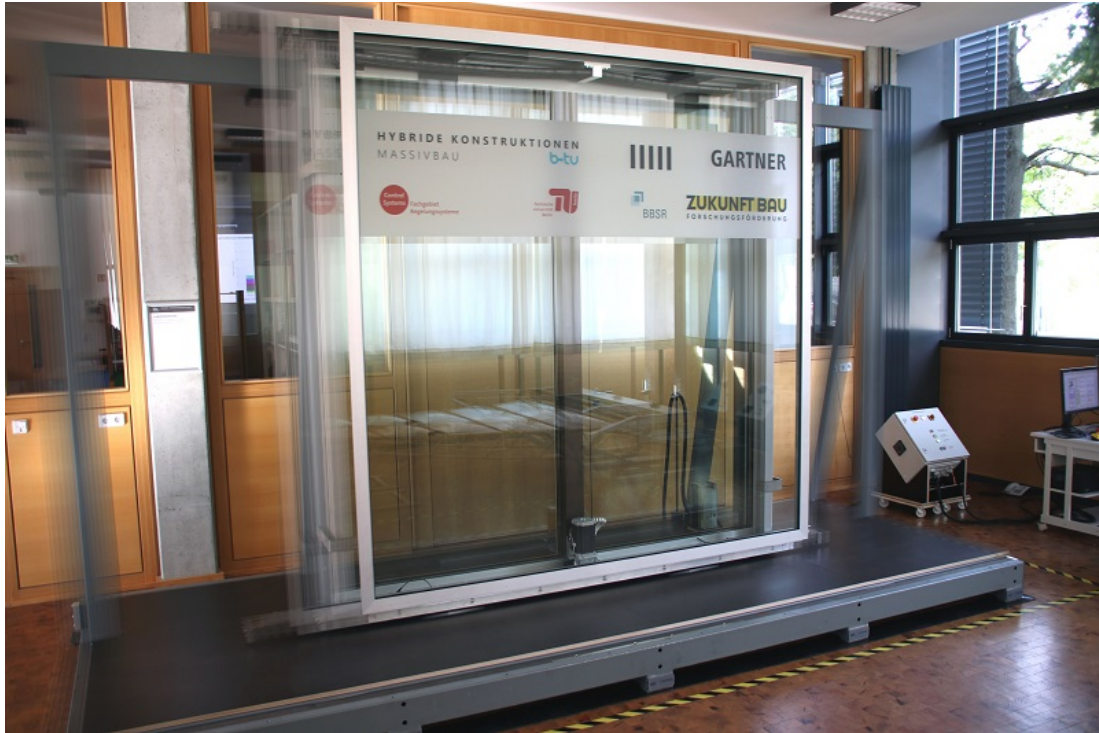


Figure 7.4: Prototype on the actuated test rig during an experimental investigation (Source: Thomas Schauer, Technische Universität Berlin).

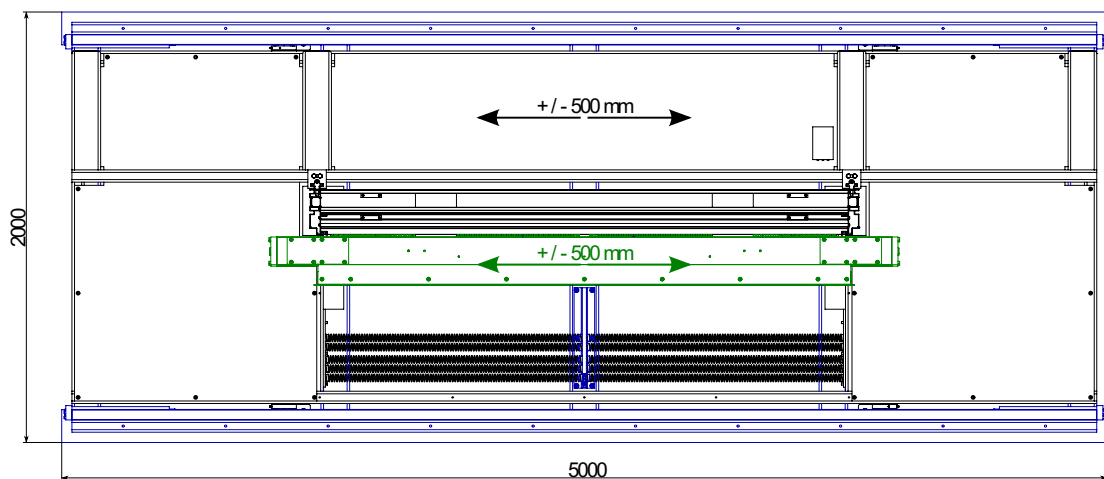


Figure 7.5: Top view of the prototype.

7.2. COMPONENTS OF THE PROTOTYPE

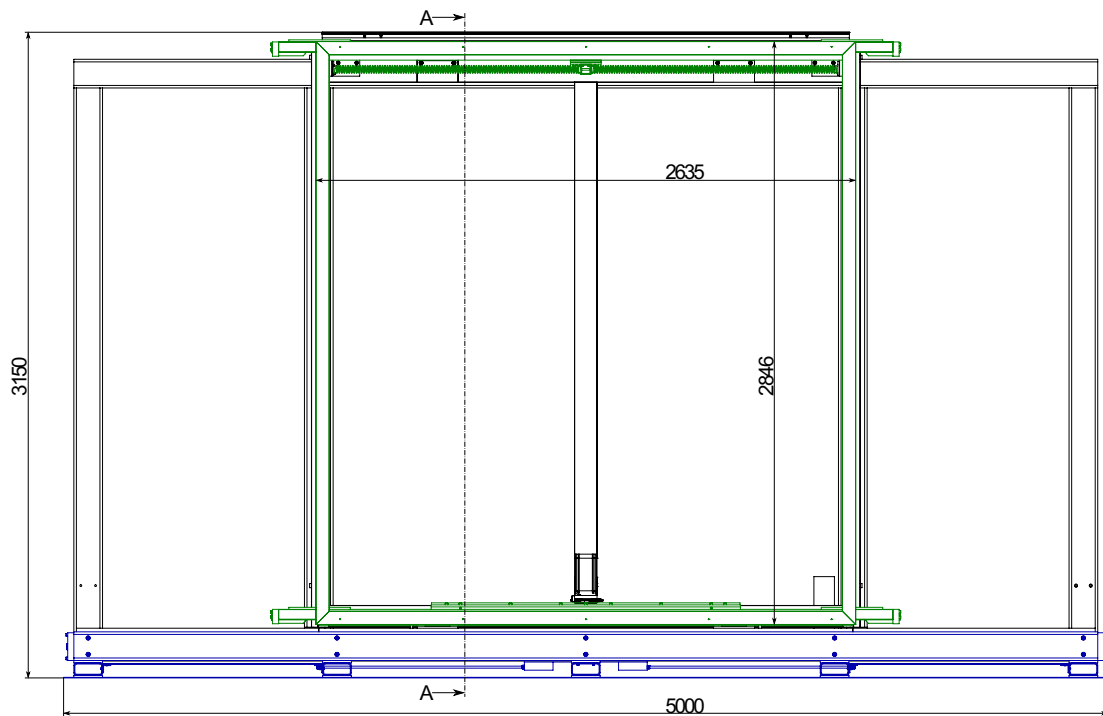


Figure 7.6: Front view of the prototype.

of each spring is approximately 81 N/mm. All the springs are fixed to the inner skin at one end (left/right side of the inner skin) and the moveable outer skin at the other end (middle of the outer skin). Eight springs are arranged to achieve the total stiffness \bar{k}_f of 644 N/m. This value of \bar{k}_f is intended to tune the moveable facade element (designed as approximately 640 kg) to the first natural frequency of the benchmark building. The spring system is modeled as a linear spring. The total stiffness \bar{k}_f is modeled as a constant. The final value of the stiffness \bar{k}_f is determined by system identification.

7.2.2 Guide rail system

As shown in Figure 7.9, the guide rail system consists of an upper guide rail and a lower guide rail with their corresponding rolling bearings (two for the upper guide rail, and two for the lower guide rail), which enables the parallel movement of the facade outer skin. The guide rails are made of precision U-profiles (Type PR 3 NbV, Winkel GmbH, Germany). Both the upper and lower guide rails are open downwards to avoid dirt accumulating on the running surface from affecting the moveability of the outer skin. Furthermore, the running surfaces of the guide rails were re-milled by the manufacturer to achieve a roughness of $R_z \leq 16$. R_z is the ten-point mean roughness, which is defined as the average value of the absolute values of the heights of five highest-profile peaks and the depths of five deepest alleys within the evaluation length. Heavy Duty Precision Bearings (Type PR 3.058, Winkel GmbH, Germany) (see Figure 7.10a) are used as the rolling bearings for the upper guide rail. Precision radial Bearings (Type PR 2.058, Winkel GmbH, Germany) (see Figure 7.10b) are used as the rolling bearings for the

7.2. COMPONENTS OF THE PROTOTYPE

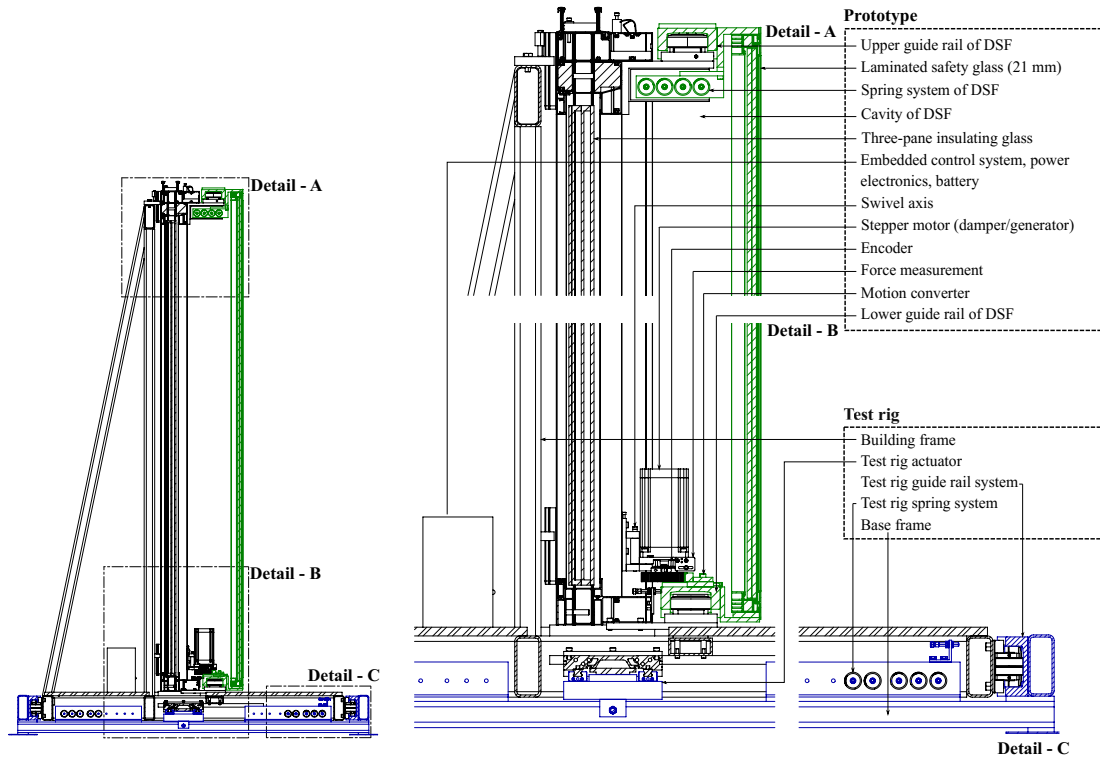


Figure 7.7: Side view of the prototype on the test rig with details (the moveable part of the prototype is marked in green).

lower guide rail. Rolling bearings ensure not only the moveability but also the load-bearing capacity.

Since Chapter 5 shows that lower friction gives better optimization results, the sealing friction of the rolling bearing can be enormously decreased by replacing the standard lip seals with gap seals. The applied rolling bearings were disassembled, degreased, and reassembled with new gap seals. The lubricating grease was also replaced by the non-resinous smooth-running oil (BALLISTOL GmbH, Germany) with good adhesion. After these modifications, the rolling friction decreased significantly.

The entire guide rail system can be described by a friction model, which is a function of the relative velocity of the moveable outer skin facade v_{fr} . The friction force of the guide rail system $\bar{f}_{fs,r}$ is the sum of the Stribeck friction $\bar{f}_{fs,Str}$, Coulomb friction $\bar{f}_{fs,Col}$ and viscous friction $\bar{f}_{fs,Vis}$ [165], as shown in Figure 7.11. Stribeck friction $\bar{f}_{fs,Str}$ is the negatively sloped and nonlinear friction-velocity characteristic occurring at low velocities, which is important for stick-slip (an alternation between sliding and sticking due to static friction). Coulomb friction $\bar{f}_{fs,Col}$ results in a force of constant magnitude $\bar{f}_{C,fs}$, acting in the direction opposite to motion. For the guide rail system, Coulomb friction is mainly caused by rolling friction. Viscous friction $\bar{f}_{fs,Vis}$ is a resistive force that is directly proportional to the relative velocity. The sum of the Coulomb and Stribeck friction near-zero velocity is often referred to as the breakaway friction $\bar{f}_{brk,fs}$. The friction of the guide rail system can be written as the following equations:

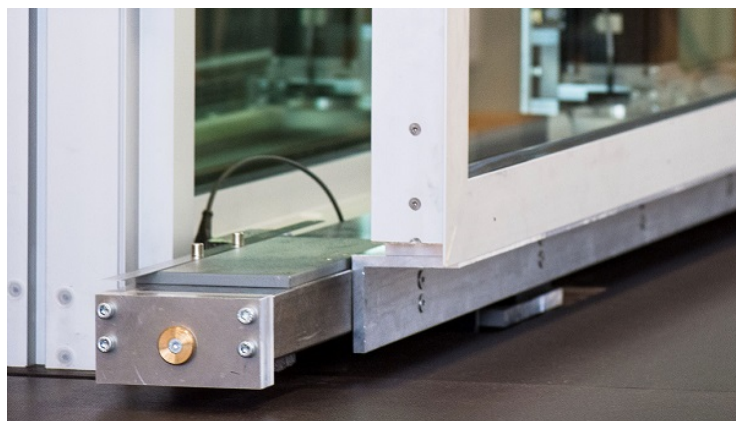
7.2. COMPONENTS OF THE PROTOTYPE



Figure 7.8: Spring system of the moveable DSF (Source: Ralf Schuster, BTU Cottbus-Senftenberg).



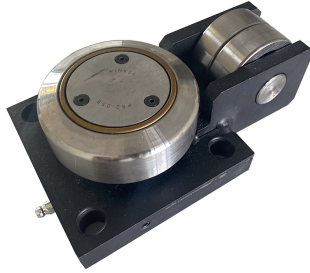
(a) Upper guide rail system



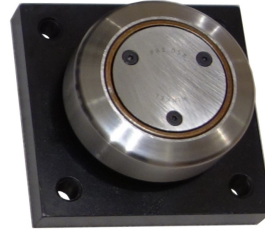
(b) Lower guide rail system

Figure 7.9: Upper/lower guide rail system (Source: Yangwen Zhang, BTU Cottbus-Senftenberg).

7.2. COMPONENTS OF THE PROTOTYPE



(a) Heavy Duty Precision Bearing (Type PR 3.058, Winkel GmbH, Germany)



(b) Precision radial Bearings (Type PR 2.058, Winkel GmbH, Germany)

Figure 7.10: Rolling bearings used in the prototype (Source: Yangwen Zhang, BTU Cottbus-Senftenberg).

$$\left\{ \begin{array}{l} \bar{f}_{fs,r} = \bar{f}_{fs,Str} + \bar{f}_{fs,Coul} + \bar{f}_{fs,Vis} \\ \bar{f}_{fs,Str} = \sqrt{2e} \cdot (\bar{f}_{brk,fs} - \bar{f}_{C,fs}) \cdot \exp\left(-\frac{v_{fr}}{v_{st}}\right)^2 \cdot \frac{v_{fr}}{v_{st}} \\ \bar{f}_{fs,Coul} = \bar{f}_{C,fs} \cdot \tanh\left(\frac{v_{fr}}{v_{Coul}}\right) \\ \bar{f}_{fs,Vis} = \bar{c}_{m,fs} \cdot v_{fr} \\ v_{st} = v_{brk} \cdot \sqrt{2} \\ v_{Coul} = v_{brk}/10, \end{array} \right. \quad (7.1)$$

where v_{brk} is the breakaway friction velocity, v_{st} is the Stribeck velocity threshold, v_{Coul} is the Coulomb velocity threshold. $\bar{c}_{m,fs}$ is the viscous friction coefficient of the whole guide rail system (upper and lower). e is Euler's number.

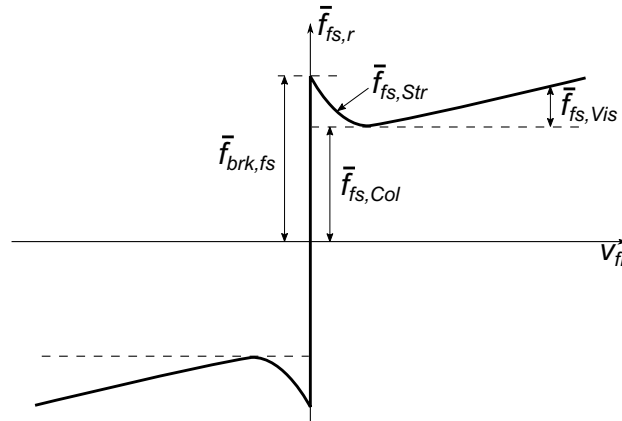


Figure 7.11: Friction model.

7.2.3 Electronically controlled damper

The electronically controlled damper is composed of the selected two-phase NEMA42 hybrid stepper motor (Type ML42HS3L4270, Moons' Electric Co., Ltd., China), as shown in Figure 7.12a, and the IVE-box mounted on the building frame, as shown in Figure 7.12b. The

7.2. COMPONENTS OF THE PROTOTYPE

selection of this stepper motor has been described in detail in Section 6.4. All other electronic components, such as the power electronics, the microcontroller, the sensors and the battery, are housed in the IVE-box described in the Section 6.5. A force sensor (Type KD60 100, ME-Meßsysteme GmbH, Germany) is also mounted to measure the motor reaction force. For semi-active control, it is not required. The installed force sensor is powered directly by the connected computer, and the measured motor reaction force is only used for system identification to further validate the semi-active control (see Section 8.1).

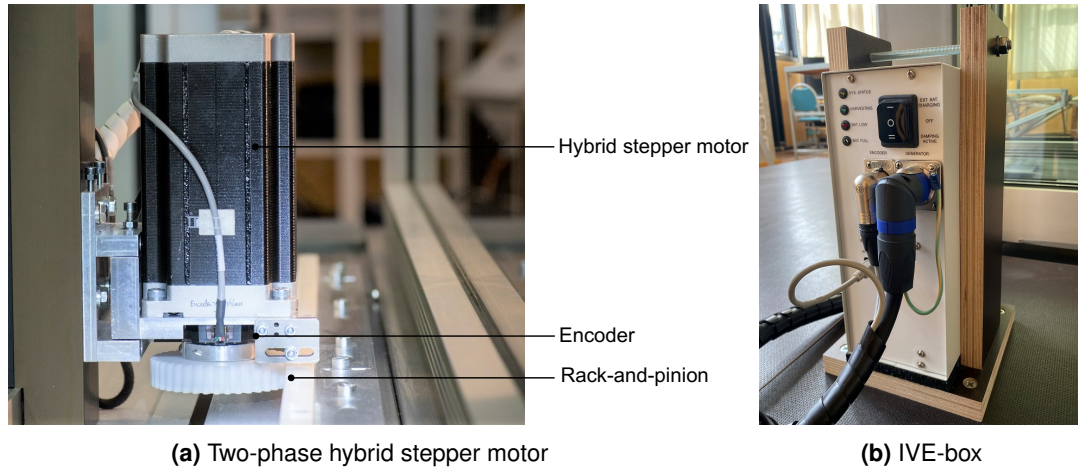


Figure 7.12: Electronically controlled damper consisting of selected two-phase stepper motor and the IVE-box mounted on the building frame ((a) Source: Ralf Schuster, BTU Cottbus-Senftenberg, (b) Source: Yangwen Zhang, BTU Cottbus-Senftenberg).

The equation of the motor reaction force \bar{f}_{sm} can be written as follows:

$$\left\{ \begin{array}{l} \bar{f}_{sm} = \bar{f}_{sm,e} + \bar{f}_{sm,det} + \bar{f}_{sm,ace} + \bar{f}_{sm,r} \\ \bar{f}_{sm,e} = C_e \cdot v_{fr} \\ \bar{f}_{sm,det} = \frac{T_d \cdot \sin(4N\theta)}{\alpha} \\ \bar{f}_{sm,ace} = \frac{J}{\alpha^2} \cdot \dot{v}_{fr} \\ \bar{f}_{sm,r} = \bar{f}_{sm,Str} + \bar{f}_{sm,Col} + \bar{f}_{sm,Vis} \end{array} \right. \quad (7.2)$$

where $\bar{f}_{sm,det}$ is caused by the detent torque in the stepper motor [166], which always exists even when the stepper motor winding is not energized. In our application, the effect of this term is mostly in the high-frequency region. Therefore, it has a very limited impact on the system. $\bar{f}_{sm,ace}$ is due to the acceleration of the motor rotor, in the steady state, this term doesn't exist. In our application, v_{fr} varies continuously, however, the rotor inertia J is quite small, so the effect of this term is also minor. $\bar{f}_{sm,r}$ refers to the mechanical frictions in the stepper motor or in the connection of the force sensor. The modeling of the friction term also includes Stribeck friction $\bar{f}_{sm,Str}$, Coulomb friction $\bar{f}_{sm,Col}$ and viscous friction $\bar{f}_{sm,Vis} = \bar{c}_{m,sm} \cdot v_{fr}$, which is equivalent as the guide rail system, as presented in Equation (7.1).

The electrical damping force $\bar{f}_{sm,e}$ is the most important term in our application, which makes adjustable damping possible. As described in the modeling of the two-phase stepper motor in

Chapter 6, the electrical damping coefficient c_e [N · s/m] for two-phase stepper motor can be derived in Equation (6.19). There is a nonlinear relationship between the rotational speed ω and the electrical damping coefficient c_e of the stepper motor. However, for small ω and small phase inductance L_a , the nonlinear influence can be neglected, the electrical damping coefficients for DC motor and stepper motor are approximately the same [107]. c_e can be adjusted by varying the connecting equivalent resistance R_l .

When operating in Discontinuous Current Mode (DCM), the buck-boost converter with a fixed duty cycle d is similar to a constant equivalent resistor, as seen in Equation (6.21). To maintain DCM, the Equation (6.20) needs to be satisfied. By varying the PWM signal, the equivalent resistance R_l can be varied, hence the electrical damping coefficient c_e can be adjusted. Meanwhile, the kinetic energy can be converted into electrical energy to power the embedded control system (microcontroller), the motion sensors, and to generate PWM signals. The remaining electrical energy is stored in the rechargeable battery. The power electronics to realize the adjustable damping and energy harvesting is shown in Figure 7.13. All the parameters of the selected stepper motor and EHC are listed in Table 7.1, which are further used for the identification of other parameters of the prototype.

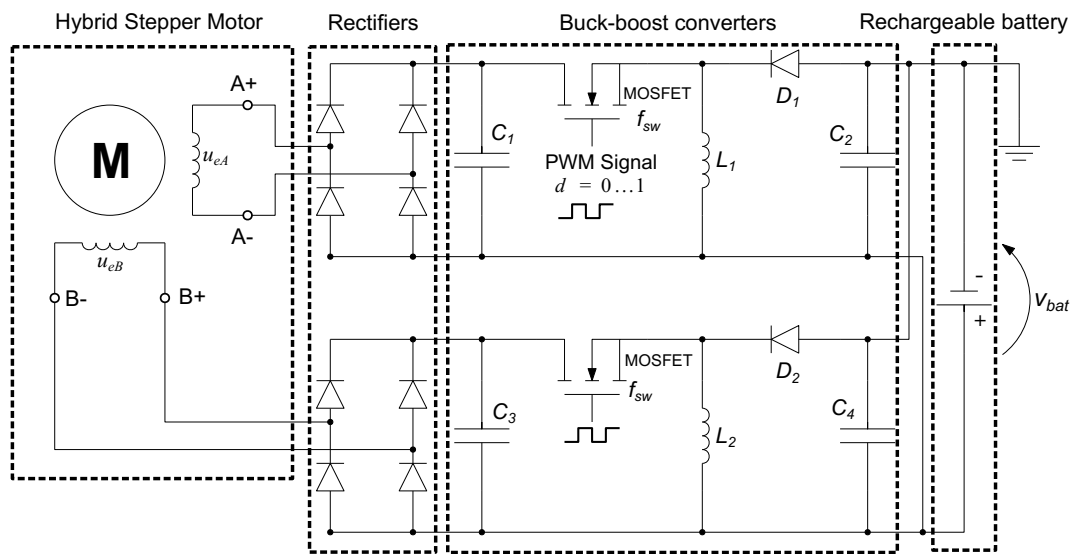


Figure 7.13: The schematic of EHC.

7.3 COMPONENTS OF THE TEST RIG

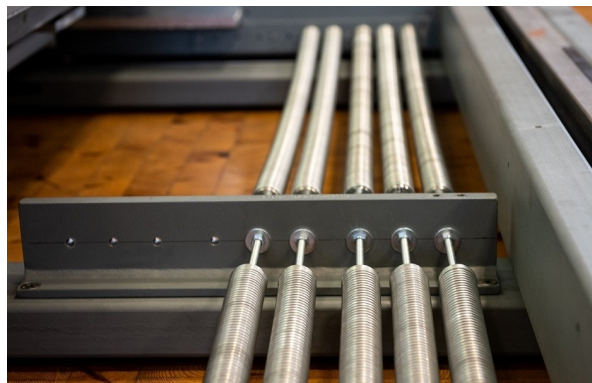
7.3.1 Spring system

As shown in Figure 7.14a, the test rig spring system between the base frame and the building frame consists of the same basic springs as used for the moveable DSF. With a symmetrical arrangement of 5 springs per side, a total of 20 springs are connected in parallel, resulting in a spring stiffness of 1620 N/m.

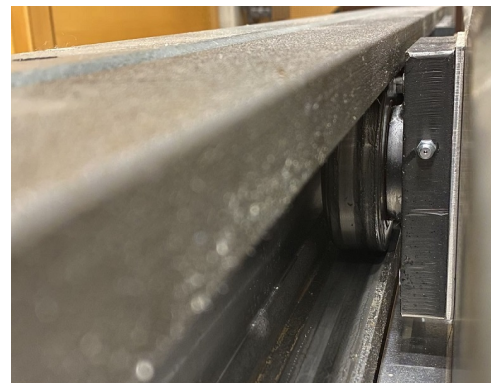
7.3. COMPONENTS OF THE TEST RIG

Table 7.1: Parameters of stepper motor and EHC.

Variable	Description	Identified Value	Data Sheet Value
α_s	Step angle	/	1.8°
N	Rotor teeth number	/	50
J	Stepper motor rotor inertia	/	0.00162 kg · m ²
T_d	Detent torque amplitude	/	0.8 Nm
k_t (k_e)	Torque constant (electrical constant)	8.38 Nm/A (V/(rad/s))	/
L_a	Stepper motor winding inductance	155 mH	/
R_a	Stepper motor winding resistance	/	4.2 Ω
C_1, C_2, C_3, C_4	Buck-boost converter capacitance	/	1 μF
L_c	Buck-boost converter inductance	/	22 μH
f_{sw}	MOSFET switching frequency	/	100 kHz
V_{bat}	Rechargeable batteries nominal voltage	/	24 V



(a) Test rig spring system



(b) Test rig guide rail system

Figure 7.14: Spring system and guide rail system of the test rig ((a) Source: Ralf Schuster, BTU Cottbus-Senftenberg, (b) Source: Yangwen Zhang, BTU Cottbus-Senftenberg).



Figure 7.15: Installed NiLAB controlled electric drive of type LM075P (Source: Ralf Schuster, BTU Cottbus-Senftenberg).

7.3.2 Guide rail system

The guide rail system of the test rig consists of the same guide rails and rolling bearings as for the upper guide rail system of the moveable facade element and differs only with regard to the installation position. The guide rail system of the test rig is as shown in Figure 7.14b. The guide rails on the base frame are open towards the inside so that the weight is supported by the large rollers. The small rollers are used for lateral guidance. The large and small rollers are as shown in Figure 7.10a.

7.3.3 Actuator system

The controlled electric drive (Type LM075P, NiLAB GmbH, Austria) is applied to reproduce the selected story motion of the benchmark building under wind excitation. The linear actuator is fixed to the building frame, and connected to the basis frame through two tie rods, as shown in Figure 7.15. The actuator is controlled by the servo drive (Type MBD12, NiLAB GmbH, Austria), which provides a corresponding CAN bus interface.

7.3.4 Electrical enclosure with electrical supply and safety sensor system

The electrical enclosure designed for the prototype's test rig fulfills several purposes. On the one hand, it ensures an electrically safe housing for all current-carrying components, in particular the servo drive, which is supplied with high-voltage current. Furthermore, the electrical enclosure serves as a control unit for switching the entire test rig on and off. It is also used as a monitoring unit for its safe operation. For this purpose, the electrical enclosure contains a relay logic that allows both immediate shutdown and safe restart after a fault has occurred.

7.3. COMPONENTS OF THE TEST RIG

During operation, the relay logic also monitors end position sensors for the building frame and the moveable facade element. The components of the electrical enclosure are as shown in Figure 7.16b.

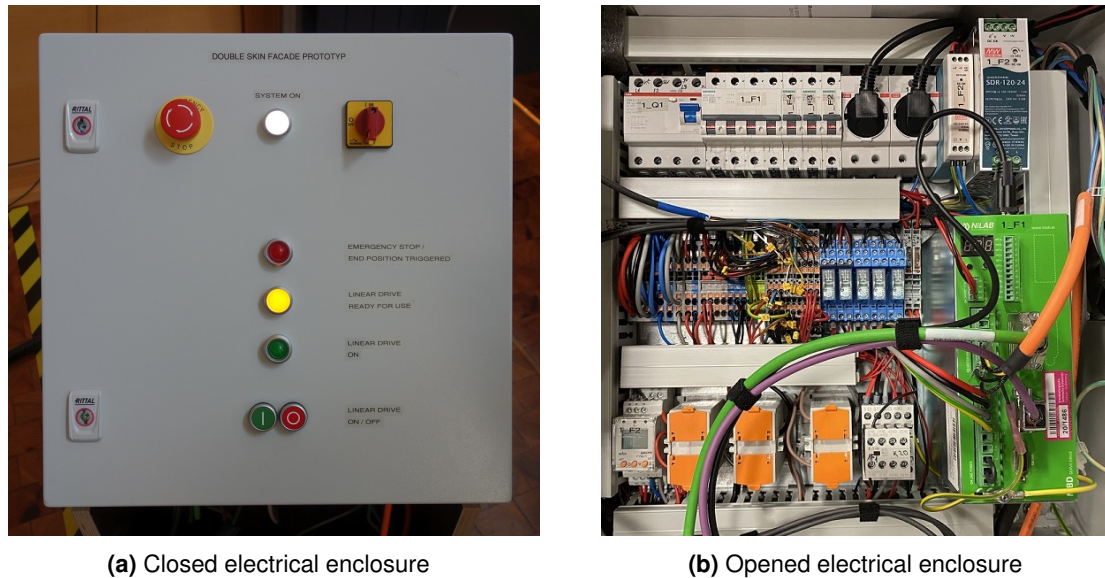


Figure 7.16: Electrical enclosure for the prototype test rig (Source: Yangwen Zhang, BTU Cottbus-Senftenberg).

7.3.5 Desktop PC with GUI for configuration, monitoring and HiL simulations

A desktop PC with Linux (Ubuntu 18.04) and MATLAB/Simulink 2020b is used for configuration and monitoring of the electrical damper as well as the HiL simulations. The 76-story high benchmark building is simulated in real-time with a sampling time of 8 ms. Through CAN bus using a USB-CAN converter (Kvaser Leaf Light HS v2, Kvaser, Schweden), the selected story motion of the benchmark building is transmitted as the target position to the control unit of the test rig actuator for position control. The measured internal signals of the electrical damper (e.g., current and voltage at the battery, relative displacement of the facade inner and outer skins, etc.), as well as the target position and measured position of the building frame, are displayed in real-time on the PC during the test. The entire Graphical User Interface (GUI) is created using the Simulink Dashboard Block Library, as shown in Figure 7.17.

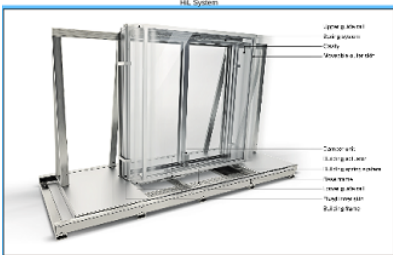
To ensure the real-time of the HiL simulations, the corresponding Simulink diagrams run in the so-called external mode. For this purpose, a real-time executable program in C++ code is generated from the Simulink diagram with a Linux target for the Mathworks Simulink Embedded Coder. Then, this program can be executed and supports the external mode of Simulink with XCP protocol for signal monitoring and online parameter updates. All measured values and interactions are logged automatically and can be viewed, evaluated, and exported in Simulink's Data Inspector after the completion of an experiment. For the acquisition of the force at the generator, the measured signal is analog-digital converted using a data acquisition card (MF634

7.3. COMPONENTS OF THE TEST RIG



(a) Desktop PC

Hardware in the Loop (HiL) Simulation for Vibration Control and Energy Harvesting



Excitation Control Panel

Position Inputs

Sinus Signal for Test

Wind data (HiL)

Sinus Signal for Test

Sinus Signal OFF

Sinus Signal ON

Sinus Signal Amplitude (mm):

0 20 40 60 80 100

Scale Parameter (Wind Excitation):

0 0.2 0.4 0.6 0.8 1

Optimized Passive DC

- 13.52% (Story 57)
- 13.59% (Story 62)
- 13.65% (Story 66)
- 14.89% (Story 71)
- 16.05% (Story 76)

Optimized Semi-Active DC_low

- DC_low (Story 57)
- DC_low (Story 62)
- DC_low (Story 66)
- DC_low (Story 71)
- DC_low (Story 76)

Wind Excitation (10m Wind Speed)

- 6 m/s
- 8 m/s
- 10 m/s
- 12 m/s
- 13.5 m/s

Optimized Semi-Active DC_high

- DC_high (Story 57)
- DC_high (Story 62)
- DC_high (Story 66)
- DC_high (Story 71)
- DC_high (Story 76)

NiLAB Control Panel

Operation Mode

- Homing Mode (6)
- Interpolated Position Mode (7)

Control Word

- Shutdown (0x06 = 06h)
- Switch On (0x07 = 07h)
- Enable Operation (0x0F = 13h)
- Activate HM & IP Mode (0x1F = 31h)
- Reset Fault (0x8F = 143h)
- HALT (0x11F = 287h)

Control Methods (Simulation)

Control Methods

- VBG Semi-Active Control
- Passive Control

IVE Control Panel

Reset Zero Position: Off On

Discharging: Off On

Control Methods: Passive Semi-Active

Passive Damping Duty Cycle (%)

0 5 10 15 20

Semi-Active Damping Duty Cycle (%)

Low 0 5 10 15 20

High 0 5 10 15 20

Energy Harvesting Lamp:

IVE Current (A)

0.1 0.05 0.15 0.2 0.25 0.3

(b) GUI in Simulink

Figure 7.17: Desktop PC and Simulink GUI for configuration of the electronically controlled damper and testing of the prototype ((a) Source: Ralf Schuster, BTU Cottbus-Senftenberg).

7.4. SUMMARY

PCI Express, HUMUSOFT s.r.o., Czech Republic). The embedded control system of the controlled damper can receive/send signals from/to Simulink via USB. The corresponding block in Simulink is programmed in C++.

7.4 SUMMARY

In this chapter, the prototype of the moveable DSF with one full-scale moveable facade element is presented from the proposal of the constructional design to the final completion. This moveable DSF is placed on the test rig for experimental tests. All the main components of the test rig are introduced. The components that realize the moveable connection between the facade outer skin and the fixed inner skin, i.e. the spring system, the guide rail system, and the adjustable electrical damper using a stepper motor, are introduced in particular. The modeling of these components is described in detail. A precise mathematical description of these components is essential for the successful grey-box system identification conducted in Chapter 8.

7.4. SUMMARY

8 Experimental verification using Hardware-in-the-Loop simulations

In this chapter, Hardware-in-the-loop (HiL) simulations were performed to validate the prototype and prove the feasibility of the dual-functional damper using a stepper motor for energy harvesting and semi-active vibration control. A virtual moveable facade element is removed from the simulated d-MTFD system and replaced by the hardware, i.e., the prototype described in Chapter 7. Actuators and sensors enable communication between the simulation part and the hardware part. The actuator located between the base frame and the building frame of the test rig is applied to reproduce the movement of selected floors on the building frame. The interaction force between the moveable facade element and the building's main structure is estimated based on the measured force using the force sensor and fed back to the simulation. To precisely conduct the HiL simulations, the grey-box system identification is applied to estimate the parameters of the prototype (see Section 8.1). Then, the simulation part needs to be updated with the estimated parameters to ensure that the same connections as the prototype are used. The whole passive/semi-active d-MTFD system was optimized again using the multi-objective GA (see Section 8.2). The optimized parameters of the selected case were configured in the simulation part and the hardware part (see Section 8.3). HiL simulations are performed when the prototype is connected to five different selected floors under across-wind excitation with a return period of 10 years. The experimental data were analyzed in Section 8.4. The following questions will be discussed and answered:

- Are the facade relative displacements measured at the prototype consistent with the simulated facade relative displacements of other moveable facade elements at the same selected story? How good is their fitness value?
- Can the required electrical damping force be generated by the stepper motor?
- Is it possible to generate sufficient energy during semi-active damping to ensure the self-sufficient operation of the system?

Copyright Statement

Parts of the research, text, and figures of this chapter are based on and have been/will be published in the following articles:

- [144] Thomas Schauer, Achim Bleicher, Yangwen Zhang, Wulf Wulff, and Laurenz Wernicke. *Schwingungsdämpfung und Energiegewinnung mit beweglichen Doppelfassaden: Entwurf, Optimierung und Validierung eines autarken verteilten semiaktiven Systems zur Reduktion Wind-induzierter Schwingungen bei schlanken Hochhäusern*. BBSR-Online-Publikation 08/2022, Bonn, April 2022
- [162] Yangwen Zhang, Wulf Wulff, Laurenz Wernicke, Michael Engelmann, Thomas Schauer, and Achim Bleicher. Experimental identification and verification of a moveable facade element for energy harvesting and vibration control. *Journal of Building Engineering*, 65:105712, 2023²⁷

All figures in this chapter have been published in [162].

²⁷Author's contribution: The author's contribution to [162] includes Conceptualization, Data curation, Methodology, Software, Formal analysis, Investigation, Writing - Original Draft, Writing - Review & Editing, Validation, Visualization. Copyright ©2020 Zhang, Wulff, Wernicke, Engelmann, Schauer and Bleicher. Under Creative Commons CC BY 4.0 license (<https://creativecommons.org/licenses/by/4.0/>).

8.1. SYSTEM IDENTIFICATION

8.1 SYSTEM IDENTIFICATION

Since the mathematical model of the system has been developed, grey-box system identification is used to identify the system. The parameters of the stepper motor, listed in Table 7.1, are used in the model to further identify other parameters of the prototype, i.e., friction, mass, and spring stiffness. There are two stages to identify the defined parameters of the prototype, as shown in Figure 8.1. The input/output data for both stages of system identification are collected in a single experiment in which a constant electrical damping coefficient is realized by the stepper motor with a fixed duty cycle $d = 11.5\%$. The input signal x_{bf} is taken from the top floor vibration of a benchmark building installed with the d-MTFD system (using assumed friction) under across-wind excitation.

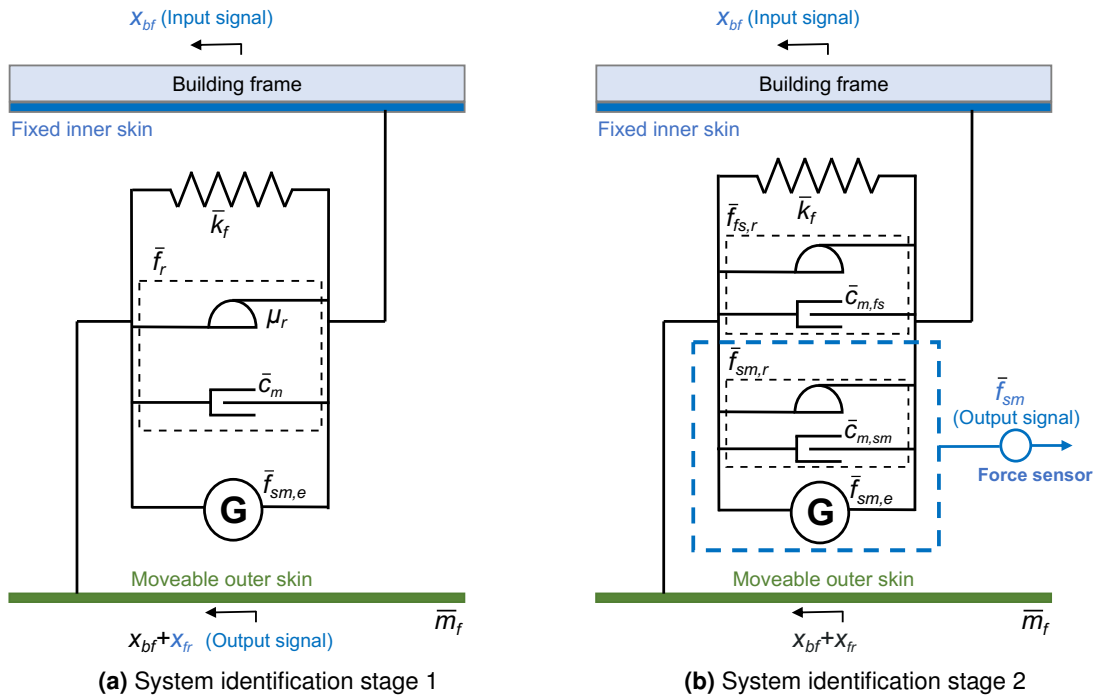


Figure 8.1: Stages for system identification.

8.1.1 Stage 1

The frictions caused by the guide rail system and the stepper motor are lumped as total friction between the fixed inner skin and the moveable outer skin of the prototype in stage 1. The equations of total friction are expressed as follows:

$$\left\{ \begin{array}{l} \bar{f}_r = \bar{f}_{fs,r} + \bar{f}_{sm,r} = \bar{f}_{r,Str} + \bar{f}_{r,Col} + \bar{f}_{r,Vis} \\ \bar{f}_{r,Str} = \sqrt{2e} \cdot (\bar{f}_{brk} - \bar{f}_C) \cdot \exp\left(-\frac{v_{fr}}{v_{st}}\right)^2 \cdot \frac{v_{fr}}{v_{st}} \\ \bar{f}_{r,Col} = \bar{f}_C \cdot \tanh\left(\frac{v_{fr}}{v_{Coul}}\right) = \mu_r \bar{m}_f g \cdot \tanh\left(\frac{v_{fr}}{v_{Coul}}\right) \\ \bar{f}_{r,Vis} = \bar{c}_m \cdot v_{fr} \end{array} \right. , \quad (8.1)$$

where $\bar{c}_m = \bar{c}_{m,fs} + \bar{c}_{m,sm}$ is the sum the of viscous friction coefficient of the guide rail system and stepper motor; $\bar{f}_C = \bar{f}_{C,fs} + \bar{f}_{C,sm} = \mu_r \bar{m}_f g$ is the sum of Coulomb friction magnitude, where μ_r is the equivalent friction coefficient, \bar{m}_f is the facade outer skin mass, and g is the gravitational acceleration; $\bar{f}_{brk} = \bar{f}_{brk,fs} + \bar{f}_{brk,sm}$ is the sum of breakaway friction. The relationship between v_{brk} and v_{st} , v_{Coul} are defined in Equation (7.1).

In stage 1, the building facade displacement x_{bf} is measured by the test rig actuator and used as the input signal of the system for the estimation. The relative displacement of the moveable facade outer skin x_{fr} is measured by the encoder and used as the output signal of the system, as shown in Figure 8.1a. The whole system is built in Simulink. The mass of the facade outer skin \bar{m}_f , the stiffness of the spring system \bar{k}_f , the total Coulomb friction magnitude \bar{f}_C , the total Breakaway friction \bar{f}_{brk} and the breakaway friction velocity v_{brk} will be estimated by using the Parameter Estimator APP from Simulink Design Optimization. The estimated parameters are listed in Table 8.1. The equivalent friction coefficient μ_r can be then calculated as 0.0022. The comparison of the measured and estimated facade outer skin relative displacement is plotted in Figure 8.2. The NRMSE (Normalized Root Mean Squared Error) fitness value of the estimated model is calculated as 92.1%

Table 8.1: Estimated parameters of stage 1.

Parameters	Description	Value
\bar{m}_f	Facade outer skin mass	611.61 kg
\bar{k}_f	Stiffness of the spring system	645.91 N/m
\bar{c}_m	Total viscous friction	46.00 N · s/m
\bar{f}_C^\dagger	Total Coulomb friction magnitude	13.09 N
μ_r^\dagger	Equivalent friction coefficient	0.0022
\bar{f}_{brk}^\dagger	Total breakaway friction	17.99 N
v_{brk}	Breakaway friction velocity	0.051 m/s
v_{st}^\dagger	Stribeck velocity threshold	0.072 m/s
v_{Coul}^\dagger	Coulomb velocity threshold	0.005 m/s

[†] parameters being further used in the friction modeling of the d-MTFD system (see Equation (8.2)).

8.1.2 Stage 2

In stage 2, the interaction force measured by the force sensor connected to the stepper motor \bar{f}_{sm} is used as the output signal of the system, as shown in Figure 8.1b. The early estimated parameters from stage 1 are further implemented in stage 2. Therefore, the sum of the Coulomb friction and viscous friction stay unchanged. Based on the measured stepper motor reaction force, the corresponding proportions of friction caused by the guide rail system and stepper motor can be determined. The Coulomb friction inside the stepper motor $\bar{f}_{C,sm}$, the breakaway friction of the stepper motor $\bar{f}_{brk,sm}$ and the viscous friction coefficient of the stepper motor $\bar{c}_{m,sm}$ are identified by using the Parameter Estimator APP from Simulink Design Optimization. The

8.2. SEMI-ACTIVE D-MTFD SYSTEM OPTIMIZATION BASED ON IDENTIFIED PROTOTYPE

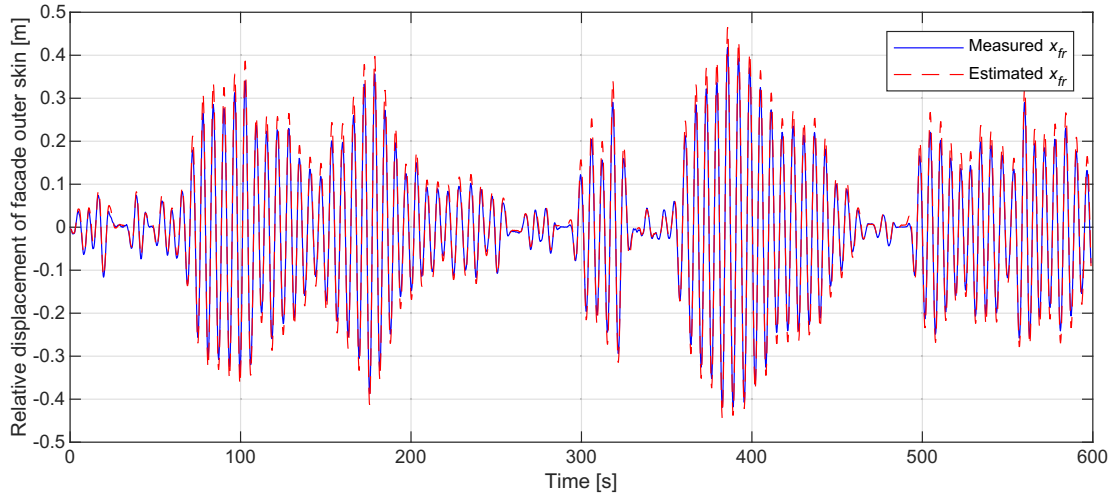


Figure 8.2: Measured/estimated relative displacement of facade outer skin.

estimated parameters are listed in Table 8.2. The comparison of the measured and estimated stepper motor interaction force is plotted in Figure 8.3. The NRMSE (Normalized Root Mean Squared Error) fitness value of the estimated model is calculated as 82.55%.

Table 8.2: Estimated parameters of stage 2.

Parameter	Description	Value
$\bar{C}_{m,fs}$	Guide rail system viscous friction coefficient	34.00 N · s/m
$\bar{C}_{m,sm}$	Stepper motor viscous friction coefficient	12.00 N · s/m
$\bar{f}_{C,fs}$	Guide rail system Coulomb friction	6.25 N
$\bar{f}_{C,sm}$	Stepper motor Coulomb friction	6.84 N
$\bar{f}_{brk,fs}$	Guide rail system breakaway friction	11.15 N
$\bar{f}_{brk,sm}$	Stepper motor breakaway friction	6.84 N

8.2 SEMI-ACTIVE D-MTFD SYSTEM OPTIMIZATION BASED ON IDENTIFIED PROTOTYPE

Based on the newly identified parameters, our proposed d-MTFD system installed on the 76-story high benchmark building can be updated. The identified friction model of the prototype, including Stribeck friction, Coulomb friction, and viscous friction, was integrated into the modeling of the friction for each story with the parallel moveable facade. Viscous friction is a viscous force. The viscous coefficient can be considered as the mechanical damping coefficient due to the friction and considered together with the electrical damping coefficient. Therefore, the facade connection friction $f_{r,i}$ concludes only the Stribeck friction and Coulomb friction, whose equation can be written as below:

8.2. SEMI-ACTIVE D-MTFD SYSTEM OPTIMIZATION BASED ON IDENTIFIED PROTOTYPE

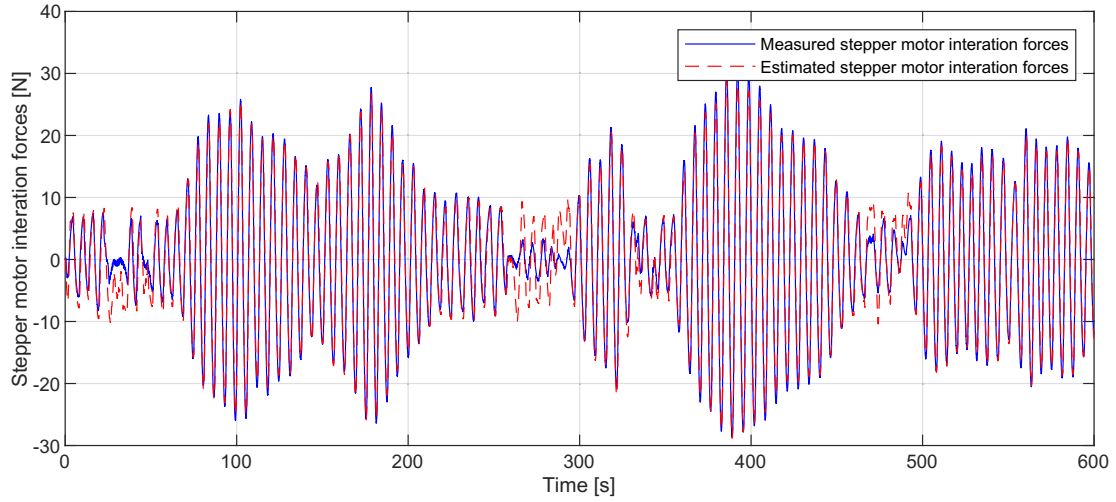


Figure 8.3: Measured/estimated stepper motor interaction force.

$$\begin{cases} f_{r,i} = f_{Str,i} + f_{Col,i} \\ f_{Col,i} = \mu_r m_{f,i} g \cdot \tanh\left(\frac{v_{fr,i}}{V_{Coul}}\right) \\ f_{Str,i} = \sqrt{2e} \cdot \left(\frac{\bar{f}_{brk}}{\bar{f}_C} - 1\right) \cdot \mu_r m_{f,i} g \cdot \exp\left(-\frac{v_{fr,i}}{V_{st}}\right)^2 \cdot \frac{v_{fr,i}}{V_{st}} \end{cases} \quad i = (1, 2, \dots, n_f), \quad (8.2)$$

where $v_{fr,i}$ is the relative velocity of the parallel moveable facade with respect to the connected floor, where $i = 1, 2, \dots, n_f$ is used to distinguish parallel moveable facade installed on different floors. The upper $n_f = 20$ stories are assumed to be installed with moveable facade element. $i = 20$ corresponds to the top floor. The activated damping mass $m_{f,i}$ is assumed as 30 tons per story. The corresponding facade connection stiffness $k_{f,i}$ can be obtained by tuning the damping mass to the first natural frequency of the benchmark building, namely $\omega_1 = 1.0053$ rad/s [119]. Based on the identified moveable facade outer skin mass \bar{m}_f and the identified stiffness of the spring system \bar{k}_f , the achieved tuned natural frequency $\bar{\omega}_1$ can be calculated as 1.0276 rad/s, which has a difference of 2.2%. As a remark, the friction, caused by the along-wind force described in Chapter 4, cannot be experimentally realized in the prototype, therefore, it is not considered in the simulation.

The facade damping coefficient $c_{f,i}$ consists of the mechanical damping coefficient $c_{m,i}$ due to the viscous friction, and the adjustable electrical damping coefficient $c_{e,i}$ by using stepper motor as electronically controlled damper. The damping coefficient can be calculated by the corresponding damping ratios $\xi_{f,i}$, $\xi_{e,i}$, and $\xi_{m,i}$. The equation is written as follows:

$$\begin{aligned} c_{f,i} &= c_{m,i} + c_{e,i} \\ &= 2 \cdot \xi_{f,i} \cdot \sqrt{m_{f,i} \cdot k_{f,i}} \quad i = (1, 2, \dots, n_f) \\ &= 2 \cdot (\xi_{m,i} + \xi_{e,i}) \cdot \omega_1 \cdot m_{f,i} \end{aligned} \quad (8.3)$$

By using semi-active control, the facade damping coefficient $c_{f,i}$ switches between $c_{f,i}^{\min}$ and $c_{f,i}^{\max}$. According to Equations (6.25) and (6.28), the electrical damping coefficient of the stepper motor is adjustable by varying the duty circle d in the connected EHC, which makes the semi-

8.2. SEMI-ACTIVE D-MTFD SYSTEM OPTIMIZATION BASED ON IDENTIFIED PROTOTYPE

active d-MTFD system possible. The on-off Velocity Based Ground-hook (VBG) control is used as the semi-active control algorithm for the experimental tests, which can be summarized in the following equations:

$$\begin{aligned} \text{if } \dot{x}_j \cdot v_{fr,i} \geq 0, \text{ then } c_{f,i} &= c_{f,i}^{\min} = 2 \cdot \xi_{f,i}^{\min} \cdot \omega_1 \cdot m_{f,i} \\ \text{if } \dot{x}_j \cdot v_{fr,i} < 0, \text{ then } c_{f,i} &= c_{f,i}^{\max} = 2 \cdot \xi_{f,i}^{\max} \cdot \omega_1 \cdot m_{f,i} \end{aligned} \quad (8.4)$$

where \dot{x}_j is the velocity at the story j of the 76-story benchmark building connected with the moveable facade i ($j = 56 + i$).

The damping ratio is a dimensionless parameter. The facade damping ratios were optimized using multi-objective Genetic Algorithms (GA) from the Optimization Toolbox of MATLAB (The MathWorks, Inc., USA). Two objectives are defined to optimize the d-MTFD system. The first objective J_1 is to reduce the peak acceleration of the top floor. The second objective J_2 is to reduce the peak relative displacement of all the moveable facades at the upper n_f stories. The details of the multi-objective optimization are described in Chapter 5. The optimized results are presented in the form of a Pareto front, as shown in Figure 8.4.

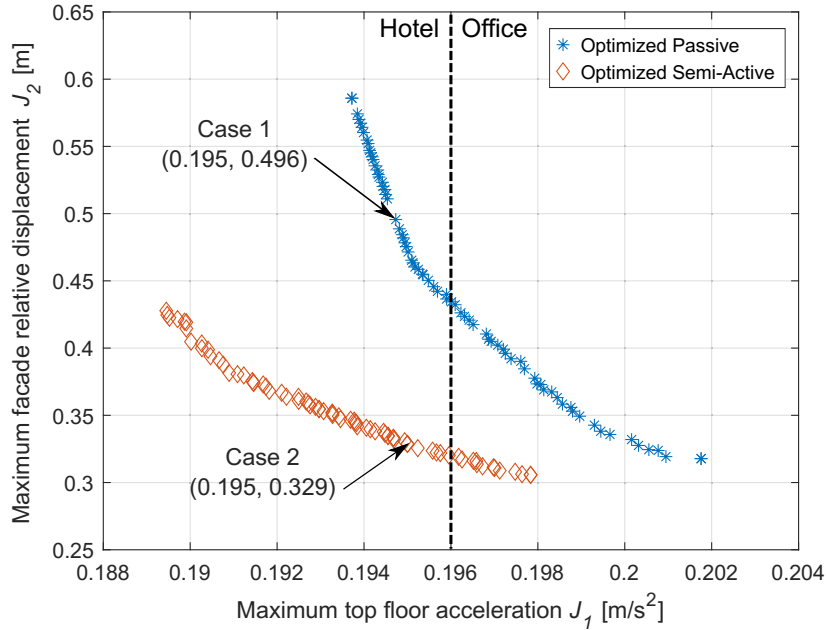


Figure 8.4: Pareto front for the optimized passive and semi-active system.

Two optimized cases are selected for the passive and semi-active system, as marked in Figure 8.4. Since a larger facade movement leads to better structural vibration mitigation, Case 1 is selected for the passive system with a maximum facade relative displacement of 0.496 m, which almost reaches the design limit (± 0.5 m). The maximum top floor acceleration for Case 1 is 0.195 m/s^2 , which has been reduced by about 30% compared with the uncontrolled benchmark building (0.269 m/s^2). Case 2 is selected for the semi-active control, which achieves the same maximum top floor acceleration as Case 1. Both cases have achieved the serviceability requirement for the use of hotel ($0.147 - 0.196 \text{ m/s}^2$) [1]. With semi-active control, the max-

imum facade relative displacement can be significantly reduced by 34% to 0.330 m. The use of semi-active control is limited in further reducing structural vibrations compared with the optimized passive control. However, the facade outer skin motion can be significantly reduced by using semi-active control.

The selected semi-active Case 2 is further investigated using Hardware-in-the-Loop simulation in the following Section 8.3.

8.3 HARDWARE-IN-THE-LOOP (HIL) SIMULATION

Hardware-in-the-Loop (HiL) simulations are applied to prove the feasibility of the semi-active control and the energy harvesting performance of the d-MTFD system under across-wind excitation. As an example, the previously selected Case 2 using semi-active control is further investigated. For Case 2, the upper 20 stories ($n_f = 20$), i.e., from 57th story to 76th story of the benchmark building, are assumed to be installed with the proposed moveable facade elements. To implement in the HiL simulation, the selected Case 2 needs to be rebuilt in the simulation part and the hardware part. The simulation part is the virtual 76-story benchmark building installed with the d-MTFD system under across-wind excitation, with one piece of missing moveable facade element on the selected story j . This missing moveable facade element is physically realized as our prototype representing the hardware part of the HiL simulation.

The diagram of the HiL simulation is illustrated in Figure 8.5. Actuators and sensors enable communication between the simulation part and the hardware part. The test rig actuator located between the base frame and the building frame is used to reproduce the movement x_j of the selected floor $j = (57, 58, \dots, 76)$ on the building frame. The target position of the selected floor x_j generated from the simulation part and the measured position x_{bf} from the hardware part are the input variables for the position controller to ensure real-time generation of the selected floor motion under wind-excitation. Since the position control has a sufficiently high bandwidth, the building frame can follow the target position x_j without significant delay. The encoder connected with the stepper motor measures the relative displacement $x_{fr,i}$ of the facade outer skin, where $i = j - 76 + n_f = j - 56$. A force sensor measures the force of the stepper motor \bar{f}_{sm} . The interaction force \bar{f}_{int} between the prototype and the virtual benchmark building can be calculated based on the measured data and the identified parameters, as shown in the following equation.

$$\bar{f}_{int} = \bar{f}_{sm} + \bar{k}_f \cdot x_{fr,i} + \bar{f}_{ts,r}(v_{fr,i}), \quad (8.5)$$

where the facade relative displacement $x_{fr,i}$ and the facade relative velocity $v_{fr,i} = \dot{x}_{fr,i}$ are obtained from the measured data of the encoder.

According to the selected story j for the prototype, the minimum and maximum damping ratios determined in the chosen Case 2 need to be set on the adjustable electrical damper. The minimum and total facade damping coefficient can be first calculated depending on the mass \bar{m}_f and the spring stiffness \bar{k}_f of the prototype, then the minimum and maximum electrical damping coefficient can be calculated by subtracting the identified total mechanical viscous damping coefficient \bar{c}_m . The equation is shown as follows:

8.3. HARDWARE-IN-THE-LOOP (HiL) SIMULATION

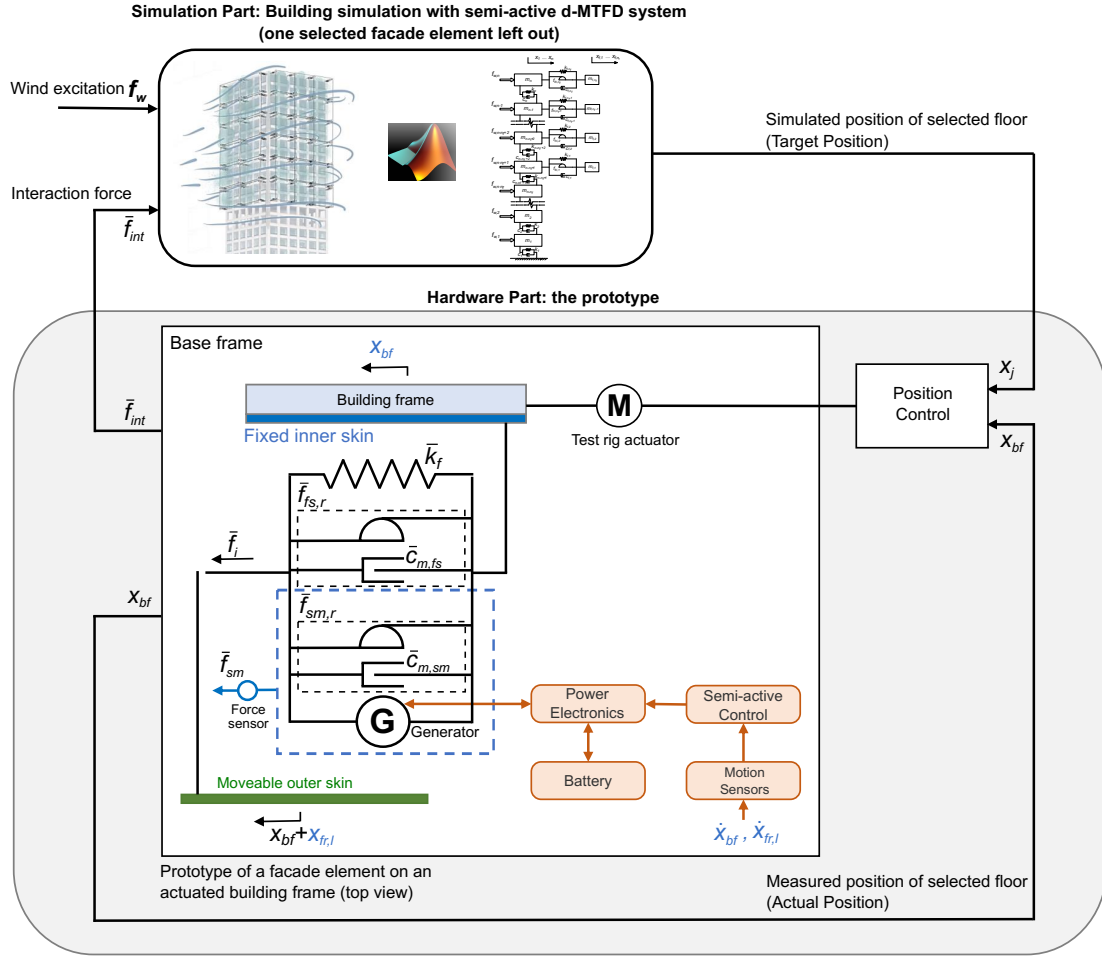


Figure 8.5: Hardware-in-the-Loop (HiL) simulation.

$$\begin{cases} \bar{c}_{e,i}^{\min} = 2 \cdot \xi_{f,i}^{\min} \cdot \bar{\omega}_1 \cdot \bar{m}_f - \bar{c}_m \\ \bar{c}_{e,i}^{\max} = 2 \cdot \xi_{f,i}^{\max} \cdot \bar{\omega}_1 \cdot \bar{m}_f - \bar{c}_m \end{cases} \quad (8.6)$$

The corresponding duty cycles d_i^{\min} and d_i^{\max} of the PWM signal to generate $\bar{c}_{e,i}^{\min}$ and $\bar{c}_{e,i}^{\max}$ can be calculated based on the derived Equations (6.25) to (6.28) from Chapter 6.

During the HiL simulation, the current and voltage at the input of the battery are measured by the applied INA226 current voltage sensor to determine the harvested power. The average harvested power P_h can then be calculated. The energy harvesting efficiency η_{le} of the power electronics can be calculated as follows:

$$\eta_{le} = \frac{P_h}{P_{sm,e}}, \quad (8.7)$$

where $P_{sm,e}$ is the average dissipated energy due to time-varying electrical damping of the

stepper motor, which can be calculated as:

$$P_{sm,e} = \frac{1}{T} \int_{t=0}^T \bar{c}_{e,i}(t) \cdot v_{fr,i}^2(t) dt \quad (8.8)$$

With consideration of all the power loss in the connection, the total efficiency of energy harvesting η can be calculated as:

$$\eta = \frac{P_h}{P_{sm,e} + P_p}, \quad (8.9)$$

in which P_p is the average power loss due to parasitic damping, i.e., inevitable friction in the stepper motor and the guide rail system. P_p can be calculated as:

$$P_p = \frac{1}{T} \int_{t=0}^T \left[\bar{f}_{r,i}(t) \cdot v_{fr,i}(t) + \bar{c}_{m,i}(t) \cdot v_{fr,i}^2(t) \right] dt, \quad (8.10)$$

in which $\bar{f}_{r,i}$ is equivalent to Equation (8.2), but calculated with the estimated facade outer skin mass \bar{m}_f .

The total energy harvesting efficiency describes the ratio of harvested electrical power in the battery and total dissipated mechanical power in one moveable facade element. This efficiency can be increased by using more efficient power electronics (increasing η_{le}) or by reducing parasitic damping losses (reducing the friction of the guide rail system).

The semi-active control requires a constant basic power consumption P_g of 0.61 W, which includes the power consumption of the required power electronics, microcontroller and all the sensors. To ensure the self-sufficient operation of semi-active control, the following condition needs to be met:

$$P_h \geq P_g = 0,61 \text{ W}. \quad (8.11)$$

8.4 EXPERIMENTAL RESULTS ANALYSIS

The prototype was tested respectively on five evenly distributed stories of the benchmark building, namely the 57th, 62nd, 66th, 71st, and 76th story. The optimized damping ratios ($\xi_{f,i}^{\min}$, $\xi_{f,i}^{\max}$) are given for Case 2. The corresponding optimized electrical damping coefficients ($\bar{c}_{e,i}^{\min}$, $\bar{c}_{e,i}^{\max}$), equivalent load resistances of the EHC ($R_{l,i}^{\min}$, $R_{l,i}^{\max}$), and the input duty cycles (d_i^{\min} , d_i^{\max}) are listed in Table 8.3. HiL simulation was configured according to the calculated duty cycles for each tested story. Five HiL simulations were conducted to investigate the functionality of the semi-active control by using the stepper motor as an electronically controlled damper and its energy harvesting performance. The results are analyzed and discussed by the following

8.4. EXPERIMENTAL RESULTS ANALYSIS

aspects.

Table 8.3: HiL simulation setup for five different selected stories according to the optimized Case 2.

Story number j	min				max			
	$\xi_{n-j+n_f}^{\min}$	$\bar{c}_{e,n-j+n_f}^{\min}$	$R_{l,n-j+n_f}^{\min}$	$d_{n-j+n_f}^{\min}$	$\xi_{n-j+n_f}^{\max}$	$\bar{c}_{e,n-j+n_f}^{\max}$	$R_{l,n-j+n_f}^{\max}$	$d_{n-j+n_f}^{\max}$
57	0.109	90.99	304.27	11.94%	0.120	104.31	264.85	12.78%
62	0.112	95.16	290.74	12.21%	0.157	151.50	180.97	15,41%
66	0.115	98.50	380.75	12.41%	0.187	189.26	143.98	17.22%
71	0.144	131.85	208.60	14.37%	0.215	220.34	123.04	18.58%
76	0.168	165.20	165.59	16.09%	0.237	251.42	107.28	19.85%

8.4.1 Comparison of simulated and measured facade relative displacement

The entire Simulink model used for system identification can be updated with all the newly estimated parameters listed in Table 8.1 and Table 8.2. The same settings as for the HiL test can be configured in the Simulink model for each tested story. The simulated facade relative displacement can be compared with the measured facade relative displacement of the prototype at the five selected stories. As an example, the simulated and measured facade relative displacements for the 76th story are plotted in Figure 8.6. Both time courses match very closely with each other.

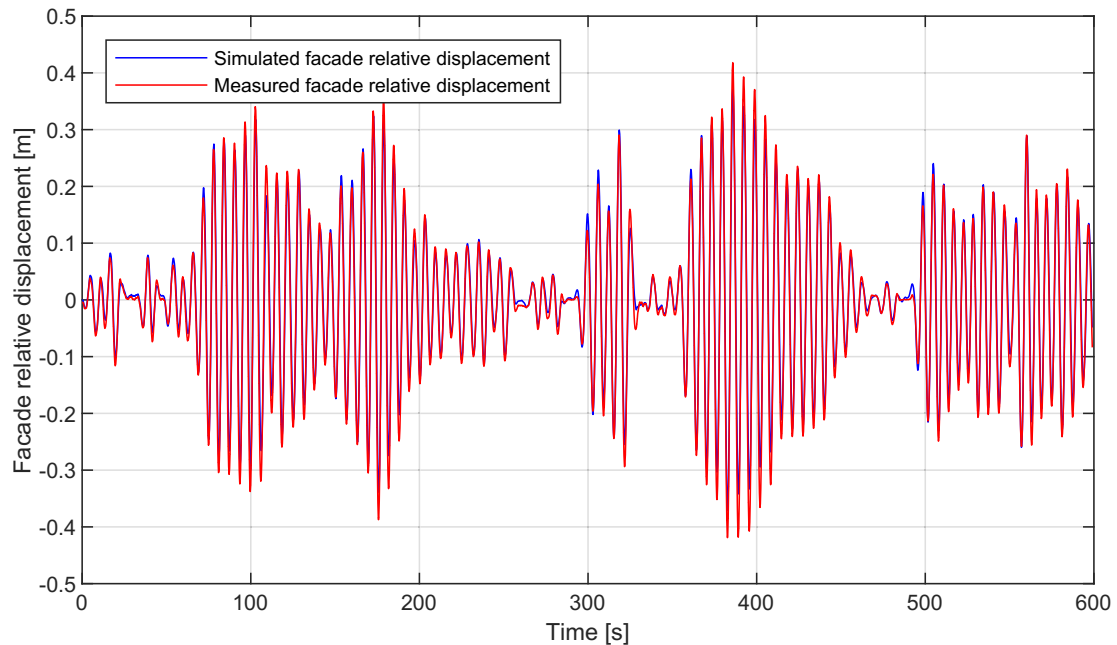


Figure 8.6: Comparison of simulated and measured facade relative displacement.

The NRMSE (Normalized Root Mean Squared Error) fitness value and NMSE (Normalized Mean Squared Error) fitness value are calculated for each tested story, as shown in Ta-

ble 8.4. The average NRMSE fitness value reaches 86.87%, and the average NMSE fitness value reaches 98.15%. Such high fitness values indicate that the estimated parameters are highly accurate.

Table 8.4: NRMSE/NMSE fitness value of the facade relative displacement based on the identified model.

Story number j	NRMSE fitness value	NMSE fitness value
57	91.14%	99.21%
62	87.24%	98.37%
66	82.87%	97.07%
71	85.23%	97.82%
76	86.88%	98.28%

8.4.2 Realization of the desired damping coefficients with the stepper motor

The recorded electrical damping force on the prototype can be determined based on the measured stepper motor forces and the identified parameters. The time course of the actual recorded electrical damping force on the prototype for the 76th story is plotted together with the time course of the desired ideal electrical damping force, as shown in Figure 8.7. As observed, the electrical damper using stepper motor behaves mostly according to the requirements. The NRMSE fitness value achieves 80.36%, and the NMSE fitness value achieves 96.14%. The NRMSE fitness value and NMSE fitness value are also calculated for each tested story, as shown in Table 8.5.

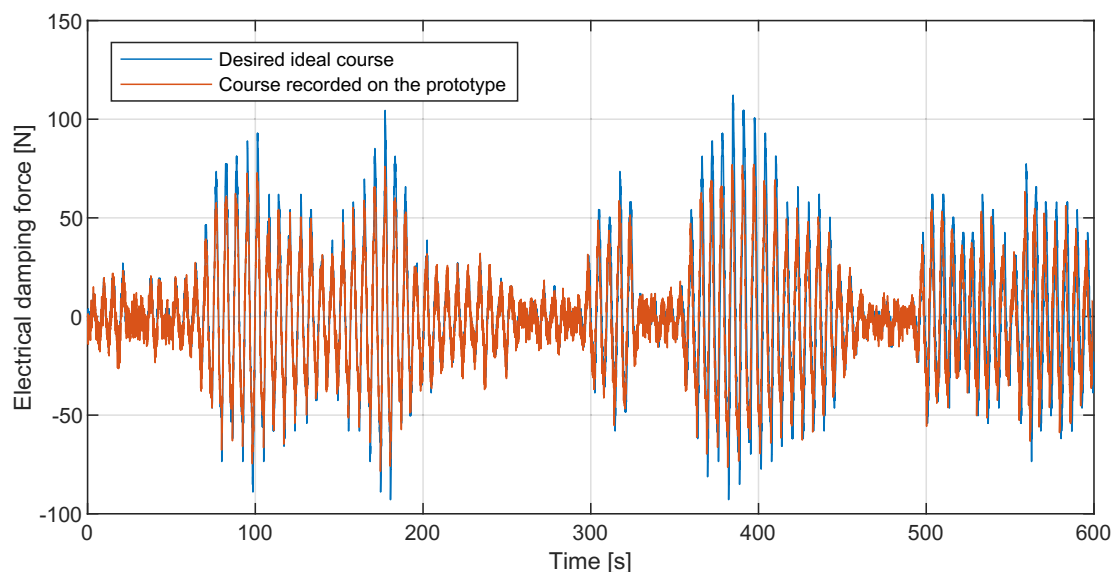


Figure 8.7: Comparison of the desired and recorded actual damping force.

8.4. EXPERIMENTAL RESULTS ANALYSIS

The relationship between the electrical damping force with the facade relative velocity $v_{fr,i}$ is exemplary plotted in Figure 8.8. It can be easily observed that the semi-active system is designed to switch between two designed damping coefficients (the slopes of the two straight lines), i.e., the desired minimum and desired maximum damping. For stepper motor as an electrical damper, the rotational speed, i.e., the facade relative velocity, has an influence on the electrical damping coefficient. For lower rotational speed, the influence can be neglected. When at higher rotational speeds, significant deviations between the desired ideal electrical damping coefficient and the actual recorded electrical damping coefficient can be observed. This can be possibly remedied by a duty cycle that depends on the speed. The theoretical damping for stepper motor, which considers the influence of rotational speed, is also plotted in Figure 8.8. It matches well with the recorded damping on the prototype, which verifies the accuracy of the identified model.

Table 8.5: NRMSE/NMSE fitness value of the electrical damping force based on the identified model.

Story number j	NRMSE fitness value	NMSE fitness value
57	82.94%	97.09%
62	84.82%	97.70%
66	85.41%	97.87%
71	84.12%	97.48%
76	80.36%	96.14%

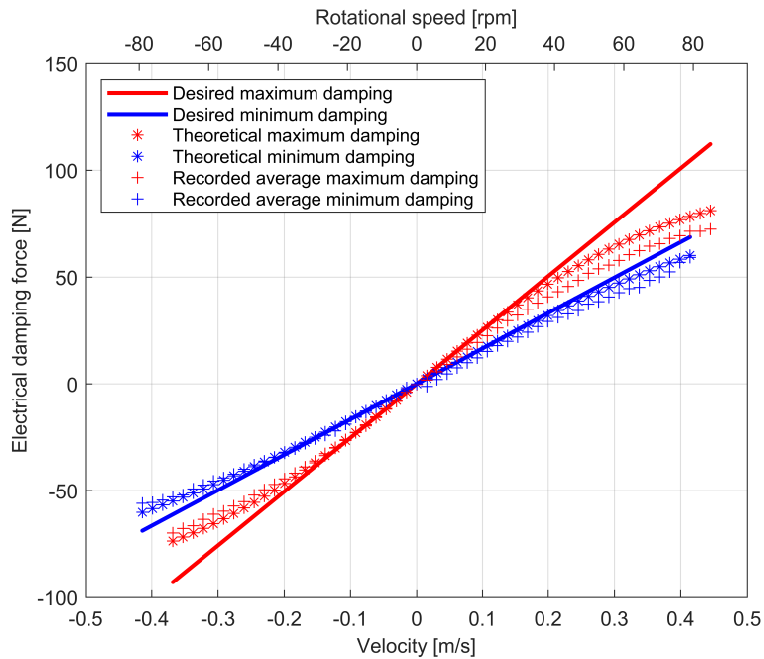
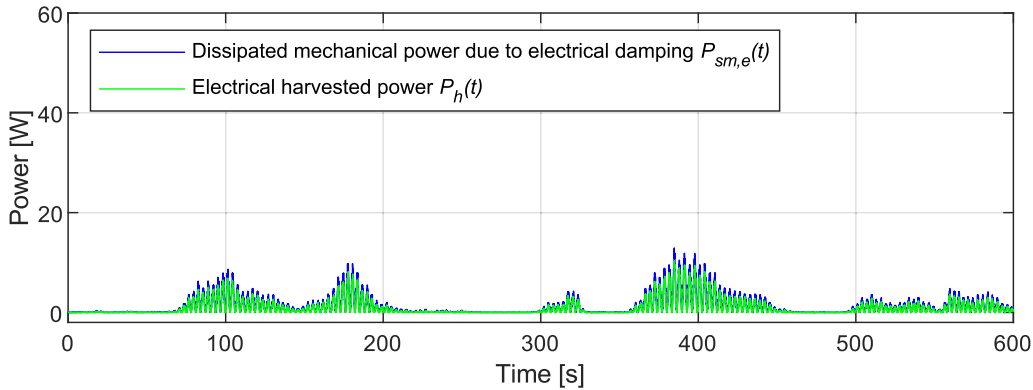


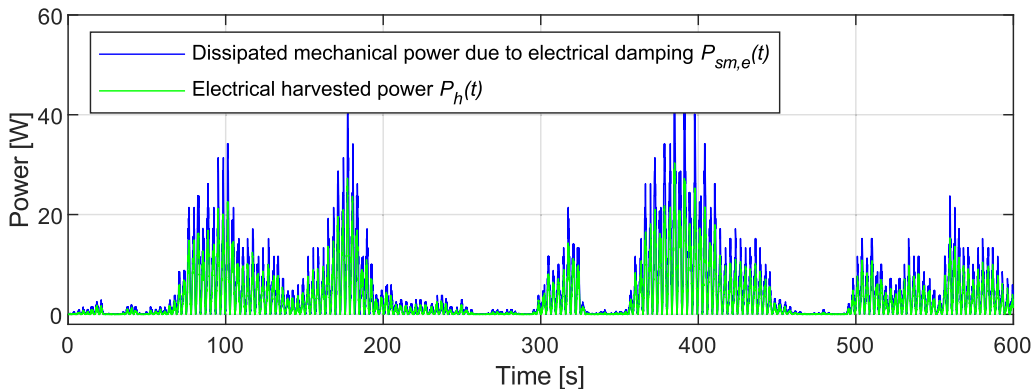
Figure 8.8: Comparison of the minimum and maximum desired and actual damping force.

8.4.3 Energy generation and self-sufficient operation

Figure 8.9 shows the recorded time courses of the power flow for the lowest tested story (the 57th story) and the top story (the 76th story). The dissipated mechanical power due to electrical damping and the electrical harvested power are both plotted for comparison and further analysis.



(a) Power flow for the prototype installed on the 57th story



(b) Power flow for the prototype installed on the 76th story

Figure 8.9: Measured power flow for the 57th and 76th stories.

The average harvested power P_h , the average dissipated mechanical power $P_{sm,e}$, and the average power loss due to parasitic damping P_p are all listed for the five tested stories in Table 8.6 together with the calculated energy harvesting efficiency. The condition for self-sufficient operation ($P_h \geq 0.61 \text{ W}$) can be always satisfied. The average energy harvesting efficiency can be calculated as 74.7% for η_{le} , and 48.3% for η . The energy harvesting efficiency can be increased by using more efficient power electronics, or by reducing the friction of the guide rail system to reduce parasitic power loss. The currently used optical encoder requires about 0.4 W for its operation, which consumes 65% of the total power consumption for semi-active control. From the power consumption point of view, there is still big potential to reduce the total power consumption.

8.4. EXPERIMENTAL RESULTS ANALYSIS

Table 8.6: Average dissipated mechanical power $P_{sm,e}$, average power loss due to parasitic damping P_p , and average harvested power P_h as well as the average energy harvesting efficiency at different story

Story number j	$P_{sm,e}$ [W]	P_p [W]	P_h [W]	η_{le}	η
57	1.09	1.01	0.85	78.0%	40.5%
62	1.69	1.16	1.29	76.3%	45.3%
66	2.30	1.24	1.72	74.8%	48.6%
71	3.03	1.17	2.22	73.3%	52.9%
76	3.97	1.05	2.82	71.0%	56.2%

8.4.4 Total energy assessment for the benchmark building

The benchmark building is assumed to be installed with moveable facade elements on its upper 20 stories. The activated damping mass per story is designed as $m_{f,i} = 30$ tons in one direction, which is realized by the moveable facade outer skin mass. It can be assumed that 25 moveable facade elements with a width of 1.6 m are installed on each side of each floor. The total length of the moveable facade elements at each side is then 40 m, leaving 1 m space at each corner of the building for the unhindered facade movement. This building has a square $42\text{m} \times 42\text{m}$ cross-section by assuming there is no cut at its corners. 50 moveable facade elements on the windward and leeward sides are activated as damping mass at each story of the benchmark building under the investigated across-wind excitation, so that the weight of each moveable facade outer skin \bar{m}_f needs to be designed as 600 kg. The same rolling bearings (two for the upper guide rail, and two for the lower guide rail) and the same stepper motor of the prototype are applied for each 600 kg moveable facade element, which ensures the same viscous friction \bar{c}_m as identified from the prototype. Therefore, the mechanical damping ratio $\xi_{m,i}$ in Equation (8.3) can be calculated as:

$$\xi_{m,i} = \bar{\xi}_m = \frac{\bar{c}_m}{2 \cdot \omega_1 \cdot \bar{m}_f(600 \text{ kg})} = 0.0381. \quad (8.12)$$

Then the total dissipated power due to electrical damping for the upper 20 stories can be calculated as:

$$\begin{aligned} P_{T,e} &= \sum_{i=1}^{20} \frac{1}{T} \int_{t=0}^T c_{e,i}(t) \cdot v_{fr,i}^2(t) dt \\ &= \sum_{i=1}^{20} \frac{1}{T} \int_{t=0}^T 2 \cdot (\xi_{f,i} - \bar{\xi}_m) \cdot \omega_1 \cdot m_{f,i} \cdot v_{fr,i}^2(t) dt, \end{aligned} \quad (8.13)$$

in which $\xi_{f,i}$ is determined by using multi-objective Genetic Algorithms (GA). The optimized $\xi_{f,i}$ of Case 2 in Figure 8.4 is further used. The total dissipated energy in the electrical domain can be calculated as 1706 W. Since the average energy harvesting efficiency of the power electronics has been obtained as 74.7% by the prototype, the average harvested power by the

whole high-rise benchmark building can be predicted as 1275 W.

The weight of the moveable facade element consists of the guide rails and the facade itself. The weight of the applied guide rails is given by the manufacturer as 25.4 kg/m. Based on the identified facade outer skin mass of the prototype, the area density of the facade can be calculated. Based on the designed 600 kg facade outer skin mass on the benchmark building, the desired facade area density can also be calculated. The calculation is shown in Table 8.7. For the benchmark building, the facade elements have a much larger height (respectively span). Therefore, we can assume larger necessary facade area density due to increased glass thickness. Shown are values yielding an element mass of 600 kg.

Table 8.7: Mass calculation of moveable facade elements for the benchmark building.

Facade size (W × H)	Guide rail (upper+lower)	Facade	Total
Prototype (2.6 m × 2.8 m)	$25.4 \times 2.6 \times 2 \approx 132$ kg	→ 480 kg ← ↓ facade area density: $480/2.6/2.8 \approx 66$ kg/m ²	612 kg (estimated)
Benchmark building story 75 - 76 (1.6 m × 4.5 m)	$25.4 \times 1.6 \times 2 \approx 81$ kg	→ 519 kg ← ↓ desired facade area density: $519/1.6/4.5 \approx 72$ kg/m ²	600 kg (designed)
story 57 - 74 (1.6 m × 3.9 m)	$25.4 \times 1.6 \times 2 \approx 81$ kg	→ 519 kg ← ↓ desired facade area density: $519/1.6/3.9 \approx 83$ kg/m ²	600 kg (designed)

8.5 DISCUSSION

A stepper motor together with the connecting EHC is applied in our prototype as the adjustable electrical damper and simultaneously as the energy harvester. Based on the HiL simulations, its feasibility for semi-active control has been validated, and its energy harvesting efficiency has also been experimentally determined.

Some limitations of our experiments using HiL need to be discussed. The friction due to the self-weight of the facade element has been considered and also been accurately estimated. However, there is also the part of the friction due to the along-wind force acting directly on the parallel moveable facade element (see Chapter 5). This part of the friction cannot be considered in the current experiments. Therefore, it is also not considered in the optimization based on the benchmark building in Section 8.2 to ensure the comparison. But even though the friction due to along-wind forces is not considered, there is no influence to verify the functionality of the adjustable electrical damping using a stepper motor and to investigate its energy harvesting efficiency. The self-sufficient semi-active control can be achieved without taking the influence of the along-wind force into account. With along-wind force in the reality, the self-sufficient semi-active control might become more difficult, if each facade element is still equipped with all the components. However, in the real application, the facade elements at the same story can share

8.6. SUMMARY AND CONCLUSIONS

the sensors and microcontroller. Therefore, the total power consumption for the semi-active d-MTFD system could be dramatically reduced. The facade elements at the same story can also share the rolling bearings, which reduces the parasitic damping due to the total viscous friction of the rolling bearings. This reduced part of damping can be replaced by electrical damping to harvest more energy.

This research is based on a benchmark building under across-wind excitation with a return period of 10 years. The self-sufficient semi-active control is discussed under this condition. However, if the facade vibration is not severe under relatively small wind excitation, semi-active control would not be necessary.

8.6 SUMMARY AND CONCLUSIONS

In this chapter, grey-box system identification is applied to estimate the parameters of the prototype. The high fitness values of the measured data and simulated data based on the estimated parameters verify the accuracy of the estimated parameters and the correctness of the mathematical model describing the prototype. The accurate system identification gives the basis for the successful Hardware-in-the-Loop (HiL) simulations. Five experiments using HiL simulations have been conducted by connecting the hardware part, namely the prototype, to different stories of the benchmark building (simulation part). Based on the experimental results and discussion, some conclusions can be summarized as follows:

(1) By comparing the simulated and measured facade relative displacement at the same selected story, the average NRMSE fitness value can achieve 86.87%, and the average NMSE fitness value can achieve 98.15%. Such high fitness values indicate that the estimated parameters of the prototype are accurate and the mathematical models, such as the friction model, used to describe the prototype are also suitable. It also proves that the HiL simulations are successful, and the simulated and measured data are trustable.

(2) The feasibility of using the stepper motor as an adjustable electrical damper for semi-active control has been successfully validated based on the HiL simulations. The nonlinear relationship between the facade relative velocity and the electrical damping coefficient can be clearly observed, which is also theoretically well explainable according to the derived equation.

(3) The average energy harvesting efficiency of power electronics is about 74.7%. When the parasitic loss is considered, then the average energy harvesting efficiency is 48.3%. The same EHC is used for all the experiments. Therefore, it makes sense that the energy harvesting efficiencies of the power electronics at five different stories are similar. The average harvested power at the lowest tested story is larger than the constant power consumption of 0.61 W for the semi-active control, so the self-sufficient operation of semi-active control can be achieved based on the prototype without consideration of friction due to along-wind excitation.

8.6. SUMMARY AND CONCLUSIONS

9 Conclusions and future work

9.1 CONCLUSIONS

In this research, a novel distributed-Multiple Tuned Facade Damping (d-MTFD) system has been proposed to reduce wind-induced vibrations of high-rise buildings. Its feasibility was experimentally validated by Hardware-in-the-Loop (HiL) simulations. Traditional single TMD systems are widely installed in many high-rise buildings and have proven to be very effective in reducing wind-induced vibrations. However, the traditional TMD system requires large additional damping mass and huge installation space at the top floors of the building. For the proposed d-MTFD system, the outer skin of the Double-Skin Facade (DSF) on the upper stories is innovatively mounted on the smooth-running guide rail system with rolling bearings. Therefore, the facade's outer skin is moveable in parallel with respect to the inner skin. Several facade elements are able to be horizontally coupled with each other per story side and function as a single damping mass. The spring system and electrical dampers are installed in the cavity of the DSF. No additional mass and no internal installation space are required. Multi-objective Genetic Algorithms can be applied to optimize the system based on two defined objectives: minimizing the peak top floor acceleration and controlling the maximum peak relative displacement of all the moveable facade's outer skin. A compromise has to be found between these two competing objectives to ensure that the designed serviceability of the high-rise building can be achieved under the condition of acceptable outer skin motion.

The passive d-MTFD system and the semi-active d-MTFD system were investigated respectively. A 76-story 306 m high benchmark building was assumed to be installed with the d-MTFD system and applied for all the investigations. The corresponding across-wind excitation acting on the benchmark building was also available, which was determined from the wind tunnel test based on a scaled model. The reference mean wind velocity is 13.5 m/s at 10 m above ground level with a return period of 10 years, which represents the serviceability level wind velocity. For both passive and semi-active systems, the spring systems are tuned to the first natural frequency of the benchmark building, as the first mode is mainly excited under across-wind excitation due to vortex shedding. The damping ratios of the electrical dampers for the passive system are constant, but story-dependent. The damping ratios at some selected floors were used as optimization parameters, and the damping ratios of other stories were ob-

tained by linear interpolation. For semi-active control, two different control policies, groundhook control (VBG, DBG) and displacement-reducing bang-bang (DBB) control, have been investigated. Based on their control policies, the semi-active system can switch between the low and high damping coefficients at each story. Linear interpolation is also used for semi-active control. The passive and semi-active d-MTFD systems were optimized using multi-objective Genetic Algorithms. The rolling friction caused by the guide rail system was also considered and proven to have a considerable impact on the optimization results. For both, the passive and semi-active d-MTFD systems, a larger rolling friction coefficient leads to unfavorable optimization results. Therefore, rolling bearings with lower friction are desired. In practice, except for the rolling friction, viscous friction and static friction also need to be considered. According to the optimized results in the form of Pareto front, the optimized passive and semi-active d-MTFD systems have both significantly improved the structural responses under across-wind excitation compared with the uncontrolled structure. The use of semi-active control can only slightly reduce structural vibrations compared with the optimized passive d-MTFD system. However, the movement of the DSF's outer skin can be significantly mitigated using semi-active control. For benchmark buildings using the optimized semi-active d-MTFD system, serviceability for hotel and office use can be guaranteed with peak relative displacements of the facade's outer skin under 0.5 m.

Together with Josef Gartner GmbH, the constructional design of a parallel moveable Double-Skin Facade (DSF) was proposed for the d-MTFD system, and a prototype with one full-scale parallel moveable facade element (2.6 m × 2.8 m) was constructed for experimental validation using Hardware-in-the-Loop (HiL) simulations. A stepper motor in generator mode is used as the adjustable electrical damper and simultaneously as the energy harvester. The optimized damping coefficient for the passive and semi-active systems can be realized by the stepper motor. The harvested energy can be stored in the battery. For semi-active control, the harvested energy is used as the energy source for the sensors and microcontroller. The microcontroller determined the low or high damping coefficient for the semi-active system based on the control policies using measured data by the sensors. Information exchange between different stories is not required for the semi-active system.

Based on the built prototype and test rig, grey-box system identification was applied to estimate the parameters of the model. As a result, the equivalent friction coefficient of 0.0022 has been achieved on the prototype. The functionality of the moveable facade element was investigated using Hardware-in-the-Loop simulations. The 76-story high benchmark building under wind excitation was completely simulated with one missing facade element on the tested floor. This missing facade element in the simulation was physically presented as the prototype (i.e. hardware part of the HiL simulations). Actuators and sensors enable communication between the simulation part and the hardware part. A controlled linear actuator was applied to reproduce the movement of selected floors on the building frame. The interaction force between the moveable facade element and the building's main structure was estimated based on the measured force using the force sensor and fed back to the simulation.

The experiment showed that the average harvested power P_h at the considered wind speed

9.2. FUTURE WORK

of 13.5 m/s was sufficient to supply the embedded system (microcontroller, sensors, and power electronics) for the facade elements on all the installed upper floors. For each facade element, the condition for self-sufficient operation ($P_h \geq 0.61 \text{ W}$) can be always satisfied. The average energy harvesting efficiency of the power electronics was calculated as about 75%. Self-sufficient operation of the entire semi-active damping system is thus possible for this wind situation. The power flow for a high-rise building installed with the d-MTFD system can be summarized in Figure 9.1.

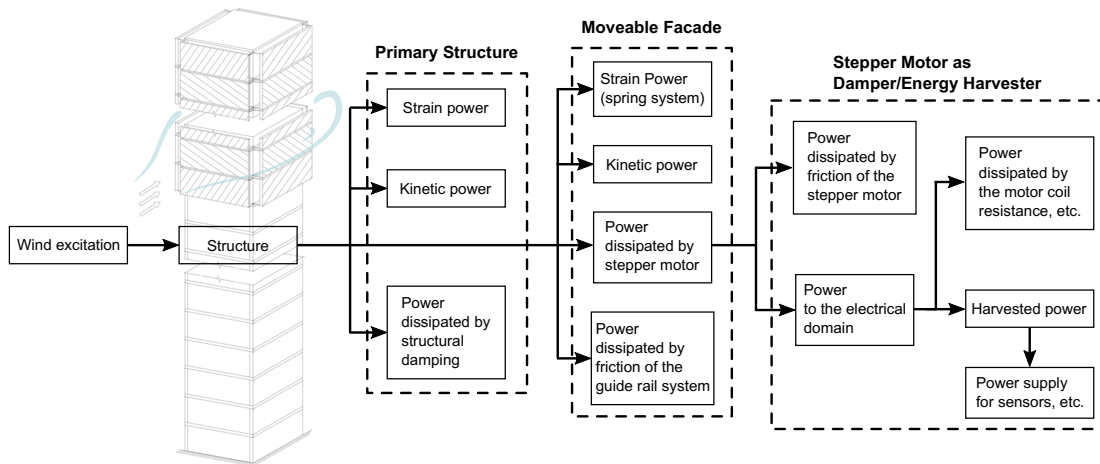


Figure 9.1: Power flow of a high-rise building installed with d-MTFD system.

This interdisciplinary research combines structural engineering, control engineering, and electrical engineering to provide innovative damping solutions for vibration problems of slender high-rise buildings. The developed adjustable electrical damper enables the damping device to evolve from the traditional energy dissipation strategy to the novel energy harvesting strategy, which paves a new way for semi-active control without an external power supply. This novel strategy increases the reliability and self-sustainability of semi-active control systems. The activation of the facade's outer skin as the damping mass enables the usage of existing building mass for vibration control. Compared with the traditional solutions, the proposed d-MTFD system does not require large additional damping mass, which significantly minimizes the need for building materials. Therefore, this system makes a contribution to the reduction of the carbon footprint of high-rise buildings.

9.2 FUTURE WORK

The influence of the along-wind excitation on the friction coefficient cannot be experimentally considered. In future work, as the average energy harvesting efficiency of power electronics has been obtained from the experiment, the harvested energy can be then approximately calculated by simulations, where the along-wind forces are also considered. The calculated harvested energy will then be applied as an additional optimization objective in the multi-objective optimization. Together with the two existing objectives, a Pareto surface can be generated af-

9.2. FUTURE WORK

ter the multi-objective optimization. The final self-sufficient semi-active d-MTFD system will be proven.

In the current investigation, only the 10-year wind event was considered. Different levels of wind excitation will also be applied to test the effectiveness of the semi-active d-MTFD system in the future. Inerter can be possibly integrated in the cavity of the DSF. By using inerter, fewer moveable DSF need to be activated in the upper stories of high-rise buildings to achieve the same damping performance. The current investigation is to reduce the structural vibration in the across-wind direction. The performance of reducing torsional vibration of high-rise buildings can be further studied. A more intelligent control system that can switch between passive and semi-active control under different environmental conditions will be further developed.

A Appendix

A.1 EXPLICIT MATRICES IN THE GOVERNING EQUATION

The matrices in the governing equation can be explicitly expressed as below by assuming the high-rise building as a shear building for simplicity. For an accurate description of the slender high-rise building, a shear bending model is suggested, where the rotational DoFs are also considered in the modelling. In our applied benchmark building with a slenderness ratio of 7.3, the rotational DOFs have been considered but removed using static condensation [119].

Mass matrix of the entire system:

$$\mathbf{M}_S = \begin{bmatrix} m_1 & 0 & \cdots & 0 & 0 & 0 & 0 & \cdots & 0 & 0 \\ 0 & m_2 & \cdots & 0 & 0 & 0 & 0 & \cdots & 0 & 0 \\ \vdots & \vdots & \ddots & \vdots & \vdots & \vdots & \vdots & \ddots & \vdots & \vdots \\ 0 & 0 & \cdots & m_{n-1} & 0 & 0 & 0 & \cdots & 0 & 0 \\ 0 & 0 & \cdots & 0 & m_n & 0 & 0 & \cdots & 0 & 0 \\ 0 & 0 & \cdots & 0 & 0 & m_{f,1} & 0 & \cdots & 0 & 0 \\ 0 & 0 & \cdots & 0 & 0 & 0 & m_{f,2} & \cdots & 0 & 0 \\ \vdots & \vdots & \ddots & \vdots & \vdots & \vdots & \vdots & \ddots & \vdots & \vdots \\ 0 & 0 & \cdots & 0 & 0 & 0 & 0 & \cdots & m_{f,n_f-1} & 0 \\ 0 & 0 & \cdots & 0 & 0 & 0 & 0 & \cdots & 0 & m_{f,n_f} \end{bmatrix} \quad (\text{A.1})$$

A.1. EXPLICIT MATRICES IN THE GOVERNING EQUATION

Damping matrix of the entire system:

$$\mathbf{C}_S = \begin{bmatrix}
 c_1 + c_2 & -c_2 & \cdots & 0 & \cdots & 0 & 0 & 0 & \cdots & 0 & 0 \\
 -c_2 & c_2 + c_3 & \cdots & 0 & \cdots & 0 & 0 & 0 & \cdots & 0 & 0 \\
 \vdots & \vdots & \ddots & \vdots & \ddots & \vdots & \vdots & \vdots & \ddots & \vdots & \vdots \\
 0 & 0 & \cdots & c_{n-n_f+1} + c_{n-n_f+2} + c_{f,1} & \cdots & 0 & 0 & -c_{f,1} & \cdots & 0 & 0 \\
 \vdots & \vdots & \ddots & \vdots & \ddots & \vdots & \vdots & \vdots & \ddots & \vdots & \vdots \\
 0 & 0 & \cdots & 0 & \cdots & c_{n-1} + c_n + c_{f,n_f-1} & -c_n & 0 & \cdots & -c_{f,n_f-1} & 0 \\
 0 & 0 & \cdots & 0 & \cdots & -c_n & c_n + c_{f,n_f} & 0 & \cdots & 0 & -c_{f,n_f} \\
 0 & 0 & \cdots & -c_{f,1} & \cdots & 0 & 0 & c_{f,1} & \cdots & 0 & 0 \\
 \vdots & \vdots & \ddots & \vdots & \ddots & \vdots & \vdots & \vdots & \ddots & \vdots & \vdots \\
 0 & 0 & \cdots & 0 & \cdots & -c_{f,n_f-1} & 0 & 0 & \cdots & c_{f,n_f-1} & 0 \\
 0 & 0 & \cdots & 0 & \cdots & 0 & -c_{f,n_f} & 0 & \cdots & 0 & c_{f,n_f}
 \end{bmatrix} \quad (\text{A.2})$$

Stiffness matrix of the entire system:

$$\mathbf{K}_S = \begin{bmatrix}
 k_1 + k_2 & -k_2 & \cdots & 0 & \cdots & 0 & 0 & 0 & \cdots & 0 & 0 \\
 -k_2 & k_2 + k_3 & \cdots & 0 & \cdots & 0 & 0 & 0 & \cdots & 0 & 0 \\
 \vdots & \vdots & \ddots & \vdots & \ddots & \vdots & \vdots & \vdots & \ddots & \vdots & \vdots \\
 0 & 0 & \cdots & k_{n-n_f+1} + k_{n-n_f+2} + k_{f,1} & \cdots & 0 & 0 & -k_{f,1} & \cdots & 0 & 0 \\
 \vdots & \vdots & \ddots & \vdots & \ddots & \vdots & \vdots & \vdots & \ddots & \vdots & \vdots \\
 0 & 0 & \cdots & 0 & \cdots & k_{n-1} + k_n + k_{f,n_f-1} & -k_n & 0 & \cdots & -k_{f,n_f-1} & 0 \\
 0 & 0 & \cdots & 0 & \cdots & -k_n & k_n + k_{f,n_f} & 0 & \cdots & 0 & -k_{f,n_f} \\
 0 & 0 & \cdots & -k_{f,1} & \cdots & 0 & 0 & k_{f,1} & \cdots & 0 & 0 \\
 \vdots & \vdots & \ddots & \vdots & \ddots & \vdots & \vdots & \vdots & \ddots & \vdots & \vdots \\
 0 & 0 & \cdots & 0 & \cdots & -k_{f,n_f-1} & 0 & 0 & \cdots & k_{f,n_f-1} & 0 \\
 0 & 0 & \cdots & 0 & \cdots & 0 & -k_{f,n_f} & 0 & \cdots & 0 & k_{f,n_f}
 \end{bmatrix} \quad (\text{A.3})$$

Excitation influence matrix:

$$\boldsymbol{\eta} = \begin{bmatrix} I_n \\ 0_{n_f, n} \end{bmatrix}, \quad (\text{A.4})$$

where I_n is an identity matrix of size n , and $0_{n_f, n}$ is a $n_f \times n$ zero matrix.

Friction influence matrix:

$$\mathbf{B}_f = \begin{bmatrix} 0_{n-n_f, n_f} \\ I_{n_f} \\ -I_{n_f} \end{bmatrix}, \quad (\text{A.5})$$

where $0_{n-n_f, n_f}$ is a $n - n_f \times n_f$ zero matrix, and I_{n_f} is an identity matrix of size n_f .

Bibliography

- [1] Mark Sarkisian. *Designing tall buildings: structure as architecture (2nd ed.)*. Routledge, Taylor & Francis Group, New York, 2016.
- [2] Jiro Takagi and Akira Wada. Higher performance seismic structures for advanced cities and societies. *Engineering*, 5(2):184–189, 2019.
- [3] Michael D. Symans, Finley A. Charney, A. S. Whittaker, Michael C. Constantinou, C. A. Kircher, Martin W. Johnson, and Robert J. McNamara. Energy Dissipation Systems for Seismic Applications: Current Practice and Recent Developments. *Journal of Structural Engineering*, 134(1):3–21, jan 2008.
- [4] Emil Simiu and DongHun Yeo. *Wind effects on structures: Modern structural design for wind*. John Wiley & Sons, 2019.
- [5] Kyoung Sun Moon. Vertically distributed multiple tuned mass dampers in tall buildings: performance analysis and preliminary design. *The Structural Design of Tall and Special Buildings*, 19(3):347–366, 2010.
- [6] EAN Al-awag and IA Wahab. Perspectives in double-skin façade (DSF) advantages and disadvantages. In *IOP Conference Series: Earth and Environmental Science*, volume 1022, page 012003. IOP Publishing, 2022.
- [7] Kyoung Sun Moon. Structural design of double skin facades as damping devices for tall buildings. *Procedia Engineering*, 14:1351–1358, 2011.
- [8] Tat S Fu and Rui Zhang. Integrating double-skin facades and mass dampers for structural safety and energy efficiency. *Journal of Architectural Engineering*, 22(4):04016014, 2016.
- [9] Lucio Blandini, Walter Haase, Stefanie Weidner, Michael Böhm, Timon Burghardt, Daniel Roth, Hansgeorg Binz, Oliver Sawodny, and Werner Sobek. Der demonstrator d1244: das weltweit erste adaptive hochhaus. *Bautechnik*, 99(6):452–462, 2022.
- [10] Achim Bleicher. Aktive schwingungskontrolle einer spannbandbrücke mit pneumatischen aktuatoren. *Bautechnik*, 89(2):89–101, 2012.
- [11] CTBUH Staff. Tall buildings in 2020: Covid-19 contributes to dip in year-on-year completions. *CTBUH Journal 2021 Issue I*, pages 40–47, 2021.
- [12] Jason Gabel, Annan Shehadi, Shawn Ursini, and Marshall Gerometta. CTBUH Year in Review: Tall Trends of 2016. *The Council on Tall Buildings and Urban Habitat (CTBUH): Chicago, IL, USA*, 2016.

- [13] Jerzy Szolomicki and Hanna Golasz-Szolomicka. Analysis of technical problems in modern super-slim high-rise residential buildings. *Budownictwo i Architektura*, 20(1):83–116, 2021.
- [14] Jerome J. Connor. *Introduction to Structural Motion Control*. MIT-Prentice Hall series on civil, environmental, and systems engineering. Prentice Hall Pearson Education, Incorporated, 2003.
- [15] Hugo. Bachmann and Walter. Ammann. *Vibrations in structures: induced by man and machines*. Structural engineering documents. International Association for Bridge and Structural Engineering, 1987.
- [16] Philip Oldfield, Dario Trabucco, Antony Wood, Philip Oldfield, and Dario Trabucco. Five energy generations of tall buildings : an historical analysis of energy consumption in high-rise buildings Five energy generations of tall buildings : an historical analysis of energy consumption in high-rise buildings. *The Journal of Architecture*, 2365(September), 2015.
- [17] Elisabeth Gratia and André De Herde. Greenhouse effect in double-skin facade. *Energy and Buildings*, 2007.
- [18] Mauricio Hernandez Tascon. *Experimental and computational evaluation of thermal performance and overheating in double skin facades*. PhD thesis, University of Nottingham, 2008.
- [19] Diana Üрге Vorsatz, Nick Eyre, Peter Graham, Danny Harvey, Edgar Hertwich, Yi Jiang, Christian Kornevall, Mili Majumdar, James E. McMahon, Sevastianos Mirasgedis, and et al. *Energy End-Use: Buildings*. Cambridge University Press, 2012.
- [20] Michael A. Kraus, Michael Drass, and Jens Schneider. Potenzial von künstlicher intelligenz im bereich von gebäudehüllen. *ce/papers*, 4(5):187–196, 2021.
- [21] Ahsan Kareem. Methods to control wind-induced building motions. In *Structures Congress XII*, pages 654–659. ASCE, 1994.
- [22] Kyoung Sun Moon. Tall building motion control using double skin façades. *Journal of architectural engineering*, 15(3):84–90, 2009.
- [23] Kyoung Sun Moon. Integrated damping systems for tall buildings: tuned mass damper/-double skin facade damping interaction system. *The Structural Design of Tall and Special Buildings*, 25(5):232–244, 2016.
- [24] Yangwen Zhang, Thomas Schauer, Laurenz Wernicke, Wulf Wulff, and Achim Bleicher. Facade-Integrated Semi-Active Vibration Control for Wind-Excited Super-Slender Tall Buildings. *IFAC-PapersOnLine*, 53(2):8395–8400, 2020.
- [25] Richard GJ Flay. Bluff body aerodynamics. *Advanced structural wind engineering*, pages 59–84, 2013.
- [26] T.T. Soong and G.F. Dargush. Passive energy dissipation and active control. *Structural engineering handbook*, pages 1–28, 1999.
- [27] Ahsan Kareem, Tracy Kijewski, and Yukio Tamura. Mitigation of motions of tall buildings with specific examples of recent applications. *Wind and Structures, An International Journal*, 1999.
- [28] Jiro Takagi and Akira Wada. Recent earthquakes and the need for a new philosophy for earthquake-resistant design. *Soil Dynamics and Earthquake Engineering*, 2019.

BIBLIOGRAPHY

- [29] Ahsan Kareem, Enrica Bernardini, and Seymour M. J. Spence. *Control of the Wind Induced Response of Structures*, pages 377–410. Springer Japan, Tokyo, 2013.
- [30] Jerome Connor and Simon Laflamme. *Structural motion engineering*, volume 9783319062. Springer International Publishing Switzerland, 2014.
- [31] J.P. Den Hartog. *Mechanical Vibrations*. Civil, Mechanical and Other Engineering Series. Dover Publications, 1985.
- [32] Ahsan Kareem. Mitigation of wind induced motion of tall buildings. *Journal of Wind Engineering and Industrial Aerodynamics*, 1983.
- [33] Mc Constantinou, Tt Soong, and Gf Dargush. Passive Energy Dissipation Systems for Structural Design and Retrofit. *Multidisciplinary Center for Earthquake Engineering Research*, 1998.
- [34] Mika Gröndahl. Reducing Skyscraper Sway. <https://www.nytimes.com/interactive/2015/08/06/realestate/Reducing-Skyscraper-Sway.html>, aug 2015. Accessed: 2019-09-23.
- [35] Christian Meinhardt, Nikolaos Nikitas, and Demetris Demetriou. Application of a 245 metric ton dual-use active tmd system. *Procedia engineering*, 199:1719–1724, 2017.
- [36] P. Lukkunaprasit and A. Wanitkorkul. Inelastic buildings with tuned mass dampers under moderate ground motions from distant earthquakes. *Earthquake Engineering and Structural Dynamics*, 30(4):537–551, 2001.
- [37] Lei Zuo. Effective and robust vibration control using series multiple tuned-mass dampers. *Journal of Vibration and Acoustics, Transactions of the ASME*, 2009.
- [38] K. Iwanami and K. Seto. Optimal design of dual tuned mass dampers and their effectiveness. In *Proc. JSME(C)*, pages 44–52, 1984.
- [39] Takeru Igusa and Kangming Xu. Vibration reduction characteristics of distributed tuned mass dampers. In *roc. 4th int. conf struct. dyn.: recent advances*, pages 596–605, 1991.
- [40] Takeru Igusa and Kangming Xu. Wide-band response of multiple subsystems with high modal density. In Y. K. Lin and I. Elishakoff, editors, *Stochastic Structural Dynamics 1*, pages 131–145, Berlin, Heidelberg, 1991. Springer Berlin Heidelberg.
- [41] Kangming Xu and Takeru Igusa. Dynamic characteristics of multiple substructures with closely spaced frequencies. *Earthquake engineering & structural dynamics*, 21(12):1059–1070, 1992.
- [42] Takeru Igusa and Kangming Xu. Vibration control using multiple tuned mass dampers. *Journal of Sound and Vibration*, 175(4):491–503, 1994.
- [43] Hiroki Yamaguchi and Napat Harnpornchai. Fundamental characteristics of Multiple Tuned Mass Dampers for suppressing harmonically forced oscillations. *Earthquake Engineering & Structural Dynamics*, 1993.
- [44] Masato Abé and Yozo Fujino. Dynamic characterization of multiple tuned mass dampers and some design formulas. *Earthquake Engineering & Structural Dynamics*, 1994.
- [45] Ahsan Kareem and Samuel Kline. Performance of multiple mass dampers under random loading. *Journal of Structural Engineering (United States)*, 1995.
- [46] A. S. Joshi and R. S. Jangid. Optimum parameters of multiple tuned mass dampers for base-excited damped systems. *Journal of Sound and Vibration*, 1997.

- [47] R. S. Jangid. Optimum Multiple Tuned Mass Dampers for base-excited undamped system. *Earthquake Engineering and Structural Dynamics*, 1999.
- [48] Chunxiang Li. Performance of multiple tuned mass dampers for attenuating undesirable oscillations of structures under the ground acceleration. *Earthquake Engineering and Structural Dynamics*, 2000.
- [49] Chunxiang Li. Optimum multiple tuned mass dampers for structures under the ground acceleration based on DDMF and ADMF. *Earthquake engineering & structural dynamics*, 31(4):897–919, 2002.
- [50] Chunxiang Li and Yanxia Liu. Active multiple tuned mass dampers for structures under the ground acceleration. *Earthquake engineering & structural dynamics*, 31(5):1041–1052, 2002.
- [51] Chunxiang Li, Yanxia Liu, and Zhaomin Wang. Active multiple tuned mass dampers: A new control strategy. *Journal of Structural Engineering*, 129(7):972–977, 2003.
- [52] Chunxiang Li. Multiple active–passive tuned mass dampers for structures under the ground acceleration. *Earthquake engineering & structural dynamics*, 32(6):949–964, 2003.
- [53] Chunxiang Li and Dai Zhou. Evaluation of multiple active lever-type tuned mass dampers for structures under ground acceleration. *Engineering structures*, 26(3):303–317, 2004.
- [54] Nam Hoang and Pennung Warnitchai. Design of multiple tuned mass dampers by using a numerical optimizer. *Earthquake engineering & structural dynamics*, 34(2):125–144, 2005.
- [55] Lei Zuo and Samir A Nayfeh. Optimization of the individual stiffness and damping parameters in multiple-tuned-mass-damper systems. *Journal of Vibration and Acoustics*, 127(1):77–83, 2005.
- [56] Hong-Nan Li and Xiang-Lei Ni. Optimization of non-uniformly distributed multiple tuned mass damper. *Journal of Sound and Vibration*, 308(1-2):80–97, 2007.
- [57] Mohtasham Mohebibi, Kazem Shakeri, Yavar Ghanbarpour, and Hossein Majzoub. Designing optimal multiple tuned mass dampers using genetic algorithms (gas) for mitigating the seismic response of structures. *Journal of Vibration and Control*, 19(4):605–625, 2012.
- [58] Genda Chen and Jingning Wu. Experimental study on multiple tuned mass dampers to reduce seismic responses of a three-storey building structure. *Earthquake engineering & structural dynamics*, 32(5):793–810, 2003.
- [59] Rubia Borges Carneiro, Suzana Moreira Avila, and JosE LuS Vital De Brito. Parametric study on multiple tuned mass dampers using interconnected masses. *International Journal of Structural Stability and Dynamics*, 8(01):187–202, 2008.
- [60] Xiudong Tang and Lei Zuo. Passive, active, and semi-active series tuned mass dampers. In *Active and Passive Smart Structures and Integrated Systems 2010*, volume 7643, page 76432P. International Society for Optics and Photonics, 2010.
- [61] Tao Ni, Lei Zuo, and Ahsan Kareem. Assessment of energy potential and vibration mitigation of regenerative tuned mass dampers on wind excited tall buildings. In *ASME 2011 International Design Engineering Technical Conferences and Computers and Information in Engineering Conference*, pages 333–342. Citeseer, 2011.

BIBLIOGRAPHY

- [62] Lei Zuo and Wen Cui. Dual-functional energy-harvesting and vibration control: electromagnetic resonant shunt series tuned mass dampers. *Journal of vibration and acoustics*, 135(5), 2013.
- [63] N.R. Peterson. Design of Large Scale Tuned Mass Dampers. In *Proceedings of ASCE Convention and Exposition*, Boston, 1978.
- [64] JR Sladek and RE Klingner. Using tuned mass dampers to reduce seismic response. In *Proceedings of the World Conference on Earthquake Engineering*, volume 7, page 265, 1980.
- [65] L. A. Bergman, D. M. McFarland, J. K. Hall, E. A. Johnson, and A. Kareem. Optimal distribution of tuned mass dampers in wind-sensitive structures. In *Proc ICOSAR 89 5th Int Conf Struct Saf Reliab*, pages 95–102. Publ by ASCE, 1989.
- [66] Genda Chen. Multi-stage tuned mass damper. In *Proceedings of 11th World Conference on Earthquake Engineering, Acapulco, Mexico*, 1996.
- [67] Genda Chen and Jingning Wu. Optimal placement of multiple tune mass dampers for seismic structures. *Journal of Structural Engineering*, 127(9):1054–1062, 2001.
- [68] Mohammad Sabbir Rahman, Md Kamrul Hassan, Seongkyu Chang, and Dookie Kim. Adaptive multiple tuned mass dampers based on modal parameters for earthquake response reduction in multi-story buildings. *Advances in Structural Engineering*, 20(9):1375–1389, 2017.
- [69] Said Elias and Vasant Matsagar. Distributed multiple tuned mass dampers for wind vibration response control of high-rise building. *Journal of Engineering*, 2014, 2014.
- [70] Said Elias and Vasant Matsagar. Wind response control of 76-storey benchmark building with distributed multiple tuned mass dampers. *Journal of Wind and Engineering*, 11(2):37–49, 2014.
- [71] Said Elias, Vasant Matsagar, and TK Datta. Distributed tuned mass dampers for multi-mode control of benchmark building under seismic excitations. *Journal of Earthquake Engineering*, 23(7):1137–1172, 2019.
- [72] Said Elias, Vasant Matsagar, and TK Datta. Effectiveness of distributed tuned mass dampers for multi-mode control of chimney under earthquakes. *Engineering Structures*, 124:1–16, 2016.
- [73] Said Elias, Vasant Matsagar, and Tushar Kanti Datta. Along-wind response control of chimneys with distributed multiple tuned mass dampers. *Structural Control and Health Monitoring*, 26(1):e2275, 2019.
- [74] Hamid Radmard Rahmani and Carsten Könke. Passive Control of Tall Buildings Using Distributed Multiple Tuned Mass Dampers. *submitted to Elsevier*, pages 1–43, 2019.
- [75] Olena Kalyanova. *Double-skin facade: modelling and experimental investigations of thermal performance*. PhD thesis, Department of Civil Engineering, Aalborg University, 2008.
- [76] Vijaya Yellamraju. *Evaluation and design of double-skin facades for office buildings in hot climates*. PhD thesis, Texas A&M University, 2004.
- [77] Ali Ghaffarianhoseini, Amirhosein Ghaffarianhoseini, Umberto Berardi, John Tookey, Danny Hin Wa Li, and Shahab Kariminia. Exploring the advantages and challenges of double-skin façades (DSFs). *Renewable and Sustainable Energy Reviews*, 60:1052–1065, 2016.

- [78] SY Kim and KD Song. Determining photosensor conditions of a daylight dimming control system using different double-skin envelope configurations. *Indoor and Built Environment*, 16(5):411–425, 2007.
- [79] Lei Xu and Toshio Ojima. Field experiments on natural energy utilization in a residential house with a double skin façade system. *Building and Environment*, 42(5):2014–2023, 2007.
- [80] ALS Chan, Tin Tai Chow, KF Fong, and Z Lin. Investigation on energy performance of double skin façade in Hong Kong. *Energy and buildings*, 41(11):1135–1142, 2009.
- [81] MA Shameri, MA Alghoul, Kamaruzzaman Sopian, M Fauzi M Zain, and Omkalthum Elayeb. Perspectives of double skin façade systems in buildings and energy saving. *Renewable and sustainable energy reviews*, 15(3):1468–1475, 2011.
- [82] Juan Zhou and Youming Chen. A review on applying ventilated double-skin facade to buildings in hot-summer and cold-winter zone in China. *Renewable and Sustainable Energy Reviews*, 14(4):1321–1328, 2010.
- [83] Cui Xu, Qiao Xi, and Qingsong Ma. Technical Characteristics and Energy Performance of Double Skin Faces: A Review. In *E3S Web of Conferences*, volume 248, page 01029. EDP Sciences, 2021.
- [84] Umberto Berardi and Taoning Wang. Daylighting in an atrium-type high performance house. *Building and Environment*, 76:92–104, 2014.
- [85] Eleanor Lee, Stephen Selkowitz, Vladimir Bazjanac, Vorapat Inkrojrit, and Christian Kohler. High-performance commercial building façades. 2002.
- [86] Ahsan Kareem, Enrica Bernardini, and Seymour MJ Spence. Control of the wind induced response of structures. In *Advanced Structural Wind Engineering*, pages 377–410. Springer, 2013.
- [87] Ali Azad, T Ngo, and Bijan Samali. Control of wind-induced motion of tall buildings using smart façade systems. *Electronic Journal of Structural Engineering*, 2015.
- [88] Tat S Fu and Erik A Johnson. Distributed mass damper system for integrating structural and environmental controls in buildings. *Journal of Engineering Mechanics*, 137(3):205–213, 2010.
- [89] Tat S Fu and Erik A Johnson. Active control for a distributed mass damper system. *Journal of Engineering Mechanics*, 140(2):426–429, 2013.
- [90] Tat S Fu. Double skin facades as mass dampers. In *2013 American Control Conference*, pages 4742–4746. IEEE, 2013.
- [91] Giorgio Barone, Alessandro Palmeri, and A Khetawat. Passive control of building structures using double-skin facades as vibration absorbers. in: Kruis, j., tsompanakis, y. and topping, bhv. In *Proceedings of the Fifteenth International Conference on Civil, Structural and Environmental Engineering Computing, Prague, 1st-4th Sept., Paper*, volume 94. Civil-Comp Press, 2015.
- [92] Giovanni Pipitone, Giorgio Barone, and Alessandro Palmeri. Optimal design of double-skin façades as vibration absorbers. *Structural Control and Health Monitoring*, 25(2):e2086, 2018.
- [93] Obayashi-Corporation. Hula Mass Damper System. https://www.obayashi.co.jp/solution_technology/detail/tech60.html, 2012. Accessed: 2019-09-23.

BIBLIOGRAPHY

- [94] Yoko Nagayama. Obayashi renews the building in omotesando, pouring the latest technology. <https://toyokeizai.net/articles/-/13523?page=3>, 2013. Accessed: 2022-03-07.
- [95] B M Nandish and Bhagyashree Hosamani. A Review of Energy Harvesting From Vibration using Piezoelectric Material. *International Journal of Engineering Research and Technology (IJERT)*, 3(7):1607–1611, 2014.
- [96] Steven R. Anton and Henry A. Sodano. A review of power harvesting using piezoelectric materials (2003-2006). *Smart Materials and Structures*, 16(3), jun 2007.
- [97] Alper Erturk. Piezoelectric energy harvesting for civil infrastructure system applications: Moving loads and surface strain fluctuations. *Journal of Intelligent Material Systems and Structures*, 22(17):1959–1973, 2011.
- [98] Abhijit Gupta, J. A. Jendrzejczyk, T. M. Mulcahy, and J. R. Hull. Design of electromagnetic shock absorbers. *International Journal of Mechanics and Materials in Design*, 3(3):285–291, sep 2006.
- [99] Brian Scully, Lei Zuo, Jurgen Shestani, and Yu Zhou. Design and characterization of an electromagnetic energy harvester for vehicle suspensions. In *ASME International Mechanical Engineering Congress and Exposition, Proceedings*, 2010.
- [100] S. Rani. Bose breakthrough: electromagnetic auto suspension, 2005.
- [101] Yasuhiro Kawamoto, Y Suda, H Inoue, and T Kondo. Electro-mechanical suspension system considering energy consumption and vehicle manoeuvre. *Vehicle System Dynamics*, 46(S1):1053–1063, 2008.
- [102] Ging-Long Lin, Chi-Chang Lin, Yu-Jing Chen, and Ta-Chih Hung. Experimental verification of electromagnetic multiple tuned mass dampers for energy harvesting and structural control. *Earthquake Engineering & Structural Dynamics*, 50(13):3483–3504, 2021.
- [103] Rogelio Palomera-Arias, Jerome J Connor, and John A Ochsendorf. Feasibility study of passive electromagnetic damping systems. *Journal of Structural Engineering*, 134(1):164–170, 2008.
- [104] Ian L. Cassidy, Jeffrey T. Scruggs, and Sam Behrens. Design of electromagnetic energy harvesters for large-scale structural vibration applications. *Active and Passive Smart Structures and Integrated Systems 2011*, 7977(919):79770P, 2011.
- [105] Alicia Gonzalez-Buelga, LR Clare, SA Neild, SG Burrow, and DJ Inman. An electromagnetic vibration absorber with harvesting and tuning capabilities. *Structural Control and Health Monitoring*, 22(11):1359–1372, 2015.
- [106] Maziar Jamshidi and Chih Chen Chang. A new self-powered electromagnetic damper for structural vibration control. In *Sensors and Smart Structures Technologies for Civil, Mechanical, and Aerospace Systems 2017*, volume 10168, page 101682E. International Society for Optics and Photonics, 2017.
- [107] Wenai Shen, Songye Zhu, You-Lin Xu, and Hong-ping Zhu. Energy regenerative tuned mass dampers in high-rise buildings. *Structural Control and Health Monitoring*, 25(2):e2072, 2018.
- [108] Fatemeh Rahimi, Reza Aghayari, and Bijan Samali. Application of tuned mass dampers for structural vibration control: a state-of-the-art review. *Civil Engineering Journal*, pages 1622–1651, 2020.

- [109] Sinan Korkmaz. A review of active structural control: challenges for engineering informatics. *Computers & Structures*, 89(23-24):2113–2132, 2011.
- [110] TT Soong. State-of-the-art review: active structural control in civil engineering. *Engineering Structures*, 10(2):74–84, 1988.
- [111] BF Spencer Jr and S Nagarajaiah. State of the art of structural control. *Journal of structural engineering*, 129(7):845–856, 2003.
- [112] Ahad Javanmardi, Khaled Ghaedi, Fuyun Huang, Muhammad Usman Hanif, and Alireza Tabrizikahou. Application of structural control systems for the cables of cable-stayed bridges: state-of-the-art and state-of-the-practice. *Archives of Computational Methods in Engineering*, 29(3):1611–1641, 2022.
- [113] Werner Sobek and Patrick Teuffel. Adaptive systems in architecture and structural engineering. In *Smart Structures and Materials 2001: Smart Systems for Bridges, Structures, and Highways*, volume 4330, pages 36–45. SPIE, 2001.
- [114] Gennaro Senatore. Designing and prototyping adaptive structures—an energy-based approach beyond lightweight design. *Robotic Building*, pages 169–189, 2018.
- [115] Mike Schlaich and Achim Bleicher. Spannbandbrücke mit kohlenstofffaser-lamellen. *Bautechnik*, 84(5):311–319, 2007.
- [116] Robert Jirasek, Thomas Schauer, and Achim Bleicher. Multi-variable active vibration control for a footbridge with regard to vertical bending and torsional modes, 2017.
- [117] Yoshiki Ikeda. Active and semi-active vibration control of buildings in japan—practical applications and verification. *Structural Control and Health Monitoring: The Official Journal of the International Association for Structural Control and Monitoring and of the European Association for the Control of Structures*, 16(7-8):703–723, 2009.
- [118] Yangwen Zhang, Thomas Schauer, and Achim Bleicher. Assessment of wind-induced vibration suppression and energy harvesting using facades. In *20th CONGRESS OF IABSE New York City*, pages 352–356, 2019.
- [119] Jann N Yang, Anil K Agrawal, Bijan Samali, and Jong-Cheng Wu. Benchmark problem for response control of wind-excited tall buildings. *Journal of engineering mechanics*, 130(4):437–446, 2004.
- [120] Hermann Frahm. Device for damping vibrations of bodies., April 18 1911. US Patent 989,958.
- [121] J. Ormondroyd and J.P. Den Hartog. The theory of the dynamic vibration absorber. *Trans. ASME* 49/50, A9-A22, 1928.
- [122] Isao Nishimura. *Vibration control of building structures by active tuned mass damper*. PhD thesis, The University of Tokyo, 1994.
- [123] Giulia Di Giovanni and Davide Bernardini. Vibration damping performances of buildings with moving façades under harmonic excitation. *Journal of Vibration Engineering & Technologies*, 2020.
- [124] Yangwen Zhang, Thomas Schauer, and Achim Bleicher. Optimized passive/semi-active vibration control using distributed-multiple tuned facade damping system in tall buildings. *Journal of Building Engineering*, 52:104416, 2022.

BIBLIOGRAPHY

- [125] Hideo Takabatake, Yukihiko Kitada, Izuru Takewaki, and Akiko Kishida. *Structural Properties of High-Rise Buildings*, pages 1–14. Springer Singapore, Singapore, 2019.
- [126] Naser Mostaghel and Todd Davis. Representations of coulomb friction for dynamic analysis. *Earthquake engineering & structural dynamics*, 26(5):541–548, 1997.
- [127] DIN EN 1991-1-4/NA: 2010-12. Nationaler Anhang–National festgelegte Parameter–Eurocode 1: Einwirkungen auf Tragwerke–Teil 1-4: Allgemeine Einwirkungen–Windlasten. Standard, Beuth Verlag Berlin, 2010.
- [128] André Preumont. *Vibration control of active structures: an introduction*, volume 246. Springer, 2018.
- [129] Johannes Brändlein, Paul Eschmann, Ludwig Hasbargen, and Karl Weigand. *Ball and roller bearings: theory, design and application*. Wiley, 1999.
- [130] T.A. Harris and M.N. Kotzalas. *Advanced Concepts of Bearing Technology: Rolling Bearing Analysis, Fifth Edition*. Rolling Bearing Analysis, Fifth Edition. CRC Press, 2006.
- [131] Avraham Harnoy. *Bearing design in machinery: engineering tribology and lubrication*. CRC Press, 2002.
- [132] Bijan Samali, KCS Kwok, GS Wood, and JN Yang. Wind tunnel tests for wind-excited benchmark building. *Journal of Engineering Mechanics*, 130(4):447–450, 2004.
- [133] Standards Association of Australia. *Minimum Design Loads on Structures (known as the SAA Loading Code): Wind Loads*. Standards Australia, 1989.
- [134] Emil Simiu and Robert H Scanlan. *Wind effects on structures: fundamentals and applications to design*. Wiley New York, 1996.
- [135] Thomas Duriez, Steven L Brunton, and Bernd R Noack. *Machine learning control-taming nonlinear dynamics and turbulence*, volume 116. Springer, 2017.
- [136] Douglas E Ivers and Lane R Miller. Semi-active suspension technology. an evolutionary view. *ASME, NEW YORK, NY,(USA)*., 40:327–346, 1991.
- [137] D. Karnopp, M. J. Crosby, and R. A. Harwood. Vibration Control Using Semi-Active Force Generators. *Journal of Engineering for Industry*, 96(2):619–626, 05 1974.
- [138] Jeong-Hoi Koo, Mehdi Ahmadian, Mehdi Setareh, and Thomas Murray. In search of suitable control methods for semi-active tuned vibration absorbers. *Journal of Vibration and Control*, 10(2):163–174, 2004.
- [139] Demetris Demetriou, Nikolaos Nikitas, and Konstantinos Daniel Tsavdaridis. Performance of fixed-parameter control algorithms on high-rise structures equipped with semi-active tuned mass dampers. *The Structural Design of Tall and Special Buildings*, 25(7):340–354, 2016.
- [140] Mark H Richardson and C Jamestown. Modal mass, stiffness and damping. *Vibrant Technology, Inc., Jamestown, CA*, pages 1–5, 2000.
- [141] Silvan Marcus. The new supers: super-slender towers of new york. In *Proceedings of the CTBUH 2015 International Conference «Global Interchanges: Resurgence of the Skyscraper City»*. New York, USA. 26th, pages 60–65, 2015.
- [142] PW Bearman and ED Obasaju. An experimental study of pressure fluctuations on fixed and oscillating square-section cylinders. *Journal of Fluid Mechanics*, 119:297–321, 1982.

- [143] Said Elias, Vasant Matsagar, and TK Datta. Dynamic response control of a wind-excited tall building with distributed multiple tuned mass dampers. *International Journal of Structural Stability and Dynamics*, 19(06):1950059, 2019.
- [144] Thomas Schauer, Achim Bleicher, Yangwen Zhang, Wulf Wulff, and Laurenz Wernicke. *Schwingungsdämpfung und Energiegewinnung mit beweglichen Doppelfassaden: Entwurf, Optimierung und Validierung eines autarken verteilten semiaktiven Systems zur Reduktion Wind-induzierter Schwingungen bei schlanken Hochhäusern*. BBSR-Online-Publikation 08/2022, Bonn, April 2022.
- [145] Yangwen Zhang, Laurenz Wernicke, Wulf Wulff, Achim Bleicher, and Thomas Schauer. Design and validation of a dual-functional damper based on a stepper motor for energy harvesting and vibration control. Manuscript submitted for publication.
- [146] Neil Sclater. *Mechanisms and mechanical devices sourcebook*. McGraw-Hill Education, 2011.
- [147] Clarence W De Silva. *Modeling and control of engineering systems*. Crc Press, 2009.
- [148] Chang-liang Xia. *Permanent magnet brushless DC motor drives and controls*. John Wiley & Sons, 2012.
- [149] Farshad Khorrani, Prashanth Krishnamurthy, and Hemant Melkote. *Modeling and adaptive nonlinear control of electric motors*. Springer Science & Business Media, 2003.
- [150] Marc Bodson, John N Chiasson, Robert T Novotnak, and Ronald B Rekowski. High-performance nonlinear feedback control of a permanent magnet stepper motor. *IEEE Transactions on Control Systems Technology*, 1(1):5–14, 1993.
- [151] Tom J Kazmierski and Steve Beeby. *Energy harvesting systems*. Springer, 2014.
- [152] Neil G Stephen. On energy harvesting from ambient vibration. *Journal of sound and vibration*, 293(1-2):409–425, 2006.
- [153] Bernard H Stark, Paul D Mitcheson, Peng Miao, Tim C Green, Eric M Yeatman, and Andrew S Holmes. Converter circuit design, semiconductor device selection and analysis of parasitics for micropower electrostatic generators. *IEEE Transactions on Power Electronics*, 21(1):27–37, 2006.
- [154] Elie Lefeuvre, David Audigier, Claude Richard, and Daniel Guyomar. Buck-boost converter for sensorless power optimization of piezoelectric energy harvester. *IEEE Transactions on Power Electronics*, 22(5):2018–2025, 2007.
- [155] Suman Dwari, Rohan Dayal, Leila Parsa, and Khaled Nabil Salama. Efficient direct ac-to-dc converters for vibration-based low voltage energy harvesting. In *2008 34th Annual Conference of IEEE Industrial Electronics*, pages 2320–2325. IEEE, 2008.
- [156] Suman Dwari and Leila Parsa. An efficient ac–dc step-up converter for low-voltage energy harvesting. *IEEE Transactions on Power Electronics*, 25(8):2188–2199, 2010.
- [157] Rohan Dayal, Suman Dwari, and Leila Parsa. Design and implementation of a direct ac–dc boost converter for low-voltage energy harvesting. *IEEE transactions on industrial electronics*, 58(6):2387–2396, 2010.
- [158] Emmanuelle Arroyo and Adrien Badel. Electromagnetic vibration energy harvesting device optimization by synchronous energy extraction. *Sensors and Actuators A: Physical*, 171(2):266–273, 2011.

- [159] Takehiko Asai, Yoshikazu Araki, and Kohju Ikago. Energy harvesting potential of tuned inertial mass electromagnetic transducers. *Mechanical Systems and Signal Processing*, 84:659–672, 2017.
- [160] Robert W Erickson and Dragan Maksimovic. *Fundamentals of power electronics*. Springer Science & Business Media, 2007.
- [161] Achim Bleicher, Thomas Schauer, Robert Jirasek, Tim Höltnke, Yangwen Zhang, Paul Marker, Wulf Wulff, Johannes Manfrecola, and Therese Schmidt. Hybride Konstruktionen an der BTU Cottbus-Senftenberg. *Bautechnik*, 98(12):907–920, 2021.
- [162] Yangwen Zhang, Wulf Wulff, Laurenz Wernicke, Michael Engelmann, Thomas Schauer, and Achim Bleicher. Experimental identification and verification of a moveable facade element for energy harvesting and vibration control. *Journal of Building Engineering*, 65:105712, 2023.
- [163] Yiqiang Zhang. Experimental validation of vibration control and energy harvesting performance for a distributed-multiple tuned facade damper (d-MTFD) system using Hardware-in-the-Loop (HiL) simulations. Master thesis, Technische Universität Berlin, 2022.
- [164] Michael Engelmann, Wulf Wulff, Thomas Lorenz, Simon Frey, Laurenz Wernicke, Yangwen Zhang, Thomas Schauer, and Achim Bleicher. How to Exploit the Glass Mass for Damping a Building? In *Challenging Glass Conference Proceedings*, volume 8, 2022.
- [165] B Armstrong and C de Wit. “Canudas,” friction modeling and compensation”, the control handbook, 1995.
- [166] Paul P Acarnley. *Stepping motors: a guide to theory and practice*. IET Control Engineering Series 63. IET, 2002.

